# Microstructural imaging of the human spinal cord with advanced diffusion MRI

**Francesco Grussu**

Thesis submitted for the degree of
**Doctor of Philosophy**
of the
**University College London**

Field of study: Magnetic Resonance Physics

Department of Neuroinflammation,
Institute of Neurology

I, Francesco Grussu confirm that the work presented in this thesis is my own.

Where information has been derived from other sources,
I confirm that this has been indicated in the thesis.

# Abstract

The aim of this PhD thesis is to advance the state-of-the-art of spinal cord magnetic resonance imaging (MRI) in multiple sclerosis (MS), a demyelinating, inflammatory and neurodegenerative disease of the central nervous system.

*Neurite orientation dispersion and density imaging* (NODDI) is a recent diffusion-weighted (DW) MRI technique that provides indices of density and orientation dispersion of neuronal processes. These could be new useful biomarkers for the spinal cord, since they could better characterise overall, widespread MS pathology than conventional metrics.

In this thesis, we test innovative clinically feasible acquisitions as well as signal analysis methods to study the potential of NODDI for the spinal cord. We also design and run computer simulations that corroborate our *in vivo* findings. Furthermore, we compare NODDI metrics to quantitative histological features, with the aim of validating their specificity.

The thesis is divided in two parts. In the first part, *in vivo* experiments are described. Specific objectives are: i) to demonstrate the feasibility of performing NODDI in the spinal cord and in clinical settings; ii) to study the possibility of extracting with new approaches such as NODDI more specific microstructural information from standard DW acquisitions; iii) to assess how features typical of spinal cord microstructure, such as presence of large axons, influence NODDI metrics.

In the second part of the thesis, *ex vivo* experiments are discussed. Their objective is the validation of the specificity of NODDI metrics via comparison to quantitative histology in *post mortem* spinal cord tissue. The experiments required the implementation of high-field DW scans as well as histological procedures and complex analysis pipelines.

The results of this thesis contribute to current scientific knowledge. They prove that NODDI offers new opportunities to study how neurodegenerative diseases such as MS alter neural tissue complexity. We showed for the first time that NODDI can be performed in the spinal cord *in vivo* and in clinical scans. We also demonstrated that NODDI analysis of standard DW data is challenging, and quantified how the presence of large axons in the spinal cord influences NODDI metrics. Lastly, our *ex vivo* data highlight that unlike routine DW MRI methods, NODDI can detect reliably pathological variations of neurite orientation dispersion. NODDI is also sensitive to the density of axons and dendrites, but can not fully resolve axonal loss and demyelination in MS.

We believe that the technique is a key element of a more general multi-modal MRI approach, which is necessary to obtain a complete description of complex diseases such as MS.

*A babai, mamai e fradi miu*

# Acknowledgements

One of the major challenges I faced during the writing of this PhD thesis was to find an appropriate way of acknowledging the support of those without whom this PhD project would not have been completed. This section aims to demonstrate my warm and sincere gratitude to all of them.

I am thankful to my PhD supervisors, Professor Claudia Gandini Wheeler-Kingshott and Professor Daniel Alexander, for their excellent supervision during the past three years. I acknowledge their unconditional support, that never made me feel alone in the difficult world of MRI research. I thank them for their invaluable feedback, and for creating two wonderful research groups (the Physics team within the NMR Research Unit and the MIG/POND groups) where working was a great pleasure. I really believe that my supervisors taught me how to be a true scientist, and I will always carry with me their useful lessons.

I am grateful to Doctor Torben Schneider. Torben was for me a true third supervisor, other than a good friend. I thank him for useful discussion and advice during the Monday morning meetings, for teaching me how to set up and control our 3T MRI scanner, for showing me how to perform high-field *ex vivo* MRI experiments and for helping me keep the collaboration between London and Oxford viable and fruitful. Working with Torben was very stimulating, indeed one of the nicest things that happened during my PhD in London.

I would like to express sincere gratitude to Professor Gabriele DeLuca from the University of Oxford. He was a fantastic collaborator, and his invaluable expertise contributed heavily to this PhD thesis. He made me feel an honorary member of his research team, and always showed kind hospitality when I went to Oxford. He made me feel at home even in his Canada, in Toronto, where he went with me through my ISMRM presentation. I really hope to have again the opportunity of working with him.

I am also thankful to Doctor Gary Hui Zhang. My work has focussed on NODDI, and certainly has benefited a lot of his useful suggestions and of his thorough reviews, which directed my choices towards the simplest and most elegant solutions.

I would like to thank everyone else who was directly involved in the projects presented in this thesis: Doctor Carmen Tur for her invaluable statistical expertise; Doctor Mohamed Tachrount for his help with the high-field MRI acquisitions; Doctor Jia Newcombe for providing spinal cord tissue specimens; Richard Yates and Janis Carter for their help with histological procedures; Doctor Andrada Ianus for her help with the implementation of the DTI-Dot model; Doctor Enrico Kaden for his

script drawing samples from a Watson distribution; Doctor Ferran Prados for his suggestions about spinal cord image registration.

I am grateful to Doctor Hugh Kearney, who gave me access to his data in 2012 to familiarise with diffusion weighted images of the spinal cord, and to Doctor Marios Yiannakas, always ready to share one of his MRI sequences for a quick test and willing to give a hand during the MRI sessions.

Many thanks go to Professor David Miller and to Professor Olga Ciccarelli, who led the NMR Research Unit during my PhD and made it a stimulating research team.

Also, I would like to thank all members of the NMR Research Unit, of the Microstructure Imaging Group and of the Progression of Neurodegenerative Disease team, for useful discussion and suggestions during our regular meetings and for being real friends. In particular, I would like to thank those who offered to review individual chapters of my thesis: Carmen, Torben, Marco, Andrada, Becky, Neil and Viktor.

Thanks to radiographers Mr Luke Hoy and Ms Chichi Ugorji who often helped during my MRI scans, and to Mr Jon Steel for support with IT and software issues.

Thanks to everyone who volunteered to be a “second person” during my MRI sessions and to those who ran MRI scans of myself for my studies.

Thanks to all my volunteers, who offered a bit of their time for me to have MRI data to work with.

Thanks to the UCL NeuroResource tissue bank and to the Oxford brain bank (Thomas Willis brain collection) for providing spinal cord tissue specimens for my investigations.

Thanks to the UCL Grand Challenge Studentships program that funded my PhD.

Thanks to Ms Ifrah Iidow for helping me print my posters always so promptly.

Thanks to the examiners of my MPhil/PhD transfer and to the examiners of my final PhD viva for taking some time to evaluate my scientific production.

Thanks to my friends Daniele Farris, Marco Caria, Giacomo Scheich, Emanuele Corriga and Marco Battiston, who were always ready to support me during the toughest periods of my PhD.

Thanks to wonderful Carmen, for supporting me so much during these last, stressful months, and for making my days better with her smile.

I conclude the acknowledgements thanking my family: my father Pietro, my mother Marisa and my brother Giuseppe. In spite of the distance, they made me feel as if they were always here with me in London, celebrating my achievements and having a laugh together to forget about difficulties. *Est su praghere prus mannu de totus a iscriere ca seis sa fortza mia!*

Francesco

18th of December 2015

# Contributors

The work presented in this thesis would not have been possible without the following contributions.

- Prof Claudia Gandini Wheeler-Kingshott (UCL): supervision; discussion and results interpretation.
- Prof Daniel Alexander (UCL): supervision; discussion and results interpretation.
- Dr Torben Schneider (UCL): help with MRI data acquisition (both *in vivo* and *ex vivo*) and with the implementation of the MRI-histology pipeline; discussion and results interpretation.
- Prof Gabriele C. DeLuca (University of Oxford): carried out histological procedures; provided spinal cord tissue specimens; discussion and results interpretation.
- Dr Hui Zhang (UCL): discussion and results interpretation.
- Dr Mohamed Tachrount (UCL): help with *ex vivo* MRI data acquisition.
- Dr Carmen Tur (UCL): statistical advice and useful discussion.
- Dr Enrico Kaden, Dr Ferran Prados and Dr Andrada Ianus (UCL): provided useful suggestions and some practical help with data synthesis and analysis.
- Dr Jia Newcombe (UCL): provided spinal cord tissue specimens.
- Mr Richard Yates and Ms Janis Carter (University of Oxford): contributed to the histological procedures.

*“B’a’ cosas chi pro las cumprendere bi chere’ tempus e isperienzia;*
*e cosas chi cand’un’at isperienzia no las cumprende’ prusu.”*

Mialinu Pira, *Sos Sinnos*

# Contents

**List of Figures** 14

**List of Tables** 17

**List of Abbreviations** 18

**List of Frequent Symbols** 20

**1 Introduction** 22
1.1 Background . . . 22
1.2 Problem statement . . . 22
1.3 Aims . . . 22
1.4 Scientific relevance of the work . . . 23
1.5 Structure of the thesis . . . 25

**2 Neuroanatomy and multiple sclerosis: an overview** 26
2.1 Neurons and neural tissue . . . 26
2.2 The human spinal cord . . . 27
2.3 Multiple sclerosis . . . 28

**3 Background** 30
3.1 Introduction to magnetic resonance imaging . . . 30
3.2 Spins and magnetic moments . . . 31
3.2.1 Dynamics of a spin from classical mechanics . . . 31
3.2.2 Larmor precession of a spin . . . 32
3.2.3 The rotating reference frame . . . 33
3.3 Bloch equations and relaxation . . . 34
3.3.1 The Bloch equations . . . 35
3.3.2 Relaxation time constants . . . 35
3.3.3 Evolution of the magnetisation under a static field . . . 37
3.3.4 Response of the magnetisation to *on resonance* excitation . . . 38
3.3.5 Multicomponent relaxation . . . 39
3.3.6 Bloch-Torrey equations . . . 40

3.4 Signal detection and imaging equation . . . . . . . . . . . . . . . . . . . . . . . . . . 40
    3.4.1 From the magnetisation to a measurable signal . . . . . . . . . . . . . . . . . 40
    3.4.2 The imaging problem . . . . . . . . . . . . . . . . . . . . . . . . . . . . . . . 41
3.5 Common MRI signal weightings . . . . . . . . . . . . . . . . . . . . . . . . . . . . 42
    3.5.1 Free induction decay and gradient echo . . . . . . . . . . . . . . . . . . . . 43
    3.5.2 Inversion recovery . . . . . . . . . . . . . . . . . . . . . . . . . . . . . . . . 43
    3.5.3 Spin echo experiment . . . . . . . . . . . . . . . . . . . . . . . . . . . . . . 44
    3.5.4 Stimulated echo acquisition mode (STEAM) . . . . . . . . . . . . . . . . . . 46
    3.5.5 Repeated sequences . . . . . . . . . . . . . . . . . . . . . . . . . . . . . . . 47
3.6 Sampling methods . . . . . . . . . . . . . . . . . . . . . . . . . . . . . . . . . . . . 48
    3.6.1 Field-of-view and resolution . . . . . . . . . . . . . . . . . . . . . . . . . . . 48
    3.6.2 2D and 3D imaging . . . . . . . . . . . . . . . . . . . . . . . . . . . . . . . . 50
    3.6.3 Echo planar imaging . . . . . . . . . . . . . . . . . . . . . . . . . . . . . . . 52
3.7 Noise and signal-to-noise ratio . . . . . . . . . . . . . . . . . . . . . . . . . . . . . 53
3.8 Speeding up the MR experiment: parallel and multiband imaging . . . . . . . . . . . 54
3.9 Diffusion MRI . . . . . . . . . . . . . . . . . . . . . . . . . . . . . . . . . . . . . . 55
    3.9.1 q-space imaging . . . . . . . . . . . . . . . . . . . . . . . . . . . . . . . . . 57
    3.9.2 Phenomenological models . . . . . . . . . . . . . . . . . . . . . . . . . . . . 57
    3.9.3 Multi-compartment models . . . . . . . . . . . . . . . . . . . . . . . . . . . . 59
    3.9.4 Alternative diffusion encoding approaches . . . . . . . . . . . . . . . . . . . 59
3.10 Quantitative MRI of the spinal cord . . . . . . . . . . . . . . . . . . . . . . . . . . 60
    3.10.1 Cardiac gating . . . . . . . . . . . . . . . . . . . . . . . . . . . . . . . . . . 61
    3.10.2 Reduced field-of-view acquisitions . . . . . . . . . . . . . . . . . . . . . . . 62
    3.10.3 Diffusion: DTI studies . . . . . . . . . . . . . . . . . . . . . . . . . . . . . . 63
    3.10.4 Diffusion: non-DTI studies . . . . . . . . . . . . . . . . . . . . . . . . . . . . 63
3.11 Validation of quantitative MRI . . . . . . . . . . . . . . . . . . . . . . . . . . . . . 64
    3.11.1 Phantom studies . . . . . . . . . . . . . . . . . . . . . . . . . . . . . . . . . 64
    3.11.2 Histological validation . . . . . . . . . . . . . . . . . . . . . . . . . . . . . . 64

**4 Demonstration of NODDI in the healthy spinal cord 68**
4.1 Introduction . . . . . . . . . . . . . . . . . . . . . . . . . . . . . . . . . . . . . . . 68
4.2 Research dissemination . . . . . . . . . . . . . . . . . . . . . . . . . . . . . . . . . 69
4.3 Theory: the NODDI model . . . . . . . . . . . . . . . . . . . . . . . . . . . . . . . . 69
4.4 Methods . . . . . . . . . . . . . . . . . . . . . . . . . . . . . . . . . . . . . . . . . 70
    4.4.1 Data acquisition . . . . . . . . . . . . . . . . . . . . . . . . . . . . . . . . . 70
    4.4.2 Motion correction . . . . . . . . . . . . . . . . . . . . . . . . . . . . . . . . . 70
    4.4.3 Segmentation . . . . . . . . . . . . . . . . . . . . . . . . . . . . . . . . . . . 71
    4.4.4 Model fitting . . . . . . . . . . . . . . . . . . . . . . . . . . . . . . . . . . . . 72
    4.4.5 Analysis . . . . . . . . . . . . . . . . . . . . . . . . . . . . . . . . . . . . . . 73
4.5 Results . . . . . . . . . . . . . . . . . . . . . . . . . . . . . . . . . . . . . . . . . . 76
    4.5.1 Data acquisition and tissue segmentation . . . . . . . . . . . . . . . . . . . 76

4.5.2 Model fitting . . . . . . . . 77
4.5.3 Characterisation of the metrics . . . . . . . . 78
4.5.4 Reproducibility . . . . . . . . 80
4.5.5 Relationship NODDI-DTI . . . . . . . . 82
4.5.6 Quality of fit . . . . . . . . 82
4.5.7 Effect of crossing fibres . . . . . . . . 84
4.6 Discussion . . . . . . . . 86
4.7 Conclusion . . . . . . . . 89

**5 NODDI analysis of single-shell data: a feasibility study 90**
5.1 Introduction . . . . . . . . 90
5.2 Research dissemination . . . . . . . . 90
5.3 Methods . . . . . . . . 91
5.3.1 Data acquisition . . . . . . . . 91
5.3.2 Motion correction . . . . . . . . 91
5.3.3 Segmentation . . . . . . . . 91
5.3.4 Model fitting . . . . . . . . 91
5.4 Comparison between single-shell and two-shell analyses . . . . . . . . 92
5.5 Results . . . . . . . . 93
5.6 Discussion . . . . . . . . 96
5.7 Conclusion . . . . . . . . 98

**6 Influence of axon diameter distribution on NODDI metrics 99**
6.1 Introduction . . . . . . . . 99
6.2 Research dissemination . . . . . . . . 100
6.3 Methods . . . . . . . . 100
6.3.1 *In silico* study . . . . . . . . 100
6.3.2 *In vivo* study . . . . . . . . 106
6.4 Results . . . . . . . . 110
6.4.1 *In silico* study . . . . . . . . 110
6.4.2 *In vivo* study . . . . . . . . 115
6.5 Discussion . . . . . . . . 116
6.6 Conclusion . . . . . . . . 121

**7 A pipeline for the histological validation of NODDI in the spinal cord 125**
7.1 Introduction . . . . . . . . 125
7.2 Research dissemination . . . . . . . . 126
7.3 Methods . . . . . . . . 126
7.3.1 Samples and MRI sessions . . . . . . . . 126
7.3.2 Adaptation of NODDI analysis for *ex vivo* DW data . . . . . . . . 129
7.3.3 Strategy to determine the radiographic position of histological sections . . . . 132
7.4 Results . . . . . . . . 134

7.4.1 Samples and MRI sessions . . . . . . . . . . 134
7.4.2 Adaptation of NODDI analysis for *ex vivo* DW data . . . . . . . . . . 134
7.4.3 Strategy to determine the radiographic position of histological sections . . . . 136
7.5 Discussion . . . . . . . . . . 137
7.6 Conclusion . . . . . . . . . . 141

**8 Estimation of neurite orientation dispersion from histological images 143**
8.1 Introduction . . . . . . . . . . 143
8.2 Research dissemination . . . . . . . . . . 144
8.3 Theory . . . . . . . . . . 144
8.3.1 Linear symmetry detection . . . . . . . . . . 144
8.3.2 Patch-wise statistics of ST orientation . . . . . . . . . . 146
8.4 Methods . . . . . . . . . . 150
8.4.1 Data acquisition . . . . . . . . . . 150
8.4.2 ST calculation . . . . . . . . . . 150
8.4.3 ST implementation efficiency . . . . . . . . . . 152
8.4.4 Variation of the local scale . . . . . . . . . . 152
8.4.5 Analysis . . . . . . . . . . 153
8.5 Results . . . . . . . . . . 153
8.5.1 Data acquisition . . . . . . . . . . 153
8.5.2 ST implementation efficiency . . . . . . . . . . 153
8.5.3 ST calculation on histological images . . . . . . . . . . 155
8.5.4 Analysis . . . . . . . . . . 160
8.6 Discussion . . . . . . . . . . 160
8.7 Conclusion . . . . . . . . . . 166

**9 Histological correlates of NODDI metrics 168**
9.1 Introduction . . . . . . . . . . 168
9.2 Research dissemination . . . . . . . . . . 169
9.3 Methods . . . . . . . . . . 169
9.3.1 Samples . . . . . . . . . . 169
9.3.2 High-field DW MRI . . . . . . . . . . 170
9.3.3 DW MRI signal model fitting . . . . . . . . . . 172
9.3.4 Histological procedures . . . . . . . . . . 172
9.3.5 Histological feature calculation . . . . . . . . . . 174
9.3.6 MRI-histology registration . . . . . . . . . . 175
9.3.7 Visual inspection of quantitative maps . . . . . . . . . . 176
9.3.8 Statistical analysis . . . . . . . . . . 176
9.4 Results . . . . . . . . . . 178
9.4.1 Histological feature calculation . . . . . . . . . . 178
9.4.2 Quantitative maps from NODDI, DTI and histology . . . . . . . . . . 178

9.4.3 Statistical analysis . . . . . . . . . . . . . . . . . . . . . . . . . . . . . . . . . . . . . 179
9.5 Discussion . . . . . . . . . . . . . . . . . . . . . . . . . . . . . . . . . . . . . . . . . . . . 187
9.6 Conclusion . . . . . . . . . . . . . . . . . . . . . . . . . . . . . . . . . . . . . . . . . . . . 193

**10 Conclusions** **194**
10.1 Key findings . . . . . . . . . . . . . . . . . . . . . . . . . . . . . . . . . . . . . . . . . . . 194
10.2 Summary . . . . . . . . . . . . . . . . . . . . . . . . . . . . . . . . . . . . . . . . . . . . 194
10.3 General conclusions . . . . . . . . . . . . . . . . . . . . . . . . . . . . . . . . . . . . . . 195
10.4 Specific conclusions from *in vivo* studies . . . . . . . . . . . . . . . . . . . . . . . . . 196
10.5 Specific conclusions from *ex vivo* studies . . . . . . . . . . . . . . . . . . . . . . . . . 197
10.6 Future directions . . . . . . . . . . . . . . . . . . . . . . . . . . . . . . . . . . . . . . . . 198

**A Example of SOP document used to plan histological procedures** **202**

**B Fitting of linear regression models: relationship MRI-histology** **209**

**Bibliography** **220**

# List of Figures

2.1 Illustration of a neuron. . . . . . . . . . . . . . . . . . . . . . . . . . . . . . . . . . . . . . . 26
2.2 Illustration of the anatomy of the human spinal cord. . . . . . . . . . . . . . . . . . . . 27

3.1 Illustration of a spinning proton and of a current loop. . . . . . . . . . . . . . . . . . . 33
3.2 Dependence of relaxation times $T_1$ and $T_2$ on the correlation time $\tau_c$ for water. . . . . 37
3.3 Behaviour of the magnetisation under a static magnetic field. . . . . . . . . . . . . . 38
3.4 Behaviour of the magnetisation after *on resonance* RF excitation. . . . . . . . . . . . 39
3.5 Free induction decay signal for various flip angles. . . . . . . . . . . . . . . . . . . . 43
3.6 Effect of the ratio $\mathrm{T_I}/T_1$ on the inversion recovery signal. . . . . . . . . . . . . . . . 44
3.7 Magnitude of the spin echo signal in presence of magnetic field inhomogeneities. . . 46
3.8 Schematic describing the sequence of RF pulses employed in STEAM. . . . . . . . 46
3.9 Example of the impact of $\mathrm{T_R}$ in a free induction decay experiment. . . . . . . . . . . 48
3.10 Example of two-dimensional k-space. . . . . . . . . . . . . . . . . . . . . . . . . . . . 49
3.11 Toy example highlighting the importance of the design of the FOV. . . . . . . . . . . 50
3.12 Schematic of a 2D MRI experiment. . . . . . . . . . . . . . . . . . . . . . . . . . . . . 51
3.13 Sampling of k-space in single-shot and multi-shot Cartesian EPI. . . . . . . . . . . . 52
3.14 Toy example of Gaussian-distributed and Rician-distributed noisy MRI images. . . . 54
3.15 Transmission electron micrograph of an axon and of its surrounding. . . . . . . . . . 55
3.16 Schematic of the PGSE sequence. . . . . . . . . . . . . . . . . . . . . . . . . . . . . . 56
3.17 Schematic of the OGSE sequence. . . . . . . . . . . . . . . . . . . . . . . . . . . . . . 60
3.18 Time intervals of the cardiac cycle exploited in cardiac gating. . . . . . . . . . . . . . 61
3.19 Schematic of ZOOM EPI. . . . . . . . . . . . . . . . . . . . . . . . . . . . . . . . . . . 62

4.1 Illustration of the algorithm used to segment GM from DW images of the spinal cord. 72
4.2 Examples of DW and non-DW images of the human spinal cord *in vivo*. . . . . . . . 75
4.3 Tissue segmentation for the *in vivo* demonstration of NODDI. . . . . . . . . . . . . . 77
4.4 Examples of DW signals and NODDI fittings from one GM and one WM voxel *in vivo*. 77
4.5 NODDI metrics and DTI FA in the spinal cord of two healthy volunteers. . . . . . . . 78
4.6 Medians of NODDI and DTI metrics within GM, WM and at whole-cord level. . . . . 79
4.7 Contrast and contrast-to-noise ratio between GM and WM for NODDI and DTI metrics. 80
4.8 Relationships between NODDI indices $v_{\mathrm{in}}$ and ODI and DTI metrics. . . . . . . . . . 83
4.9 Voxel-wise map of $\delta$BIC comparing the goodness of NODDI and DTI fits *in vivo*. . . . 84

4.10 Examples of WM voxels likely to contain crossing fibres. . . . . . . . . . . . . . . . . 84
4.11 Permutation test assessing the impact of crossing fibres on NODDI metrics. . . . . . 85

5.1 Voxel-wise percentage relative error for $v_{\text{r}}$ from single-shell analysis. . . . . . . . . . 94
5.2 Voxel-wise percentage relative error for ODI from single-shell analysis. . . . . . . . . 95
5.3 Scatter plots and distributions of errors characterising single-shell NODDI analysis. . 96

6.1 Illustration of the substrates employed in Monte Carlo simulations. . . . . . . . . . . 102
6.2 Model of PGSE sequence employed to run simulations. . . . . . . . . . . . . . . . . 104
6.3 Metric $v_{\text{iso}}$ obtained from fitting NODDI to simulated data. . . . . . . . . . . . . . . 109
6.4 Metric $v_{\text{in}}$ obtained from fitting NODDI to simulated data. . . . . . . . . . . . . . . . 110
6.5 Metric $v_{\text{r}}$ obtained from fitting NODDI to simulated data. . . . . . . . . . . . . . . . 111
6.6 Metric ODI obtained from fitting NODDI to simulated data. . . . . . . . . . . . . . . . 112
6.7 NODDI metrics *in vivo* as the diffusion time varies (first MRI session). . . . . . . . . 113
6.8 NODDI metrics *in vivo* as the diffusion time varies (second MRI session). . . . . . . 114
6.9 Distributions of NODDI metrics in WM as the diffusion time varies (first session). . . 116
6.10 Distributions of NODDI metrics in GM as the diffusion time varies (first session). . . 117
6.11 Distributions of NODDI metrics in WM as the diffusion time varies (second session). 118
6.12 Distributions of NODDI metrics in GM as the diffusion time varies (second session). 120

7.1 Example of a manually drawn sketch used to plan the histological procedures. . . . 131
7.2 Example of axial MRI views used to plan the histological procedures. . . . . . . . . . 132
7.3 Examples of SNR maps calculated to compare DW MRI protocols *ex vivo*. . . . . . . 135
7.4 Quantitative $T_2$ map obtained from *ex vivo* spinal cord tissue. . . . . . . . . . . . . 135
7.5 Distributions of BIC for models NODDI and NODDI-Dot *ex vivo* (control cases). . . . 136
7.6 Distributions of BIC for models NODDI and NODDI-Dot *ex vivo* (MS cases). . . . . . 138
7.7 Distributions of BIC for models DTI and DTI-Dot *ex vivo* (control cases). . . . . . . . 140
7.8 Distributions of BIC for models DTI and DTI-Dot *ex vivo* (MS cases). . . . . . . . . . 140
7.9 Examples of the good correspondence between MRI and histological images. . . . . 141

8.1 Meaning of angle $\theta$ employed in Structure Tensor equations. . . . . . . . . . . . . . 145
8.2 Polar diagram of the Watson distribution. . . . . . . . . . . . . . . . . . . . . . . . . 148
8.3 Bivariate weighted-Watson distribution. . . . . . . . . . . . . . . . . . . . . . . . . . 151
8.4 Marginal distributions of $\theta$ and $\alpha$ from the bivariate weighted-Watson distribution. . . 151
8.5 Examples of histological images employed to study Structure Tensor analysis. . . . 154
8.6 Computational efficiency of the parallel implementation of Structure Tensor analysis. 155
8.7 Hue-saturation-value encoding of the Structure Tensor in WM. . . . . . . . . . . . . 156
8.8 Hue-saturation-value encoding of the Structure Tensor in GM. . . . . . . . . . . . . . 157
8.9 Distributions of Structure Tensor orientations in WM. . . . . . . . . . . . . . . . . . . 158
8.10 Distributions of Structure Tensor orientations in GM. . . . . . . . . . . . . . . . . . . 159
8.11 Distributions of Structure Tensor anisotropy index in WM. . . . . . . . . . . . . . . . 161
8.12 Distributions of Structure Tensor anisotropy index in GM. . . . . . . . . . . . . . . . . 162

8.13 Values of the maximised log-likelihood for the Watson and weighted-Watson models. 163
8.14 Values of circular variance from the Watson and weighted-Watson models. . . . . . 164
8.15 Contrast and contrast-to-noise ratio of circular variance between GM and WM. . . . 165

9.1 Features derived from histological images for the quantitative comparison MRI-histology.180
9.2 Quantitative maps from MRI and histology (upper thoracic control case). . . . . . . . 183
9.3 Quantitative maps from MRI and histology (upper lumbar control case). . . . . . . . 184
9.4 Quantitative maps from MRI and histology (upper thoracic MS case). . . . . . . . . . 185
9.5 Quantitative maps from MRI and histology (upper lumbar MS case). . . . . . . . . . 186

# List of Tables

4.1 Medians and ranges of NODDI and DTI metrics in the spinal cord *in vivo*. . . . . . . 80
4.2 Coefficient of variation (CoV) of NODDI and DTI metrics from *in vivo* DW data. . . . 81
4.3 Intraclass correlation coefficient (ICC) of NODDI and DTI metrics from *in vivo* DW data. 81

5.1 Summary of the four NODDI analyses comparing single and double-shell fitting. . . 92
5.2 Correlation coefficients between single and two-shell NODDI metrics. . . . . . . . . 96

6.1 Summary of the characteristics of the substrates employed in Monte Carlo simulations.102
6.2 Summary of the four simulated PGSE experiments. . . . . . . . . . . . . . . . . . . . 105
6.3 Summary of the three PGSE experiments performed in the first *in vivo* MRI session. 107
6.4 Summary of the three PGSE experiments performed in the second *in vivo* MRI session.107

7.1 Information regarding the specimens of spinal cord tissue used for the *ex vivo* studies.127
7.2 Details of the diffusion MRI protocols implemented for the *ex vivo* studies. . . . . . . 129

9.1 Information about the specimens of MS spinal cord included in the *ex vivo* study. . . 171
9.2 Details of the diffusion MRI protocols employed for the comparison MRI-histology. . 171
9.3 MRI-derived and histology-derived metrics analysed for the validation of NODDI. . . 173
9.4 Linear regression models relating MRI-derived and histology-derived metrics. . . . . 176

B.1 Fitting of linear regression model no. 1 in the control cases. . . . . . . . . . . . . . . 210
B.2 Fitting of linear regression model no. 1 in the MS cases. . . . . . . . . . . . . . . . . 211
B.3 Fitting of linear regression model no. 2 in the control cases. . . . . . . . . . . . . . . 212
B.4 Fitting of linear regression model no. 2 in the MS cases. . . . . . . . . . . . . . . . . 213
B.5 Fitting of linear regression model no. 3 in the control cases. . . . . . . . . . . . . . . 214
B.6 Fitting of linear regression model no. 3 in the MS cases. . . . . . . . . . . . . . . . . 215
B.7 Fitting of linear regression model no. 4 in the control cases. . . . . . . . . . . . . . . 216
B.8 Fitting of linear regression model no. 4 in the MS cases. . . . . . . . . . . . . . . . . 217
B.9 Fitting of linear regression model no. 5 in the control cases. . . . . . . . . . . . . . . 218
B.10 Fitting of linear regression model no. 5 in the MS cases. . . . . . . . . . . . . . . . . 219

# List of Abbreviations

| Abbreviation | Full name |
|---|---|
| AD | Axial diffusivity |
| ADC | Apparent diffusion coefficient |
| ALS | Amyotrophic lateral sclerosis |
| ASF | Astrocyte staining fraction |
| BPP | Bloembergen-Purcell-Pound |
| BW | Bandwidth |
| CHARMED | Composite hindered and restricted model of diffusion |
| CNR | Contrast-to-noise ratio |
| CNS | Central nervous system |
| CoV | Coefficient of variation |
| CSF | Cerebrospinal fluid |
| CV | Circular variance |
| DBSI | Diffusion basis spectrum imaging |
| DKI | Diffusion kurtosis imaging |
| dODF | Diffusion orientation distribution function |
| DoG | Derivative-of-Gaussian |
| DTI | Diffusion tensor imaging |
| DVF | Dot volume fraction |
| DW | Diffusion weighted |
| EDSS | Expanded disability status scale |
| EPI | Echo planar imaging |
| FA | Fractional anisotropy |
| FE | Fractional eccentricity |
| FFE | Fast field echo |
| FID | Free induction decay |
| fODF | Fibre orientation distribution function |
| FOV | Field-of-view |
| GFA | Generalised fractional anisotropy |
| GFAP | Glial fibrillary acidic protein |
| GM | Grey matter |
| GRAPPA | Generalized autocalibrating partially parallel acquisitions |
| HARDI | High angular resolution diffusion imaging |
| HSV | Hue-saturation-value |
| Iba1 | Ionized calcium-binding adapter molecule 1 |
| ICC | Intraclass correlation coefficient |
| IVIM | Intravoxel incoherent motion |

| Abbreviation | Full name |
|---|---|
| mcDESPOT | Multicomponent driven equilibrium single pulse observation of $T_1/T_2$ |
| MD | Mean diffusivity |
| mPFG | Multiple pulsed field gradient |
| MR | Magnetic resonance |
| MRI | Magnetic resonance imaging |
| MS | Multiple sclerosis |
| MSF | Myelin staining fraction |
| $\mu$GSF | Microglia staining fraction |
| NMR | Nuclear magnetic resonance |
| NODDI | Neurite orientation dispersion and density imaging |
| NSF | Neurofilament staining fraction |
| ODI | Orientation dispersion index |
| OGSE | Oscillating gradient spin echo |
| OVS | Outer volume suppression |
| PBS | Phosphate buffered saline |
| PGSE | Pulse gradient spin echo |
| PLP | Proteolipid protein |
| PPMS | Primary progressive multiple sclerosis |
| QBI | q-ball imaging |
| qMRI | Quantitative magnetic resonance imaging |
| QSI | q-space imaging |
| RD | Radial diffusivity |
| RF | Radio frequency |
| rFOV | Reduced field-of-view |
| ROI | Region-of-interest |
| RRMS | Relapsing remitting multiple sclerosis |
| RSI | Restriction spectrum imaging |
| SCI | Spinal cord injury |
| SD | Spherical deconvolution |
| SE | Spin echo |
| SENSE | Sensitivity encoding |
| SNR | Signal-to-noise ratio |
| SOCS | Serial optical coherence scanning |
| SOP | Standard-operating-procedure |
| SPMS | Secondary progressive multiple sclerosis |
| ST | Structure tensor |
| STEAM | Stimulated echo acquisition mode |
| TDI | Track-density imaging |
| VERDICT | Vascular, extracellular and restricted diffusion for cytometry in tumors |
| WM | White matter |
| WMFL | White matter focal lesion |
| ZOOM | Zonal oblique multi-slice |

# List of Frequent Symbols

| Symbol | Meaning |
|---|---|
| $\alpha$ | Structure tensor anisotropy index |
| $b$ | Diffusion weighting strength ($b$-value) |
| $\mathbf{B}$ | Magnetic field |
| $\mathbf{B_0}$ | Static magnetic field (polarisation) |
| $\mathbf{B_1}$ | RF magnetic field (excitation) |
| $\Delta B_z$ | Longitudinal magnetic field inhomogeneity |
| $\beta_0$, $\beta_1$, ... | Coefficients of linear regression models |
| $\mathbf{D}$ | Diffusion tensor |
| $D$ | Diffusivity |
| $d_{\|}$ | NODDI neural tissue diffusivity |
| $d_{\text{iso}}$ | NODDI isotropic compartment diffusivity |
| $\delta$ | Magnetic field gradient duration (PGSE sequence) |
| $\Delta$ | Pulse separation (PGSE sequence) |
| $f_0$ | Larmor frequency |
| $\mathbf{G}$ | Magnetic field gradient |
| $\mathbf{g}$ | Magnetic field gradient direction |
| $G$ | Magnetic field gradient strength |
| $\gamma$ | Gyromagnetic ratio |
| $\theta$ | Structure tensor orientation |
| $\theta_f$ | Flip angle |
| $I_0$ | Modified Bessel function of the first kind and order zero |
| $\mathbf{J}$ | Structure tensor |
| $\mathbf{k}$ | Spatial frequency vector |
| $\kappa$ | Concentration parameter of directional distributions |
| $\log L$ | Logarithm of the likelihood (log-likelihood) |
| $\lambda_1$, $\lambda_2$, ... | Eigenvalues of structure/diffusion tensors |
| $\mathbf{M}$ | Magnetisation vector |
| $\mathbf{M}_\perp$, $M_\perp$ | Transverse component of the magnetisation |
| $m$ | Symbol used to indicate one among a list of metrics |
| $\boldsymbol{\mu}$, $\mu$ | Mean orientation of directional distributions |
| $\boldsymbol{\mu}$ | Magnetic moment (in chapter 3) |
| $\nu$ | Spread parameter of a Rician distribution |
| $\mathbf{p}$ | Set of parameters of a model |
| $\mathbf{q}$ | q-vector |
| $\mathbf{r}$ | Spatial position vector |
| $R^2$ | Coefficient of determination |

| Symbol | Meaning |
|---|---|
| $\rho_0$ | Spin density |
| $s$ | Magnetic resonance signal |
| $t$ | Time |
| $t_{\mathsf{del}}$ | Delay used in simulated PGSE sequences (chapter 6) |
| $t_s$ | Sampling time |
| $T_1$ | Spine-lattice (longitudinal) relaxation time |
| $T_2$ | Spine-spin (transverse) relaxation time |
| $T_2^*$ | Relaxation time of non-refocussed transverse magnetisation |
| $T_d$ | Diffusion time |
| $\mathsf{T_E}$ | Echo time |
| $\mathsf{T_I}$ | Inversion time |
| $\mathsf{T_R}$ | Repetition time |
| $\tau_c$ | Correlation time |
| $\phi$ | Phase |
| $v_{\mathsf{dot}}$ | *Dot* volume fraction |
| $v_{\mathsf{in}}$ | NODDI intra-neurite tissue volume fraction |
| $v_{\mathsf{iso}}$ | NODDI isotropic volume fraction |
| $v_{\mathsf{r}}$ | NODDI intra-neurite voxel volume fraction |
| $\sigma_{\mathsf{B}}^2$ | Between-subject variance |
| $\sigma_{\mathsf{TOT}}^2$ | Total variance |
| $\sigma_{\mathsf{W}}^2$ | Within-subject variance |
| $\sigma$ | Standard deviation of kernels in structure tensor analysis |
| $\boldsymbol{\omega}_0$ | Larmor frequency vector (radial frequency) |
| $\omega_0$ | Larmor frequency (radial frequency) |

# Chapter 1

# Introduction

## 1.1 Background

Magnetic resonance imaging (MRI) is an important diagnostic tool employed routinely in clinical practice. MRI is key in monitoring disorders affecting the spinal cord, such as multiple sclerosis (MS), a disabling disease of the central nervous system. Current clinical MRI protocols for imaging the spinal cord in MS rely on conventional techniques that detect the number and volume of focal lesions and spinal cord atrophy. These are useful outcome measures, but alone do not capture the complexity of the disease. They underestimate the overall, widespread effects that MS has on the spinal cord [96], and provide only a partial explanation for the progression of the disability.

## 1.2 Problem statement

Novel MRI biomarkers are urgently needed to measure specific features of tissue pathology in neurological disorders. The intrinsic limitations of conventional MRI techniques, which detect macroscopic aspects of disease processes and are not sensitive to early microscopic tissue damage, demand efforts by the MRI research community to develop new quantitative imaging methods.

Innovative MRI metrics are required in neurological conditions such as MS, in order to disentangle the pathophysiological components of the disease in a non-invasive fashion. This could potentially lead to earlier diagnosis and more accurate prognosis. Moreover, such new MRI measures could also offer more effective ways of monitoring treatment efficacy than current techniques, with the benefit of reducing sample sizes in clinical trials of emerging neuroprotective treatments.

## 1.3 Aims

New quantitative MRI techniques are currently being developed to study tissue pathology in neurological conditions *in vivo*. One such technique, *neurite orientation dispersion and density imaging* (NODDI) [215], is a model-based diffusion-weighted (DW) MRI method that provides estimates of density and orientation dispersion of neuronal fibres. NODDI has previously been applied in studies of the brain in neurological disorders, and we hypothesise that it could provide useful biomarkers for microstructural changes occurring in the spinal cord.

In this PhD thesis, we aim to evaluate the potential of NODDI metrics as new biomarkers in spinal cord disorders, with a particular focus on MS. Innovative clinically feasible acquisition strategies and MRI signal analysis methods are tested on the spinal cords of healthy volunteers *in vivo*. Additionally, the specificity of the indices obtained with NODDI is examined in specimens of *post mortem* human spinal cord via systematic comparison to measures obtained from histology.

Our objectives are:

1. to demonstrate that innovative acquisition methods such as NODDI, which could potentially provide new quantitative biomarkers of pathology, are feasible in the human spinal cord *in vivo* and in a clinical setting (i.e. in about 20 minutes);
2. to relate NODDI-derived indices to results from a routine DW MRI method employed in clinical studies of the spinal cord, known as *diffusion tensor imaging* (DTI) [12];
3. to study the possibility of applying NODDI analysis to standard DW data;
4. to investigate the influence of specific microstructural features of the spinal cord on NODDI metrics;
5. to test the specificity of NODDI indices and the validity of the model assumptions in the presence of MS pathology via comparison to quantitative histological features.

## 1.4 Scientific relevance of the work

This thesis provides a number of innovative contributions to MRI research, which led to a published peer-reviewed journal article and to several abstracts accepted for presentation at international scientific meetings. Three further manuscripts are also currently in preparation to be submitted for publication in peer-reviewed journals.

Specific contributions to the research field are listed below.

1. NODDI was demonstrated for the first time in the human spinal cord *in vivo*. This study is shown in chapter 4. Preliminary results were presented at international meetings as:
    - "*In vivo* estimation of neuronal orientation dispersion and density of the human spinal cord". Grussu F. et al, International Society for Magnetic Resonance in Medicine (ISMRM) workshop "Multiple sclerosis as a whole-brain disease" (2013), oral presentation.
    - "Neurite orientation dispersion and density imaging of the cervical cord *in vivo*". Grussu F. et al, ISMRM annual meeting (2014), p.1720, traditional poster.

    The full study was later published in a peer-reviewed scientific journal as:

    - "Neurite orientation dispersion and density imaging of the healthy cervical spinal cord *in vivo*", Grussu F. et al, NeuroImage (2015), vol. 111, p.590-601 (reference [67]).

2. The limitations of NODDI analysis of standard DW data of the spinal cord were identified. These are reported in chapter 5, and the work was presented to the scientific community as:
    - "Single-shell diffusion MRI NODDI with *in vivo* cervical cord data". Grussu F. et al, ISMRM annual meeting (2014), p.1716, traditional poster.
    - "Characterisation of single-shell NODDI fitting in spinal cord grey and white matter". Grussu F. et al, British Chapter of ISMRM annual meeting (2014), traditional poster.
3. The influence of spinal cord axon diameter distribution on NODDI metrics was evaluated via computer simulations and *in vivo*. This work is described in chapter 6. A scientific abstract describing the study has also been submitted for consideration to the 2016 ISMRM annual meeting. Additionally, a manuscript is currently in preparation for submission to a peer-reviewed scientific journal. The ISMRM abstract submission was:
    - "Axon diameter distribution influences diffusion-derived axonal density estimation in the human spinal cord: *in silico* and *in vivo* evidence". Grussu F. et al, ISMRM annual meeting (2016), p.2009, poster presentation.
4. A high-field, high-resolution diffusion MRI protocol for fixed *ex vivo* spinal cord specimens was implemented, as well as a procedure for NODDI analysis of the acquired data. These implementations are described in chapter 7.
5. A strategy to identify the radiographic position of histological material derived from spinal cord specimens was designed, and is discussed in chapter 7.
6. A framework based on *structure tensor* (ST) analysis [16] for the estimation of neurite orientations from optical images of spinal cord tissue was developed. The framework is described in chapter 8, and a manuscript is currently in preparation.
7. The associations between NODDI indices and quantitative histological features were identified in a study involving MRI and histological analysis of non-pathological and MS spinal cord tissue. The study is discussed in chapter 9 and relies on the technical achievements listed in previous points 4, 5 and 6. We plan to publish it in a peer-reviewed scientific journal. Results of preliminary analyses were submitted in abstract form to two scientific meetings, and presented as:
    - "Histological metrics confirm microstructural characteristics of NODDI indices in multiple sclerosis spinal cord". Grussu F. et al, ISMRM annual meeting (2015), p.0909, oral presentation.
    - "Quantitative histological correlates of NODDI orientation dispersion estimates in the human spinal cord". Grussu F. et al, ISMRM annual meeting (2015), p.0154, oral presentation.

- “Quantitative histological validation of NODDI MRI indices of neurite morphology in multiple sclerosis spinal cord”. Grussu F. et al, 31st congress of the European Committee for the Research and Treatment in Multiple Sclerosis (ECTRIMS 2015), p.0469, traditional poster presentation.

## 1.5 Structure of the thesis

This thesis is structured as follows. In chapter 2, an overview of the anatomy of the spinal cord and of its involvement in MS is presented. In chapter 3, background MRI theory and literature on which the methods of this thesis rely is summarised. In chapters 4, 5 and 6, experiments performed to investigate the potential of NODDI for applications in the human spinal cord *in vivo* are discussed. *Ex vivo* investigations are described in chapters 7, 8 and 9. The ultimate objective of that part of the thesis is the direct comparison of NODDI indices to quantitative histological features, to test their specificity in the non-pathological and MS spinal cord. Lastly, in chapter 10, a general discussion of the findings and the conclusions of the entire work are reported, as well as potential future directions.

# Chapter 2

# Neuroanatomy and multiple sclerosis: an overview

## 2.1 Neurons and neural tissue

Neurons are the elementary cells of the human central nervous system (CNS). They are made of a body or *soma*, containing the nucleus, and of several *neurites* emanating from the soma, as shown in figure 2.1.

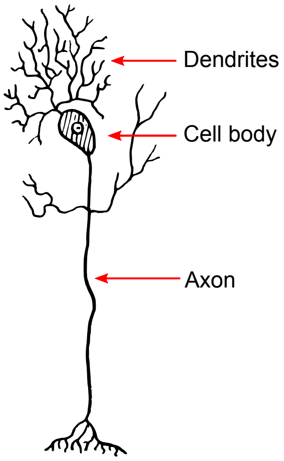

Figure 2.1: illustration of a neuron, showing the soma (cell body), dendrites and an axon. Axons and dendrites are referred to as neurites. The figure was adapted from an image by Pearson Scott Foresman, licensed via Wikimedia Commons (`https://commons.wikimedia.org/wiki/File:Dendrite_(PSF).svg`) and made available under the Creative Commons CC0 1.0 Universal Public Domain Dedication license.

Neurites can be *dendrites*, small protuberances collecting input information from neighbouring neurons, or *axons*, generally long projections transmitting information via action potentials. In the human CNS most axons are protected by a sheath that improves the conduction speed and whose thickness is about 40% of the radius of the bare axon. This sheath is made of *myelin*, a substance produced by specialised cells. Myelin is made by a mixture of lipids and proteins and is affected in several neurological conditions, such as MS.

Neurons are not the only elements of the neural tissue, which in fact contains also blood vessels and several types of *glial cells*. Glial cells provide important support functions to neurons, such as production of myelin and immune response. Neural tissue can be distinguished into *grey* and *white matter* (GM/WM). GM is made of neuronal cell bodies, dendritic arborisations as well as afferent and efferent myelinated and unmyelinated axons, glial cells and capillaries. WM represents the cabling connecting GM regions to other GM areas and to the periphery, and is made of myelinated axons and glial cells.

## 2.2 The human spinal cord

The spinal cord is part of the human CNS and is also made of GM and WM. The spinal cord has a tubular structure and runs in the superior-inferior direction, within the spinal cavity, surrounded by the *cerebrospinal fluid* (CSF). It extends from the medulla oblongata in the brainstem and its diameter, of the order of the centimetre, varies with the spinal level, as well as the composition in terms of GM and WM. A summary representation of spinal cord anatomy is shown in figure 2.2.

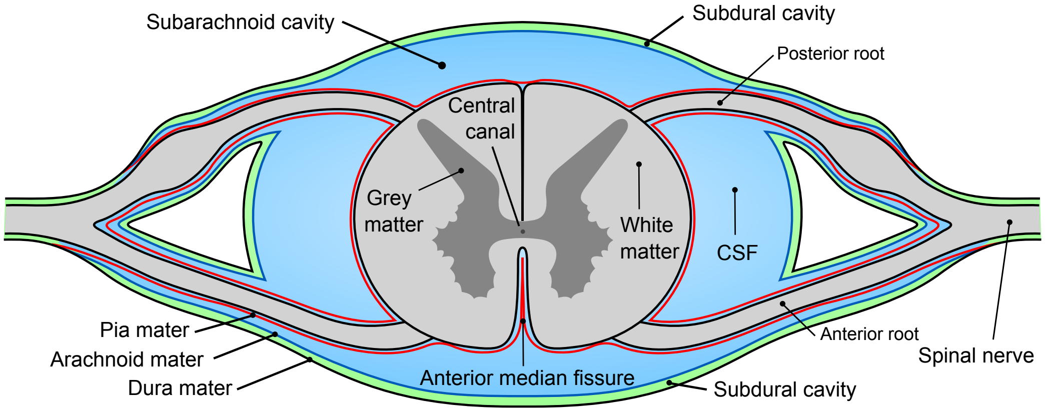

Figure 2.2: illustration of the anatomy of the human spinal cord. Adapted from image `https://commons.wikimedia.org/wiki/File:Gray770-en.svg`, released into the public domain for any purpose and without any condition via Wikimedia Commons.

The spinal cord contains GM in the inner part, whereas WM is more external and divided into several fibre bundles or *tracts*. Nerve roots emanate from white matter and contain peripheral axons delivering motor programs to muscles and conveying sensory information from the periphery to the brain. Three meningeal membranes (*pia*, *arachnoid* and *dura mater*) surround and protect the spinal cord, with the subarachnoid cavity being filled with CSF. CSF also fills a tight, anterior invagination known as *anterior median fissure*, and the *central canal* running longitudinally from the ventricular system of the brain to the lumbar level.

In spite of its small size, the spinal cord has essential functions, and spinal cord pathology can have severe consequences on the vital functions. As an example, traumatic spinal cord injury (SCI) is a complex phenomenon involving a cascade of noxious events that follow the primary injury [121, 179], and is often associated to major clinical disability. Several other diseases can also affect the the spinal cord, such as MS, a neurodegenerative condition that often leads to an important accrual of disability [112].

## 2.3 Multiple sclerosis

MS is an inflammatory and demyelinating disease affecting brain, spinal cord and optic nerves. In MS, several pathological features can coexist [31, 115], and some of them are thought to be genetically driven [188].

In around 85% of the patients, the disease starts with an acute neurological episode, generally followed by other acute relapses, which alternate with periods of high level of functional recovery [47]. This form of the disease, called *relapsing remitting* MS (RRMS), is characterised by acute inflammation, disruption of the blood-brain-barrier [141] and demyelination. RRMS is usually followed after 15-20 years from the symptom onset by a progressive stage, or *secondary progressive* MS (SPMS), whose main feature is the irreversible accrual of disability. However, in 10-15% of MS cases, the disease starts as a progressive neurological condition from the beginning, and it is called *primary progressive* MS (PPMS).

MS leads to neurodegeneration, which is believed to be triggered by the inflammatory demyelinating disease process of the early stages [115]. Phenomena such as microglia activation [39], oxidative stress [72] due to the release of iron in the extra-cellular space and toxic intra-axonal sodium accumulation due to the redistribution of sodium channels after demyelination [149] are thought to be involved in neurodegeneration.

Spinal cord involvement in MS is very common, and MRI of the spinal cord in clinical practice is recommended [96]. Although spinal cord involvement in MS is expected to affect the clinical status of patients, the correlation between clinical disability and MRI-derived spinal lesion number is moderate [96]. Conventional MRI, despite being able to detect focal MS pathology, lacks in sensitivity and specificity, and underestimates the real overall effect of the disease. Recent advances in MRI technology and efforts in developing quantitative approaches may help to overcome this intrinsic limitation, providing novel, specific metrics able to better characterise non-focal abnormalities and to detect intrinsic cord damage [63]. These new metrics may lead to more accurate prediction of prognosis, to the improvement of our understanding of the disease and to better treatment monitoring, with consequent reduction of sample sizes in clinical trials.

Several, innovative quantitative MRI techniques have shown promise in the MS brain and spinal cord. Among them: *quantitative magnetization transfer imaging*, providing indices of macromolecular proton fraction [164]; *myelin water imaging*, estimating myelin water fraction [107]; DTI [12], sensitive to demyelination and diffuse changes in normal-appearing spinal cord [99]; *diffusion basis spectrum imaging* (DBSI), modelling the effect of axonal injury, demyelination and inflammation [195]; *g-ratio mapping*, a potential tool to reveal between-lesion heterogeneity [173]; NODDI [215], capturing the density and the spread of neurite orientations, shown to be affected by MS [156]; *quantitative susceptibility mapping*, sensitive to iron deposition in lesions [210]; sodium MRI, detecting pathological sodium accumulation [144].

# Chapter 3

# Background

## 3.1 Introduction to magnetic resonance imaging

MRI refers to a family of non-invasive medical imaging methods that produce images of the human body with magnetic fields. These images reflect how differently tissues immersed in a strong, static magnetic field react to externally applied radio frequency (RF) pulses, leading to between and within-tissue contrasts. MRI is based on the nuclear magnetic resonance (NMR) effect, which is the interaction between nuclei magnetic moments and a static magnetic field. Also, MRI exploits spatially variant magnetics fields (magnetic field gradients) to encode the position of the measured signals.

To date, MRI is an important diagnostic tool in several clinical disciplines and an active field of research. The success of MRI is related to the lack of employment of ionising radiation and to its versatility. Several different sources of contrast among tissues of similar densities can be exploited when producing an MRI image, provided that an adequate sequence (i.e. an ordered and timed application of magnetic field pulses and gradients) is designed and employed. Therefore, the same physical machine can produce different types of images, conveying different pieces of information about the imaged tissues. A careful design of the MRI experiment can produce images optimised to emphasise the signals of specific areas or to suppress contributions from unwanted tissues. Moreover, specific biophysical properties such as cell density, myelin amount or blood flow, can be related to the measured MRI signals via mathematical models. This allows the inference of such properties when multiple images are acquired varying the sequence parameters. These quantitative approaches are often referred to as quantitative MRI (qMRI). qMRI has the potential of providing novel, sensitive and specific biomarkers capable of improving diagnosis and prognosis in a number of conditions, although the specificity and the validity of such new indices in pathology always needs to be confirmed and verified.

This thesis deals with qMRI of the human spinal cord for MS applications, and focusses on DW MRI. In this chapter, the theoretical background on which the MRI methods of this work rely is described. Elementary magnetic properties of the nuclei will be firstly introduced. Then, phenomenological equations describing the behaviour of a macroscopic ensemble of nuclei, the Bloch equations, will be presented. Afterwards, key concepts regarding the image formation process and modern solutions to accelerate the acquisition are described. These are followed by a whole section on DW MRI and by one on qMRI of the human spinal cord. Lastly, a final part introducing recent approaches commonly employed for the validation of qMRI is included. Extensive consultation of references [36, 69, 92, 180] has been essential for writing this chapter.

## 3.2 Spins and magnetic moments

Nuclei are characterised by certain physical properties such as an intrinsic *angular momentum* $\mathbf{L}$, or *spin*, which arises from the contribution of its protons and neutrons. Nuclei that do not have an even number of both protons and neutrons are characterised by a non-vanishing angular momentum, and possess a net magnetic moment $\boldsymbol{\mu}$ related to $\mathbf{L}$ via

$$\boldsymbol{\mu} = \gamma \, \mathbf{L}, \tag{3.1}$$

where $\gamma$ is the *gyromagnetic ratio*, whose value depends on the nucleus in question.

Nuclei would align their elementary magnetic moments in parallel and anti-parallel directions with respect to a static magnetic field in which they were to be immersed. A small excess of nuclei in one of the two configurations gives rise to a net magnetisation of the ensemble, which can be imaged. Several nuclei, such as $^{1}$H, $^{23}$Na, $^{31}$P and others can potentially be object of an NMR experiment. In practice, the relative amplitude of the detectable signals is limited by the physical abundance of the nucleus in the imaged tissue. In the human body, due to the abundance of water, the nucleus that is more easily employed to give rise to a net magnetisation and to produce NMR signals is $^{1}$H.$^{1}$H-MRI has improved dramatically since the first steps in the years forties of the twentieth century, and various imaging modalities based on signals from $^{1}$H are nowadays available.

This thesis deals with $^{1}$H-MRI, and focuses on the signal arising from water protons and on the effect that diffusion has on it. As common in current $^{1}$H-MRI literature, the term *spin* will be employed from now onwards as a synonymous of *water proton*.

### 3.2.1 Dynamics of a spin from classical mechanics

The rigorous description of the interaction between a spin magnetic moment and an external magnetic field relies on quantum mechanics. Nevertheless, an effective formalism based on a classical description also allows the understanding of the main phenomena occurring during an MRI experiment.

In the classical picture, a water proton is modelled as a spinning electric charge, equivalent to a tiny current loop. The magnetic moment associated to the loop can be written as a function of the the current circulating in the loop itself ($I$), the area of the surface within the loop ($A$) and the normal to such a surface ($\mathbf{u}$):

$$\boldsymbol{\mu} \; = \; I A \, \mathbf{u}. \tag{3.2}$$

For the same simple system, the gyromagnetic ratio can be calculated from the properties of the spinning charge (i.e. its mass $m$ and charge $q$) as $\gamma = \frac{q}{2\,m}$. Plugging the mass and charge of the proton would provide the gyromagnetic ratio of an isolated proton. In practice, the real value of $\gamma$ for water protons has been derived experimentally and it is equal to 2.675 $\cdot\, 10^8$ s$^{-1}$ T$^{-1}$.

If the current loop is immersed in a magnetic field $\mathbf{B}$, a net torque $\boldsymbol{\tau}$ depending on the properties of the loop and on the field itself will act upon it. This torque can be calculated as the cross product

$$\boldsymbol{\tau} \;=\; \boldsymbol{\mu} \times \mathbf{B}. \tag{3.3}$$

The temporal evolution of the loop angular momentum can be obtained from Newton's second law of motion in angular terms (conservation of angular momentum), which in this case is written as $\frac{d}{dt}\mathbf{L}(t) \;=\; \boldsymbol{\tau}(t)$. Recalling from equation 3.1 that $\mathbf{L}(t) \;=\; \frac{1}{\gamma}\,\boldsymbol{\mu}(t)$ and substituting the expression of $\boldsymbol{\tau}(t)$ from equation 3.3, the vectorial partial differential equation describing the dynamics of the spin under the external field $\mathbf{B}$ in classical terms is readily obtained as

$$\frac{d\boldsymbol{\mu}(t)}{dt} \;=\; \gamma\,\boldsymbol{\mu}(t) \times \mathbf{B}(t). \tag{3.4}$$

Equation 3.4 states that under a generic field $\mathbf{B}(t)$, the magnetic moment $\boldsymbol{\mu}(t)$ rotates with an instantaneous angular velocity $\boldsymbol{\omega}(t) \;=\; -\,\gamma\,\mathbf{B}(t)$ proportional to the field $\mathbf{B}(t)$ at any given time $t$.

### 3.2.2 Larmor precession of a spin

The solution of equation 3.4 under a static field $\mathbf{B}(t) = \mathbf{B}_0 = \begin{bmatrix}0 & 0 & B_0\end{bmatrix}^{\mathsf{T}}$ and for an initial condition $\boldsymbol{\mu}(0) = \begin{bmatrix}\mu_x(0) & \mu_y(0) & \mu_z(0)\end{bmatrix}^{\mathsf{T}}$ describes the free precession of the spin magnetic moment about the direction $\mathbf{z}$ of the static field. Describing the component of $\boldsymbol{\mu}(t)$ orthogonal to $\mathbf{B}_0$ with a complex-valued notation, i.e. defining $\mu_\perp(t) \;=\; \mu_x(t) \;+\; j\,\mu_y(t)$, the free precession solution of equation 3.4 is written as

$$\mu_\perp(t) = e^{-j\,\omega_0 t}\mu_\perp(0), \tag{3.5}$$

while $\mu_z(t) \;=\; \mu_z(0) \;\; \forall\, t \geq 0$. This is equivalent to state that the component of $\boldsymbol{\mu}(t)$ orthogonal to the main field rotates clockwise about $+\mathbf{z}$.

As illustrated by figure 3.1, the magnetic moment $\boldsymbol{\mu}(t)$ precesses with angular frequency $\omega_0 = \gamma B_0$ about the direction of the field $\mathbf{B}_0$ from the initial condition $\boldsymbol{\mu}(0)$. Such phenomenon is referred to as *Larmor precession* and the frequency $\omega_0$ is called *Larmor frequency* or *resonance frequency*. The precession is associated to the component of $\boldsymbol{\mu}(t)$ orthogonal to $\mathbf{B}_0$, while the component $\mu_z(t)$ parallel to $\mathbf{B}_0$ is constant and equal to the initial value.

The phase accrual during the free precession is the quantity $\phi(t) \;=\; \angle\mu_\perp(t) - \angle\mu_\perp(0)$, which, in the general case of spatially and time variant polarising fields aligned with the $\mathbf{z}$ direction, can be calculated as

$$\phi(\mathbf{r}, t) \;=\; -\,\gamma \int_0^t B_z(\mathbf{r}, t^{'})\, dt^{'}. \tag{3.6}$$

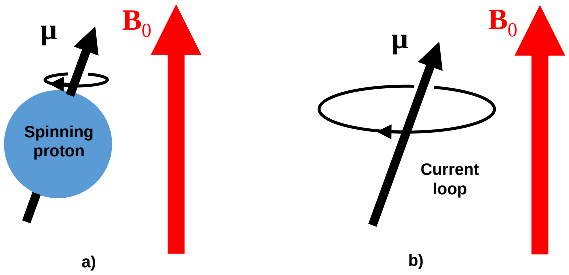

Figure 3.1: illustration showing how a spinning proton, pictured in a), is described in terms of a current loop, pictured in b), according to the classical formalism.

### 3.2.3 The rotating reference frame

Previous theory was presented expressing vectorial quantities in a generic, static reference frame. Such frame is usually referred to as *laboratory reference frame* and it can be identified by an orthonormal basis $(\mathbf{x}, \mathbf{y}, \mathbf{z})$, with $\mathbf{z}$ chosen to be aligned with the static field. It is common to describe phenomena such as the precession of the spins employing another frame, the *rotating reference frame*, since this simplifies the formalism implicitly accounting for the free precession about the static field. The rotating frame is identified by the orthonormal basis $(\mathbf{x}^{'}, \mathbf{y}^{'}, \mathbf{z}^{'})$ defined as

$$\begin{cases} \mathbf{x}^{'} \triangleq \cos(\omega_0 t)\mathbf{x} - \sin(\omega_0 t)\mathbf{y} \\ \mathbf{y}^{'} \triangleq \sin(\omega_0 t)\mathbf{x} + \cos(\omega_0 t)\mathbf{y} \\ \mathbf{z}^{'} \triangleq \mathbf{z}. \end{cases} \tag{3.7}$$

In practice, $\mathbf{x}^{'}$ and $\mathbf{y}^{'}$ rotate about $\mathbf{z}$ at the Larmor frequency counterclockwise, while $\mathbf{z}^{'}$ coincides with $\mathbf{z}$. This means that in such a frame, the magnetic moment $\boldsymbol{\mu}$ is seen as constant while performing Larmor precession.

Equation 3.4 can be re-written in the rotating frame, after expressing $\boldsymbol{\mu}$ as a linear combination of $(\mathbf{x}^{'}, \mathbf{y}^{'}, \mathbf{z}^{'})$, i.e. $\boldsymbol{\mu}(t) = \mu_{x'}(t)\mathbf{x}^{'} + \mu_{y'}(t)\mathbf{y}^{'} + \mu_{z'}(t)\mathbf{z}^{'}$. The time derivative

$$\frac{d\boldsymbol{\mu}(t)}{dt} = \frac{d\mu_{x'}(t)}{dt}\mathbf{x}^{'} + \frac{d\mu_{y'}(t)}{dt}\mathbf{y}^{'} + \frac{d\mu_{z'}(t)}{dt}\mathbf{z}^{'} + \mu_{x'}(t)\frac{d\mathbf{x}^{'}(t)}{dt} + \mu_{y'}(t)\frac{d\mathbf{y}^{'}(t)}{dt} + \mu_{z'}(t)\frac{d\mathbf{z}^{'}(t)}{dt},$$

can be written as

$$\frac{d\boldsymbol{\mu}(t)}{dt} = \frac{d\boldsymbol{\mu}^{'}(t)}{dt} + \boldsymbol{\omega}_0 \times \boldsymbol{\mu}(t), \tag{3.8}$$

where $\frac{d\boldsymbol{\mu}^{'}(t)}{dt} \triangleq \frac{d\mu_{x'}(t)}{dt}\mathbf{x}^{'} + \frac{d\mu_{y'}(t)}{dt}\mathbf{y}^{'} + \frac{d\mu_{z'}(t)}{dt}\mathbf{z}^{'}$ is the time variation of $\boldsymbol{\mu}(t)$ as seen in the rotating frame and where $\boldsymbol{\omega}_0 = -\omega_0\,\mathbf{z} = -\omega_0\,\mathbf{z}^{'}$. This can be readily proven working out the time derivatives of the expressions in equation 3.7, which lead to

$$\begin{cases} \frac{d\mathbf{x}^{'}}{dt} = -\,\omega_0\,(\sin{(\omega_0 t)}\mathbf{x} \,+\, \cos{(\omega_0 t)}\mathbf{y}) = -\,\omega_0\,\mathbf{y}^{'} \,=\, \boldsymbol{\omega}_0 \times \mathbf{x}^{'} \\ \frac{d\mathbf{y}^{'}}{dt} = \omega_0\,(\cos{(\omega_0 t)}\mathbf{x} \,-\, \sin{(\omega_0 t)}\mathbf{y}) = \,\omega_0\,\mathbf{x}^{'} \,=\, \boldsymbol{\omega}_0 \times \mathbf{y}^{'} \\ \frac{d\mathbf{z}^{'}}{dt} = \mathbf{0} = \,\boldsymbol{\omega}_0 \times \mathbf{z}^{'}. \end{cases}$$

The right side of equation 3.8 must equal that of equation 3.4, i.e. it must hold that

$$\gamma\,\boldsymbol{\mu}(t) \times \mathbf{B}(t) \equiv \frac{d\boldsymbol{\mu}^{'}(t)}{dt} + \boldsymbol{\omega}_0 \times \boldsymbol{\mu}(t).$$

Writing the term $\gamma\,\boldsymbol{\mu}(t) \times \mathbf{B}(t)$ as

$$\gamma\,\boldsymbol{\mu}(t) \times \mathbf{B}(t) = \gamma\,\boldsymbol{\mu}(t) \times \mathbf{B}_0 + \gamma\,\boldsymbol{\mu}(t) \times \mathbf{B}_{\text{ext}}(t) = \boldsymbol{\omega}_0 \times \boldsymbol{\mu}(t) + \gamma\,\boldsymbol{\mu}(t) \times \mathbf{B}_{\text{ext}}(t)$$

allows the expression of the temporal variation of the magnetic moment in the rotating frame as a function of the magnetic field from which the static, polarising component has been removed. The dynamics of the magnetic moment in the rotating frame becomes

$$\frac{d\boldsymbol{\mu}(t)}{dt} \;=\; \gamma\,\boldsymbol{\mu}(t) \times \mathbf{B}_{\text{ext}}(t). \tag{3.9}$$

## 3.3 Bloch equations and relaxation

In the previous section, the elementary magnetic moment $\boldsymbol{\mu}$ of a spin was introduced. When an ensemble of spins contained in a volume $V$ is considered, it is useful to define the net magnetisation $\mathbf{M}$ of the spin ensemble, which is the total magnetic moment per unit of volume:

$$\mathbf{M} = \frac{1}{V}\sum_n \boldsymbol{\mu}_n. \tag{3.10}$$

The net magnetisation, at equilibrium, is aligned with the static field $\mathbf{B}_0$, so that $\mathbf{M} = \mathbf{M}_0 = \begin{bmatrix} 0 & 0 & M_0 \end{bmatrix}^{\mathsf{T}}$. $M_0$ is proportional to the field strength, the spin density and inversely proportional to the temperature. Quantum physics principle lead to the following expression of $M_0$:

$$M_0 \;=\; \frac{1}{4}\,\frac{\gamma^2\hbar^2}{KT}\;B_0\,\rho_0, \tag{3.11}$$

where $K$ is the Boltzmann constant, $\hbar$ is the reduced Planck's constant, $T$ is the temperature and $\rho_0$ is the spin density.

The magnetisation $\mathbf{M}$ can be perturbed from the equilibrium condition by the exposure to radiation, in the form of time variant magnetic fields orthogonal to the main static field. In the next sections, details about the response of $\mathbf{M}$ to perturbations from the equilibrium are presented.

### 3.3.1 The Bloch equations

The behaviour of the net magnetisation $\mathbf{M}$ under the application of external magnetic fields can be described rigorously in terms of quantum mechanics. Nevertheless, it is common to employ macroscopic ordinary differential equations to predict the time evolution of $\mathbf{M}$, i.e. the so called *Bloch equations* [18]. The Bloch equations model the Larmor precession of $\mathbf{M}$ about a static field, its response to any applied time variant field and describe the return of $\mathbf{M}$ to its equilibrium value, i.e. its *relaxation*. In the laboratory reference frame introduced in section 3.2, where the static field $\mathbf{B}_0 = \begin{bmatrix}0 & 0 & B_0\end{bmatrix}^{\mathsf{T}}$ is directed along the $z$-axis, the Bloch equations can be summarised in the following vectorial ordinary differential equation describing the time evolution of $\mathbf{M}(t) = \begin{bmatrix}M_x(t) & M_y(t) & M_z(t)\end{bmatrix}^{\mathsf{T}}$:

$$\frac{d\mathbf{M}(t)}{dt} = \gamma\,\mathbf{M}(t) \times \mathbf{B}(t) - \mathbf{R}\,(\mathbf{M}(t) - \mathbf{M}_0). \tag{3.12}$$

In equation 3.12, $\times$ is the cross product, $\mathbf{M}_0$ is the equilibrium magnetisation; $\mathbf{B}(t) = \mathbf{B}_0 + \mathbf{B}_{\text{ext}}(t)$ is the total magnetic field; $\mathbf{B}_0$ is the static field; $\mathbf{R} = \text{diag}(T_2^{-1}, T_2^{-1}, T_1^{-1})$ is the relaxation matrix, with $T_1$ being the *spin-lattice relaxation time* and $T_2$ the *spin-spin relaxation time*.

The first term to the right hand side of equation 3.12 describes the instantaneous precession of $\mathbf{M}(t)$ about the total field $\mathbf{B}(t)$ with angular frequency $\boldsymbol{\omega}(t) = -\gamma\mathbf{B}(t)$, whereas the second term describes the tendency of $\mathbf{M}(t)$ to return to the equilibrium condition $\mathbf{M}(t) = \mathbf{M}_0$. Integration of equation 3.12 provides the behaviour of $\mathbf{M}(t)$ for a given field $\mathbf{B}(t)$, of which two examples are reported in sections 3.3.3 and 3.3.4.

### 3.3.2 Relaxation time constants

The spin-lattice and spin-spin relaxation times $T_1$ and $T_2$ respectively describe the rate at which the longitudinal component $M_z(t)$ of $\mathbf{M}(t)$ approaches the equilibrium value $M_0$, and the rate at which any component of $\mathbf{M}(t)$ orthogonal to the main static field decays. At 3 T, typical values of $T_1$ and $T_2$ are on the order of 1300 ms and 830 ms ($T_1$) and of 100 ms and 80 ms ($T_2$) for brain grey and white matter [197].

The molecular basis from which $T_1$ and $T_2$ originate have been extensively studied at the dawn of the NMR field, and a theory by Bloembergen, Purcell and Pound (BPP theory), which relates the values of $T_1$ and $T_2$ to the tumbling motion of the molecules, has been proposed [19].

In the BPP formalisms, $T_1$ and $T_2$ are related to the line widths of the curves describing the absorption of energy by a material immersed in a static magnetic field and exposed to radiation [19]. They can be expressed as a function of $\tau_c$, the correlation time determining the time scale of the interactions among molecules due to vibrational, rotational and translational motion. Specifically, $T_1$ is the time constant characterising the transfer of energy from the irradiated spin system to the heat reservoir comprising all remaining degrees of freedom of the substance in question. On the other hand, $T_2$ is related to the interactions among the magnetic nuclei themselves. These occur due to the fact that each spin experiences the local fluctuating magnetic field produced by neighbouring spins, which causes the spin ensemble to dephase. Local inhomogeneities of the main static field can also affect the field experienced by each spin, and a time constant $T_2^*$ smaller than the theoretical $T_2$ may need to be introduced. In [19], expressions of $T_1$ and $T_2$ as a function of $\tau_c$ are provided.

As far as water is concerned, the authors in [19] claim that for $T_1$, $\tau_c$ is driven by the interactions of each proton with its proton partner in a water molecule. $\tau_c$ is in practice approximated as the time during which the orientation of a molecule persists, and in its calculation vibrational, and, to a less extent, rotational and translational components of the thermal motion of water molecules can be neglected [19]. For a given field strength $B_0$ and a resonance angular frequency $\omega_0 = \gamma\, B_0$, the reciprocal of $T_1$ is found to be

$$\frac{1}{T_1} \;=\; C_1 \left( \frac{\tau_c}{1 + (\omega_0\, \tau_c)^2} \;+\; \frac{2\tau_c}{1 + (2\,\omega_0\, \tau_c)^2} \right), \tag{3.13}$$

with $C_1$ being a constant depending on factors such as the interproton distance, assumed to be $1.5 \cdot 10^{-10}$ m.

With regard to $T_2$, the authors of [19] provide the expression

$$\frac{1}{T_2} \;=\; \sqrt{\frac{2}{\pi}}\,\frac{1}{T_2^{'}} \;+\; \frac{1}{2\,T_1}, \tag{3.14}$$

which is a function of $T_1$ and of $T_2^{'}$, with the latter being the solution of the transcendental equation

$$\left(\frac{1}{T_2^{'}}\right)^2 \;=\; \frac{3}{\pi}\, C_1\, \mathrm{atan}\left(\frac{2\,\tau_c}{T_2^{'}}\right). \tag{3.15}$$

Figure 3.2 shows $T_1$ and $T_2$ as $\tau_c$ varies, replicating qualitatively figure 14 of reference [19]. For small values of the correlation time $\tau_c$, $T_1$ essentially equals $T_2$. The characteristic curve of $T_1$ decreases as $\tau_c$ increases, hits a minimum for $\omega_0\, \tau_c = \frac{1}{\sqrt{2}}$ and then increases again for increasing $\tau_c$. The characteristic of $T_2$, instead, is essentially linear from small values of $\tau_c$ up to $\tau_c = \frac{T_2^{''}}{\sqrt{2}}$, after which flattens reaching the asymptotic value $T_2 = T_2^{''}$, with $T_2^{''}$ related to spin-spin interactions occurring in the limiting case of a rigid lattice. In practice, different correlation times $\tau_c$ are probed in *relaxation-along-fictitious-fields* techniques [111], which measure relaxation due to molecular interactions at different time scales.

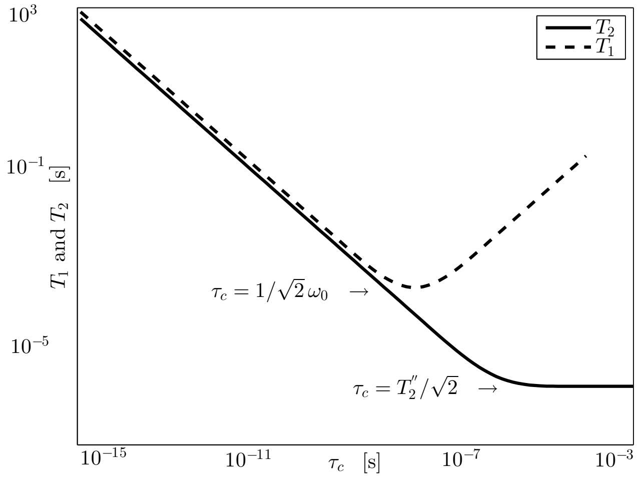

Figure 3.2: illustration replicating qualitatively figure 14 of reference [19]. The plot describes the dependence of relaxation times $T_1$ and $T_2$ on the correlation time $\tau_c$ for water.

The BPP theory was also applied to materials other than water, such as various liquids characterised by different viscosities. In those cases, experimental results confirmed the theoretical finding that the correlation time $\tau_c$ can be considered proportional to the ratio $\eta/T$, with $\eta$ and $T$ indicating the viscosity and the temperature of the liquid [19].

Lastly, it is reported that the relaxation properties depend on the field strength. In a clinical system with a field strength of the order of the Tesla, $T_1$ of water protons is longer than $T_2$. The former increases for increasing field strength, whereas the latter decreases. This fact is exploited in *field cycling MRI* as a source of contrast among tissues, since in field cycling methods the strength of the static field is varied during the experiment [152].

### 3.3.3 Evolution of the magnetisation under a static field

In figure 3.3, the behaviour of $\mathbf{M}(t)$ under the sole static field $\mathbf{B}_0$ (i.e. $\mathbf{B}(t) = \mathbf{B}_0$) is presented, for an initial condition $\mathbf{M}(0) = \begin{bmatrix} M_0 & 0 & 0 \end{bmatrix}^\mathsf{T}$ such that the magnetisation has been perturbed from the equilibrium condition $\mathbf{M} = \mathbf{M}_0$. The plots to the left and in the middle demonstrate that the two components $M_x(t)$ and $M_y(t)$ oscillate in phase quadrature, and that the amplitude of the oscillation decays over time as $e^{-t/T_2}$. The plot to the right instead shows that $M_z(t)$ approaches over time with a mono-exponential law proportional to $1-e^{-t/T_1}$ the asymptotic condition $\lim_{t\to\infty} M_z(t) = M_0$. The frequency of oscillation of $M_x(t)$ and $M_y(t)$ is proportional to the main static field, i.e. it equals $f_0 = \frac{1}{2\pi}\gamma B_0$. Figure 3.3 also demonstrates the usefulness of employing the rotating reference frame introduced previously, since this would account for the fast Larmor precession of $M_x(t)$ and $M_y(t)$, simplifying their numeric integration and their visualisation.

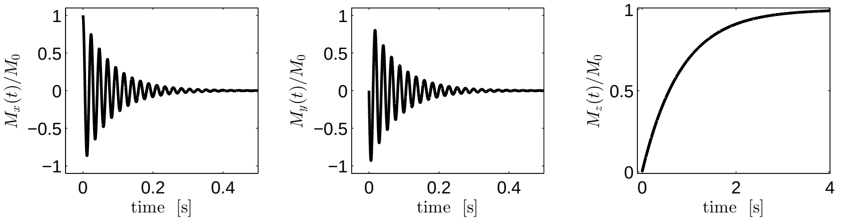

Figure 3.3: behaviour of the magnetisation under a static field $\mathbf{B}(t) = \mathbf{B}_0$ and for an initial condition $\mathbf{M}(0) = [\,M_0 \quad 0 \quad 0\,]^\mathsf{T}$, in the laboratory frame. The plot to the left describes the time evolution of $M_x(t)$; the central plot of $M_y(t)$; the plot to the right of $M_z(t)$. Values of 830 ms and of 70 ms were employed respectively for $T_1$ and $T_2$. For illustrative purposes, in practice a static field strength of $B_0 = 1\,\mu$T, corresponding to a Larmor frequency $f_0 = \frac{1}{2\pi}\gamma B_0 = 42.58$ Hz, was employed. Typical field strengths of modern MRI machines (on the order of the Tesla) would have provided oscillations at much higher frequencies, on the order of the hundreds of MHz. Oscillations at that frequency are difficult to visualise in a time interval of duration appropriate to demonstrate relaxation effects.

### 3.3.4 Response of the magnetisation to *on resonance* excitation

The second example of integration of the Bloch equations is shown in figure 3.4, which describes the evolution of $\mathbf{M}(t)$ in the rotating reference frame under a total field $\mathbf{B}(t) = \mathbf{B}_0 + \mathbf{B}_1(t)$. The field $\mathbf{B}_1(t)$ chosen for this example is a time variant field applied orthogonally to the static field $\mathbf{B}_0$, made of a sequence of two idealised *on resonance* circularly-polarised excitation pulses, each lasting 5 ms, and occurring at $t = 1$ s and $t = 2.5$ s. In the rotating reference frame $(\mathbf{x}^{'}, \mathbf{y}^{'}, \mathbf{z}^{'})$, $\mathbf{B}_1(t)$ can be written as $\mathbf{B}_1(t) = f(t)\,\mathbf{x}^{'}$, with $f(t) = \{2.3487\,\mu\text{T for } 1\,\text{s} \leq t < 1.005\,\text{s};\ \ 1.1744\,\mu\text{T for } 2.5\,\text{s} \leq t < 2.505\,\text{s};\ \ 0 \text{ otherwise}\}$, illustrated on the top plot of figure 3.4. In practice, $\mathbf{B}_1(t)$ is a field orthogonal to $\mathbf{B}_0$ that rotates at the Larmor frequency (i.e. *on resonance*) in the $(x, y)$ plane.

The plot in the central column of figure 3.4 shows the time evolution of the magnitude of $\mathbf{M}_\perp(t) = M_{x'}(t)\,\mathbf{x}^{'} + M_{y'}(t)\,\mathbf{y}^{'}$ (component of $\mathbf{M}(t)$ orthogonal to $\mathbf{B}_0$), whereas the plot in the bottom row shows $M_{z'}(t)$. For the comprehension of the effect of the pulses contained in the waveform $f(t)$, it is essential to understand that an *on resonance* pulse applied orthogonally to $\mathbf{B}_0$ and characterised by an intensity $B_1$ and a duration $\tau$ will tip $\mathbf{M}(t)$ away from the direction of the static field $\mathbf{B}_0$ (i.e. from the $+\mathbf{z}$ direction) of an angle

$$\theta_f \;=\; \gamma \int_0^\tau B_1(t)dt \;=\; \gamma\, B_1\, \tau, \tag{3.16}$$

which is referred to as *flip angle*. If $\tau$ is short compared to $T_1$ and $T_2$, this tipping can be modelled as instantaneous. In the toy example illustrated in figure 3.4, a first pulse of duration 5 ms is applied at a time $t = 1$ s. The amplitude of such a pulse is such that the corresponding flip angle is $\theta_f = 2.675 \cdot 10^8\,\text{s}^{-1}\,\text{T}^{-1}\ \ 2.3487 \cdot 10^{-6}\,\text{T}\ \ 0.005\,\text{s} = \pi$. In practice, such pulse inverts the magnetisation from $\mathbf{M} = \mathbf{M}_0$ to $\mathbf{M} = -\mathbf{M}_0$, and is often called 180°-RF pulse or *inversion pulse*. Afterwards, the $z$-component of $\mathbf{M}$ will relax to the equilibrium with the usual $T_1$-monoexponential law, and the amount of longitudinal magnetisation that has recovered when the second pulse is applied at $t = 2.5$ s is flipped of 90° to the transverse $(x, y)$ plane, since the second RF pulse has an amplitude corresponding to a flip angle of $\theta_f = 2.675 \cdot 10^8\,\mathrm{s}^{-1}\,\mathrm{T}^{-1}\;\; 1.1744 \cdot 10^{-6}\,\mathrm{T}\;\; 0.005\,\mathrm{s} = \pi/2$. Lastly, the figure shows that the magnitude of the transverse magnetisation $|\mathbf{M}_\perp(t)|$ that has been created by the second pulse decays proportionally to $e^{-(t-2.5\,\mathrm{s})/T_2}$ for $t \geq 2.5\,\mathrm{s}$, whereas the longitudinal magnetisation grows from the condition $M_{z'} = 0$ to $M_{z'} = M_0$ as $M_0(1-e^{-(t-2.5\,\mathrm{s})/T_1})$ for $t \geq 2.5\,\mathrm{s}$. The pulse sequence shown in figure 3.4 is of common employment in real clinical scenarios to obtain $T_1$-weighted structural images, and it is called *inversion recovery*.

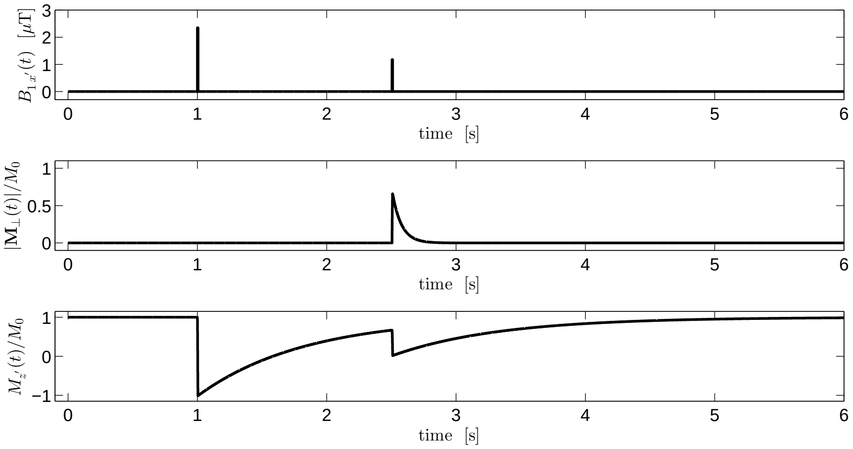

Figure 3.4: behaviour of the magnetisation under a total field $\mathbf{B}(t) = \mathbf{B}_0 + \mathbf{B}_1(t)$ for an initial condition $\mathbf{M}(0) = \mathbf{M}_0$ (equilibrium condition), in the rotating reference frame. The plot on top reports the applied time-variant field $B_1(t)$. The plot in the middle row describes the time evolution of the magnitude of the component of $\mathbf{M}(t)$ orthogonal to the static field, in the rotating frame; the plot on bottom shows the time evolution of $M_{z'}(t)$. The same relaxation constants of figure 3.3 were employed.

### 3.3.5 Multicomponent relaxation

The Bloch equations are a powerful tool for modelling the response of the magnetisation arising from a single, homogeneous water pool, characterised by monoexponential $T_1$ and $T_2$ behaviour. Nevertheless, they often prove insufficient to describe the magnetisation arising from living tissues, since biological water is compartmentalised in distinct cellular environments. Each of this compartments can be characterised by its own relaxation time constants, and the exchange of water molecules among the compartments may also have an impact on the measured relaxation rates [57].

As an example, more sophisticated approaches attempt to model multiple $T_2$ components. In the brain parenchyma, at least three $T_2$ components can be identified. They are associated to the water trapped within the myelin sheaths, the water within the intra and extra-cellular spaces, and the free water of the CSF. Methods such as *myelin water imaging* [114] provide practical ways for their estimation *in vivo*, with important applications in demyelinating diseases of the CNS such as MS [106]. Other approaches, such as *multicomponent driven equilibrium single pulse observation* *of T1/T2* (mcDESPOT) [42], try to model in a single experimental framework multicomponent transverse and longitudinal relaxation, while accounting for the residence time of the water molecules in the different physical compartments.

### 3.3.6 Bloch-Torrey equations

Section 3.3 is concluded with an extension of the Bloch equations that allows to model the effect of diffusion. Water molecules in tissues are not still but diffuse randomly due to their thermal agitation [50]. Hence, spins that diffuse in the presence of a spatially variant magnetic field probe different local fields as they vary their position in space. The ensemble average of the magnetic moments of the diffusing water molecules provides the total magnetisation $\mathbf{M}(\mathbf{r},t)$, whose evolution is described by the *Bloch-Torrey equations* [181]. They are usually written as a vectorial partial differential equation in the following form:

$$\frac{\partial \mathbf{M}(\mathbf{r},t)}{\partial t} = \gamma\,\mathbf{M}(\mathbf{r},t) \times \mathbf{B}(\mathbf{r},t) - \mathbf{R}\left(\mathbf{M}(\mathbf{r},t) - \mathbf{M}_0\right) - \nabla^{\mathsf{T}}\,\mathbf{D}(\mathbf{r})\nabla(\mathbf{M}(\mathbf{r},t) - \mathbf{M}_0). \qquad (3.17)$$

Equation 3.17 is similar to equation 3.12, with the only differences that now $\mathbf{M}(\mathbf{r},t)$ and $\mathbf{B}(\mathbf{r},t)$ are modelled as function of both time and spatial position $\mathbf{r} = \begin{bmatrix} x & y & z \end{bmatrix}^{\mathsf{T}}$ and that and additional decay term proportional to the spatial gradient of the magnetisation has been added. Such a term is related to the diffusion tensor $\mathbf{D}(\mathbf{r})$, a rank-2 tensor represented in the form of a positive semi-definite, symmetric $3 \times 3$ matrix, which describes how far along any possible spatial direction water molecules diffuse.

Analytical or numerical integration of equation 3.17 for different boundary conditions describing the domains within which water molecules diffuse and for a generic magnetic field

$$\mathbf{B}(\mathbf{r},t) = \mathbf{B}_0 + \mathbf{B}_1(t) + \mathbf{G}(t)^{\mathsf{T}}\mathbf{r} \qquad (3.18)$$

can provide useful descriptions of the MRI signal arising from porous media [130]. In equation 3.18, $\mathbf{B}_0$ and $\mathbf{B}_1(t)$ are the static polarising field and a time variant RF excitation field, whereas $\mathbf{G}(t)$ is a time variant magnetic field gradient that makes the signal sensitive to diffusion.

## 3.4 Signal detection and imaging equation

Previous sections have described how the NMR effect and relaxation create potential sources of contrast among tissues. In this section, we aim to review how this potential is in practice exploited to measure signals that reflect the properties of tissues, leading ultimately to images.

### 3.4.1 From the magnetisation to a measurable signal

Faraday's law of induction is the principle upon which the detection of the NMR signal relies. The time variant component of the magnetisation generates a time variant magnetic field in the proximity of a coil. Hence, an electromotive force is induced in the coil due to temporal variations of the field flux. Its measure ultimately allows inference about the tissues magnetisation.

The magnetic flux induced on the coil by the magnetisation can be written according to Faraday's law as $E(t) \;=\; -\frac{d}{dt}\int_A \mathbf{B}_{\mathsf{M}}(\mathbf{r},t)^{\mathsf{T}}\mathbf{n}\; d^2A$, where $\mathbf{B}_{\mathsf{M}}(\mathbf{r},t)$ is the magnetic field due to the tissue magnetisation, $A$ is the surface of the coil with $\mathbf{n}$ being the normal to the surface, $d^2A$ is the surface element. The field $\mathbf{B}_{\mathsf{M}}(\mathbf{r},t)$ can be expressed directly as a function of the magnetisation $\mathbf{M}(\mathbf{r},t)$. Also, employing the *reciprocity principle*, the expression of the flux of the magnetisation through the coil can be written as a function of the field that the coil would produce per unit of current in points where the magnetisation does not vanish. If the latter is indicated as $\boldsymbol{\beta}_{\mathsf{r}}(\mathbf{r})$, $E(t)$ can be rewritten as $E(t) \;=\; -\int_V \frac{\partial \mathbf{M}(\mathbf{r},t)}{\partial t}^{\mathsf{T}} \boldsymbol{\beta}_{\mathsf{r}}(\mathbf{r})\; d^3V$, having indicated with $V$ the volume from which the magnetisation $\mathbf{M}(\mathbf{r},t)$ arises and with $d^3V$ the volume element [69].

After excitation, $\frac{\partial \mathbf{M}(\mathbf{r},t)}{\partial t}$ is described by the Bloch equations. The transverse component $\mathbf{M}_\perp(\mathbf{r},t)$ of $\mathbf{M}(\mathbf{r},t)$ decays while rotating at the Larmor frequency $\omega_0$, whereas the longitudinal component $M_z(\mathbf{r},t)$ relaxes depending on the local value of $T_1$. It follows that the magnitude of the time variation of $\mathbf{M}_\perp(\mathbf{r},t)$ and $M_z(\mathbf{r},t)$ are respectively proportional to $\omega_0$ and $T_1^{-1}$. For modern field strengths of the order of the Tesla, $\omega_0 \gg T_1^{-1}$, and therefore the contribution of $\frac{\partial M_z(\mathbf{r},t)}{\partial t}$ can be neglected as compared to $\frac{\partial \mathbf{M}_\perp(\mathbf{r},t)}{\partial t}$. Hence, adopting the complex-valued notation $M_\perp(\mathbf{r},t) \;=\; M_x(\mathbf{r},t) + j\, M_y(\mathbf{r},t)$ and indicating with $\boldsymbol{\beta}_{\mathsf{r}\perp}(\mathbf{r}) = \beta_{\mathsf{r},x}(\mathbf{r}) + j\,\beta_{\mathsf{r},y}(\mathbf{r})$, the signal in the receiver coil can be written as

$$s(t) \;=\; \zeta\,\omega_0 \int_V M_\perp(\mathbf{r},t)\,\boldsymbol{\beta}_{\mathsf{r}\perp}(\mathbf{r})\; d^3V \tag{3.19}$$

with $\zeta$ accounting for gains from the electronics and with $s(t)$ being in general complex. In practice, a real and an imaginary channel are obtained from the induced electromotive force $E(t)$ via cosine and sine demodulation, i.e. multiplying $E(t)$ with two oscillatory signals in phase quadrature while removing oscillations at the Larmor frequency.

By virtue of equation 3.11 it is possible to express $M_\perp(\mathbf{r},t)$ in equation 3.19 as

$$M_\perp(\mathbf{r},t) \;=\; \frac{1}{4}\frac{\gamma\hbar^2}{KT}\;\omega_0\; w\left(T_1(\mathbf{r}),T_2(\mathbf{r}),T_2^*(\mathbf{r}),t\right)\;\rho_0(\mathbf{r}),$$

where $\rho_0(\mathbf{r})$ is the spin density, $\hbar$, $K$ and $T$ have been already introduced, $w\left(T_1(\mathbf{r}),T_2(\mathbf{r}),T_2^*(\mathbf{r}),t\right)$ is a relaxation-weighting factor depending on the adopted sequence of RF pulses. Ultimately, the signal measured by the receiver becomes

$$s(t) \;=\; \frac{1}{4}\,\zeta\frac{\gamma\hbar^2}{KT}\;\omega_0^2\int_V\; w\left(T_1(\mathbf{r}),T_2(\mathbf{r}),T_2^*(\mathbf{r}),t\right)\;\rho_0(\mathbf{r})\,\boldsymbol{\beta}_{\mathsf{r}\perp}(\mathbf{r})\; d^3V. \tag{3.20}$$

### 3.4.2 The imaging problem

Previous discussion has related the signal as measured by the receiver coil to the spin density. Equation 3.20 can rather be written in terms of an *effective spin density* $\rho$ such that

$$\rho\, e^{j\psi} \;=\; \frac{1}{4}\,\zeta\frac{\gamma\hbar^2}{KT}\;\omega_0^2\, w\left(T_1(\mathbf{r}),T_2(\mathbf{r}),T_2^*(\mathbf{r}),t\right)\;\rho_0(\mathbf{r})\,\boldsymbol{\beta}_{\mathsf{r}\perp}(\mathbf{r}).$$

$\rho$ depends on factors such as field strength, temperature, receiver coil geometry, electronic gains, relaxation rates, actual spin density and $\psi$ is the phase accumulated by spins in the transverse plane after signal demodulation. Equation 3.20 can the be generically reformulated as $s \;=\; \int_V \rho(\mathbf{r})\, e^{\,j\psi}\; d^3V$ having omitted the dependence of $\rho(\mathbf{r})$ on factors other than the position. Above, $\psi$ is $\psi = \phi + \gamma B_0 t$, with $\phi$ from equation 3.6.

If a magnetic field gradient $\mathbf{G}(t) \triangleq \nabla B_z(t)$ is switched on when the magnetisation has a transverse component, $\psi$ can be expressed as $\psi \;=\; -\,\gamma \left(\int_0^t \mathbf{G}(t^{'})\, dt^{'}\right)^{\mathsf{T}} \mathbf{r} \;=\; -\,\mathbf{k}^{\mathsf{T}}\mathbf{r}$, leading to

$$s(\mathbf{k}) \;=\; \int_V \rho(\mathbf{r})\, e^{\,-j\,\mathbf{k}^{\mathsf{T}}\mathbf{r}}\; d^3V. \tag{3.21}$$

Equation 3.21 is the fundamental upon which imaging relies, since it states that the measured signal, expressed as a function of the variable

$$\mathbf{k}(t) \;\triangleq\; \gamma \int_0^t \mathbf{G}(t^{'})\, dt^{'} \tag{3.22}$$

encoding the history of the magnetic field gradient, is the Fourier transform of the effective spin density in the spatial domain. Hence, knowledge of $s(\mathbf{k})$ from a set of measurements obtained while gradients are turned on (i.e. *sampling of the k-space*) can lead to the estimation of $\rho(\mathbf{r})$ via inverse Fourier transformation. Equation 3.22 implies that three independent coils capable of generating three mutually orthogonal gradient components are necessary for imaging.

## 3.5 Common MRI signal weightings

In the previous section, the fundamental principles concerning the detection of NMR signals from the body by a coil element have been described. In particular, it has been reported that the measured signals are proportional to the component of magnetisation $M_\perp = M_x + j\, M_y$ orthogonal to the static polarising field. Differences in terms of properties such as relaxation times and proton density cause $M_\perp$ to differ among tissues, leading eventually to image contrast.

Generally, an MRI experiment can be thought as composed of two stages. In the first stage, or *preparation stage*, RF pulses in combination with magnetic field gradients are employed in order to obtain the desired type of weighting of the signal, determining the driving source of contrast among tissues. For instance, for $T_1$-weighted imaging, the preparation stage will be such that the measured signals will be strongly dependent on the $T_1$ of tissues, rather than $T_2$. In the second or *acquisition stage*, the signal induced in the coil is sampled. Magnetic field gradients are employed during this stage in order to encode the spatial position from which the signals originate.

In this section, a summary review of preparation sequences of RF pulses and their corresponding signal weighting are presented. The review aims to demonstrate to the reader how relatively simple manipulations of the magnetisation can lead to a variety of contrasts.

The notation x°-pulse will be employed to indicate an RF pulse whose flip angle equals x° (for example, a 60°-pulse has a flip angle of 60°). Also, the magnitude of the signal induced in the coil will be written as proportional to $M_\perp$ via $s(t) = s_0\,|M_\perp(t)|$, with $s_0$ being a coefficient accounting for proton density, field strength and gains of the electronics.

### 3.5.1 Free induction decay and gradient echo

The *free induction decay* (FID) signal is induced in the receiving coil after the application of a single RF pulse, usually a 90°-pulse, referred to as *excitation pulse*. The spatial encoding of a FID signal leads to a *gradient echo* imaging sequence.

If a x°-pulse is applied at $t = 0$, the signal induced in the coil and sampled at $t = t_s$ is

$$s(t_s) \;=\; s_0\,|\sin\theta_f|\,e^{-\frac{t_s}{T_2^*}} \tag{3.23}$$

for $M_\perp(0) = 0, M_z(0) = 1$ and with $\theta_f$ being the flip angle in radians ($\theta_f = \frac{\pi}{180}$ x). Equation 3.23 states that the signal decays monoexponentially with a time constant $T_2^*$, which is usually shorter than the spin-spin relaxation time $T_2$. Hence, such kind of signals are essentially $T_2^*$-weighted. While $T_2$ is related to uncontrollable thermodynamics effects, local field inhomogeneities cause additional dephasing which leads to the $T_2^*$-decay of the orthogonal component of the magnetisation. Usually, $T_2^*$ is related to $T_2$ via

$$\frac{1}{T_2^*} \;=\; \frac{1}{\delta T_2} + \frac{1}{T_2}, \tag{3.24}$$

where $\delta T_2$ is a sample and machine dependent time constant associated to local variations of the static field. $\delta T_2$-signal losses can be recovered with the employment of $180°$-*refocusing* RF pulses, as shown in section 3.5.3. In the limit case $\delta T_2 \to \infty$, $T_2^* \equiv T_2$.

Figure 3.5 shows the time course of $s(t)$ for three different flip angles. The magnitude of the FID signal is maximum for $\theta_f = \frac{\pi}{2}$ and minimum for $\theta_f = 0$, and for any flip angle the signal has completely decayed if sampled at $t_s > 4\,T_2^*$.

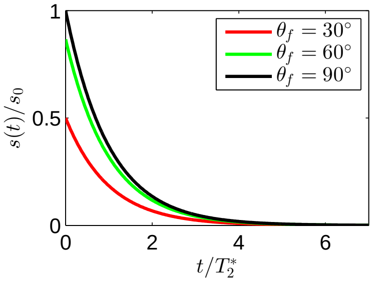

Figure 3.5: FID signal for three different flip angles $\theta_f$ as a function of the ratio $t/T_2^*$.

### 3.5.2 Inversion recovery

The preparation phase in an inversion recovery experiment is made of two RF pulses. A first RF pulse (*inversion pulse*) is applied at a flip angle of 180°, which is followed after a time interval

$\mathsf{T_I}$ (called *inversion time*) by a second RF pulse (*excitation pulse*) at a generic flip angle of $\theta_f$, usually equal to 90°. An example of the time course of the magnetisation for an inversion recovery experiment has already been shown in figure 3.4.

The first 180°-pulse inverts the magnetisation that then returns to equilibrium as predicted by the Bloch equations. Assuming that the inversion pulse is applied at $t = 0$ and that at that time $M_\perp(0) = 0, M_z(0) = M_0$, the longitudinal magnetisation at $t = \mathsf{T_I}$ is

$$M_z(\mathsf{T_I}) \; = \; M_0 \left(1 \; - \; 2\, e^{-\frac{\mathsf{T_I}}{T_1}}\right).$$

Following the second pulse, a fraction of the recovered magnetisation $M_z(\mathsf{T_I})$ is flipped to the transverse plane and eventually sampled. The signal sampled at $t = t_s$ is hence

$$s(t_s) \; = \; s_0\, |\sin\theta_f| \left|1 - 2\, e^{-\frac{\mathsf{T_I}}{T_1}}\right| e^{-\frac{t_s - \mathsf{T_I}}{T_2^*}}\,. \tag{3.25}$$

Figure 3.6 shows the term $\left|1 - 2\, e^{-\frac{\mathsf{T_I}}{T_1}}\right|$ of equation 3.25 as a function of the ratio $\mathsf{T_I}\,/\,T_1$, to which the measured signal is proportional. The most striking feature of the chart is the fact that such a term vanishes for $\mathsf{T_I} = \log 2\, T_1 \approx 0.693\, T_1$. It follows that the careful design of the inversion time can lead to the suppression of signals from tissues whose $T_1$ is such that $\mathsf{T_I} = \log 2\, T_1$, such as signal from the CSF.

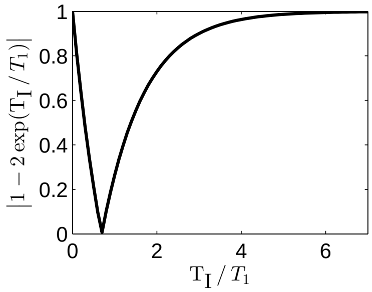

Figure 3.6: dependence of the term $\left|1 - 2\, e^{-\frac{\mathsf{T_I}}{T_1}}\right|$ on the ratio $\mathsf{T_I}\,/\,T_1$.

### 3.5.3 Spin echo experiment

In a spin echo experiment, the magnetisation is firstly flipped to the transverse plane with a $90°$-pulse, say at $t = 0$ (*excitation pulse*). Afterwards, a second 180°-pulse is applied at a time $t = \tau$ (*refocussing pulse*). Lastly, the signal is sampled at $t = t_s = 2\tau$, which is referred to as *echo time* $\mathsf{T_E}$. The magnitude of the signal sampled at the echo time is

$$s(\mathsf{T_E}) \; = \; s_0\, e^{-\frac{\mathsf{T_E}}{T_2}}, \tag{3.26}$$

which is $T_2$-weighted, rather than $T_2^*$-weighted.

The reason for the signal being $T_2$-weighted can be understood focusing on the role of the 180°-pulse. This pulse inverts the phase that each spin has accumulated, which in general varies among spins due to field inhomogeneities. If the intensity of the static field along the $z$-axis at any position $\mathbf{r}$ is written as $B_z(\mathbf{r}) = B_0 + \delta B_z(\mathbf{r})$, with $\delta B_z(\mathbf{r})$ being the local field inhomogeneity associated to a non-infinite value of $\delta T_2$, the phase accumulated from $t = 0$ to $t = \tau$ by each spin is

$$\phi(\mathbf{r}, \tau) \; = \; -\gamma \int_0^{\tau} B_z(\mathbf{r}, t^{'}) dt^{'} \; = \; -\gamma \, B_0 \tau \; - \; \gamma \, \delta B_z(\mathbf{r}) \tau$$

as predicted by equation 3.6. The $180°$-pulse changes the sign of the phase, i.e.

$$\phi(\mathbf{r}, \tau^{+}) \; = \; -\phi(\mathbf{r}, \tau^{-}) \; = \; \gamma \, B_0 \tau \; + \; \gamma \, \delta B_z(\mathbf{r}) \tau.$$

The phase at $t = 2\tau = \mathsf{T_E}$, i.e. when the signal is sampled, is at last obtained as

$$\begin{aligned} \phi(\mathbf{r}, 2\tau) = -\gamma \textstyle\int_0^{2\tau} B_z(\mathbf{r}, t^{'}) dt^{'} &= -\gamma \textstyle\int_0^{\tau} B_z(\mathbf{r}, t^{'}) dt^{'} - \gamma \textstyle\int_{\tau}^{2\tau} B_z(\mathbf{r}, t^{'}) dt^{'} = ... \\ &... = \phi(\mathbf{r}, \tau^{+}) - \gamma \textstyle\int_{\tau}^{2\tau} B_z(\mathbf{r}, t^{'}) dt^{'} \end{aligned}$$

which vanishes since $\gamma \int_{\tau}^{2\tau} B_z(\mathbf{r}, t^{'}) dt^{'} \equiv \phi(\mathbf{r}, \tau^{+})$. In practice, $\phi(\mathbf{r}, 2\tau) = 0$ means that all the spins are in phase when the signal is sampled, regardless their position and hence regardless the local field inhomogeneity. The spins have been completely refocussed and the $\delta T_2$-related signal losses have been recovered: a *spin echo* is said to occur at the echo time $\mathsf{T_E} = 2\tau$, and the $180°$-pulse has acted as a refocussing pulse.

The magnitude of the signal sampled at the echo time can be obtained integrating the Bloch equations provided that the relaxation matrix $\mathbf{R}$ in equation 3.12 is replaced by the time dependent matrix

$$\mathbf{R}(t) \; = \; \begin{cases} \text{diag}(\delta T_2^{-1} + T_2^{-1}, \delta T_2^{-1} + T_2^{-1}, T_1^{-1}) & 0 \leq t < \tau \\ \\ \text{diag}(-\,\delta T_2^{-1} + T_2^{-1}, -\,\delta T_2^{-1} + T_2^{-1}, T_1^{-1}) & \tau \leq t < 2\tau. \end{cases} \tag{3.27}$$

The integration of the Bloch equations provides a signal magnitude of which figure 3.7 shows an example. The figure demonstrates that after that the refocussing pulse is applied, the magnitude of the signal increases until the echo is fully generated. At the echo, the signal magnitude reaches a value identical to the one that an ideal $T_2$ decay would produce.

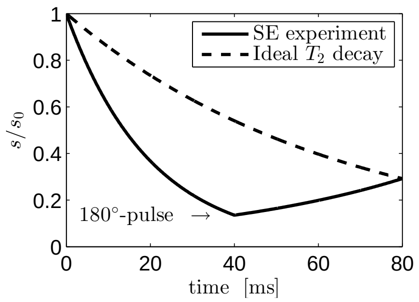

Figure 3.7: magnitude of the signal for a spin echo (SE) experiment in the presence of field inhomogeneities, i.e. when $\delta T_2 < \infty$ (solid line), and ideal $T_2$ decay (dashed line). For ease of visualisation, the following parameters where employed to generate the plot: $T_2 = 65$ ms; $T_2^* = 20$ ms (resulting in $\delta T_2 = 28.89$ ms); $\mathrm{T_E} = 80$ ms. The plot is shown for $0 \leq t \leq \mathrm{T_E}$.

### 3.5.4 Stimulated echo acquisition mode (STEAM)

In a stimulated echo acquisition mode (STEAM) experiment [61], three RF pulses are applied before the signal is sampled. The time interval between the first and the second pulse and between the second and the third pulse will be referred to as $t_1$ and $t_2$. Although the pulses are usually three 90°-pulses, they can be theoretically applied at the generic flip angles $\theta_1$, $\theta_2$ and $\theta_3$. Figure 3.8 shows a schematic of the STEAM preparation phase.

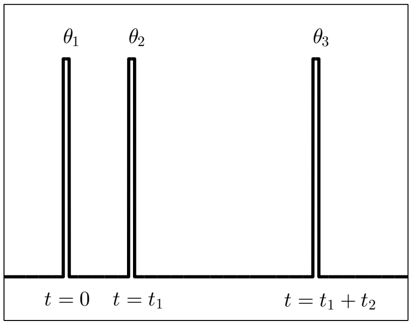

Figure 3.8: schematic describing the sequence of RF pulses employed in STEAM. A first pulse is applied at $t = 0$ and at a flip angle $\theta_1$; a second pulse is applied at $t = t_1$ and at a flip angle $\theta_2$; a third pulse is applied at a time $t = t_1 + t_2$ and at a flip angle $\theta_3$.

The sequence of three pulses shown in figure 3.8 generates five echoes, as shown extensively in previous literature [61, 69]. The time at which each echo occurs and its amplitude can be calculated employing the *extended phase graphs* formalism [199]. Such a formalism describes the magnetisation as generated by a set of configuration states, such that each of these states is associated to an ensemble of spins that are in phase, i.e. to an *isochromat*. The evolution of each isochromat phase over time (named *phase pathway*) needs to be evaluated under the application of RF pulses and gradients. In doing so, relaxation and *phase memory* are also modelled, with the latter term referring to the phenomenon by which an isochromat in the longitudinal configuration (i.e. aligned to the polarising field) stores the phase previously accumulated in a transverse configuration, i.e. while being in the transverse plane.

In practice, the echo that is usually sampled and spatially encoded is the third echo, which occurs at a time $t = 2t_1 + t_2$ and is classified as a *stimulated echo*. The amplitude of such an echo sampled at $t_s = 2t_1 + t_2$ is [61]

$$s(t_s) \;=\; \frac{1}{2}\, s_0 \, |\sin\theta_1|\,|\sin\theta_2|\,|\sin\theta_3| \;\, e^{-\frac{t_2}{T_1}}\, e^{-\frac{2\,t_1}{T_2}}\,. \tag{3.28}$$

In equation 3.28, $t_2$ is usually referred to as *mixing time* $\mathrm{T_M}$ whereas $\mathrm{T_E} = 2\,t_1$ is the *echo time* [151].

STEAM was developed as an alternative to spin echo experiments in order to i) deal with partial refocussing due to imperfections of the 180°-pulse; ii) limit the RF power deposition to the body reducing the number of required 180°-pulses; iii) obtain $T_1$-weighting in a non-time-consuming manner, since during the time interval between the second and the third pulse the magnetisation is stored in the longitudinal direction. Nevertheless, it should be noted that even in the favourable condition $t_2 \ll T_1$, implying $e^{-\frac{t_2}{T_1}} \approx 1$, STEAM can only provide half of the signal level of a spin echo experiment with matching echo time, which is clear comparing equation 3.28 and 3.26.

### 3.5.5 Repeated sequences

Pulse sequences such as those described in the previous sections are often repeated in a cyclic manner. This may be done to obtain several repetitions of a whole MRI image at each cycle for averaging or because the spatial encoding leading to an image is distributed over different cycles. In general, the *repetition time* $\mathrm{T_R}$ describes the period of these repeated cycles of acquisition, and the overall duration of the MRI experiment is proportional to the value of $\mathrm{T_R}$. In spite of a reduction of the total acquisition time as $\mathrm{T_R}$ shortens, it should be noted that often the amount of signal available for spatial encoding increases as $\mathrm{T_R}$ increases, leading to better image quality.

Figure 3.9 shows and example of the impact of $\mathrm{T_R}$ for a repeated single-pulse experiment (FID experiment introduced in section 3.5.1). Two scenarios are presented, illustrated respectively to the right and to the left of the figure. For both cases, transverse relaxation was modelled via $T_2^*$ monoexponential decay with $T_2^* = 45\,\mathrm{ms}$, whereas $T_1 = 830\,\mathrm{ms}$ was used for longitudinal relaxation. In the first case, a 60°-pulse lasting 5 ms is repeated with $\mathrm{T_R} = 100\,\mathrm{ms}$, whereas in the second case a similar pulse is repeated with $\mathrm{T_R} = 300\,\mathrm{ms}$. Pulses are shown on top, whereas the corresponding normalised signals to the bottom.

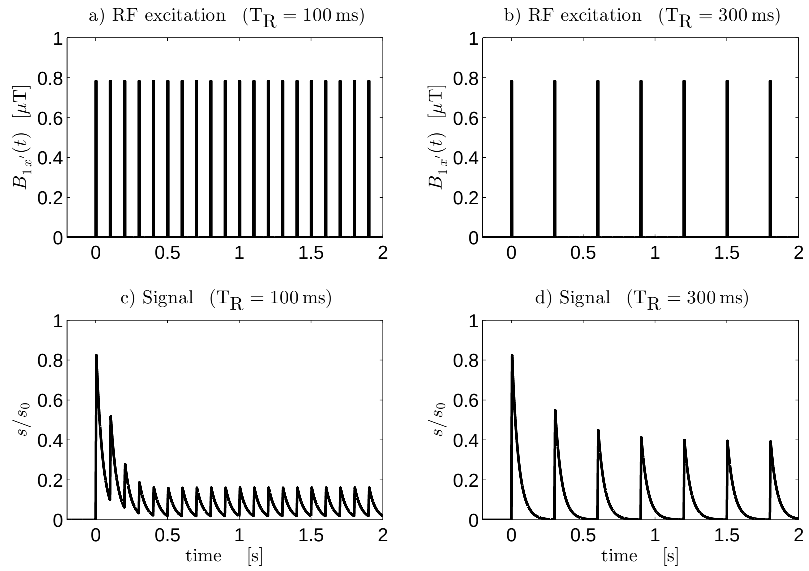

Figure 3.9: example of the impact of $\mathrm{T_R}$ in a FID experiment. a): RF excitation made of a repeated sequence of 60°-pulses of 5 ms duration, for $\mathrm{T_R} = 100$ ms. b): RF excitation made of a repeated sequence of 60°-pulses of 5 ms duration, for $\mathrm{T_R} = 300$ ms. c): magnitude signal corresponding to the excitation in a), for $T_2^* = 45$ ms and $T_1 = 830$ ms. d): magnitude signal corresponding to the excitation in b), for $T_2^* = 45$ ms and $T_1 = 830$ ms.

The figure demonstrates that in both cases, a steady state where at each cycle the amount of signal lost due to $T_2^*$ decay is recovered after each excitation is soon reached. For the short $\mathrm{T_R}$ case, such a steady state is reached earlier in time but at the price of a lower intrinsic signal level. Also, with a shorter $\mathrm{T_R}$, more repetitions can obviously be fit in the same time window, increasing the number of potential signal averages.

## 3.6 Sampling methods

In section 3.4.2, the possibility of obtaining a spatial distribution of relaxation-weighted spin density (i.e. the MRI image) from sampling the k-space was highlighted. This section describes fundamental properties related to the sampling of the k-space, as well as common techniques that are employed to achieve the sampling in practice.

### 3.6.1 Field-of-view and resolution

Knowledge of $s(\mathbf{k})$ for $\mathbf{k} \in [-\infty; +\infty] \times [-\infty; +\infty] \times [-\infty; +\infty]$ allows the reconstruction of the continuous effective spin density $\rho(\mathbf{r})$. However, in practice, the signal is a discrete and truncated version of the ideal $s(\mathbf{k})$, which will be referred to as $s_m(\mathbf{k}_n)$ for $n = ..., -1, 0, 1, ...$. Discrete, inverse Fourier transformation of $s_m(\mathbf{k}_n)$ leads to a reconstructed spin density $\rho_r(\mathbf{r}_m)$, for $m = ..., -1, 0, 1, ...$.

Theoretical considerations related to the properties of the continuous and discrete Fourier transforms [69] explain how $\rho_r(\mathbf{r}_m)$ differs from $\rho(\mathbf{r})$. Firstly, since the k-space is sampled only in a finite portion (i.e. it is truncated), the information contained in $\rho_r(\mathbf{r}_m)$ is blurred as compared to that contained in $\rho(\mathbf{r})$. Secondly, since the k-space is sampled in a discrete manner, replicas of the spin density spatial pattern arise. These replicas overlay if they extend outside the set of spatial positions $\rho_r(\mathbf{r}_m)$, $m = ..., -1, 0, 1, ...$ that are kept, giving rise to a common imaging artifact called *aliasing*.

It is possible to relate quantitatively the geometric features of the discrete image of the effective spin density to the k-space sampling. Such relations are of the uttermost importance when performing an MRI experiment, since allow the choice of an adequate *image resolution* (physical size of the discrete image samples) and of the *field of view* (FOV, the physical extent of the world that is imaged), while avoiding aliasing. Along any of the three components of $\mathbf{k}$, one can indicate with $\Delta k$ the sampling interval, whereas $\mathsf{K} = N\Delta k$ is the portion of k-space sampled, with $N$ being the number of acquired samples (usually referred to as *matrix size*), as illustrated in figure 3.10.

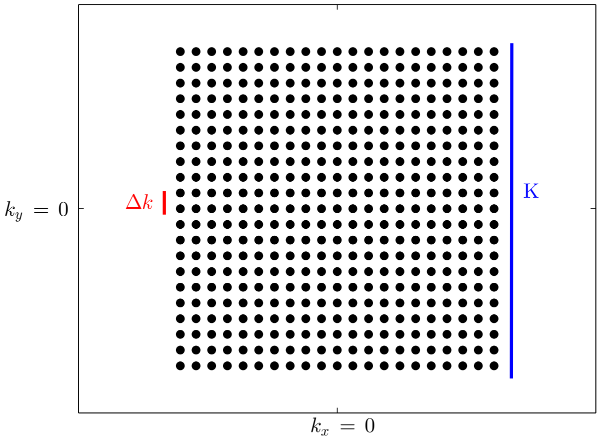

Figure 3.10: example of two-dimensional k-space, with illustration of the meaning of $\Delta k$ and K along the $k_y$-direction. The black dots represent the points of the k-space that are sampled.

It can be proven that the corresponding spatial resolution along that direction, in the space domain, is

$$\Delta r = \frac{1}{\mathsf{K}}, \tag{3.29}$$

while the FOV is

$$\mathsf{FOV} = \frac{1}{\Delta k}. \tag{3.30}$$

The condition to avoid aliasing is obtained from equation 3.30. If $L$ is the size of the object being imaged, it must hold that

$$\mathsf{FOV} \geq L, \tag{3.31}$$

which states that the FOV must be at least as big as the imaged object, to prevent signal from outside the FOV from folding over inside the FOV itself, as explicated by figure 3.11. In practice, the size $L$ refers to the part of the object that produces signal. Hence, such condition can be violated as long as signal from outside the FOV is suppressed. This principle is exploited in *reduced*-FOV (rFOV) imaging, common in areas such as the spinal cord and optic nerves.

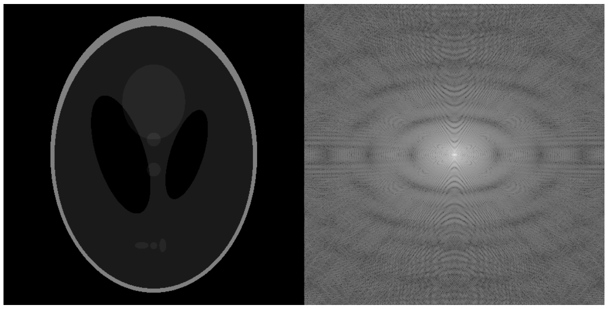

(a) image and k-space satisfying equation 3.31.

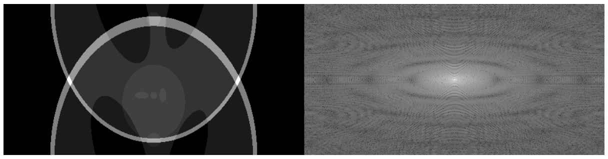

(b) aliased image and k-space violating equation 3.31.

Figure 3.11: toy example highlighting the importance of the design of the FOV, obtained from the Shepp-Logan phantom [162]. To the left, an illustrative discrete effective spin density in the spatial domain is shown. To the right, the logarithm of the magnitude of the discrete Fourier transform of the image is shown. In case a), the FOV along the vertical direction is at least as big as the object size. In b), the FOV has been halved downsampling the k-space of a factor 2, which doubles $\Delta k$. This leads to fold over of the signal from outside the FOV, giving rise to aliasing.

### 3.6.2 2D and 3D imaging

There are different ways to sample the k-space and acquire the data necessary for the reconstruction of an MRI image. The two most standard approaches are two-dimensional (2D) multi-slice imaging and three-dimensional (3D) imaging.

In 2D multi-slice imaging, only a thin slice of tissue on the order of the millimeter is excited by RF irradiation and spatially encoded. The signal is considered as originating from an object with negligible thickness and modelled as a function of $s(k_x, k_y)$. The spatial selective excitation is achieved turning on one of the gradients (say the $z$-component $G_z$, the *slice selection gradient*) during an RF excitation containing a spectrum of frequencies in the band $[\omega - \frac{1}{2}\Delta\omega;\ \omega + \frac{1}{2}\Delta\omega]$. Since the resonance frequency depends on the spatial position via $\omega_{\text{res}} = \gamma\, B_0 + \gamma\, G_z\, z$, the tissue within the interval $z \in \left[\frac{\omega - \frac{1}{2}\Delta\omega - \gamma B_0}{\gamma\, G_z};\ \frac{\omega + \frac{1}{2}\Delta\omega - \gamma B_0}{\gamma\, G_z}\right]$ is excited and available for spatial encoding. The two remaining gradient components $G_x$ and $G_y$ are employed to navigate the k-space. While one is usually quickly turned on and off to select a k-space line ($G_y$, or *phase encoding gradient*), the other is used to move along the selected line while sampling the signal ($G_x$ or *readout* or *frequency encoding gradient*). The time period at which the signal is sampled is called *dwell time*

($t_{\text{dwell}}$), and its inverse is the *readout bandwidth* or *receiver bandwidth* (BW). Figure 3.12 shows an illustration of a possible 2D spatial encoding of a FID experiment. The slice selection gradient is turned on during RF excitation, which is a rectangle in the frequency domain, i.e. a *sinc* in the time domain. Afterwards, the phase encoding gradient selects the k-space line, along which the acquisition proceeds by virtue of the readout gradient, with the signal being sampled when the readout gradient is on.

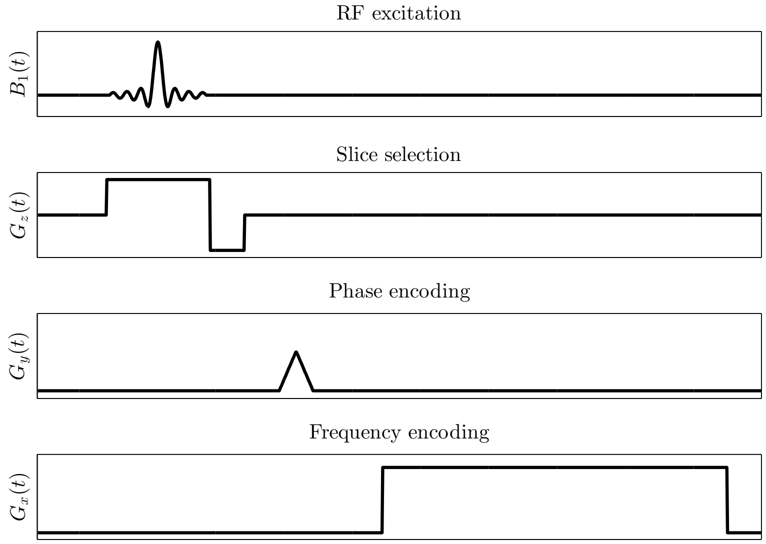

Figure 3.12: schematic of a 2D MRI experiment. From top to bottom, the RF excitation ($B_1$ field), the slice selection gradient ($G_z$), the phase encoding gradient $G_y$ and the readout gradient $G_x$ are illustrated.

In 3D imaging, a whole portion of tissue is excited by RF irradiation and spatially encoded. The k-space is a 3D space and the signal is handled as a function of $k_x$ $k_y$ and $k_z$. Two of the three gradients are used for phase encoding, while $G_x$ is employed as a readout gradient to acquire a whole column of the parallelepiped representing the 3D k-space. 3D imaging can lead to higher signal levels than 2D, and it is robust towards cross-talk among adjacent slices. Nevertheless, this comes at the expense of a longer acquisition time.

Lastly, it is reported that although the k-space is usually sampled in a Cartesian grid, other approaches are employed in specific applications. For 2D imaging, this may include radial or spiral sampling, whereas for 3D imaging sampling along spirals or cones may be used. Non-Cartesian sampling, while requiring reformatting of the data to a Cartesian structure before inverse Fourier transformation, may prove useful in critical applications, such as spatial encoding of extremely short $T_2^*$ components.

### 3.6.3 Echo planar imaging

Echo planar imaging (EPI) is a fast way of sampling the whole k-space in a few excitations, often only one [171]. EPI is a readout method that can be employed after different preparations (es. spin echo EPI, gradient echo EPI, inversion recovery EPI), and it can be 3D or 2D.

Cartesian EPI is certainly the most common version, where the k-space is sampled in a Cartesian grid. In 2D EPI adjacent lines are covered in opposite directions, and a rapid activation and deactivation of the phase encoding gradient allows the acquisition to move from one line that has been completely acquired to the next one. Each line encodes a *gradient echo* that occurs when passing through $k_x = 0$, since for $k_x = 0$ the dephasing induced by the gradient $G_x$ vanishes.

EPI can be *single-shot* or *multi-shot*, as illustrated in figure 3.13. When the whole k-space is encoded following one excitation, the readout is said to be performed in a *single shot*. In segmented or multi-shot EPI instead, only a part of the k-space is encoded after one excitation. A typical pattern of acquisition can be similar to that shown to the right of figure 3.13, such that in each shot a gap between two consecutively acquired lines is left.

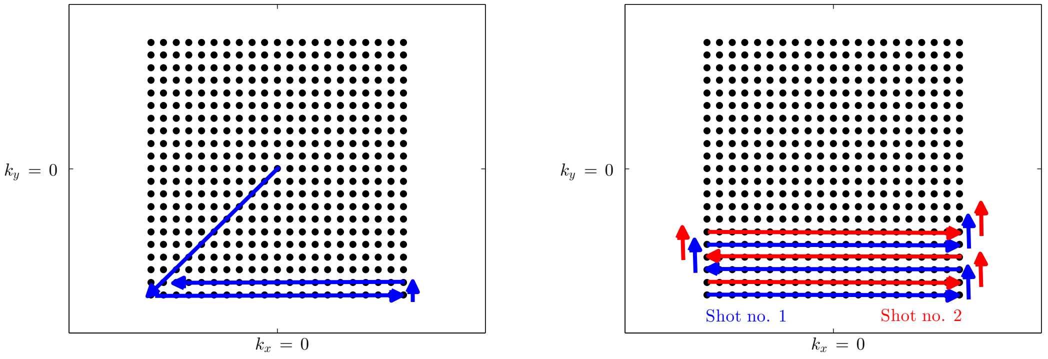

(a) single-shot EPI.

(b) multi-shot EPI with two shots.

Figure 3.13: sampling of k-space in single-shot and multi-shot Cartesian EPI. For the multi-shot case, an illustrative examples with two shots (first shot in blue, second shot in red) has been drawn.

EPI is a quick and efficient spatial encoding method. It is common in quantitative MRI techniques such as diffusion, where a high number of images is acquired during one experiment. Despite its advantages in terms of speed of acquisition, EPI images often show distortions. These distortions arise from local field inhomogeneities, which are more intense close to interfaces between tissues with significantly different magnetic susceptibility. The magnetic susceptibility inhomogeneities lead to the misplacement of voxels along a given direction of a quantity $d$ calculated as

$$d(\mathbf{r}) = \frac{\gamma}{2\,\pi} \, \text{FOV}_{\text{per-shot}} \, T_{\text{acq}} \, \Delta B_z(\mathbf{r}). \tag{3.32}$$

In equation 3.32, $\text{FOV}_{\text{per-shot}}$ is the field-of-view acquired per each shot along the direction, $T_{\text{acq}}$ is the time interval separating the acquisition of two k-space samples along the direction and $\Delta B_z(\mathbf{r})$ is the local field inhomogeneity. Equation 3.32 implicitly states that for EPI acquisitions, distortions are more intense along the phase encoding direction as compared to the readout direction. For the phase encoding direction, if $N_x$ is the number of samples in each k-space line, then $T_{\text{acq}} \approx N_x \, t_{\text{dwell}} = N_x/\text{BW}$ is much grater than the corresponding value $T_{\text{acq}} = t_{\text{dwell}} = 1/\text{BW}$ for the readout direction. From 3.32, it also follows that multi-shot acquisitions are less hampered by distortions than single-shot EPI, and that rFOV methods can help mitigate the distortions via a reduction of $\text{FOV}_{\text{per-shot}}$.

## 3.7 Noise and signal-to-noise ratio

Reconstructed MRI images are affected by noise arising from stochastic thermal fluctuation of the voltage induced in the receiver coils, referred to as *thermal noise* or Johnson-Nyquist noise [91, 139]. Thermal noise affecting the complex-valued data in k-space is well described by white noise characterised by a zero-mean, Gaussian distribution of amplitudes. Also, by virtue of the properties of the Fourier transformation, the noise is also Gaussian in the spatial domain, i.e. both real and imaginary channels of a complex-valued MRI image are affected by Gaussian noise.

A useful metric commonly employed in MRI is the *signal-to-noise ratio* (SNR), which is defined as that ration between the true underlying signal and the noise standard deviation. In an imaging experiment, the SNR depends on the parameters controlling the k-space sampling. The SNR is considered to be proportional to the quantity

$$\text{SNR} \;\propto\; \Delta x \, \Delta y \, \Delta z \sqrt{\frac{N \, N_x \, N_y \, N_z}{\text{BW}}}, \tag{3.33}$$

where $\Delta x$, $\Delta y$, $\Delta z$ are the voxel sizes, $N$ is the number of signal averages, BW is the bandwidth and $N_x$, $N_y$ and $N_z$ are the number of k-space samples along the $x$, $y$ and $z$ directions ($N_z = 1$ for 2D multi-slice imaging).

It is of common practice to combine the real and imaginary parts of an MRI image in a single, magnitude image. Magnitude images are characterised by Rician-distributed noise, rather than Gaussian [68], or even by more complicated noise distributions such as non-central chi-squared when *parallel imaging* (described in the next section) is employed [169]. In practice, a Rician distribution resembles a Gaussian distribution for SNR levels of 5 or greater. However, in low SNR regimes, the Rician-distributed signals in a homogeneous area are characterised by a distribution with asymmetric tails. Another feature of Rician noise is the presence of a *noise floor*, which is the minimum signal that is measured in absence of any true signal [169].

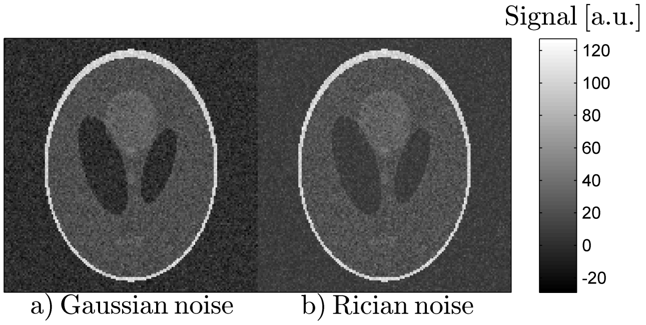

Figure 3.14: toy example of Gaussian-distributed and Rician-distributed noisy MRI images obtained from the Shepp-Logan phantom [162]. Left: Gaussian noise. Right: Rician noise. The two images differ notably in areas of low signal intensity, where the Rician-distributed image is affected by a noise floor.

## 3.8 Speeding up the MR experiment: parallel and multiband imaging

In modern MRI systems, acquisition times are reduced by the employment of innovative imaging approaches such as *parallel* and *multiband imaging*.

Parallel imaging [44] exploits modern manufacturing of receiver coils, which in fact are made of several coil elements, each characterised by a different sensitivity profile. These elements are capable of receiving signal from different parts of the excited volume, and the final MRI image is obtained as a combination of the individual images from the elements. Exploiting such a redundancy of the acquisition, the k-space is undersampled, i.e. a number of k-space lines smaller than the minimum number necessary to avoid aliasing is acquired. Combining the aliased images from the different elements allows the final reconstruction of a non-aliased image, provided that additional information, such as the sensitivity profile of each coil element, is available. The reconstruction can be performed in the image domain, as in *sensitivity encoding* (SENSE) [150], or in the k-space, as in *generalized autocalibrating partially parallel acquisitions* (GRAPPA) [66]. Parallel imaging reduces significantly the total scan time, although this is associated to a reduction of the SNR. The reduction of scan time is most significantly in experiments where one k-space line is acquired in each $T_R$. For single-shot EPI readouts, parallel imaging helps reducing the effective $T_E$, while mitigating distortions by virtue of the reduction of term $FOV_{per\text{-}shot}$ in equation 3.32.

In multiband imaging, two or more slices are excited simultaneously by a multiband RF pulse [55]. Exploiting the acquisition from multiple receiving coils, the signals from the different slices can be separated with minimal SNR losses. The acceleration factors achieved with multiband enable higher spatial resolution or number of signal averages, beneficial for qMRI.

## 3.9 Diffusion MRI

DW MRI is a qMRI method that exploits the diffusion of water molecules as a source of contrast among tissues [90, 92, 108, 124]. Water molecules diffuse by means of a ceaseless random walk known as Brownian motion [50] due to thermal agitation. In absence of confinements, molecules diffuse isotropically with equal probability along any direction, and the average root mean squared displacement of this motion over a time interval $T_d$ is [50]

$$<r> = \sqrt{6\,D\,T_d}. \tag{3.34}$$

However, water in human tissue is not free but it is compartmentalised within structures that restrict its diffusion, as demonstrated by the image of an axon and of its surrounding in figure 3.15. The patterns of diffusion in this restricted environment depart from the ideal case of equation 3.34 [138]. For instance, diffusion within cerebral and spinal white matter is characterised by anisotropy, implying that along certain directions molecules diffuse more than along others (specifically, they diffuse more along, rather than across, fibre bundles).

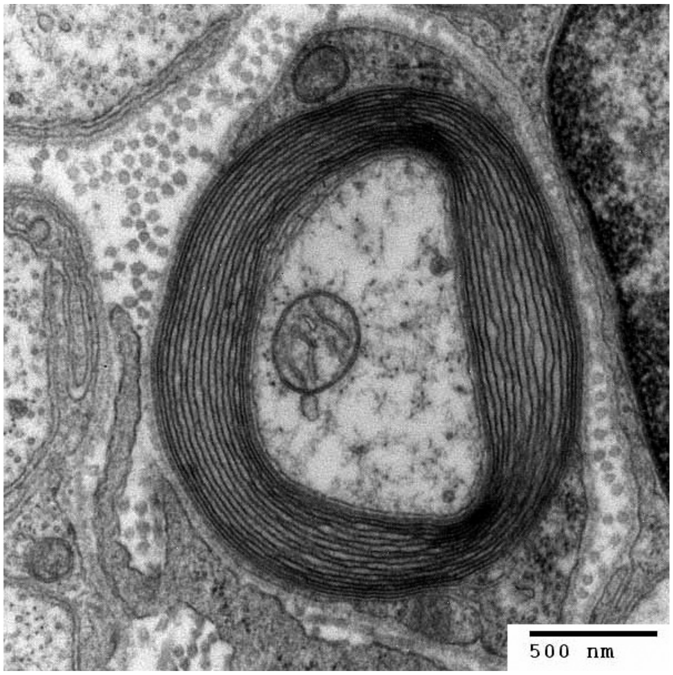

Figure 3.15: transmission electron micrograph of an axon and of its surrounding, showing three compartments: intra-axonal space, myelin space and extra-axonal space. Image obtained from `https://upload.wikimedia.org/wikipedia/commons/c/c1/Myelinated_neuron.jpg`, generated and deposited into the public domain by the Electron Microscopy Facility at Trinity College (Roadnottaken) under the GNU Free Documentation License v.1.2 via Wikimedia Commons `https://commons.wikimedia.org/wiki/File:Myelinated_neuron.jpg?uselang=it`.

The MRI signal can be made sensitive to diffusion by virtue of the application of magnetic field gradients prior to spatial encoding, as noticed by Hahn in the early 1950s [71]. These gradients are referred to as *diffusion encoding*, *diffusion sensitising* or *diffusion weighting gradients*. Following excitation, the phase accrual at sampling time $t = t_s$ due to the diffusion encoding gradient $\mathbf{G}(t)$ of a spin of random walk $\mathbf{r}_k(t)$ can be written as $\phi_k(t_s) = -\gamma \int_0^{t_s} \mathbf{G}(t^{'})^{\mathsf{T}}\, \mathbf{r}_k(t^{'})\, dt^{'}$. The ensemble average over the set of all spins in a voxel of the elementary transverse magnetic moment $e^{j\phi_k(t_s)}$ provides to the ratio between the DW signal $s$ and the non-DW signal $s_0$:

$$\frac{s}{s_0} = < e^{j\phi_k(t_s)} > . \tag{3.35}$$

Potentially, all MRI sequences can be made sensitive to diffusion, such as STEAM [123, 151]. However, the decoding of the effect that diffusion has on the signal may not be straightforward in some cases. The sequence that is most often employed to probe diffusion is the spin echo technique, in the so called *pulsed gradient spin echo* (PGSE) experiment, illustrated in figure 3.16 and coming from the work of Carr and Purcell [29] and Stejskal and Tanner [172]. In PGSE, the diffusion encoding gradients are placed on either side of the 180°-RF pulse. They are characterised by a *direction* **g**, a *strength* $G$, a *duration* $\delta$ and a *separation* $\Delta$. If spins were still, the phase accrual due to the second gradient lobe would cancel that caused by the first one. However, due to diffusion, each spin is not still but has a random walk while the sequence is played out. Therefore, the phase accrual during the second gradient lobe only partially compensates that caused by the first one. This is a direct consequence of the fact that each spin probes different locations during the first and during the second pulse, which correspond to different phase accruals, being the phase accrual position-dependent when a magnetic field gradient is on. At the echo time, each individual spin of the ensemble is characterised by a slightly different phase accrual, and summing over the whole ensemble leads to a reduction of the overall signal intensity as compared to a non-DW spin echo acquisition. The *diffusion time* $T_d = \Delta - \delta/3$ provides the time window during which spins are let diffuse before acquiring the signal, and hence defines the length scale probed by the experiment according to equation 3.34.

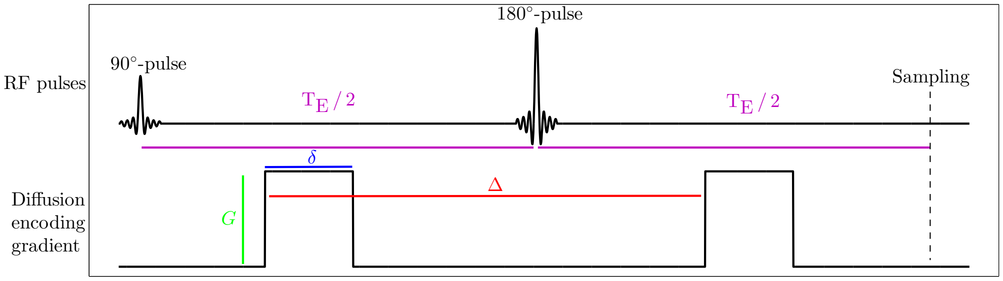

Figure 3.16: schematic of the PGSE sequence.

Spin diffusion is determined by the underlying tissue microstructure, of which the measured DW signal carries a specific signature. The challenging task becomes the retrieval of the properties of the underlying microstructure from the observation of a set of DW signals. For this purpose, different approaches have been proposed in literature, of which a brief review follows below.

### 3.9.1 q-space imaging

In *q-space imaging* (QSI), the acquired signal is related to the Fourier transform of the probability distribution of displacement of spins due to diffusion [28,43,126], named *diffusion propagator*, such that

$$s(\mathbf{q};\Delta) \;=\; \int_{\mathbb{R}^3} P(\mathbf{r};\Delta)\, e^{-j2\pi\mathbf{q}^\mathsf{T}\mathbf{r}}\, d^3\mathbf{r}. \tag{3.36}$$

In equation 3.36, $\mathbf{q} = (2\pi)^{-1}\gamma\,\delta\,G\,\mathbf{g}$ is the $q$-vector (in m$^{-3}$), $s(\mathbf{q};\Delta)$ is the acquired signal and $P(\mathbf{r};\Delta)$ is the diffusion propagator.

In some cases, such as in q-ball imaging (QBI) [186], only the angular information content of $P(\mathbf{r};\Delta)$ is retained and is described in terms of a *diffusion orientation distribution function* (dODF) [2,184], expressed as

$$\text{dODF}(\hat{\theta},\hat{\phi};\Delta) \;=\; \int_0^\infty P(\mathbf{r}(\hat{\rho},\hat{\theta},\hat{\phi});\Delta)\,\hat{\rho}^2\,d\hat{\rho}, \tag{3.37}$$

where $(\hat{\rho},\hat{\theta},\hat{\phi})$ are the spherical coordinates.

The propagator in equation 3.36 describes the probability distribution of the random walks. The equation holds true only in the *narrow pulse limit* [43], i.e. when $\delta \ll \Delta$, so that diffusion during the pulse duration $\delta$ can be neglected. This is not often the case in clinical systems, and alternative approaches need to be adopted. For instance, the phase accrual during the finite pulse duration $\delta$ is modelled as a Gaussian distribution (Gaussian phase distribution approximation [46]). Also, reformulations of equation 3.36 in terms of a mean *"centre-of-mass diffusion propagator"* [125] have been proposed. In those cases, an apparent propagator depending on the centre of mass of the random walks occurring while the pulses are turned on is introduced.

A popular example of q-space imaging technique is diffusion spectrum imaging (DSI) [198]. QSI methods such as DSI do not make assumptions about the underlying microstructure. In spite of this advantage, their employment in clinical settings is limited by the long acquisition time necessary to sample the $q$-space. Moreover, they can only measure the effects of microstructure on the shape of the propagator, without providing estimates of the geometric features that determine such a shape.

### 3.9.2 Phenomenological models

Phenomenological models aim to capture the characteristics of the signal decay, but do not parametrise the expression of the DW signal as a function of specific microstructural parameters.

#### Gaussian diffusion

In the simplest cases, it is hypothesised that the diffusion propagator is a Gaussian probability density function. This hypothesis supports signal models such as the *apparent diffusion coefficient*

(ADC) [172] model, such that

$$s(b;\mathsf{ADC}) \;=\; s_0\, e^{-b\,\mathsf{ADC}}. \tag{3.38}$$

Above, the $b$-value $b = (2\pi\, q)^2(\Delta - \delta/3)$ measures the overall diffusion-weighting strength, with $q$ being $q = (2\pi)^{-1}\gamma\,\delta\, G$. The ADC model can provide a reasonable description of the diffusion signal attenuation in biological tissues if $b$ is not too high. The ADC evaluated along a direction of restricted diffusion yields information about the local geometry, such as the surface-to-volume ratio of the structures within which spin diffuse [62]. This model can be generalised to account for spatial anisotropy of diffusion, which is a known feature of the central nervous system [108].

Diffusion anisotropy is taken into account in popular DTI [12]. In DTI, the signal attenuation in a PGSE experiment is written as

$$s(b, \mathbf{g}; \mathbf{D}) \;=\; s_0\, e^{-b\,\mathbf{g}^{\mathsf{T}}\,\mathbf{D}\,\mathbf{g}}. \tag{3.39}$$

In equation 3.39, **g** is the gradient direction and **D** is the diffusion tensor, already introduced in equation 3.17. From the three eigenvalues of **D** $\lambda_1 \geq \lambda_2 \geq \lambda_3 \geq 0$, voxel-wise metrics summarising the diffusion profile are obtained [13], such as *axial*, *radial* and *mean diffusivities* (AD, RD and MD) and *fractional anisotropy* (FA). AD quantifies the amount of diffusion along the tensor principal direction; RD orthogonal to it; MD quantifies the average amount of diffusion. FA summarises the anisotropy of the diffusion profile, minimum when it is equal to 0 (isotropic tensor) and maximum when it is 1. FA is often employed as a marker of neuronal integrity, while AD values measured in well-aligned WM fibre bundles are taken as estimates of the neuronal diffusivity.

### Non-Gaussian diffusion

Other phenomenological models extend equations 3.38 and 3.39 to relax the hypothesis of Gaussianity of diffusion [76], which does not describe the observed DW signals in neural tissue at high $b$-value [33]. This can be achieved introducing dependences on higher-order terms, proportional to powers of $b$, i.e. via cumulant expansion of the DW signal [59, 137]. For example, *diffusion kurtosis imaging* (DKI) [84] is currently a standard method to quantify the amount of non-Gaussian diffusion. In one dimension, the DKI model can be written as

$$s(b; D_{\mathsf{app}}, K) \;=\; s_0\, e^{-b\, D_{\mathsf{app}} + \frac{1}{6}\, K\, (b\, D_{\mathsf{app}})^2}, \tag{3.40}$$

where $D_{\mathsf{app}}$ is the apparent diffusivity and $K$ is the kurtosis. Non-Gaussian behaviours are quantified directly by $K$. They are believed to arise from the presence of structures that impede and restrict the diffusion of water molecules, such as axons in WM, whose density can be estimated from the maximum kurtosis [59].

### Other phenomenological models

Some categories of biophysical models are used to estimate complex distributions of fibre bundles within WM voxels [79], recovering quantities such as the *fibre orientation distribution function* (fODF). As an example, *spherical deconvolution* (SD) [182] and its improved constrained version [183] model the measured DW signals in WM as the contribution of several elementary fibre bundles weighted by their fODF. The elementary fibre bundles are usually modelled as identical compared to each other, but this assumption is relaxed in *restriction spectrum imaging* (RSI) [207], where a spectrum of diffusivities across the fibre bundles is allowed to account for different levels of restriction.

Other phenomenological models have been introduced in literature. In spite of their capability of describing well the variability of the measured DW signals [136], their main limitation is that they are unable to provide direct estimates of microstructural parameters, which is necessary to better understand the pathophysiology of disease.

### 3.9.3 Multi-compartment models

In multi-compartment DW MRI methods, the signal is written as the contributions coming from $N$ tissue compartments, or *pores*, each occupying a relative voxel volume fraction $v_i$ for $i = 1, ..., N$ and representing water pools in different environments (such as intra and extra-axonal). When the system is observed at diffusion times much shorter than the time scale at which compartments exchange water, the signal can be written as

$$s(\mathbf{g}, \Delta, \delta, G; \mathbf{p}) \ = \ s_0 \sum_{i=1}^{N} v_i \, s_i(\mathbf{g}, \Delta, \delta, G; \mathbf{p}_i), \tag{3.41}$$

under the constraint $\sum_{i=1}^{N} v_i \ = 1$, with $s_0$ being the non-DW signal. In equation 3.41, the characteristic signal $s_i(\mathbf{g}, \Delta, \delta, G; \mathbf{p}_i)$ of the $i$-th compartment depends in general on a set of parameters $\mathbf{p}_i$. The overall set of parameters $\mathbf{p} \ = \ \{s_0, \mathbf{p}_1, \mathbf{p}_2, ..., \mathbf{p}_N, v_1, v_2, ..., v_{N-1}\}$ is estimated fitting the adopted model to a set of $M$ measurements [87, 135, 170].

Practical representations of the tissue in the form of combinations of simple geometric domains are of common usage, such as cylinders or sticks modelling axons, hindered spaces for the extracellular water or isotropic compartments ("balls") modelling CSF [147]. Models such as CHARMED [8] (or *composite hindered and restricted model of diffusion*), *ball-and-stick* [15] and the model proposed in [87] mainly aim to quantify neurite density; AxCaliber [7] and ActiveAx [4] mainly focus on axon diameter; *ball-and-rackets* [168] and NODDI [215] model neurite orientation dispersion; the *spherical mean technique* provides indices of *per axon* anisotropy [95]; DBSI [196] separates different rates of diffusion; *intravoxel incoherent motion* (IVIM) distinguishes diffusion from perfusion-related pseudo-diffusion [109]; *vascular, extracellular and restricted diffusion for cytometry in tumors* (VERDICT) MRI was designed for applications in cancer research [148].

### 3.9.4 Alternative diffusion encoding approaches

Diffusion encoding approaches different from PGSE have been explored in literature. A brief overview of those is presented to the reader in this section.

Oscillating gradient spin echo (OGSE) sequences are similar to PGSE, but oscillating gradient waveforms, rather than pulsed, are placed on other side of the refocusing pulse, as illustrated in figure 3.17. They can be used to probe very small spatial scales, as they allow the achievement of appreciable diffusion weighting even for extremely short diffusion times [154]. Although some *in vivo* applications of OGSE sequences have been shown [10], they are not routinely available in commercial MRI scanners and they remain challenging when the maximum gradient strength is low.

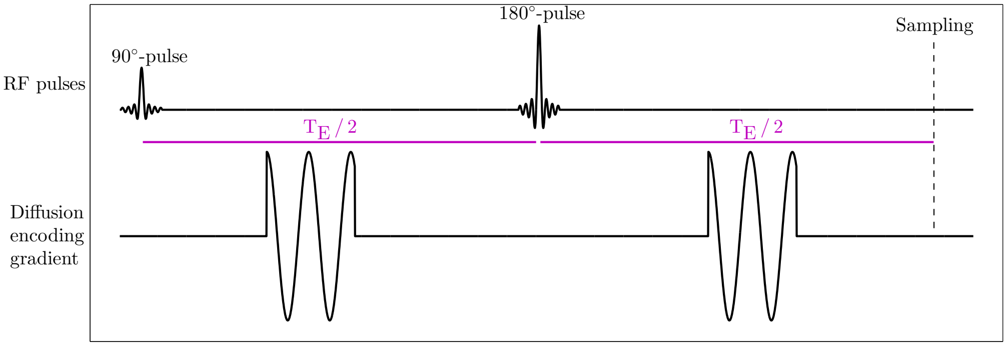

Figure 3.17: summary representation of an example of OGSE sequence.

*Multiple pulsed field gradient* (mPFG) sequences apply multiple diffusion encoding gradients in a single or multiple refocussed spin echo experiment [142, 160]. They probe correlations of spin displacements along different directions and provide metrics characterising specific geometrical features of the pore space. These may include *fractional eccentricity* (FE), characterising the intrinsic anisotropy of compartments [89], or *displacement correlation tensors*, related to the surface-to-volume ratio of the pore space [86]. They can also separate the opposing effects that restriction and exchange of water among compartments have on the DW signal at long diffusion times. This has the potential to provide *in vivo* cell membrane permeability or exchange rate mapping, such as in *filter exchange imaging* (FEXI) [134]. Similarly to OGSE, mPFG methods are not currently implemented as off-the-shelf sequences in clinical MRI systems, and they require relatively long echo times leading to $T_2$-related signal losses.

Lastly, innovative methods vary the diffusion sensitising gradient over a 3D trajectory continuously during diffusion encoding, leading to *diffusion encoding tensors* [202] that enable isotropic and anisotropic diffusion weighting [103]. These new approaches provide innovative indices of microscopic FA, promising in conditions such as brain tumours [177]. Similarly to mPFG-derived FE, microscopic FA quantifies the anisotropy of single pores factoring out the effect of pore orientation dispersion, which confounds DTI FA.

## 3.10 Quantitative MRI of the spinal cord

qMRI is potentially useful in the spinal cord, with implications in the diagnosis and prognosis of conditions such as MS [37, 41, 112, 131], SCI [179] or amyotrophic lateral sclerosis (ALS) [153].

In spite of its importance, qMRI of the spinal cord is challenging. The spinal cord is small compared to the brain, but high resolution is still required for precise localisation of GM and WM [129]. Instrumental and physiological artifacts may add undesired distortions to the images [175,191]. For instance, distortions due to differences in terms of magnetic susceptibility between the spinal cord and the surrounding tissues (such as the vertebrae) can deteriorate EPI-based acquisitions, leading to irreparable signal dropouts and pileups [36]. Also, physiological noise due to pulsation and respiration can introduce outliers that may require careful handling in model-based approaches [129].

### 3.10.1 Cardiac gating

Cardiac gating is a useful practice for qMRI of the spinal cord: it mitigates the consequences of CSF pulsation [205], such as ghosting artifacts and signal fluctuations [176]. It consists of synchronising the acquisition of MRI data with the cardiac cycle [180], at the price of reduced scan efficiency and variable repetition time.

Cardiac gating requires the acquisition of additional physiological signals that monitor the cardiac cycle, such as an *electrocardiogram* (ECG) [180], which records the electrical activity of the heart with electrodes placed on the body of the subject. In figure 3.18, an illustration of an ECG recording corresponding to two heart beats is shown. The signal corresponding to each beat is characterised by regular depolarisations and polarisations, called *waves*. The QRS complex consists of the concatenation of the Q, R and S waves, and represents ventricular depolarization [185]. In practice, the R peak is usually the most evident feature of an ECG, and is used to synchronise the MRI acquisition to the cardiac cycle. The MRI sequence repetition time $T_R$ is set to a multiple of the RR interval, and the acquisition is performed after a certain delay following the R peak [180]. This allows the exploitation of the period of relative quiescence of the cardiac cycle where flow effects are minimal [176].

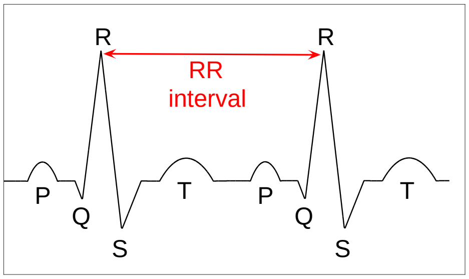

Figure 3.18: Illustration of the ECG signal corresponding to two heart beats. The figure shows the P, Q, R, S and T waves. In cardiac gated MRI, the repetition time $T_R$ is set to a multiple of the RR interval.

Cardiac gating can also be based on other physiological signals, different from the ECG. As an example, pulse oximetry [94] can also be used. This technique measures the changes in light absorption properties of blood over time, caused by the variation of oxygen saturation of haemoglobin.

The employment of pulse oximeters at peripheral level allows the acquisition of signals that reflect the heart cycle, and are also used for cardiac gating with benefits for qMRI methods such as DW MRI [176].

### 3.10.2 Reduced field-of-view acquisitions

In qMRI of the spinal cord, specialised readout approaches may be adopted, with the aim of reducing the amount of distortion and the duration of the readout itself. This leads to better image quality and higher SNR, while achieving a satisfactory resolution in the axial plane. Common approaches are rFOV methods, already mentioned in sections 3.6.1 and 3.6.3, which exploit the fact that a FOV smaller than the imaged volume size can be encoded if only part of the volume is in fact producing signal. This allows the violation Nyquist criterion (equation 3.31) without producing aliasing artifacts, while sampling a relatively small k-spaces leading to little distortion by virtue of a reduction of term $\text{FOV}_{\text{per-shot}}$ in equation 3.32.

Among the most popular rFOV methods, spin echo *zonal oblique multi-slice* (ZOOM) EPI [206] can be mentioned. The original ZOOM scheme is illustrated in figure 3.19.

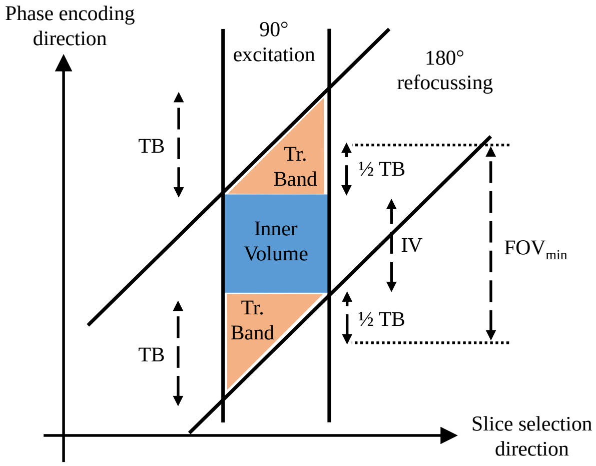

Figure 3.19: the ZOOM scheme, replicating qualitatively figure 1 of reference [206]. The inner volume (fully refocussed) is shown in light blue. The transition bands (partially refocussed) are shown in light orange.

In the original spin echo ZOOM EPI technique [206], the spatially selective 180°-RF pulse does not refocus a thin slice orthogonal to the slice selection direction, but a thin slab that is tilted in the plane of slice selection and phase encoding directions. This is achieved turning on both slice selection ($G_z$) and phase encoding ($G_y$) gradients when the refocussing pulse is played. As a result, only an *inner volume* of size IV along the phase encoding direction is fully refocussed, while two *transition bands* of size TB along the phase encoding direction are partially refocussed. The minimum FOV that needs to be encoded along the phase encoding direction to avoid aliasing within the IV region is $\text{FOV}_{\text{min}} = \text{IV} + \text{TB}$, in general much smaller than the size of the object along that direction. This leads to a mitigation of EPI distortions due to a reduction of the k-space matrix size, while also allowing shorter echo times. However, for the implementation of multi-slice imaging, a suitable gap between slices acquired one after the other needs to be set, since the 180°-RF pulse acting as a refocussing pulse for a certain slice inverts the magnetisation of adjacent slices.

rFOV methods are often preceded by preparation stages of *outer volume suppression* (OVS) [208], with the aim of saturating the magnetisation from outside the inner volume to further minimise the risk of signal aliasing. This is for instance the strategy employed in clinical Philips MRI systems, where in fact the excitation pulse is tilted, rather than the refocussing one.

### 3.10.3 Diffusion: DTI studies

The majority of DW MRI studies in the spinal cord still rely on conventional DTI, due to several technical challenges [174, 203]. DTI of the spinal cord has shown good reproducibility in normal subjects [166], and improved DTI methods at 3T have been recently proposed [213].

Several studies have also proven the sensitivity of DTI metrics to pathology effects in the spinal cord. For instance, a study in ALS recently showed that DTI FA is a good predictor of disease severity, and that changes in RD may reflect abnormalities in myelination [35]. DTI indices characterised diffuse cord pathology [3] and discriminated pathology levels in MS [140]. DTI-based tractography provided connectivity measurements that were reduced in patients with MS compared to controls at cervical level [32].

Furthermore, DTI has also shown good sensitivity in acute spinal cord compression [52] and cervical compression myelopathy [116] and in SCI patients [34], although in the latter case its indices were not specific to sensorimotors scores. Despite its good sensitivity towards changes in tissue microstructure, DTI indices are inherently non-specific [14], since they are influenced by several factors, only provide surrogate information and are hence prone to misinterpretations [203, 204].

### 3.10.4 Diffusion: non-DTI studies

Advanced DW MRI techniques may help to provide more specific markers than DTI for spinal cord applications. QSI was applied to the MS spinal cord *in vivo* [54], demonstrating that MS pathology does alter the diffusion profile of water molecules. DTI and QBI were successfully performed on SCI patients [34]. Both DTI FA and QBI-derived generalised FA (GFA) detected differences between the normal-appearing WM of patients and controls' WM, but the latter showed higher correlations with disability scores. More recently, very long diffusion times were probed in the healthy spinal cord *in vivo* with STEAM [151]; axon diameter was estimated in the cervical cord of healthy volunteers [48] with a modified AxCaliber [7] method and cutting edge 300 mT $m^{-1}$ gradients; *track-density imaging* (TDI) [27] was related to magnetic resonance spectroscopy in cervical spondylotic myelopathy [51].

## 3.11 Validation of quantitative MRI

qMRI has the potential of providing novel and highly specific biomarkers. However, it is essential that these innovative methods undergo systematic validation in phantoms and, ideally, comparison to histology. This can help to confirm the specificity of the indices and to exclude the influence of other confounding factors, especially in the presence of pathology. To date, a huge effort in this direction was made by the research community, and this section of the thesis aims to report notable results for the reader.

### 3.11.1 Phantom studies

Validation may include the development of controlled imaging phantoms. These are of particular interest for DW MRI methods aiming to quantify geometric features such as size or diameter of pores, and a few examples are listed below. A phantom of highly ordered glass has been built to validate a mPFG-based pore diameter estimation method [100], with promising results. Co-axial electrospinning has been successfully employed to build a phantom mimicking WM [75], whereas co-axial electrospraying to build a phantom made of a collection of polymer spheres mimicking cancer tissue [122]. A phantom of yeast cells, ordered and disordered crystal was instead employed to validate the estimation of microscopic FA, quantifying the anisotropy of the single pore after factoring out dispersion of pore orientations [103].

### 3.11.2 Histological validation

In literature, qMRI techniques such as DW MRI have often been compared to indices from conventional 2D histology, as in the cases listed below. Manual delineation of neuronal processes in the rat brain identified the histological correlates of DTI principal direction and FA [110]. The rat brain was also employed as a model for the comparison and validation of four different model-based PGSE approaches in [85], with good agreement between neurite density and dendrite complexity indices and optical intensity of myelin stained sections. DTI-derived information, such as local dominant direction, was also found to agree well with estimates derived from 2D Fourier domain analysis of owl monkey brain histology [30]. Extensive 2D structure tensor [16] analysis of the rat brain [22] and of the human cortex [159] showed good correspondence of local neurite orientation and DW MRI indices of dominant orientation. Recently, RSI was validated in the rat brain using myelin staining [207]. *In vivo* DW microimaging of the mice brain was shown to provide constrained SD [182] and TDI maps that qualitatively confirmed histology [211]. Also, a method for *in vivo* myelin g-ratio quantification was designed with applications in MS after validation in the macaque brain [173].

Novel 3D histology overcomes the main limitation of 2D methods, which neglect through-section fibre information. Confocal microscopy has been used to reconstruct the 3D morphology of ferret individual neurons [88] and to perform ST analysis of the Rhesus macaque hippocampus [98]. *Polarised light imaging* (PLI) [9] provides detailed 3D information of neural fibre architecture, but its application in demyelinating diseases remains challenging since it relies on optical properties of the myelin sheath. Recently, *serial optical coherence scanning* (SOCS) [192,193], which integrates optical coherence tomography and serial cutting with a vibratome, has shown unique information in the human medulla oblongata correlating with DTI indices.

Several studies have also investigated the histological correlates of qMRI in pathological tissue. For instance, MS effects have been extensively studied. DTI AD and RD have been proposed as surrogate markers of axonal loss and demyelination respectively, as suggested in animal models *in vivo* [24] and *ex vivo* [78,167], in unfixed human brain [155] and unfixed [131] and fixed [99] human spinal cord. Quantitative $T_1$ and $T_2$ estimation and *magnetisation transfer ratio* MRI were compared to histopathology in the MS spinal cord [20]. Recently, positive magnetic susceptibility in MS lesion was associated to iron deposition via histology [210].

DTI indices were compared to histology in several other models of diseases. For instance, stained sections demonstrating myelin, neurofilaments and immunoreactive material in *experimental autoimmune encephalomyelitis* (EAE) mice were compared to DTI in [25], while in [23] the investigation focussed on 2D Fourier domain analysis of sections imaged with confocal laser microscopy in a model of traumatic brain injury. To date, other DW MRI methods such as DKI [84] and DBSI [214] have also been proven useful to detect demyelination in a cuprizone mouse model [53] and to distinguish inflammation, demyelination and axonal injury in EAE mice [194] and MS [195].

Lastly, it is reported that DW MRI has been compared to histology also in cancer, as for example in xenografts of mice tumours [148] or in human brain meningiomas and glioblastomas [177]. These results show that DW MRI has a potential to characterise the microstructure of tumours in a clinically feasible and non-invasive manner.

# *In vivo* diffusion MRI of the human spinal cord

## Background and motivations

Previous background information has underlined the need of novel and more specific MRI biomarkers for spinal cord diseases such as MS. The new MRI indices should better characterise diffuse pathology and focal damage, as well as their association to clinical disability, leading ultimately to earlier diagnosis and more accurate prognosis.

This part of the thesis describes the investigation of a recent DW MRI method known as NODDI for *in vivo* spinal cord applications. NODDI enables the characterisation of key features of neuronal morphology in clinically feasible scans, and its employment in spinal cord conditions is appealing and potentially useful. The objectives of this first part of the dissertation are: i) to demonstrate the feasibility of NODDI and characterise its metrics in the spinal cord; ii) to study its reproducibility and relation with a routine diffusion method known as DTI; iii) to study the feasibility of its application to standard DW data; iv) to assess how axon diameter distributions typical of the spinal cord influence NODDI metrics.

## Experiments

Three experimental chapters report our work carried out *in vivo*. In chapter 4, NODDI is demonstrated in the healthy cervical spinal cord, its reproducibility is assessed and its metrics are characterised and compared to DTI indices. In chapter 5, the application of NODDI to routine single-shell DW MRI data of the spinal cord is discussed. Lastly, as a conclusion for the *in vivo* part, the influence of axon diameter distribution on NODDI metrics is studied in chapter 6.

## Conclusions

The chapters of this first *in vivo* part demonstrate that the recent NODDI technique is feasible in the spinal cord and in a clinical setting. NODDI can disentangle key factors contributing to the patterns of diffusion anisotropy as measured by DTI, namely the density and the orientation dispersion of neurites. Nevertheless, its reproducibility is slightly lower than that of DTI indices, and its application to standard DW MRI data appears challenging. Lastly, our experiments suggest that typical features of spinal cord microstructure (i.e. presence of large axons) can have an impact on NODDI metrics.

# Chapter 4

# Demonstration of NODDI in the healthy spinal cord

## 4.1 Introduction

This chapter shows the demonstration of NODDI in the healthy cervical spinal cord *in vivo*. NODDI has already shown promise in brain applications [17, 101, 156, 200, 209], and it may prove useful also in the spinal cord. NODDI provides indices of neurite morphology, namely neurite density and orientation dispersion, in a clinically feasible acquisition. The former index may be employed to characterise axonal loss and other pathological mechanisms underlying pathology in MS. The latter metric may instead be of interest at the level of nerve roots or to assess the integrity of neuronal processes or the complexity of dendritic trees. Also, it is known that neurite orientation dispersion is a non-negligible feature at the MRI voxel scale even in coherent brain WM areas such as the corpus callosum [21, 58]. Therefore, we hypothesise that it may be an important feature also in the tightly packed WM of the spinal cord.

For this study, five healthy volunteers were scanned in London with the 3T Philips Achieva MRI system in Queen Square House, Queen Square MS Centre, UCL Institute of Neurology. The main objectives were i) to demonstrate the feasibility of NODDI in the spinal cord and to obtain trends of its metrics; ii) to study its reproducibility and relation to routine DTI. Specifically, the following points were investigated in detail:

1. characterisation of NODDI metrics, in terms of GM and WM differences and contrast;
2. quantification of their reproducibility;
3. quantification of their relationship with DTI indices;
4. comparison of the quality of fit of NODDI and DTI models;
5. assessment of the impact of collateral WM fibres on NODDI indices.

## 4.2 Research dissemination

Some of the results described in this chapter have been presented in abstract form at international meetings as:

- "*In vivo* estimation of neuronal orientation dispersion and density of the human spinal cord". Grussu F. et al, ISMRM workshop "Multiple sclerosis as a whole-brain disease" (2013), oral presentation.
- "Neurite orientation dispersion and density imaging of the cervical cord *in vivo*". Grussu F. et al, ISMRM annual meeting (2014), p.1720, traditional poster.

Some of the findings were also published in a peer-reviewed journal as "Neurite orientation dispersion and density imaging of the healthy cervical spinal cord *in vivo*", Grussu F. et al, NeuroImage (2015), vol. 111, p.590-601 (reference [67]).

## 4.3 Theory: the NODDI model

NODDI considers water protons in each MRI voxel as belonging to three pools: i) isotropic water; ii) intra-neurite water; iii) extra-neurite water. The isotropic compartment is designed to capture CSF contamination; the intra-neurite compartment models axons and dendrites, excluding myelin; the extra-neurite compartment describes the extra-cellular environment, glial cells and neuronal cell bodies. The DW signal for a PGSE experiment is written as

$$s(\mathbf{g},b) \;=\; s_0\left(v_{\text{iso}}\, s_{\text{iso}}(b) \;+\; \big(1-v_{\text{iso}}\big)\Big(v_{\text{in}}\, s_{\text{in}}(\mathbf{g},b) \;+\; \big(1-v_{\text{in}}\big)\, s_{\text{en}}(\mathbf{g},b)\Big)\right). \tag{4.1}$$

Above, $s_0$ is the non-DW signal; $v_{\text{iso}}$ is the voxel volume fraction of the the isotropic compartment; $v_{\text{in}}$ is the intra-neurite tissue volume fraction; $s_{\text{iso}}$, $s_{\text{in}}$ and $s_{\text{en}}$ are the characteristic signal decays for the isotropic, intra and extra-neurite compartments respectively. The signal decays depend on the gradient direction **g** and on the $b$-value, as explained below.

$s_{\text{iso}}$ models signal decay due to isotropic diffusion characterised by a diffusivity $d_{\text{iso}}$:

$$s_{\text{iso}}(b) \;=\; e^{-b\, d_{\text{iso}}}. \tag{4.2}$$

$s_{\text{in}}$ describes the signal attenuation due to restricted diffusion within Watson-distributed zero-radius cylinders, or *sticks*, characterised by intrinsic diffusivity $d_{\|}$:

$$s_{\text{in}}(\mathbf{g},b) \;=\; \oint\limits_{\|\mathbf{n}\|=1} f(\mathbf{n};\kappa,\boldsymbol{\mu})\; e^{-b\, d_{\|}\, (\mathbf{g}^{\mathsf{T}}\mathbf{n})^2}\; d^2\mathbf{n}. \tag{4.3}$$

In equation 4.3, $f(\mathbf{n};\kappa,\boldsymbol{\mu})$ is the neurite orientation distribution, modelled as a Watson distribution with concentration $\kappa \in (0;\infty)$ and mean orientation $\boldsymbol{\mu}$. In [215], the orientation dispersion index (ODI) was proposed as a more intuitive representation of $\kappa$. ODI is monotonically related to $\kappa$ as

ODI $= \frac{2}{\pi}$ arctan$\left(\frac{1}{\kappa}\right)$, and it ranges from 0 (neurites all aligned in a voxel) to 1 (neurites isotropically, randomly oriented).

Lastly, $s_{\text{en}}$ describes the attenuation due to anisotropic hindered diffusion in the extraneurite space:

$$s_{\text{en}}(\mathbf{g}, b) \;=\; \exp\Bigg( -b\,\mathbf{g}^{\mathsf{T}} \Big( \oint_{\|\mathbf{n}\|=1} f(\mathbf{n}; \kappa, \boldsymbol{\mu})\; \mathbf{D}(\mathbf{n}; v_{\text{in}}, d_{\|})\; d^2\mathbf{n} \Big) \mathbf{g} \Bigg), \tag{4.4}$$

where

$$\mathbf{D}(\mathbf{n}; v_{\text{in}}, d_{\|}) \;=\; v_{\text{in}}\, d_{\|}\, \mathbf{n}\,\mathbf{n}^{\mathsf{T}} \;+\; (1 - v_{\text{in}})\, d_{\|}\, \mathbf{I} \tag{4.5}$$

is a cylindrically symmetric diffusion tensor with diffusivity $d_{\|}$ parallel to the generic direction $\mathbf{n}$ and diffusivity perpendicular to $\mathbf{n}$ constrained by a tortuosity model to $(1 - v_{\text{in}})\, d_{\|}$.

Multiple $b$-value DW data are required to fit the model parameters. The $b$-values and the total number of measurements were optimised to be performed in a clinically feasible time [215], and consist of two *high angular resolution diffusion imaging* (HARDI) [187] DW shells with $b$-values of $b = 711\,\text{s}\,\text{mm}^{-2}$ (30 directions) and $b = 2855\,\text{s}\,\text{mm}^{-2}$ (60 directions).

## 4.4 Methods

### 4.4.1 Data acquisition

Five healthy volunteers (2 males, median age of 34 years, range 25-47) provided informed written consent and were scanned on a 3T Philips Achieva scanner, in ethically approved experimental sessions. The MRI scans were performed on the system in Queen Square House, Queen Square, Institute of Neurology (NMR Unit, Department of Neuroinflammation). Four volunteers (subjects 1 to 4) were scanned twice, within eight months of the first scan. The protocol lasted about 25 minutes and followed the optimised multi-shell diffusion encoding prescribed in [215] (30 directions at $b = 711\,\text{s}\,\text{mm}^{-2}$ and 60 at $b = 2855\,\text{s}\,\text{mm}^{-2}$), plus 6 interleaved non-DW measurements. A rFOV PGSE ZOOM-EPI sequence [206] with OVS [208] and oxymeter-based peripheral cardiac gating was employed, as described in sections 3.10.1 and 3.10.2 of chapter 3.

Twelve axial slices were acquired with the following parameters: $\text{T}_\text{R} = 12$ RR repeats (as explained in figure 3.18), $\text{T}_\text{E} = 65.50$ ms (minimum $\text{T}_\text{E}$ achievable at $b = 2855\,\text{s}\,\text{mm}^{-2}$), rFOV of $64 \times 48\,\text{mm}^2$, SENSE factor of 1.5, resolution of $1 \times 1 \times 5\,\text{mm}^3$, triggering delay of 150 ms. We varied the gradient strength to achieve the two $b$-values, and employed $\Delta = 32.20$ ms and $\delta = 20.50$ ms for both shells, resulting in a diffusion time of $T_d = 25.37$ ms, constrained by the $\text{T}_\text{E}$ that was kept to minimum.

### 4.4.2 Motion correction

Motion was corrected realigning all acquired images to the first (non-DW) one, which was taken as registration reference. Currently, there are no well established motion correction pipelines for DW MRI of the spinal cord. However, it has been suggested that slice-wise linear registration is the most effective strategy to correct the motion [129]. Therefore, we adopted such a strategy, and used FSL *flirt* [64, 82, 83] to implement the linear registration.

Let $n = 1, ..., 6$ be the index of the $n$-th $b = 0$ volume and let $x$, $y$ and $z$ be the subjects' right-left, posterior-anterior and inferior-superior directions, so that $z = 1, ..., 12$ is the slice index. Motion correction was implemented as follows.

- Firstly, we estimated the transformations

  $$\mathbf{T}_n(z) = \begin{bmatrix} \mathbf{I} & \mathbf{p}_n(z) \\ \mathbf{0}^\mathsf{T} & 1 \end{bmatrix}$$

  with FSL *flirt* (correlation ratio search cost) for $n = 2, ..., 6$ and all $z$ values. $\mathbf{T}_n(z) \in \mathbb{R}^{4 \times 4}$ is a rigid transformation warping slice $z$ of the $n$-th $b = 0$ volume to the same slice of $b = 0$ volume $n = 1$. $\mathbf{T}_n(z)$ accounts for in-plane translations $\mathbf{p}_n(z) = [\delta x_n(z) \quad \delta y_n(z) \quad 0]^\mathsf{T}$.

- Secondly, transformations $\mathbf{T}_n(z)$ were applied to the corresponding slices of the non-DW volumes to correct the motion.

- Lastly, we also employed $\mathbf{T}_n(z)$ to warp slice $z$ of all DW volumes acquired between the $n$-th and $(n + 1)$-th $b = 0$ volumes.

Quality assessment of the motion correction stage was always performed by visual comparison of the motion-corrected and motion-uncorrected data.

### 4.4.3 Segmentation

For each subject and scan, the spinal cord was segmented on the mean $b = 0$ image, calculated after motion correction. A semi-automatic active surface method [74] available in Jim (`http://www.xinapse.com/home.php`) was employed to create a binary mask (*fitting cord mask*) of the spinal cord. The fitting cord mask was then eroded slice-by-slice to limit CSF contamination and cropped to the 6 central slices (*whole-cord mask*).

Afterwards, manual grey matter (GM) outlining was carried out on the average DW volume obtained according to the method described in [97], which is illustrated in figure 4.1. The method averages DW images obtained for gradient directions at an angle smaller than a threshold from the longitudinal spinal cord axis, since they show good contrast between GM and WM. The threshold was set to 45°, as some tests demonstrated that this value is a reasonable choice.

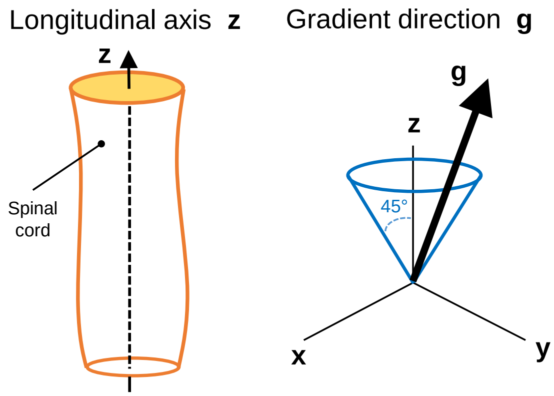

Figure 4.1: illustration of the algorithm used to create an image with good contrast between GM and WM from DW data of the spinal cord. We selected and averaged DW images obtained for gradient directions $\mathbf{g}$ at an angle smaller than 45° from the longitudinal cord axis, which in our reference frame is aligned with the slice selection direction $\mathbf{z}$.

After GM segmentation, a WM mask was also evaluated as the set of voxels within the whole-cord mask not contained in GM.

### 4.4.4 Model fitting

The NODDI and DTI models were fitted within the fitting cord mask for all scans and rescans. The NODDI Matlab (The MathWorks, Inc., Natick, Massachusetts, USA) Toolbox was employed for NODDI, whilst group-internal Matlab code for DTI. For NODDI, the two diffusivities $d_{\text{iso}}$ and $d_{\|}$ were fixed as in [215] to $d_{\text{iso}} = 3.00\ \mu\text{m}^2\,\text{ms}^{-1}$ and $d_{\|} = 1.70\ \mu\text{m}^2\,\text{ms}^{-1}$.

Both NODDI and DTI were fitted to the whole double-shell data set. DTI was also fitted to the $b = 711\,\text{s}\,\text{mm}^{-2}$ shell, since departures from non-Gaussian decay are smaller at low diffusion weighting [33, 54]. The following voxel-wise maps were obtained. For NODDI: isotropic voxel volume fraction $v_{\text{iso}}$; intra-neurite tissue volume fraction $v_{\text{in}}$; intra-neurite voxel volume fraction $v_{\text{r}} = (1 - v_{\text{iso}})\,v_{\text{in}}$; orientation dispersion index (ODI). For DTI, we calculated standard FA, AD, RD and MD, previously introduced in chapter 3.

The fitting was carried out maximising the likelihood of the measurements in each voxel for a Rician noise model [68], i.e. finding the DW signal model parameters $\mathbf{p}$ that maximise

$$\log L(\mathbf{p}) = -2M \log \nu + \sum_{m=1}^{M} \left( \log I_0\left(\frac{A_m S_m(\mathbf{p})}{\nu^2}\right) + \ldots \right.$$
$$\left. \ldots + \log A_m - \frac{A_m^2 + S_m(\mathbf{p})^2}{2\nu^2} \right). \quad (4.6)$$

Above, $A_m$ is the $m$-th measurement, $S_m$ is the NODDI/DTI prediction for the sequence settings corresponding to $A_m$, $\nu$ is the spread of the Rician distribution and $I_0$ is the modified Bessel function of first kind and 0-th order. In practice, equation 4.6 is maximised in two steps that follow the estimation of $\nu$ as the standard deviation of the non-DW measurements. A plausible set of model parameters is found performing an initial grid search. These parameters are then used as a starting point for a gradient descent, where $-\log L(\mathbf{p})$ is minimised.

The fitting settings of the NODDI Toolbox were tested. We found that the default options are not well suited for spinal cord MRI. By default, the Toolbox divides the estimate of the Rician noise level by 100, pulling the noise model to a Gaussian regime. While this has little impact on brain data where the SNR is on the order of 20, simulations proved that NODDI metrics are biased when obtained from fitting with such an option enabled on data with low SNR. This option was therefore disabled.

### 4.4.5 Analysis

**Characterisation of the metrics**

We visually inspected the fitted metrics and characterised GM/WM variation calculating the medians of each metric within each *region-of-interest* (ROI) (GM, WM and whole-cord), focusing on metrics obtained from the $b = 711\,\mathrm{s\,mm^{-2}}$ shell for DTI. We also calculated the *contrast* C and the *contrast-to-noise ratio* (CNR) between GM and WM for all metrics from NODDI and DTI. C and CNR were calculated similarly to [65]:

$$\mathrm{C} = \frac{|m_{\mathrm{GM}} - m_{\mathrm{WM}}|}{\frac{1}{2}(m_{\mathrm{GM}} + m_{\mathrm{WM}})} \tag{4.7}$$

and

$$\mathrm{CNR} = \frac{|m_{\mathrm{GM}} - m_{\mathrm{WM}}|}{\sqrt{s_{\mathrm{GM}}^2 + s_{\mathrm{WM}}^2}}, \tag{4.8}$$

where $m_{\mathrm{GM}}$, $m_{\mathrm{WM}}$ are the sample means of the metric in GM and WM and where $s_{\mathrm{GM}}$ and $s_{\mathrm{WM}}$ are the sample standard deviations of the metric in GM and WM.

**Reproducibility**

The reproducibility of NODDI metrics was investigated in Matlab for the GM, WM and whole-cord ROIs separately, with the aim of quantifying: i) the total variability associated to each metric; ii) the within-subject and between-subject fractions of the total variability. The two fractions are representative of the variation due to measurement errors (within-subject) and biological variation (between-subject) [11].

For this purpose, we calculated for each metric and ROI a percentage coefficient of variation (CoV) and the intraclass correlation coefficient (ICC). CoV, expressed in percentage points, measures the total variability of a metric with respect to the average value of the same metric across subjects and scans. Conversely, ICC was defined as the ratio between the variance associated to biological variation and the total variance. If ICC $>$ 0.5, the total variability is driven by biological differences in the cohort, whereas an ICC $<$ 0.5 suggests that the total variability is driven by measurements errors.

Let $m_{i,j}$ be the median of a metric within a fixed ROI for subject $i = 1, ..., 4$ and scan $j = 1, 2$. We estimated the within-subject ($\sigma^2_{\mathsf{W}}$) and between-subject ($\sigma^2_{\mathsf{B}}$) variances as $\sigma^2_{\mathsf{W}} = \frac{1}{4}\sum_{i=1}^{4}\left(\sum_{j=1}^{2}\left(m_{i,j} - \bar{m}_i\right)^2\right)$ and as $\sigma^2_{\mathsf{B}} = \frac{1}{3}\sum_{i=1}^{4}\left(\bar{m}_i - \bar{m}\right)^2$, with $\bar{m}_i$ and $\bar{m}$ being $\bar{m}_i = \frac{1}{2}\sum_{j=1}^{2} m_{i,j}$ and $\bar{m} = \frac{1}{4}\sum_{i=1}^{4}\bar{m}_i$.

The total variance of the metric within the ROI was quantified as $\sigma^2_{\mathsf{TOT}} = \sigma^2_{\mathsf{B}} + \sigma^2_{\mathsf{W}}$, while the percentage CoV and the ICC were ultimately calculated as

$$\mathsf{CoV} = 100\,\frac{\sqrt{\sigma^2_{\mathsf{TOT}}}}{\bar{m}} \tag{4.9}$$

and

$$\mathsf{ICC} = \frac{\sigma^2_{\mathsf{B}}}{\sigma^2_{\mathsf{TOT}}}. \tag{4.10}$$

For comparison, CoV and ICC were also calculated for DTI metrics obtained from the $b = 711\,\mathrm{s\,mm^{-2}}$ shell.

### Relationship NODDI-DTI

We investigated the experimental relationship between DTI metrics and NODDI $v_{\mathsf{in}}$ and ODI scattering values of $v_{\mathsf{in}}$ and ODI and colour-coding the points according to FA, AD, RD and MD. We employed DTI metrics obtained from the $b = 711\,\mathrm{s\,mm^{-2}}$ shell and only studied voxels with low isotropic volume fraction ($v_{\mathsf{iso}} < 0.05$). In order to support the relationships observed *in vivo*, we also evaluated via computer simulations the theoretical patterns of DTI indices as functions of $v_{\mathsf{in}}$ and ODI for a NODDI-like substrate at $b = 711\,\mathrm{s\,mm^{-2}}$.

The simulations were run as follows. The noise-free DW signal was synthesised according to equation 4.1 with the NODDI Matlab Toolbox. We varied parameters $v_{\mathsf{in}}$ and ODI in a grid of $64 \times 64$ uniform values in $[\,0.05;\ 0.95\,] \times [\,0.005;\ 0.5\,]$, while fixing $s_0 = 1$, $v_{\mathsf{iso}} = 0$, $d_{\|} = 1.70\,\mu\mathrm{m}^2\,\mathrm{ms}^{-1}$ and $\boldsymbol{\mu} = [\,0 \quad 0 \quad 1\,]^{\mathsf{T}}$. The signal was synthesised for the gradient directions of the $b = 711\,\mathrm{s\,mm^{-2}}$ shell with $b = 711\,\mathrm{s\,mm^{-2}}$. Subsequently, Rician noise was added to the synthesised signals (SNR of 10, comparable to the SNR of our data and of other *in vivo* studies [189]). Lastly, the DTI model was fitted to the noise-free and noisy synthetic data for all combinations of $v_{\mathsf{in}}$ and ODI. DTI indices FA, AD, RD and MD were then obtained and ultimately displayed as functions of $v_{\mathsf{in}}$ and ODI.

### Quality of fit

We investigated the quality of fit of NODDI and DTI models on the first scan of each of the five subjects, employing the whole double-shell set of measurements. The Bayesian Information Criterion (BIC) [158] was employed for this purpose, as in [147]. BIC is a useful statistics to compare models of different complexity, since lower BIC values imply better fit, while accounting for the number of free model parameters.

Voxel-wise BIC maps were calculated for both NODDI and DTI as

$$\text{BIC} \;=\; -2\log(L) \;+\; P\log(M) \tag{4.11}$$

with $L$ being the likelihood of the fitted model parameters (either NODDI or DTI), $P$ the number of model parameters and $M$ the total number of measurements (here $M = 96$). We calculated in all voxels within the fitting mask the percentage relative difference between BIC values of NODDI and DTI, with respect to those of DTI, as

$$\delta\text{BIC} \;=\; 100\,\frac{\text{BIC}_{\text{NODDI}} - \text{BIC}_{\text{DTI}}}{|\text{BIC}_{\text{DTI}}|}. \tag{4.12}$$

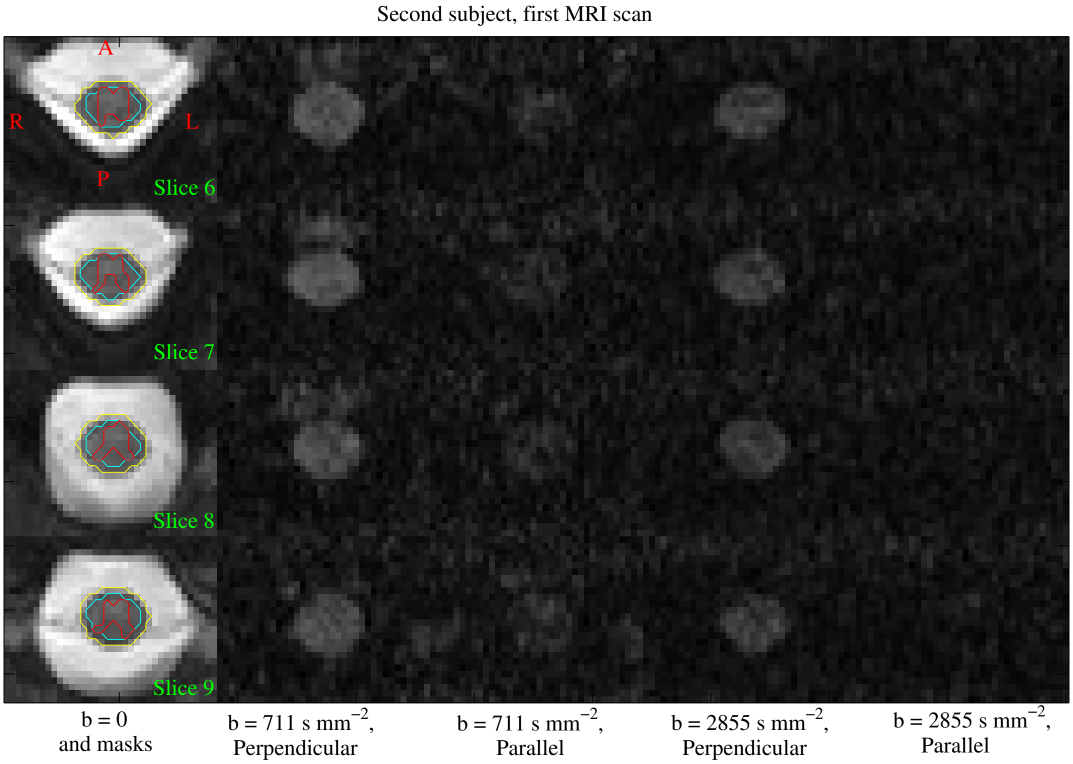
Second subject, first MRI scan
A
R
L
P
Slice 6
Slice 7
Slice 8
Slice 9
b = 0
and masks
b = 711 s mm$^{-2}$,
Perpendicular
b = 711 s mm$^{-2}$,
Parallel
b = 2855 s mm$^{-2}$,
Perpendicular
b = 2855 s mm$^{-2}$,
Parallel

Figure 4.2: example of DW and non-DW images from one of the subjects (first scan of subject 2). First column: mean $b = 0$ image and outline of ROIs (yellow for the fitting mask, light blue for the whole-cord mask and red for GM). WM is considered as the portion within the light blue mask not contained in GM. Second column: DW images at $b = 711\,\text{s}\,\text{mm}^{-2}$ for a gradient almost perpendicular to the longitudinal cord axis. Third column: DW images at $b = 711\,\text{s}\,\text{mm}^{-2}$ for a gradient almost parallel to the cord axis. Fourth and fifth columns: similar information as the second and the third columns is shown, but for $b = 2855\,\text{s}\,\text{mm}^{-2}$. Slice position varies along rows. Obtained from adaptation of the source files of figure 1 of reference [67], distributed under a Creative Commons Attribution 4.0 International license (`http://creativecommons.org/licenses/by/4.0/`) at `http://www.sciencedirect.com/science/article/pii/S1053811915000701` (ScienceDirect NeuroImage).

**Effect of crossing fibres**

WM fibres in the spinal cord are mainly directed along the superior-inferior direction. However, several collateral axons orthogonal to this dominant direction project into GM [113]. The areas where these axons branch are therefore characterised by crossing fibres. NODDI does not account directly for multiple fibre populations, and in this piece of analysis we investigated the effect of crossing fibres on its metrics. We proceeded in two steps: i) firstly, WM voxels likely to contain crossing fibres were detected; ii) secondly, a permutation test was performed to compare WM areas likely and unlikely to contain crossing fibres.

*Detection of crossing fibres*: voxels likely to contain collateral fibres were selected from the WM mask thresholding the mode of the diffusion tensor obtained from the $b = 711\ \mathrm{s\,mm^{-2}}$ shell, as proposed in [113]. The method hypothesises that voxels with significant crossing fibres have a planar diffusion tensor, and proposes to threshold the tensor mode as a way to distinguish between true and noise-induced planarity. In [113], the optimal threshold is provided as a function of the SNR via simulations. We estimated that in the WM of our subjects the SNR was roughly 13, implying a threshold of 0.88. Lastly, the number of false positives was reduced by eliminating voxels that intersect the dilated GM mask.

*Permutation test*: for each subject $i = 1, ..., 5$ the medians of all NODDI metrics were calculated for WM voxels likely and unlikely to contain crossing fibres (indicated as $m_i^{\text{xing}}$ and $m_i^{\text{non-xing}}$), and their difference ($d_i = m_i^{\text{xing}} - m_i^{\text{non-xing}}$) was calculated. The calculation was repeated 1000 times permuting over the labels of groups “*xing*” and “*non-xing*” in order to obtain a distribution of differences $d_i$ and of the mean difference $\bar{d} = \frac{1}{5}\sum_{i=1}^{5} d_i$. A two-tailed test with significance level of $p = 0.05$ was performed comparing the measured differences $d_i$ and $\bar{d}$ with their distributions over the permutations (significance guaranteed by a measured difference either bigger than the 97.5 percentile or smaller than the 2.5 percentile of the distribution).

## 4.5 Results

### 4.5.1 Data acquisition and tissue segmentation

Figure 4.2 shows DW and non-DW images and ROIs from the first scan of the second subject. The figure shows that stronger signal decay occurs for gradients along the cord axis, and that at $b = 2855\ \mathrm{s\,mm^{-2}}$ the signal is almost completely attenuated for encoding along that direction.

Figure 4.3 shows an example of the images that were used for tissue segmentation. The figure demonstrates that in the mean $b = 0$ image GM and WM can not be told apart. However, contrast between the two tissue types is visible in the average DW image obtained as described in section 4.4.3. In that image, the MRI signal in GM is more intense than in WM, due to the less strong signal decay. This fact enables the possibility of outlining manually GM. Lastly, the figure demonstrates that the erosion of the fitting cord mask reduces the possibility of inclusion of voxels contaminated by CSF.

### 4.5.2 Model fitting

Figure 4.4 shows an example of the measured DW signal and of NODDI fitting from one GM and one WM voxel of the second subject. The signal is plotted as a function of $|\mathbf{g}^{\mathsf{T}}\mathbf{n}|$, i.e. the absolute value of the dot product between the gradient and the fitted dominant neurite direction ($\mathbf{g}$ and $\mathbf{n}$). The metric $|\mathbf{g}^{\mathsf{T}}\mathbf{n}|$ is 0 for gradients orthogonal to $\mathbf{n}$ and 1 for gradients parallel to $\mathbf{n}$. The figure demonstrates that the DW signal in WM has a stronger dependence on the gradient orientation than in GM, and that in WM the signal reaches the level of noise floor at the highest $b$-value and for values of $|\mathbf{g}^{\mathsf{T}}\mathbf{n}|$ close to 1.

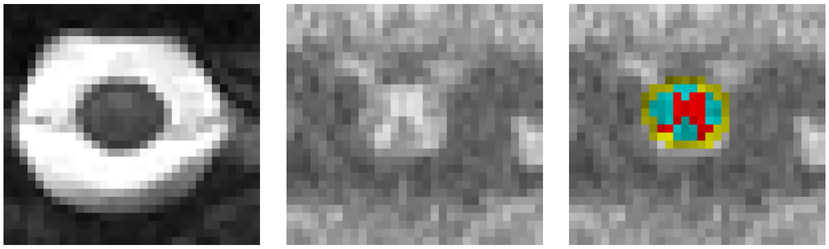

(a) mean $b = 0$ image (b) average DW image (c) segmentation from (b)

Figure 4.3: examples of images employed for segmentation, obtained from the first scan of subject 2. a): mean $b = 0$ image. b): average DW image obtained according to reference [97] and used for manual delineation of GM. c): image shown in b), onto which the GM and WM masks are overlaid. GM is in shades of red, while WM in shades of cyan. The part of the fitting mask that was removed by slice-wise erosion when calculating the whole-cord mask is also illustrated, in shades of yellow.

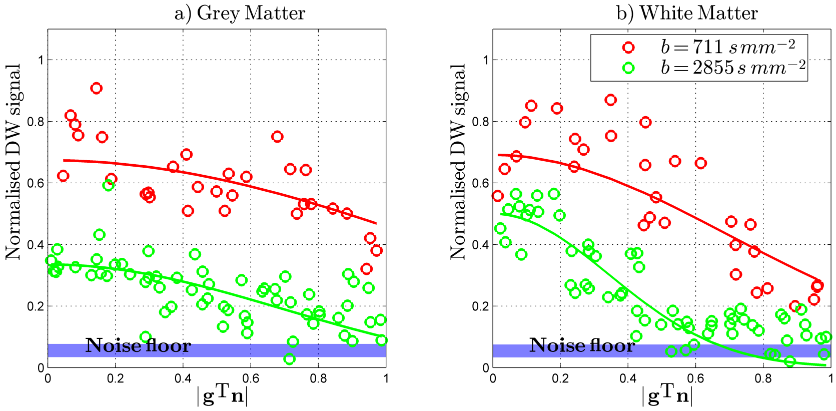

Figure 4.4: examples of DW signals and corresponding NODDI fittings from one GM (left) and one WM (right) voxel (second subject). For both tissues, signals are normalised by the mean non-DW intensity and plotted as a function of the absolute value of the dot product between the gradient direction and the fitted neurite direction. In both plots, circles represent measurements whereas a solid line shows the fit. Red is used for the $b = 711\,\mathrm{s\,mm^{-2}}$ shell, whereas green for the $b = 2855\,\mathrm{s\,mm^{-2}}$ shell. An estimate of the noise floor is provided in shadowed light blue. The amplitude of the shadowed area is the inter-quartile range of a Rayleigh distribution whose spread parameter equals the standard deviation of the $b = 0$ measurements.

### 4.5.3 Characterisation of the metrics

Figure 4.5 illustrates NODDI metrics and DTI FA in the two scans of the second and third subjects.

It can be noted that $v_{\mathrm{iso}}$ is close to 1 on the boundaries of the fitting mask, where CSF partial volume is likely. In those voxels, $v_{\mathrm{in}}$ is also high but the total voxel volume fraction $v_{\mathrm{r}}$ is low. ODI is characterised by a good contrast between GM and WM areas, comparable to that of FA. On the other hand, $v_{\mathrm{in}}$ and especially $v_{\mathrm{r}}$ show a lower contrast between the two tissue types, and a non-negligible contribution of the isotropic compartment in WM ($v_{\mathrm{iso}}$ close to 0.1) is seen.

In figure 4.6, the medians of the metrics within the GM, WM and whole-cord ROIs are reported for the first scans, with colours encoding subjects. Table 4.1 summarises the median values of these five points.

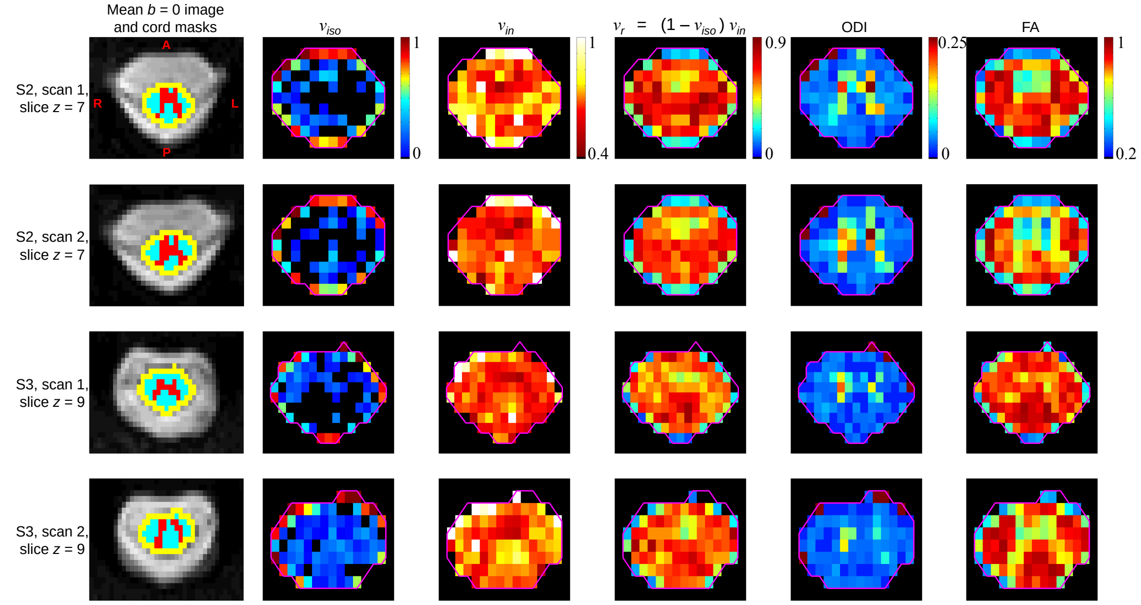
Mean $b$ = 0 image and cord masks
$v_{iso}$
$v_{in}$
$v_r$ = $(1 - v_{iso})\, v_{in}$
ODI
FA
S2, scan 1, slice $z$ = 7
S2, scan 2, slice $z$ = 7
S3, scan 1, slice $z$ = 9
S3, scan 2, slice $z$ = 9
A
R
L
P
1
0
1
0.4
0.9
0
0.25
0
1
0.2

Figure 4.5: NODDI metrics and DTI FA in the spinal cord of two subjects, including both scan and rescan. First row: subject 2, first scan, seventh slice; second row: subject 2, second scan, seventh slice; third row: subject 3, first scan, ninth slice; fourth row: subject 3, second scan, ninth slice. From left to right: mean $b = 0$ and masks (fitting mask in yellow; whole-cord in light blue; GM in red); NODDI $v_{\mathrm{iso}}$, $v_{\mathrm{in}}$, $v_{\mathrm{r}}$ and ODI; DTI FA. Obtained from figure 2 of reference [67], distributed under a Creative Commons Attribution 4.0 International license (`http://creativecommons.org/licenses/by/4.0/`) at `http://www.sciencedirect.com/science/article/pii/S1053811915000701` (ScienceDirect NeuroImage).

The results displayed in figure 4.6 confirm that the contribution of the isotropic compartment in WM is higher than in GM (median across scans of 0.12 in WM and of 0.004 in GM). The median $v_{\mathrm{in}}$ is 0.57 in WM and 0.49 in GM, whereas the median $v_{\mathrm{in}}$ is 0.45 in GM and 0.49 in WM. ODI is approximately three times higher in GM than in WM (median of 0.027 in WM and of 0.086 in GM). Figure 4.6 also shows the same information for DTI-derived metrics. FA, AD and MD are lower in GM than in WM (median of 0.80 in WM and of 0.57 in GM for FA; of 2.16 $\mu\mathrm{m}^2\,\mathrm{ms}^{-1}$ in WM and

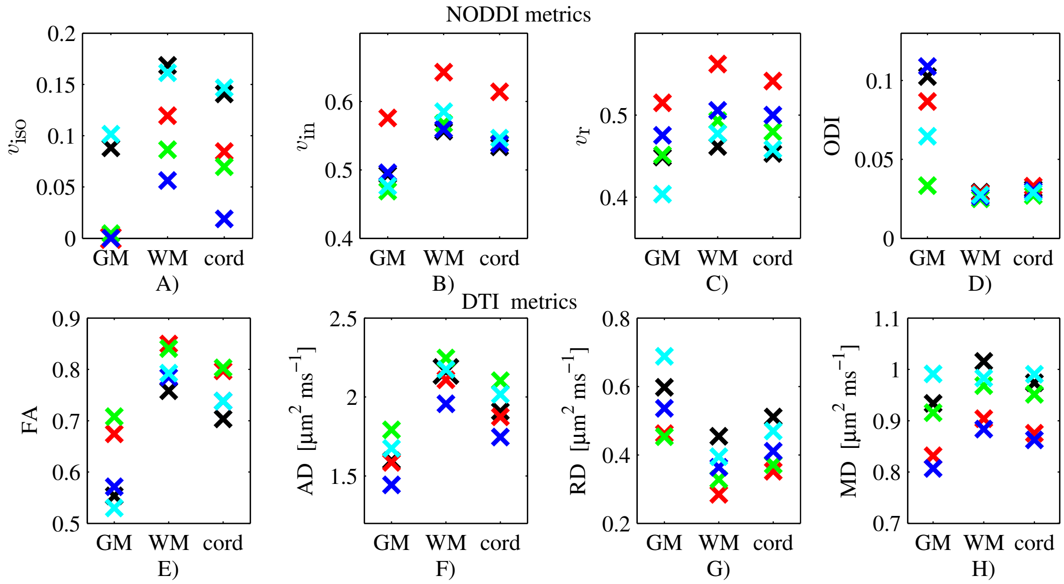

Figure 4.6: medians of NODDI and DTI metrics within the GM, WM and whole-cord ROIs (rescans omitted). Top row: NODDI $v_{\text{iso}}$ in A); $v_{\text{in}}$ in B); $v_{\text{r}}$ in C); ODI in D). Bottom row: DTI FA in E); AD in F); RD in G); MD in H). Black data points stand for the first subject; red for the second; green for the third; blue for the fourth; light blue for the fifth. Obtained from adaptation of the source files of figure 3 of reference [67], distributed under a Creative Commons Attribution 4.0 International license (`http://creativecommons.org/licenses/by/4.0/`) at `http://www.sciencedirect.com/science/article/pii/S1053811915000701` (ScienceDirect NeuroImage).

of 1.60 in GM for AD; of 0.97 $\mu\text{m}^2\,\text{ms}^{-1}$ in WM and of 0.92 $\mu\text{m}^2\,\text{ms}^{-1}$ in GM for MD), while RD is higher in GM than in WM (median of 0.36 $\mu\text{m}^2\,\text{ms}^{-1}$ in WM and of 0.54 $\mu\text{m}^2\,\text{ms}^{-1}$ in GM).

Figure 4.7 shows the distribution of metrics C and CNR between GM and WM obtained from the first scans of the five subjects. For NODDI, $v_{\text{iso}}$ and especially ODI show the highest values of contrast C. In particular, C of ODI is much higher than the values of C provided by DTI indices. Furthermore, $v_{\text{in}}$ and $v_{\text{r}}$ provide similar values of C as compared to DTI MD. Lastly, figure 4.7 shows that CNR values for NODDI are comparable to values of DTI. ODI shows the highest CNR for NODDI, which however is slightly lower than the CNR of DTI FA and AD. The CNR of DTI AD is the highest among all metrics.

|  | GM | WM | whole-cord |
|---|---|---|---|
| NODDI: |  |  |  |
| $v_{\text{iso}}$ | 0.004 (0.10) | 0.12 (0.11) | 0.08 (0.13) |
| $v_{\text{in}}$ | 0.49 (0.11) | 0.57 (0.09) | 0.54 (0.08) |
| $v_{\text{r}}$ | 0.45 (0.11) | 0.49 (0.10) | 0.50 (0.09) |
| ODI | 0.086 (0.08) | 0.027 (0.003) | 0.030 (0.006) |
|  |  |  |  |
| DTI: |  |  |  |
| FA | 0.57 (0.18) | 0.80 (0.09) | 0.74 (0.10) |
| AD $[\mu\text{m}^2\,\text{ms}^{-1}]$ | 1.60 (0.35) | 2.16 (0.29) | 1.91 (0.36) |
| RD $[\mu\text{m}^2\,\text{ms}^{-1}]$ | 0.54 (0.23) | 0.36 (0.17) | 0.41 (0.16) |
| MD $[\mu\text{m}^2\,\text{ms}^{-1}]$ | 0.92 (0.18) | 0.97 (0.13) | 0.95 (0.13) |

Table 4.1: Medians and ranges (difference between the maximum and the minimum value) of the five data points shown in figure 4.6 (rescans omitted).

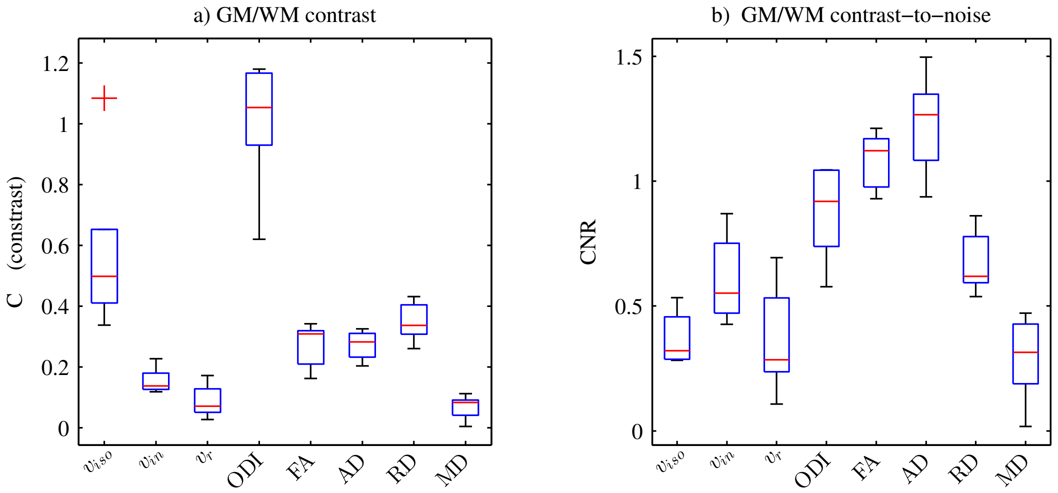

Figure 4.7: contrast (C, to the left) and contrast-to-noise ratio (CNR, to the right) between GM and WM for NODDI and DTI metrics. Values of C and CNR from the first scan of all subjects are summarised by a box plot. Obtained from adaptation of the source files of figure 4 of reference [67], distributed under a Creative Commons Attribution 4.0 International license (`http://creativecommons.org/licenses/by/4.0/`) at `http://www.sciencedirect.com/science/article/pii/S1053811915000701` (ScienceDirect NeuroImage)

### 4.5.4 Reproducibility

In tables 4.2 and 4.3, the reproducibility figures CoV and ICC are reported. The total variability, quantified by CoV, is the highest for $v_{\text{iso}}$ among all NODDI metrics (CoV up to 140% in GM). It is below 10% for $v_{\text{in}}$ and $v_{\text{r}}$ in all ROIs, and for ODI in GM and at whole-cord level. For DTI indices, CoV is above 10% for FA in GM and for RD in all ROIs.

We measure an ICC greater than 0.5 for $v_{\text{iso}}$ in GM and for $v_{\text{r}}$ and ODI in all ROIs. ICC is just

|  | GM | WM | whole-cord |
|---|---|---|---|
| NODDI: |  |  |  |
| $v_{\text{iso}}$ | 140 | 41 | 69 |
| $v_{\text{in}}$ | 9 | 6 | 6 |
| $v_{\text{r}}$ | 9 | 7 | 7 |
| ODI | 44 | 7 | 7 |
|  |  |  |  |
| DTI: |  |  |  |
| FA | 13 | 5 | 6 |
| AD | 9 | 7 | 8 |
| RD | 16 | 19 | 17 |
| MD | 8 | 7 | 7 |

Table 4.2: CoV in $\%$ points of NODDI and DTI indices within the three ROIs (rescans omitted).

|  | GM | WM | whole-cord |
|---|---|---|---|
| NODDI: |  |  |  |
| $v_{\text{iso}}$ | 0.63 | 0.33 | 0.41 |
| $v_{\text{in}}$ | 0.54 | 0.62 | 0.54 |
| $v_{\text{r}}$ | 0.70 | 0.84 | 0.91 |
| ODI | 0.86 | 0.66 | 0.70 |
|  |  |  |  |
| DTI: |  |  |  |
| FA | 0.95 | 0.75 | 0.75 |
| AD | 0.87 | 0.77 | 0.84 |
| RD | 0.88 | 0.76 | 0.82 |
| MD | 0.81 | 0.84 | 0.88 |

Table 4.3: ICC of NODDI and DTI indices within the three ROIs (rescans omitted).

above 0.5 for $v_{\text{in}}$ in the three ROIs. As far as DTI metrics FA, AD, RD and MD are concerned, we report that ICC is found to be well above 0.5 for all of them, with a peak of 0.95 for FA in GM.

### 4.5.5 Relationship NODDI-DTI

Figure 4.8 shows results from simulations and from *in vivo* data.

Simulations performed at SNR $\rightarrow \infty$ prove that for a NODDI-like substrate, different combinations of metrics $v_{\text{in}}$ and ODI, simulating different cytoarchitectural scenarios, can generate signals that provide the same values of DTI indices. The simulations also suggest that a decreased FA can be caused by a decreased ODI or by an increased $v_{\text{in}}$ independently. A similar independent dependence on $v_{\text{in}}$ and ODI is seen for AD, RD and less for MD, which is independent of ODI. AD decreases with increasing ODI, and shows little dependence on $v_{\text{in}}$ for physiologically-plausible values. RD increases for decreasing $v_{\text{in}}$ and increasing ODI. Lastly, MD shows a very weak dependence on ODI, and decreases for increasing $v_{\text{in}}$.

The trends observed in simulated signals at SNR $\rightarrow \infty$ are replicated at SNR $= 10$, although the patterns are noisier and contours less defined. Even at low SNR, different combinations of $v_{\text{in}}$ and ODI provide similar patterns of DTI indices.

Lastly, colour-coded scatter plots obtained from real data, shown to the right, in figure 4.8, agree well with the patterns of the synthetic data. In particular, FA decreases for increasing ODI and decreasing $v_{\text{in}}$. AD depends more on ODI rather than $v_{\text{in}}$, RD decreases for increasing $v_{\text{in}}$ and for decreasing ODI. MD increases as $v_{\text{in}}$ decreases, although the patterns of MD are not as clearly defined as in simulations. On average, AD, RD and MD are slightly higher when evaluated *in vivo*, than from synthetic data.

### 4.5.6 Quality of fit

Voxel-wise maps of $\delta$BIC are shown in figure 4.9 for the first scan of the five subjects (slices 4 to 9). Positive $\delta$BIC values imply $\text{BIC}_{\text{NODDI}} > \text{BIC}_{\text{DTI}}$, i.e. that DTI fits the data better than NODDI, whereas negative $\delta$BIC implies $\text{BIC}_{\text{NODDI}} < \text{BIC}_{\text{DTI}}$, i.e. that NODDI fits the data better than DTI. The illustration proves that NODDI fits the data better than DTI in the vast majority of voxels. A few scattered voxels where DTI performs better than NODDI are orange and yellow in a few slices of the second and the fifth subjects. Instead, $\delta$BIC as low as $-70\%$ can be observed at the edge of the spinal cord, as for subjects 1, 2 and 5. Similar findings hold for the remaining slices that are not displayed in the figure.

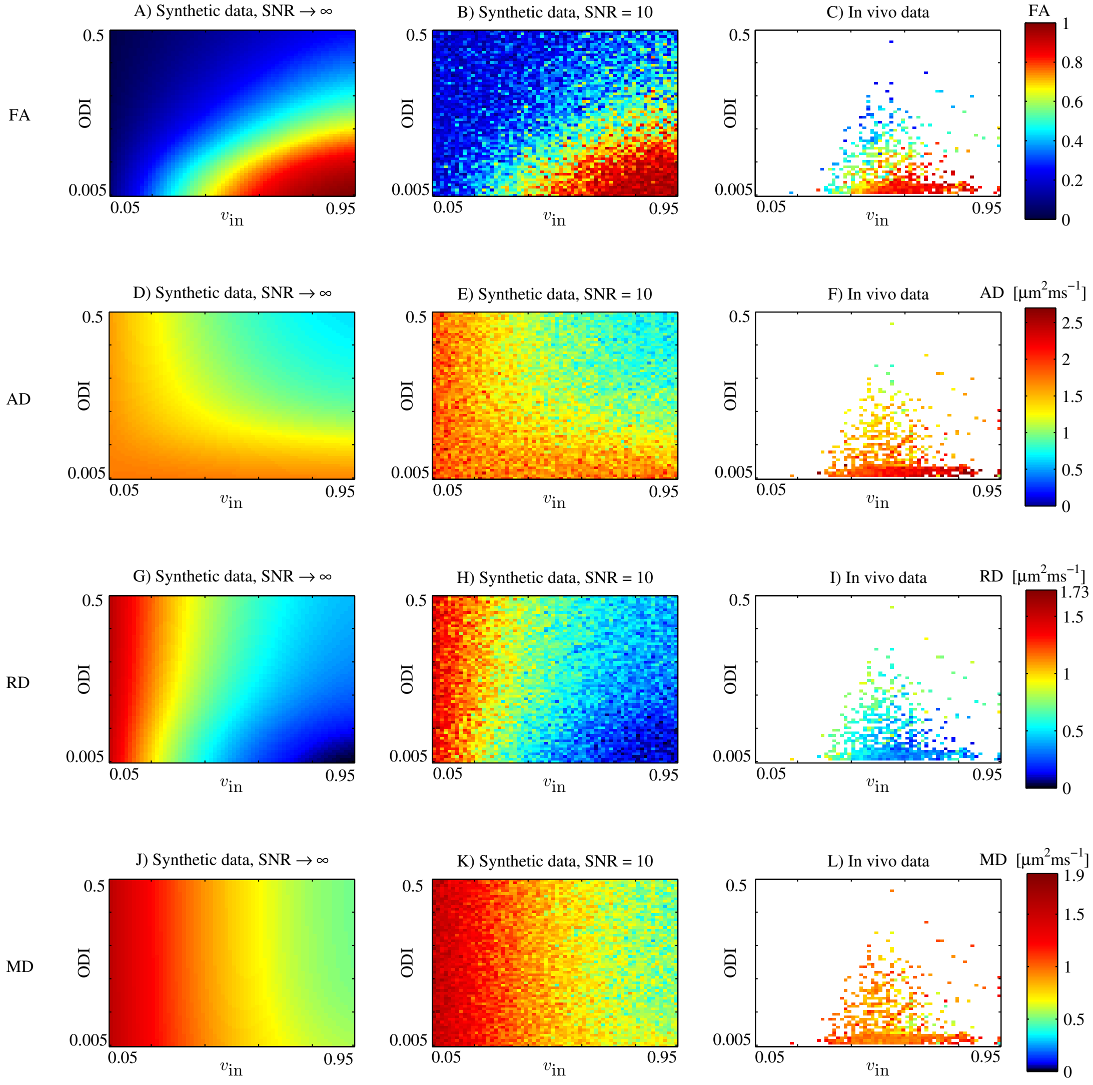

Figure 4.8: relationships between NODDI indices $v_{\text{in}}$ and ODI and DTI FA, AD, RD and MD from synthetic and *in vivo* data. Left column: relationships obtained from simulations performed with no noise. Central column: relationships obtained from simulations performed at SNR $=$ 10. Right column: scatter plots obtained from real *in vivo* data. From top to bottom: different rows respectively convey information about FA, AD, RD and MD. Obtained from adaptation of the source files of figure 5 of reference [67], distributed under a Creative Commons Attribution 4.0 International license (`http://creativecommons.org/licenses/by/4.0/`) at `http://www.sciencedirect.com/science/article/pii/S1053811915000701` (ScienceDirect NeuroImage).

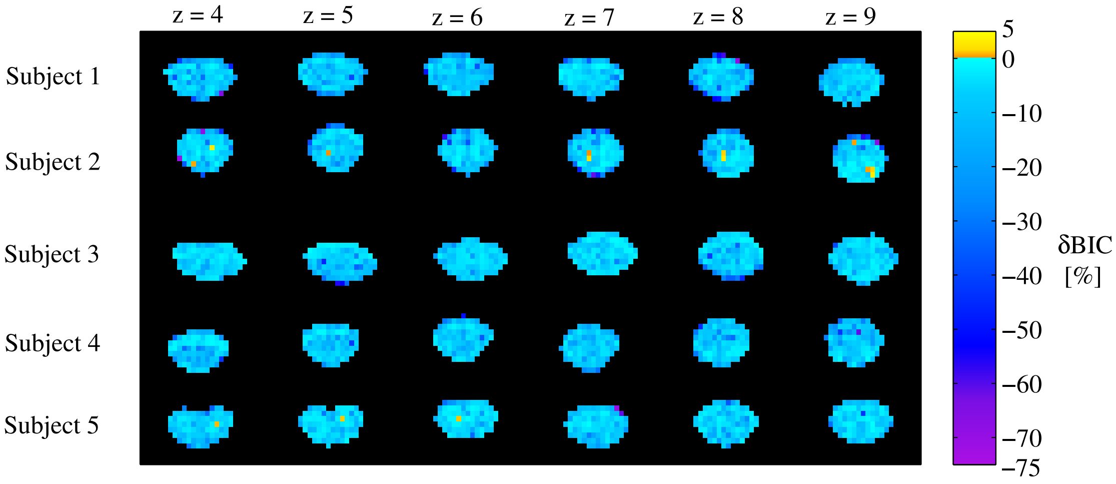

Figure 4.9: voxel-wise map of $\delta$BIC within the fitting cord mask. Negative values of $\delta$BIC suggest that NODDI fits the data better than DTI, and vice versa for positive $\delta$BIC. Different subjects are reported in different rows while different slices (from the fourth to the ninth) along different columns. Obtained from adaptation of the source files of figure 6 of reference [67], distributed under a Creative Commons Attribution 4.0 International license (`http://creativecommons.org/licenses/by/4.0/`) at `http://www.sciencedirect.com/science/article/pii/S1053811915000701` (ScienceDirect NeuroImage).

### 4.5.7 Effect of crossing fibres

Figure 4.10 shows in green some examples of WM voxels likely to contain crossing fibres. These voxels are mainly located in the lateral funiculi, close to nerve roots. However, voxels in other locations, such as the anterior and posterior funiculi, were also identified.

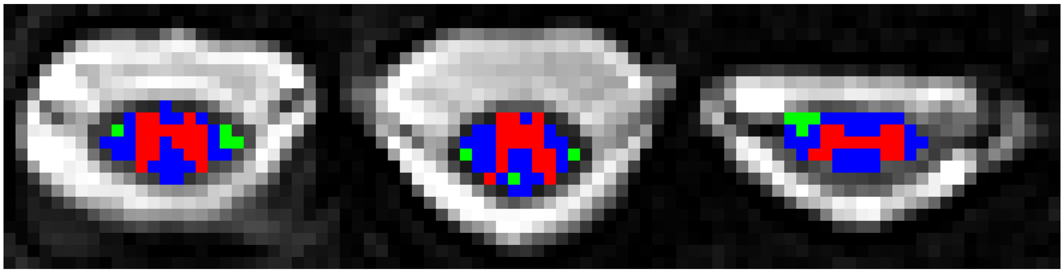

Figure 4.10: examples of WM voxels likely to contain crossing fibres. From left to right: slice $z = 8$ of first subject; slice $z = 7$ of second subject; slice $z = 4$ of third subject. Blue and green respectively represent WM voxels where the mode of the DT was higher and lower than the value of 0.88 adopted as a threshold. Hence, green voxels are likely to contain collateral fibres crossing with the dominant fibre direction. The GM mask has also been reported, coloured in red. Obtained from figure 1 of supplementary material of reference [67], distributed under a Creative Commons Attribution 4.0 International license (`http://creativecommons.org/licenses/by/4.0/`) at `http://www.sciencedirect.com/science/article/pii/S1053811915000701` (ScienceDirect NeuroImage).

Figure 4.11 illustrates the results of the permutation test comparing NODDI metrics in WM areas likely and unlikely to contain crossing fibres. The plots report the distribution of the difference $d_i = m_i^{\text{xing}} - m_i^{\text{non-xing}}$ provided by the permutation test for subjects $i = 1, ..., 5$, as well as the 2.5 and 97.5 percentiles (red lines) and the measured differences $d_i$ as dashed black lines. It can clearly be seen from the figure that only in one case a significant difference between the two portions of WM is observed. In subject 2, significantly higher ODI is measured in WM likely to contain crossing fibres as compared to WM where the presence of crossing fibres is unlikely ($d_i = 4.7098 \cdot 10^{-3}$, $p = 0.0362$).

At group level, the mean difference over the five subjects $\bar{d}$ is never significantly different from zero for all NODDI metrics.

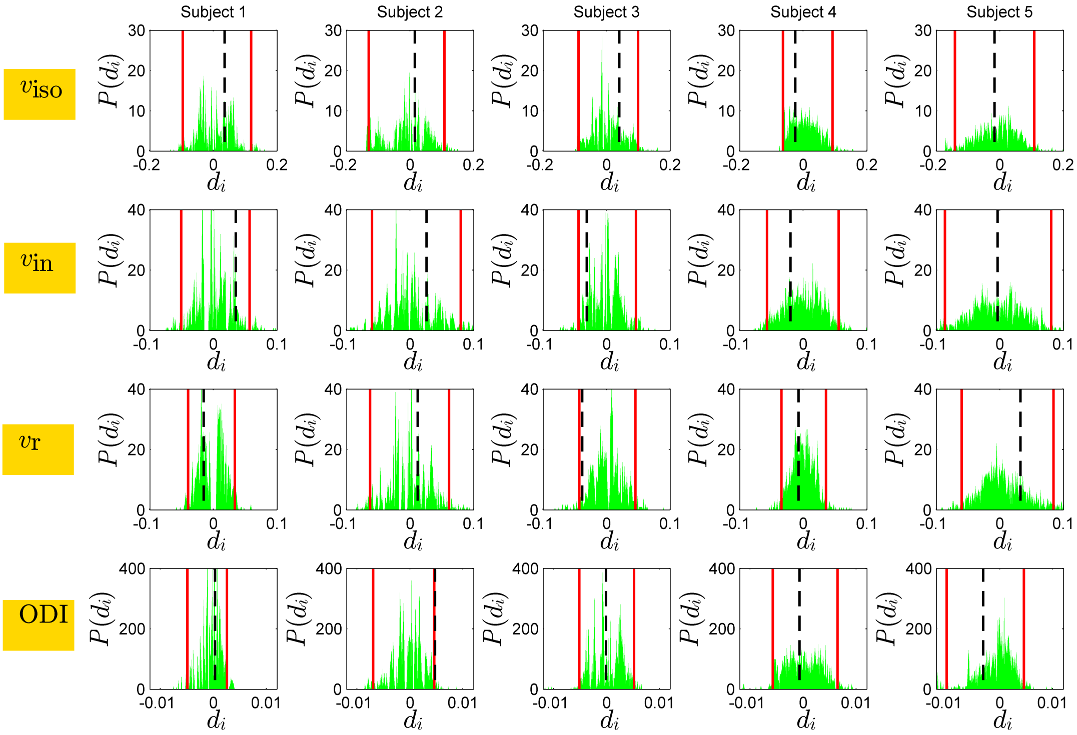

Figure 4.11: results of the permutation test assessing the impact of crossing fibres on NODDI metrics of spinal WM. Different columns show results from different subjects, where along rows different metrics are reported. From top to bottom: $v_{\text{iso}}$, $v_{\text{in}}$, $v_{\text{r}}$ and ODI. Each plot shows the distribution of the difference $d_i = m_i^{\text{xing}} - m_i^{\text{non-xing}}$ for a specific NODDI metric and a specific subject $i = 1, ..., 5$, with $m_i^{\text{xing}}$ and $m_i^{\text{non-xing}}$ being respectively the medians of the metric in voxels likely and unlikely to contain crossing fibres. Vertical red lines are placed in correspondence of the 2.5 and 97.5 percentiles of the permutation distribution, whereas a dashed, vertical black line shows the measured difference $d_i$.

## 4.6 Discussion

The work presented in this chapter demonstrates the feasibility of applying NODDI to the healthy spinal cord *in vivo*. Five healthy volunteers were scanned at 3T following a multi-shell diffusion encoding protocol to obtain for the first time NODDI metrics of the spinal cord. These metrics map specific features of neurite morphology and may be relevant biomarkers for spinal cord conditions. Trends of NODDI indices seen in the brain were replicated, although some differences were seen. For comparison, conventional DTI metrics were also evaluated, and they were found to agree with previous literature [189, 205, 213].

*Characterisation of the metrics*

Our analysis suggests that $v_{\text{iso}}$ captures CSF contamination, being close to 1 in the edge of the fitting cord mask, where CSF partial volume may occur. In those voxels, $v_{\text{in}}$ is also high. This is likely due to the inherent difficulty of determining properties of the restricted compartment when high CSF contamination occurs, which causes a poorly defined $v_{\text{in}}$. Our work reveals that $v_{\text{iso}}$ is not negligible within the spinal cord, especially in WM (median across the five subjects of 0.12, against 0.004 in GM). A number of reasons may explain this fact. Firstly, we speculate that CSF contamination in the anterior median fissure and the central canal may contribute to a high $v_{\text{iso}}$. Secondly, it may be that the isotropic compartment captures contributions from the water pool that can not be characterised directly by restricted diffusion. Although a high $v_{\text{iso}}$ may be a simple effect of noise, it was initially speculated that the isotropic compartment may capture contributions from the biggest axons, whose diameter in the spinal cord can be as high as 15 $\mu$m [56, 70, 117, 201]. In this study, a diffusion time of $T_d = 25.37$ ms was employed, corresponding to a mean square displacement of $L_d = \sqrt{2\, D_{\text{free}}\, T_d} = 10.5\,\mu$m, if one adopts the observed median AD in WM as an estimate of the free diffusivity ($D_{\text{free}}$). Therefore, diffusion within the biggest axons may not have reached the long diffusion time limit, and may appear as relatively free. Further investigation was carried out to study in detail this possibility. Results presented in chapter 6 suggest that although NODDI parameter estimation is influenced by the choice of the diffusion time when large axons are present, $v_{\text{iso}}$ values as high as roughly 0.10 are simply attributable to noise.

The ROI analysis proved that ODI reflects differences in terms of neurite morphology between GM and WM. This is in line with previous qualitative findings in the brain [215]. On the one hand, ODI shows the highest contrast C between GM and WM among all metrics. On the other hand, its CNR is just below 1 and is surpassed by FA and AD. This shows the potential of NODDI for characterising differences in terms of microstructure between spinal GM and WM, but also suggests that future optimisation may help reduce the variability of the metrics. This would potentially lead to higher CNR values for ODI and help improve the reproducibility, as discussed below. Furthermore, volume fractions $v_{\text{in}}$ and $v_{\text{r}}$ show a reduced contrast between GM and WM, if compared to ODI, similar to DTI MD. Although GM-WM partial volume effects due to the coarse in-plane resolution may have contributed, this may indicate that $v_{\text{in}}$ and $v_{\text{r}}$ are more homogeneous between GM and WM compared to the brain. For instance, it was originally speculated that the presence in GM of axons that originates from spinal nerve roots and WM funiculi, or the presence in WM (especially at cervical level) of the *formatio reticularis*, made of GM strands separated by interwoven fibres, may have contributed to a reduced heterogeneity in terms of neurite density between GM and WM. However, recent work carried out subsequently and described in chapter 6 points to incomplete restriction of diffusion within the biggest axons as another factor contributing to the relatively low $v_{\text{in}}$ and $v_{\text{r}}$ in WM. This could potentially cause the measured values of $v_{\text{in}}$ and $v_{\text{iso}}$ to be underestimated and hence similar to those of GM.

*Reproducibility*

The aim of the reproducibility analysis was the quantification of the total variability of NODDI metrics, and the estimation of the fractions of variability due to biological differences in the cohort and to measurement errors. The analysis shows that the total variability of NODDI $v_{\text{in}}$, $v_{\text{r}}$ and ODI is comparable to that of DTI FA, AD, RD and MD, whilst the variability of $v_{\text{iso}}$ is considerably greater, causing CoV to be as high as $140\%$ in GM. This last fact is not surprising, since $v_{\text{iso}}$ is found to be negligible on average within the GM mask (median across subjects of 0.004), and hence poorly defined. Also, our work highlights that the total variability is driven by biological differences in the cohort for $v_{\text{r}}$ and ODI, by measurement errors for $v_{\text{iso}}$, whilst the two sources contribute equally to the variability of $v_{\text{in}}$ (ICC close to 0.5 in all ROIs). On the other hand, DTI indices are less variable than NODDI ones, and biological variation drives the total variability. As compared to DTI, the worse reproducibility scores of NODDI may be due to the higher susceptibility of its non-linear model to thermal and physiological noise, imperfect $B_0$ field shimming and different alignment of the spinal cord with the main field between scans and rescans. Nevertheless, our analysis suggests that NODDI in the current form can be applied in spinal cord studies. However, the technique could be further optimised for spinal cord anatomy and potentially improved.

*Relationship NODDI-DTI*

We performed computer simulations to visualise the theoretical dependence of DTI metrics on NODDI $v_{\text{in}}$ and ODI, and compared these theoretical patterns to colour-coded scatter plots obtained from *in vivo* data. Both synthetic and *in vivo* data show an important fact: a similar value of all DTI metrics can be produced by combinations of $v_{\text{in}}$ and ODI sensibly different from each other, representing different cytoarchitectures. For instance, the dependence of FA on $v_{\text{in}}$ and ODI observed on the *in vivo* data resembles pattern previously reported in [215]. It reveals that a decrease of FA can be caused independently by an increase of ODI or by a decrease of $v_{\text{in}}$. The two effects have clearly different biological meaning, but they cannot be distinguished only looking at FA, a conventional marker of neuronal integrity. Therefore, NODDI appears to provide indices that disentangle two of the main microarchitectural sources contributing to DTI metrics: the density and the orientation complexity of neuronal processes.

*Quality of fit*

The last focus of our analysis was the study of the performance of NODDI and DTI in terms of goodness of fit. We derived the BIC for the two models on the full double-shell data set and calculated their percentage relative difference $\delta$BIC, positive when DTI fits better than NODDI, negative when the opposite holds. The inspection of voxel-wise $\delta$BIC maps clearly demonstrates that NODDI outperforms DTI in terms of quality of fit. Only a few scattered voxels are characterised by $\delta$BIC $>$ 0. Negative $\delta$BIC values, as low as $-70\%$, are seen in the boundary of the fitting mask. This demonstrates how multi-compartment models such as NODDI are more flexible than mono-compartment DTI and can fit the data better in presence of partial volume.

*Effect of crossing fibres*

A published method based on the thresholding of the diffusion tensor mode was employed to detect areas in WM likely to contain collateral fibres crossing with the main fibre population directed along the superior-inferior direction. Values of all NODDI metrics were then compared with a permutation tests between WM voxels likely and unlikely to contain such crossing fibres. The investigation suggests that the presence of crossing fibres may affect NODDI metrics. In most of cases, no significant differences between the two portions of WM are observed. However, in one case, a significantly higher ODI is measured in WM voxels likely to contain crossing fibres, as compared to voxels where their presence is unlikely. Despite the preliminary nature of this analysis and the small size of the sample, results point towards a potential weak but measurable impact on NODDI metrics of crossing fibres in spinal cord WM at the present MRI voxel resolution. In particular, the major sign of presence of crossing fibres seems to be an increase in ODI. Therefore, ODI appears as an intriguing index for the characterisation of neurite organisation complexity in the spinal cord and of its changes due to pathology. Nonetheless, future analysis with a higher number of subjects would be needed to further confirm this finding.

*Limitations*

This work demonstrates that NODDI can be applied to the human spinal cord *in vivo*. However, a number of limitations of our approach need to be acknowledged. The main limitation is probably the fact that the diffusion encoding protocol was not optimised explicitly for the spinal cord. Therefore, the $b$-values adopted in this study may not be optimal, since they were designed for priors on $d_{||}$ and $d_{\text{iso}}$ typically employed for the brain *in vivo*. For instance, a slightly higher prior on $d_{||}$, similar to the AD measured here in WM, would have resulted in a slightly lower maximum $b$-value, and hence in a better SNR of the experiment due to the lower $\text{T}_\text{E}$ that could have been used. Also, the choice of $d_{\text{iso}} = 3.00\,\mu\text{m}^2\,\text{ms}^{-1}$ may not be able to account for pseudo-diffusion effects due to flow and pulsation, such as in voxels characterised by partial volume with the branches of the anterior spinal artery and vein, which pass into the anterior median fissure. As far as the diffusion-weighting protocol is concerned, we also speculate that the directional sampling scheme, here isotropic as in [215], may have been optimised according to single fibre approaches similar to those followed in [157], in order to reduce the total acquisition time.

Another limitation of our work is that the reproducibility scores of DTI may have been underestimated for two reasons. Firstly, a different number of measurements compared to NODDI were employed. Secondly, the $\text{T}_\text{E}$ employed to acquire the $b = 711\,\text{s}\,\text{mm}^{-2}$ shell was not the minimum achievable at that $b$-value. We acquired both $b$-shells with the same $\text{T}_\text{E}$ to achieve the same $T_2$-weighting. However, this caused the SNR of the $b = 711\,\text{s}\,\text{mm}^{-2}$ shell on its own to be suboptimal.

The choices of the free water and neural tissue diffusivities, i.e. $d_{\text{iso}} = 3.00\,\mu\text{m}^2\,\text{ms}^{-1}$ and $d_{\|} = 1.70\,\mu\text{m}^2\,\text{ms}^{-1}$), may not be optimal in the presence of pathology. In our approach, the diffusion coefficients were fixed rather than fitted as in [215]. However, the adopted values may not be the best ones in presence of phenomena such as oedema or inflammation, leading to biases in the other fitted metrics. In those cases, data-driven priors for $d_{\text{iso}}$ and $d_{\|}$ may be evaluated, while sensitivity analysis would help assess the impact of fixing such diffusivites on other NODDI indices.

Lastly, the motion correction strategy may also have represented a limiting factor of our pipeline. We exploited the interleaved position of the non-DW images and estimated motion only on those images, given the challenge of co-registering DW and non-DW images of the spinal cord reliably. Although in other studies DW images were registered to non-DW ones [34, 129, 213], it should be noticed that in those works weaker diffusion weighting was employed.

## 4.7 Conclusion

In this chapter, we demonstrated the feasibility of applying the published NODDI technique to the healthy cervical cord *in vivo* and in a clinical setting. NODDI provides metrics that have the potential to be valid biomarkers for spinal cord conditions describing specific features of pathology at sub-voxel scale.

NODDI fits the acquired data better than DTI, and provides contrast between GM and WM in terms of neurite orientation dispersion, a key source of diffusion anisotropy. This is in line with recent findings, which showed that orientation dispersion at the MRI voxel scale is an important characteristic even in organised areas such as the corpus callosum [21], improving the performance of diffusion models [58] when accounted for. The measured reproducibility of NODDI metrics, despite being slightly lower than that of DTI, would allow its application in studies involving larger groups of subjects.

In conclusion, at present NODDI is a valid and feasible alternative to DTI for spinal cord applications. Future optimisation may help further reduce the variability of the metrics with benefits in terms of contrast and reproducibility.

# Chapter 5

# NODDI analysis of single-shell data: a feasibility study

## 5.1 Introduction

NODDI provides indices of neurite density and orientation dispersion in clinically feasible acquisitions, with potential applications in several neurological conditions, such as MS [112], SCI [179] and ALS [153]. The published NODDI technique relies on the acquisition of two HARDI shells with different $b$-values. Although a standard single-shell acquisition allows the quantification of the orientation dispersion, the estimation of neurite and isotropic compartment volume fractions requires at least two shells [215]. However, in [215], it was not tested whether the neurite compartment volume fraction could be estimated from single-shell data, when the isotropic compartment is not included.

The objective of this chapter is to study whether a reduced NODDI model without isotropic compartment could be fitted to standard single-shell DW data. We focussed on the impact that the $b$-value and the number of diffusion encoding directions have on single-shell estimates of NODDI metrics, as compared to two-shell gold standard. For our study, we employed the same data employed in the previous chapter (five healthy volunteers scanned at 3T with a rFOV DW ZOOM-EPI sequence).

Our analysis is informative for those interested in applying retrospective NODDI analysis on routine DW scans of the spinal cord, which are common, especially a low $b$-value [34, 129, 213]. Single-shell analysis, if proven to be feasible, would enable the investigation of new research questions without requiring the acquisition of new data and would facilitate the design of new studies.

## 5.2 Research dissemination

Some of the results described in this chapter have been presented in abstract form at international meetings as:

- “Single-shell diffusion MRI NODDI with *in vivo* cervical cord data”. Grussu F. et al, ISMRM annual meeting (2014), p.1716, traditional poster.
- “Characterisation of single-shell NODDI fitting in spinal cord grey and white matter”. Grussu F. et al, British Chapter of ISMRM annual meeting (2014), traditional poster.

## 5.3 Methods

### 5.3.1 Data acquisition

Data from the the same healthy volunteers of chapter 4 were studied, omitting rescans. Briefly, our data set consisted of five rFOV PGSE ZOOM-EPI [206] scans with OVS [208] obtained from five different healthy volunteers. Salient parameters were: $\mathrm{T_R} = 12$ RR repeats (oxymeter-based peripheral cardiac gating, triggering delay of 150 ms), $\mathrm{T_E} = 65.50$ ms, rFOV of $64\times48\,\mathrm{mm}^2$, SENSE factor of 1.5, resolution of $1\times1\times5\,\mathrm{mm}^3$, 6 non-DW images, 30 diffusion directions at $b = 711\,\mathrm{s\,mm}^{-2}$ and 60 at $b = 2855\,\mathrm{s\,mm}^{-2}$ ($\Delta = 32.20$ ms, $\delta = 20.50$ ms for both shells).

### 5.3.2 Motion correction

Motion was corrected as described in chapter 4, section 4.4.2. The correction relied on slice-wise linear registration accounting for in-plane translations, with registration transformations estimated among $b = 0$ images exploiting their interleaved acquisition throughout the MRI scan.

### 5.3.3 Segmentation

The same segmentation methods followed for the study in chapter 4 were employed, after performing motion correction. Segmentation allowed the identification of a whole-cord, a GM and a WM mask for each subject.

The spinal cord was segmented on the mean $b = 0$ image with an active surface method [74]. On the other hand, GM was segmented manually on an image obtained averaging DW images with good contrast between GM and WM, as firstly shown in [97] and previously discussed in section 4.4.3 of chapter 4. Finally, WM voxels were defined as voxels within the eroded spinal cord mask not containing voxels from the GM mask.

### 5.3.4 Model fitting

The full NODDI model and a reduced version without the isotropic compartment were fitted to different subsets of data with the NODDI Matlab toolbox. The original model was introduced by equation 4.1, whilst the reduced model is written as

$$s(\mathbf{g}, b) \;=\; s_0\Big(v_{\mathrm{r}}\, s_{\mathrm{in}}(\mathbf{g}, b) \,+\, \big(1 - v_{\mathrm{r}}\big)\, s_{\mathrm{en}}(\mathbf{g}, b)\Big), \tag{5.1}$$

| Fitting | Model | $b$-value(s) $\left[\mathrm{s\,mm^{-2}}\right]$ | Number of directions |
|---|---|---|---|
| *FullNODDI* | Full | 711, 2855 | 30, 60 |
| *bLow30Dir* | Reduced | 711 | 30 |
| *bHigh60Dir* | Reduced | 2855 | 60 |
| *bHigh30Dir* | Reduced | 2855 | 30 |

Table 5.1: summary of the four NODDI analyses that were performed to study the feasibility of single-shell fitting.

where $s_{\text{in}}$ and $s_{\text{en}}$ are the intra-neurite and extra-neurite signals, computed respectively with equations 4.3 and 4.4, and where $v_{\text{r}}$ is the voxel volume fraction occupied by neurites, corresponding to quantity $(1 - v_{\text{iso}})\, v_{\text{in}}$ in the full NODDI model.

In practice, for each subject, four different NODDI analyses were performed, with the same constraint on the diffusivity $d_{\|}$ as chapter 4 ($d_{\|} = 1.70\ \mu\mathrm{m}^2\,\mathrm{ms}^{-1}$) and, for the full model, on $d_{\text{iso}}$ ($d_{\text{iso}} = 3.00\ \mu\mathrm{m}^2\,\mathrm{ms}^{-1}$). They were:

1. analysis *FullNODDI*: full model fitted to the whole double-shell data set (same fitting as that of chapter 4);
2. analysis *bLow30Dir*: reduced model fitted to the 30 measurements at $b = 711\,\mathrm{s\,mm^{-2}}$;
3. analysis *bHigh60Dir*: reduced model fitted to the 60 measurements at $b = 2855\,\mathrm{s\,mm^{-2}}$;
4. analysis *bHigh30Dir*: reduced model fitted to the 30 measurements at $b = 2855\,\mathrm{s\,mm^{-2}}$ corresponding to gradient directions of *bHigh60Dir* most evenly spread over the sphere (minimum electrostatic energy criterion [77]), extracted with Camino diffusion MRI toolkit [38] (command *subsetpoints*).

Table 5.1 summarises the four NODDI analyses.

## 5.4 Comparison between single-shell and two-shell analyses

We studied the voxel volume fraction of the intra-neurite compartment and ODI with the objective of characterising the errors of these metrics obtained from single-shell fitting with respect to two-shell parameters. As far as the intra-neurite volume fraction is concerned, we point out that parameter $v_{\text{r}}$ of equation 5.1 (single-shell model) was compared to quantity $(1 - v_{\text{iso}})\, v_{\text{in}}$ (also indicated as $v_{\text{r}}$ in chapter 4) from equation 4.1 (two-shell model). This is due to the fact that in single-shell fitting, $v_{\text{r}}$ yields part of the information conveyed by the factor $1 - v_{\text{iso}}$ in the two-shell fitting, being $v_{\text{iso}}$ constrained to $0$.

We proceeded as follow.

1. The percentage relative errors of the parameters obtained from single-shell fitting as compared to the two-shell gold standard were calculated (quantities $\delta v_{\text{r}}$ for $v_{\text{r}}$ and $\delta$ODI for ODI).

2. The distributions of $\delta v_\text{r}$ and $\delta$ODI within GM and WM were approximated via calculation of normalised histograms (group level).
3. Pearson correlation coefficients between two-shell and single-shell values of metrics $v_\text{r}$ and ODI were calculated for voxels within the GM and the WM masks separately (group level).

## 5.5 Results

Figure 5.1 shows percentage relative error for $v_\text{r}$ in absolute value ($|\delta v_\text{r}|$) for one representative case, whereas figure 5.2 shows percentage relative error for ODI, also in absolute value ($|\delta$ODI$|$). All other subjects show similar patterns of errors.

Errors $\delta v_\text{r}$, in absolute value, appear higher along the border of the fitting mask, where CSF partial volume is likely to occur. Differences between single and two-shell estimates of $v_\text{r}$ are more severe for analysis *bLow30Dir* as compared to *bHigh60Dir* and *bHigh30Dir*.

Errors $\delta$ODI, in absolute value, are similar for the three single-shell analyses, with $|\delta$ODI$|$ surpassing $100\%$ in some voxels.

Figure 5.3, illustrates scatter plots between single and two-shell metrics (from top: first row for $v_\text{r}$, third row for ODI) and corresponding distributions of errors (from top: second row for $\delta v_\text{r}$, fourth row for $\delta$ODI). Scatter plots show that single-shell metrics follow the trend of two-shell metrics. The distributions of errors were similar in GM and WM for $v_r$, while they are slightly broader in GM for ODI as compared to WM, where they exhibit multiple peaks. The distributions of $\delta v_\text{r}$ points towards the underestimation of volume fraction $v_\text{r}$ in analysis *bLow30Dir*, as compared to values from two-shell analysis.

Table 5.2 reports Pearson correlation coefficient between single and two-shell metrics ($p \ll 10^{-4}$ for all table entries). For $v_\text{r}$, correlations are similarly high in both GM and WM for all single-shell analyses. On the other hand, correlation coefficients for ODI are always lower in WM as compared to GM. Notably, in analysis *bLow30Dir*, correlation in WM is as low as 0.13, whereas in GM equals 0.75. Lastly, table 5.2 suggests that higher $b$-value causes correlations to improve more than a higher number of measurements.

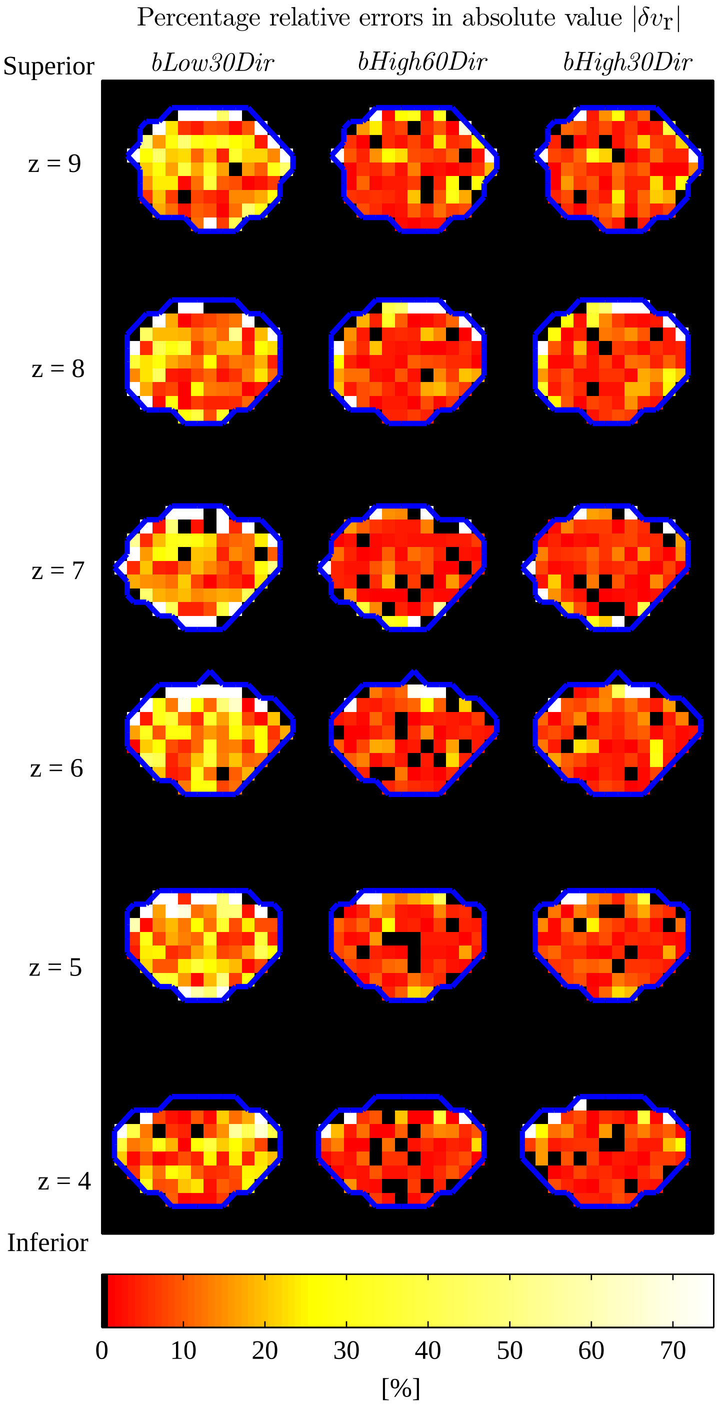
Percentage relative errors in absolute value $|\delta v_{\mathrm{r}}|$
Superior
bLow30Dir
bHigh60Dir
bHigh30Dir
z = 9
z = 8
z = 7
z = 6
z = 5
z = 4
Inferior
0
10
20
30
40
50
60
70
[%]

Figure 5.1: voxel-wise maps of percentage relative error for $v_{\mathrm{r}}$ in absolute value ($|\delta v_{\mathrm{r}}|$) in one representative subject. Slices vary along rows, whereas different columns represent different analyses. From left to right: analysis *bLow30Dir*, *bHigh60Dir* and *bHigh30Dir*.

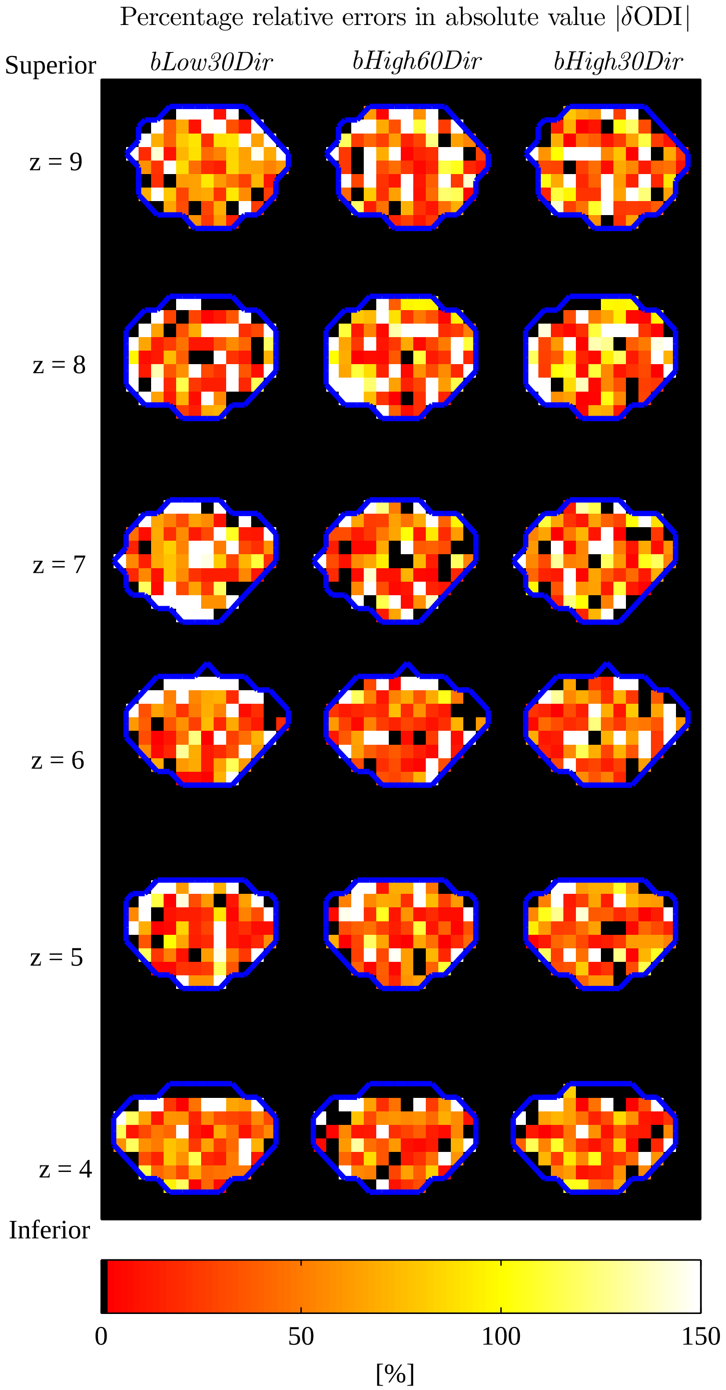
Percentage relative errors in absolute value |δODI|
Superior
bLow30Dir
bHigh60Dir
bHigh30Dir
z = 9
z = 8
z = 7
z = 6
z = 5
z = 4
Inferior
0
50
100
150
[%]

Figure 5.2: voxel-wise maps of percentage relative error for ODI in absolute value ($|\delta\text{ODI}|$) in one representative subject. Slices vary along rows, whereas different columns represent different analyses. From left to right: analysis *bLow30Dir*, *bHigh60Dir* and *bHigh30Dir*.

|  | Analysis |  |  |  |  |  |
|---|---|---|---|---|---|---|
| Metric | *bLow30Dir* |  | *bHigh60Dir* |  | *bHigh30Dir* |  |
|  | GM | WM | GM | WM | GM | WM |
| $v_{\mathrm{r}}$ | 0.78 | 0.76 | 0.88 | 0.88 | 0.86 | 0.86 |
| ODI | 0.75 | 0.13 | 0.85 | 0.67 | 0.79 | 0.63 |

Table 5.2: correlations between single-shell and two-shell NODDI metrics in GM and WM.

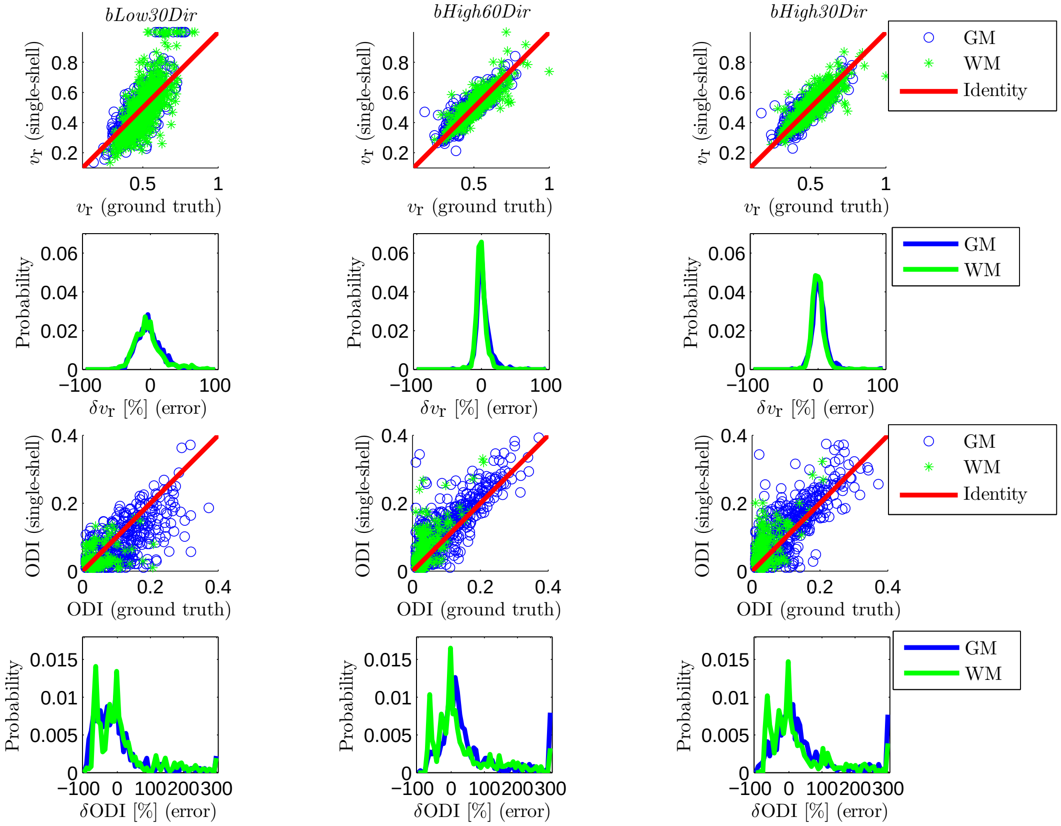

Figure 5.3: values of $v_{\mathrm{r}}$ and ODI and distributions of errors $\delta v_{\mathrm{r}}$ and $\delta$ODI in GM and WM. Scatter plots relating two-shell gold standard and single-shell estimates of $v_{\mathrm{r}}$ and ODI are reported in the first and third row from top. Distributions of errors $P(\delta v_{\mathrm{r}})$ and $P(\delta \mathrm{ODI})$ are shown in the second and fourth rows from top. Different columns represent different NODDI analyses. From left to right: analysis *bLow30Dir*, *bHigh60Dir* and *bHigh30Dir*.

## 5.6 Discussion

In this chapter, we have compared NODDI metrics $v_{\mathrm{r}}$ and ODI obtained from single-shell NODDI analysis to their two-shell counterparts, taken as a gold standard. Single-shell analysis was performed employing a reduced NODDI model without isotropic compartment. Three different single-shell analyses were compared to two-shell gold standard: one performed on a DW data set with low $b$-value and 30 gradient directions; one on a DW data set with high $b$-value and 60 gradient directions; one on a DW data set with high $b$-value and 30 gradient directions. Errors of single-shell analysis with respect to the gold standard were calculated in GM and WM, as well as their distributions. Moreover, correlations between single and double-shell metrics were evaluated within GM and WM separately.

*Voxel-wise percentage relative errors*

The calculation of errors demonstrates that stronger differences between single and two-shell analysis may be observed where CSF partial volume occurs, due to the lack of the isotropic compartment in the model employed for single-shell fitting. At a glance, voxel-wise maps of errors also highlight that differences between single and two-shell values of $v_{\mathrm{r}}$ are stronger at low $b$-value, whereas for ODI errors appear more homogeneous across single-shell analyses, as high as 150$\%$ in certain voxels.

*Tissue-specific distributions of errors*

Distributions show that errors in estimating $v_{\mathrm{r}}$ are similar between GM and WM for all single-shell analyses. The distributions show a single peak, and, at low $b$-value, demonstrate that $v_{\mathrm{r}}$ is biased and in general underestimated. As far as ODI is concerned, the error distributions have more complex shapes than those of $v_{\mathrm{r}}$, with multiple peaks in WM. They suggest that relative errors in estimating ODI can be higher than for $v_{\mathrm{r}}$.

*Correlation coefficients*

Lastly, association between single-shell estimates of $v_{\mathrm{r}}$ and ODI and their two-shell counterparts was assessed calculating a Pearson correlation coefficient in GM and WM. Fitting to data acquired with higher diffusion weighting provides in general higher correlations, possibly because as $b$ increases, subtler differences in terms of neurite morphology can be captured, due to a sharper diffusion signal profile [93]. Correlations are similar between GM and WM for $v_{\mathrm{r}}$, whereas they are always lower for WM as compared to GM for ODI (as low as 0.13 at low $b$-value). The lower correlation in WM may be due to the difficulty of resolving subtle variations in terms of neurite orientation dispersion in a well organised structure such as the spinal cord, when a simple, single-shell diffusion encoding protocol is employed. Lastly, the analysis reveals that a higher number of directions is beneficial (i.e. compare analysis *bHigh60Dir* with *bHigh30Dir*), but not as much as increases in terms of $b$-value.

*Limitations*

This work presents a number of limitations. Two of them are the same of those discussed in chapter 4, i.e. the choice of the intrinsic diffusivities and the motion correction strategy.

Here, $d_{\parallel} = 1.70\,\mu\mathrm{m}^2\,\mathrm{ms}^{-1}$ was fixed for both single and two-shell analyses, whereas $d_{\mathrm{iso}} = 3.00\,\mu\mathrm{m}^2\,\mathrm{ms}^{-1}$ was employed for the two-shell case. These values are usually employed in diffusion

MRI of the brain, and slightly different values may provide minor improvements when performing NODDI in the spinal cord.

As far as the motion correction is concerned, we recall that motion was estimated studying the $b = 0$ images only. Minor improvements to NODDI analysis of spinal cord data may come, in general, from a more precise motion correction approach.

A specific limitation of this chapter is related to the small number of $b$-values that were sampled. The same data employed for chapter 4 was analysed, due to time constraints. A more precise quantification of the effect of the choice of the $b$-value could be evaluated by sampling more $b$-shells. For instance, this would enable the investigation of whether a *breakdown* between poor and acceptable single-shell analysis as a function of $b$ exists.

## 5.7 Conclusion

In this chapter we have investigated the feasibility of performing single-shell NODDI analysis in the healthy spinal cord *in vivo*, with the aim of informing those interested in retrospective NODDI analysis of standard DW data.

Our results suggest that single-shell NODDI metrics obtained with a simplified NODDI model agree reasonably well with two-shell counterparts in certain conditions, whereas they differ in others. In particular, the volume fraction of the intra-neurite compartment ($v_{\mathrm{r}}$) is underestimated at low $b$-value, whereas the orientation dispersion index ODI is less dependent on $b$ but exhibits notable differences between GM and WM.

In conclusion, single-shell NODDI analysis of DW spinal cord data appears more suitable for GM rather than WM. It should be performed at high $b$-value to reduce biases, bearing in mind that free diffusion cannot be modelled [215], limiting the analysis to areas without CSF partial volume effects or other sources of isotropic diffusion.

# Chapter 6

# Influence of axon diameter distribution on NODDI metrics

## 6.1 Introduction

NODDI models axons and dendrites as "*sticks*" (zero-radius cylinders), neglecting heterogeneities in terms of neurite diameters. This simplification is reasonable in the long diffusion time limit, a condition practically achievable in most brain WM, as for example the genu of the corpus callosum where the diameter of myelinated axons does not exceed 2 $\mu$m [1].

However, in other WM regions, diffusion times of 20-30 ms conventionally employed in DW PGSE may not be sufficiently long to support the *stick* model. For example, in spinal cord WM, the tails of the axon diameter distribution may extend up to 15 $\mu$m and beyond [56, 70, 117, 201]. Water molecules diffusing within large axons may not fully experience the effect of boundaries for conventional diffusion times. This can potentially lead to underestimation of neurite density due to considerable departures from the *stick* signal model.

Underestimation of neurite density due to the employment of short diffusion times should be accounted for in multi-modal approaches such as g-ratio mapping [173], where neurite density indices from diffusion MRI are combined to myelin maps to provide new biomarkers. Also, since biological variability in terms of axon diameter distribution is expected, the level of underestimation may differ from subject to subject. This could potentially lead to an increase of the between-subject variability of neurite density maps, and ultimately to the requirement of bigger sample sizes in clinical studies to detect significant differences.

In this chapter, we explore whether in clinical settings the employment of certain diffusion times in presence of axons characterised by large diameters can influence neurite density estimation, as well as of other NODDI microstructural indices, in the spinal cord. For this purpose, diffusion-time dependency of NODDI metrics was studied *in silico* and *in vivo*.

Monte Carlo computer simulation of the diffusion process were run to obtain idealised DW signals for different diffusion times and microstructural geometries, studying clinically realistic PGSE protocols. These signals were analysed with NODDI to obtain estimates of neurite density (and of other microstructural indices) to be compared to a known ground truth.

*In vivo* MRI scans were also performed in three healthy volunteer after obtaining informed written consent, in experimental sessions approved by a local research ethics committee. The same MRI scanner used for acquiring the data used in chapter 4 was employed (a 3T Philips Achieva MRI system). The *in vivo* part of the study assessed whether NODDI metrics of the spinal cord may exhibit diffusion time dependency in clinical scenarios, to confirm results from simulations.

## 6.2 Research dissemination

Some of the results described in this chapter have been submitted in abstract form as: "Axon diameter distribution influences diffusion-derived axonal density estimation in the human spinal cord: *in silico* and *in vivo* evidence". Grussu F. et al, ISMRM annual meeting (2016), p.2009, traditional poster. Also, a manuscript is currently in preparation for submission to a peer-reviewed scientific journal.

## 6.3 Methods

In this section, the methods to analyse synthetic and *in vivo* DW signals are described.

### 6.3.1 *In silico* study

The *in silico* study aimed to assess theoretically and in a fully controlled fashion whether the choice of the diffusion time in presence of large axons can influence NODDI neurite density estimates (as well as other metrics) in spinal cord WM. For this purpose, DW signals were generated from the simulation of water diffusion within two models of WM. Afterwards, NODDI was fitted to the synthesised data to get an index of neurite density, which, as well as other NODDI indices, was compared to the ground truth value.

#### Substrates

Two substrates were designed to model WM as a two-compartment space, made of a collection of impermeable and parallel cylinders aligned along the $z$-axis. The material inside and outside the cylinders was characterised by the same diffusivity, equal to 1.70 $\mu$m$^2$ ms$^{-1}$. This value is of common usage in literature to describe the intrinsic diffusivity of water in neural tissue at body temperature [215]. Axon radii followed a Gamma distribution $P(r\,|\,p_1, p_2)$ defined as [4,7]

$$P(r\,|\,p_1, p_2) \;=\; \frac{1}{p_2^{p_1}\,\Gamma(p_1)}\, r^{p_1-1}\, e^{-\frac{r}{p_2}}, \tag{6.1}$$

where $r$ is the radius, $p_1$ and $p_2$ are respectively the *shape* and *scale* parameters and $\Gamma(x) = \int_0^{\infty} \eta^{x-1}\, e^{-\eta}\, d\eta$.

The first substrate, named substrate *BigAxons*, models the microstructure of a WM voxel containing giant axons, representative of spinal cord fibre bundles characterised by large diameters. For this substrate, the cylinder volume fraction was set to 0.65, whilst the cylinder radii were drawn from a Gamma distribution with shape $p_1 = 8$ and scale $p_2 = 0.5\,\mu$m, shown in green in figure 6.1. The distribution of radii/diameters employed for substrate *BigAxons* is biologically plausible. As a comparison, in references [70] ("*Kurve 5, Zone 4*") and [117] (figure 6), axon diameter distributions show peaks even for diameters as large as $13\,\mu$m.

The second substrate, named *SmallAxons*, was designed to be similar to the model of WM characterised by small axon diameters (splenium of the human corpus callosum) employed in [4]. The shape and scale parameters of the Gamma distribution of radii were $p_1 = 9.063$ and $p_2 = 0.1429\,\mu$m, and the cylinder volume fraction was 0.65.

In practice, a third substrate was simulated averaging the signals from substrate *SmallAxons* and *BigAxons*. This provided signals whose intra-axonal component arises from cylinders following a radius distribution as that shown in red to the bottom of figure 6.1. The cylinder volume fraction of the third substrate equals 0.65, since both substrates *BigAxons* and *SmallAxons* are also characterised by a cylinder volume fraction of 0.65.

Table 6.1 summarises other characteristics of the substrates (size, number of cylinders, number of spins, diffusivity of the material inside and outside the cylinders), whereas figure 6.1 provides an illustrative example of the two.

| Substrate name | Shape parameter (dimensionless) | Scale parameter [$\mu$m] | Cylinder volume fraction (dimensionless) | No. of cylinders | Side size [$\mu$m] | No. of spins | Diffusivity [$\mu$m$^2$ ms$^{-1}$] |
|---|---|---|---|---|---|---|---|
| *BigAxons* | 1.000 | 0.5000 | 0.65 | 2862 | 500 | $3 \cdot 10^5$ | 1.70 |
| *SmallAxons* | 9.063 | 0.1429 | 0.65 | 2617 | 165 | $3 \cdot 10^5$ | 1.70 |

Table 6.1: summary of the characteristics of substrates *BigAxons* and *SmallAxons*.

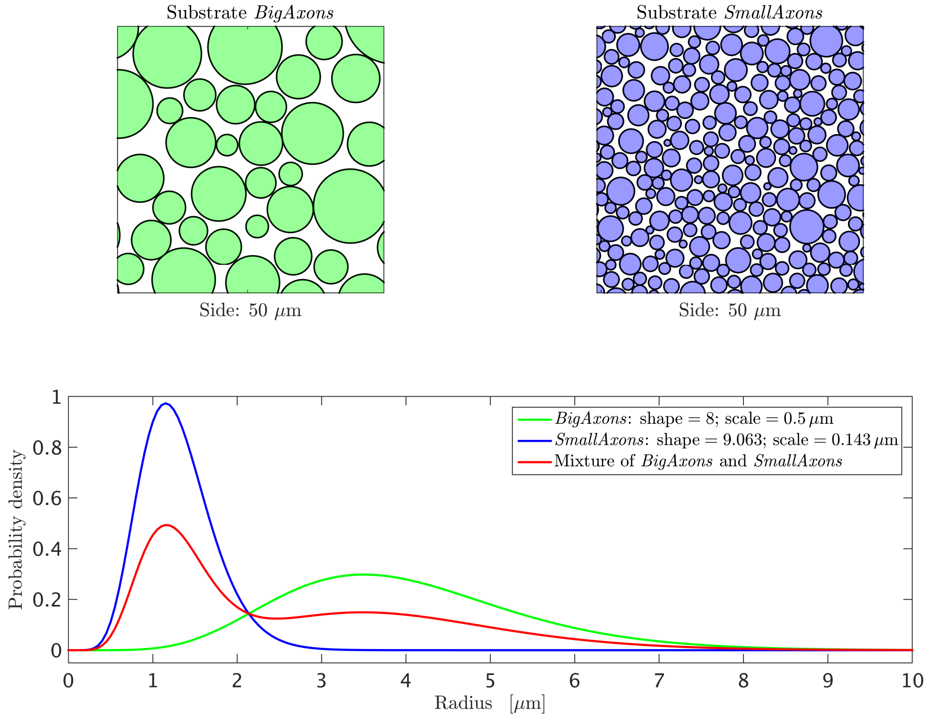

Figure 6.1: substrates employed for computer simulations of clinically realistic PGSE experiments. Top: detail of 50 $\mu$m × 50 $\mu$m of substrate *BigAxons* (to the left, with axons in green) and *SmallAxons* (to the right, with axons in blue). Bottom: radius distribution of substrates *BigAxons* (green), *SmallAxons* (blue) and of a mixture of those two (red). For all substrates, the cylinder volume fraction was set to 0.65.

### DW signal synthesis

DW signals were generated from substrates *BigAxons* and *SmallAxons* running Monte Carlo simulations of the diffusion process with Camino diffusion MRI toolkit [38] (command *datasynth* with 2000 time steps). Signals from the two substrates were also averaged to simulate a mixture of their axon radius distributions, while maintaining the same cylinder volume fraction.

The command *datasynth* simulates the random motion of water molecules while a DW pulse sequence is played out. A number of spins specified by the user is positioned evenly within a substrate. Then, at each time step of the simulation, the position of the spins is updated, so that from time step $t$ to time step $t + \Delta t$ each spin is displaced according to equation 3.34 of a quantity equal to $\sqrt{6D\,\Delta t}$ along a random direction, with $D$ being the diffusivity of the substrate. Elastic reflection of spin positions in case of collision with a substrate surface is implemented when substrates are impermeable, as those employed in this study. The phase accrual $\phi_k$ of the generic $k$-th spin over the whole sequence is then calculated given the simulated spin trajectory $\mathbf{r}_k(t)$ and the applied gradient waveform $\mathbf{G}(t)$. Ultimately, a DW signal is provided summing over the whole spin ensemble as $|\sum_k e^{j\phi_k}|$.

*Design of simulated PGSE experiments*

In our simulations, we modelled clinically realistic PGSE sequences as shown in figure 6.2, limiting the maximum gradient strength to $G_{\text{max}} = 72\,\text{mT}\,\text{m}^{-1}$ and the maximum echo time to $\text{T}_{\text{E}\,\text{max}} = 124\,\text{ms}$. Diffusion encoding gradients were characterised by a duration $\delta$, a separation $\Delta$, an amplitude $G$ and a direction $\mathbf{g}$. The position of the gradients was varied on both sides of the 180°-refocussing RF pulse, but it was not allowed in certain areas, shown as coloured bands in figure 6.2. These are parts of the sequence that could be used for other purposes, such as: i) slice excitation (8 ms, in light red, which also allows slice refocussing); ii) spoiling (2 ms on both sides of the refocussing pulse, in light green); iii) spin refocussing (8 ms, in light violet); iv) signal acquisition (12 ms, in light yellow, representing the time necessary to reach the origin of the k-space at the occurrence of the DW spin echo). In addition to those, the first gradient lobe was not allowed in a brief interval of 4 ms that follows the excitation stage (cyan in figure 6.2), in order to guarantee consistency of the sequence timing.

Four different PGSE experiments were modelled. For each experiment, a different diffusion time $T_d = \Delta - \delta/3$ was adopted. We fixed $\delta = 18\,\text{ms}$ and controlled $\Delta$ modifying the delay between the end of the gradient pulse and the beginning of the spoiling-refocussing block ($t_{\text{del}}$). Such a delay equals by construction the delay between the end of the same spoiling-refocussing block and the beginning of the second gradient pulse (see figure 6.2). In particular, we remark that although $\delta = 18\,\text{ms}$ may appear a relatively high value, it is necessary to achieve sufficient diffusion weighting in a clinical scenario with limited gradient strength ($b = \gamma^2\,\delta^2\,G^2\,T_d$ increases as the second power of $\delta$). Long $\delta$ is also beneficial since it would make our simulated cylinders appear smaller than their actual size [125].

Each PGSE experiment consisted of 9 non-DW measurements and of two NODDI-like DW shells ($b = 711\,\text{s}\,\text{mm}^{-2}$, 30 directions; $b = 2855\,\text{s}\,\text{mm}^{-2}$, 60 directions), obtained for different combinations of $\Delta$ and $G$.

The four diffusion times $T_d$ were $T_d = \{24,\ 41.33,\ 58.67,\ 76\}$ ms. For each diffusion time $T_d$, we calculated:

1. the required gradient separation $\Delta$ as $\Delta = T_d + \delta/3$;
2. the required delay $t_{\text{del}}$ as $t_{\text{del}} = \frac{\Delta - \delta - 12\,\text{ms}}{2}$, which follows from the identity $\Delta \equiv \delta + t_{\text{del}} + 12\,\text{ms} + t_{\text{del}}$ demonstrated by figure 6.2;
3. the required echo time $\text{T}_\text{E}$ as $\text{T}_\text{E} = 2\,\delta + 2\,t_{\text{del}} + 36\,\text{ms}$, using an expression also suggested by the sequence model shown in figure 6.2.

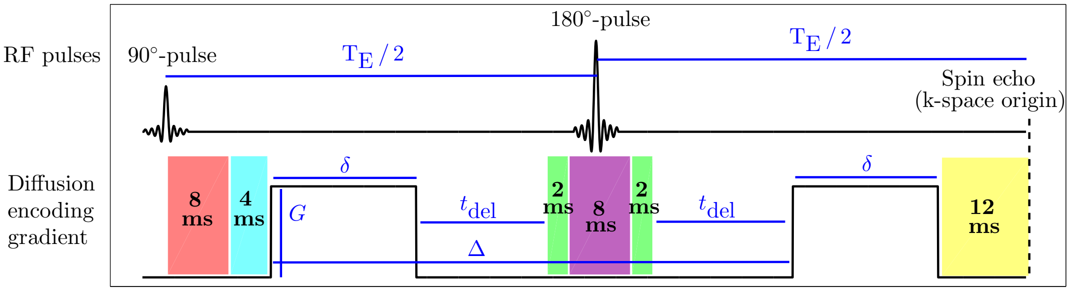

Figure 6.2: model of clinically realistic PGSE sequence employed to run simulations. The diffusion encoding gradients are characterised by a duration, separation and amplitude respectively of $\delta$, $\Delta$ and $G$, whilst $\text{T}_\text{E}$ is the echo time. The coloured bands represent areas where the diffusion encoding gradient cannot be placed. They are points of the sequence that are usually employed for excitation (light red, 8 ms), spoiling of undesired spin pathways (light green, 2 ms on both sides of the 180°-refocussing pulse), spin refocussing (light violet, 8 ms), signal acquisition (light yellow, lasting 12 ms, a value plausible when Partial Fourier imaging and SENSE are used in rFOV acquisitions with bandwidths of the order of 150 KHz). In addition to those, a brief interval of 4 ms after excitation (shown in cyan) was not made available for diffusion weighting, in order to guarantee consistency of the timings. The duration of the coloured bands, although being conservative, is realistic. It was inferred from summary consultation of the pulse sequence diagram of the PGSE experiment performed with a 3T Philips Achieva system described in chapter 4.

Our Monte Carlo simulations provide signals at SNR $\rightarrow \infty$. Noisy signals were also obtained adding Rician noise at an SNR level determined by the calculated echo time $\text{T}_\text{E}$. For each $\text{T}_\text{E}$, the SNR at $b = 0$ was calculated according to a signal loss due to mono-exponential $T_2$-decay as

$$\text{SNR}(\text{T}_\text{E}) = 13\,e^{\frac{72\,\text{ms}\,-\,\text{T}_\text{E}}{T_2}}, \tag{6.2}$$

having set $T_2 = 73$ ms, a plausible value for spinal cord WM at 3T [165]. Equation 6.2 relies on a reference SNR of 13 for $\text{T}_\text{E} = 72$ ms, similar to the SNR measured in spinal cord WM *in vivo* for a similar $\text{T}_\text{E}$ (chapter 4).

| Experiment number | $\delta$ [ms] | $\Delta$ [ms] | $T_d$ [ms] | $t_{\text{del}}$ [ms] | $\mathrm{T_E}$ [ms] | $G$ at low $b$ [mT m$^{-1}$] | $G$ at high $b$ [mT m$^{-1}$] | SNR at $b = 0$ |
|---|---|---|---|---|---|---|---|---|
| 1 | 18.00 | 30.00 | 24.00 | 0.00 | 72.00 | 35.74 | 71.63 | 13 |
| 2 | 18.00 | 47.33 | 41.33 | 8.67 | 89.33 | 27.24 | 54.58 | 10.25 |
| 3 | 18.00 | 64.67 | 58.67 | 17.34 | 106.67 | 22.86 | 45.81 | 8.09 |
| 4 | 18.00 | 82.00 | 76.00 | 26.00 | 124.00 | 20.07 | 40.25 | 6.38 |

Table 6.2: summary of the four simulated PGSE experiments.

Table 6.2 summarises the characteristics of the four simulated PGSE experiments and the corresponding SNR levels.

*Simulation of orientation dispersion*

The effect of orientation dispersion of cylinder directions was also modelled running the Monte Carlo simulations for seven rotations of the substrates and averaging their signals. In practice, since the direction of the cylinders is constrained by Camino to be aligned to $\mathbf{z} = \begin{bmatrix} 0 & 0 & 1 \end{bmatrix}^{\mathsf{T}}$, we rotated rigidly the whole set of gradient directions, implementing in Matlab the following procedure.

1. Seven random directions $\mathbf{n}_i$ $i = 1, ..., 7$ were drawn from a Watson distribution characterised by a mean orientation $\mathbf{z}$ and a concentration $\kappa$, as shown in [60], with $\mathbf{n}_i$ representing a new orientation of the cylinders;
2. the rotation matrix $\mathbf{R}_i$ mapping $\mathbf{z}$ onto $\mathbf{n}_i$ (i.e. such that $\mathbf{n}_i = \mathbf{R}_i\,\mathbf{z}$) was calculated as

$$\mathbf{R}_i = \mathbf{I} + \mathbf{M}_i + \frac{1 - c_i}{s_i^2}\mathbf{M}_i\,\mathbf{M}_i,$$

   where

$$\mathbf{M}_i = \begin{bmatrix} 0 & -m_{i\,z} & m_{i\,y} \\ m_{i\,z} & 0 & -m_{i\,x} \\ -m_{i\,y} & m_{i\,x} & 0 \end{bmatrix}$$

   and where $\mathbf{m}_i = \begin{bmatrix} m_{i\,x} & m_{i\,y} & m_{i\,z} \end{bmatrix}^{\mathsf{T}} = \mathbf{z} \times \mathbf{n}_i$, $s_i = ||\mathbf{m}_i||$ and $c_i = \mathbf{z}^{\mathsf{T}}\,\mathbf{n}_i$;
3. the inverse rotation $\mathbf{R}_i^{-1}$ was applied to the whole set of gradient directions of each of the 4 PGSE protocols before running the Monte Carlo simulations.

Two different $\kappa$ were used: $\kappa = 63.66$ (corresponding to[1] ODI $= 0.01$) and $\kappa = 6.31$ (corresponding to ODI $= 0.1$).

### Model fitting

The NODDI model was fitted to the DW signals generated with Monte Carlo simulations, fixing the diffusivities $d_{\text{iso}}$ and $d_{\parallel}$ to $d_{\text{iso}} = 3.00$ $\mu$m$^2$ ms$^{-1}$ and $d_{\parallel} = 1.70$ $\mu$m$^2$ ms$^{-1}$, as in previous chapters.

---

[1] We recall that ODI $= \frac{2}{\pi}\arctan\left(\frac{1}{\kappa}\right)$.

Fitting on noisy signals was performed maximising the Rician log-likelihood of the measurements, whose expression was reported in equation 4.6. On the other hand, NODDI was fitted to signals characterised by SNR $\rightarrow \infty$ with ordinary least square approach, i.e. finding the NODDI parameters $\mathbf{p}$ that minimised the sum of squared errors

$$\epsilon(\mathbf{p}) \; = \; \sum_{m=1}^{M} \left(S_m(\mathbf{p}) \, - \, A_m\right)^2, \tag{6.3}$$

with $S_m$ being the NODDI model predictions, $A_m$ the synthetic measurements and $M$ their number.

### Analysis

NODDI metrics $v_{\mathsf{iso}}$ (isotropic voxel volume fraction ), $v_{\mathsf{in}}$ (intra-neurite tissue volume fraction), $v_{\mathsf{r}} = (1 - v_{\mathsf{iso}})\, v_{\mathsf{in}}$ (intra-neurite voxel volume fraction) and ODI (orientation dispersion index) were plotted against diffusion times. A separate plot was obtained for each level of orientation dispersion and SNR level.

In order to obtain confidence intervals of parameters estimates, NODDI was fitted for 1000 unique instantiations of Rician noise. For the signals at SNR $\rightarrow \infty$ instead, fitting was run 1000 times on 1000 sub-protocols obtained extracting at random 25 unique directions out of 30 at $b = 711\,\mathrm{s\,mm^{-2}}$ and 50 out of 60 at $b = 2855\,\mathrm{s\,mm^{-2}}$.

## 6.3.2 *In vivo* study

### Subjects and MRI acquisition

Three healthy volunteers (2 males, 27 years old; 1 female, 26 years old) were scanned on a 3T Philips Achieva MRI system after obtaining informed written consent and approval by a local research ethics committee. The subjects were scanned in two sessions, with the second session performed within five months of the first one. The MRI scans were performed on the same system employed for the previous *in vivo* studies, located in Queen Square House, Queen Square, Institute of Neurology (NMR Unit, Department of Neuroinflammation). Each MRI session lasted about an hour. In each of the two sessions, three multi-shell DW ZOOM-EPI [206] experiments with OVS [208] were performed. In each experiment, NODDI-like diffusion encoding was followed (20 directions at $b = 711\,\mathrm{s\,mm^{-2}}$; 40 directions at $b = 2855\,\mathrm{s\,mm^{-2}}$; 9 interleaved $b = 0$ measurements) using a different diffusion time. The three diffusion times $T_d$ were

$$T_d \; = \; \{21.17, \; 44.67, \; 68.67\}\,\mathrm{ms},$$

obtained by variation of the gradient separation in the range $\Delta \; = \; \{28.5, \; 52, \; 76\}\,\mathrm{ms}$, while fixing the gradient duration to $\delta = 22\,\mathrm{ms}$.

In the first scanning session, the echo time $\mathrm{T_E}$ employed of each of the three multi-shell experi-

| Experiment number | $\delta$ [ms] | $\Delta$ [ms] | $T_d$ [ms] | $\mathrm{T_E}$ [ms] | $G$ at low $b$ [mT m$^{-1}$] | $G$ at high $b$ [mT m$^{-1}$] | SNR at $b = 0$ |
|---|---|---|---|---|---|---|---|
| 1 | 22.00 | 28.50 | 21.17 | 67.00 | 31.44 | 63.00 | 11.45, 13.99, 9.00 |
| 2 | 22.00 | 52.00 | 44.67 | 87.20 | 21.64 | 43.36 | 9.14, 10.56, 6.76 |
| 3 | 22.00 | 76.00 | 68.67 | 111.00 | 17.45 | 34.97 | 7.35, 8.98, 5.71 |

Table 6.3: summary of the three PGSE experiments performed in the first *in vivo* MRI session. To facilitate the comparison to table 6.2, the median SNR within the whole spinal cord of the three subjects is reported to the rightmost column of the table.

| Experiment number | $\delta$ [ms] | $\Delta$ [ms] | $T_d$ [ms] | $\mathrm{T_E}$ [ms] | $G$ at low $b$ [mT m$^{-1}$] | $G$ at high $b$ [mT m$^{-1}$] | SNR at $b = 0$ |
|---|---|---|---|---|---|---|---|
| 1 | 22.00 | 28.50 | 21.17 | 111.00 | 31.44 | 63.00 | 7.60, 6.00, 8.67 |
| 2 | 22.00 | 52.00 | 44.67 | 111.00 | 21.64 | 43.36 | 7.45, 5.26, 8.27 |
| 3 | 22.00 | 76.00 | 68.67 | 111.00 | 17.45 | 34.97 | 7.73, 6.68, 8.51 |

Table 6.4: summary of the three PGSE experiments performed in the second *in vivo* MRI session. To facilitate the comparison to table 6.2, the median SNR within the whole spinal cord of the three subjects is reported to the rightmost column of the table.

ments was chosen as the minimum value allowed by the adopted diffusion time. This provided

$$\mathrm{T_E} \; = \; \{67, \; 87.20, \; 111\} \, \mathrm{ms}.$$

In the second scanning session instead, the $\mathrm{T_E}$ was kept to the same value for the three experiments ($\mathrm{T_E} = 111$ ms), to uniform the three experiments in terms of relaxation-weighting and SNR.

Other salient parameters of the DW experiments were: rFOV of $64 \times 48 \times 60$ mm$^3$, SENSE factor of 1.5, resolution of $1 \times 1 \times 5$ mm$^3$, triggering delay of 150 ms, $\mathrm{T_R}$ of 12 RR repeats. Tables 6.3 and 6.4 summarise the parameters of the diffusion experiments carried out in sessions 1 and 2.

In each session, a $T_2^*$-weighted gradient echo image (*fast field echo* or FFE) was also acquired for anatomical reference. Salient acquisition parameters were: FOV of $240 \times 180 \times 60$ mm$^3$, $\mathrm{T_R}$ of 20 ms, $\mathrm{T_E}$ of 4.1 ms , resolution of $0.75 \times 0.75 \times 5$ mm$^3$, 4 signal averages.

### Preprocessing

*In vivo* data was preprocessed as described in chapter 4. For each two-shell DW experiment performed with fixed diffusion time, we proceeded as follows.

1. Data were corrected for motion employing slice-wise linear registration, with registration transformations estimated among non-DW images with FSL *flirt* [64, 82, 83].

2. The spinal cord was segmented on the mean $b = 0$ image obtained after motion correction with an active surface method [74], also employed for the studies shown in previous chapters (similar segmentation was performed also on the FFE image).

3. GM was segmented manually after motion correction on an image obtained averaging DW images with good contrast between GM and WM, as firstly shown in [97] and previously discussed in section 4.4.3 of chapter 4.

4. WM voxels were defined as voxels within the eroded spinal cord mask that did not belong to the GM mask.

### Model fitting

NODDI was fitted to the *in vivo* data with the NODDI Matlab toolbox, maximising the likelihood of the data for a Rician noise model. In practice, the opposite of the log-likelihood was minimised in two steps. An initial grid search was used to find a plausible set of NODDI model parameters, which were then used as a starting point for a gradient descent minimisation. In our fitting, the diffusivities $d_{\text{iso}}$ and $d_{\parallel}$ on which the NODDI model depends were fixed as by default to $d_{\text{iso}} = 3.00\ \mu\text{m}^2\,\text{ms}^{-1}$ and $d_{\parallel} = 1.70\ \mu\text{m}^2\,\text{ms}^{-1}$,

Due to the low SNR levels, especially at the highest echo time, *multi-start fitting* was performed to reduce the risk of routines finding suboptimal solutions in local minima of the fitting objective function. The gradient descent was performed 100 times per voxel, perturbing the starting point of the descent from the grid search and returning the best fit out of 100 iterations.

### Analysis

For each subject, each scanning session and each diffusion time, we evaluated the distribution of all NODDI metrics ($v_{\text{iso}}$, $v_{\text{in}}$, $v_{\text{r}} = (1 - v_{\text{iso}})\,v_{\text{in}}$ and ODI) within the GM and WM masks.

For the visualisation of voxel-wise maps, the mean $b = 0$ image from each experiment with fixed diffusion time was registered to an image obtained averaging all the $b = 0$ images after slice-wise realignment. The estimated transformations, accounting for in-plane translations only and calculated with FSL *flirt* slice-by-slice, were also applied to the fitted NODDI metrics.

Originally, it was planned to exploit the anatomical FFE image for the segmentation of WM and GM. Descriptive statistics from the two tissue types could have then been extracted after warping NODDI metrics to the FFE image space, or vice versa.

We planned to estimate the warping transformations between the mean $b = 0$ image of each multi-shell experiment and the anatomical FFE image. A preliminary co-registration pipeline between diffusion and FFE spaces was implemented with a combination of the tools offered by the software packages *NiftyReg* [127,128] and FSL. It consisted of the following steps:

1. straightening of the spinal cord in both FFE and mean $b = 0$ images, obtained moving the centre of mass of the spinal cord mask slice-by-slice to the centre of the image;

2. re-sampling of the FFE to the resolution of the diffusion images;

3. estimation of a 3D affine transformation or a slice-wise affine transformation to warp the mean $b = 0$ image to the FFE, with the transformation obtained considering only voxels within the spinal cord mask dilated of a controlled amount.

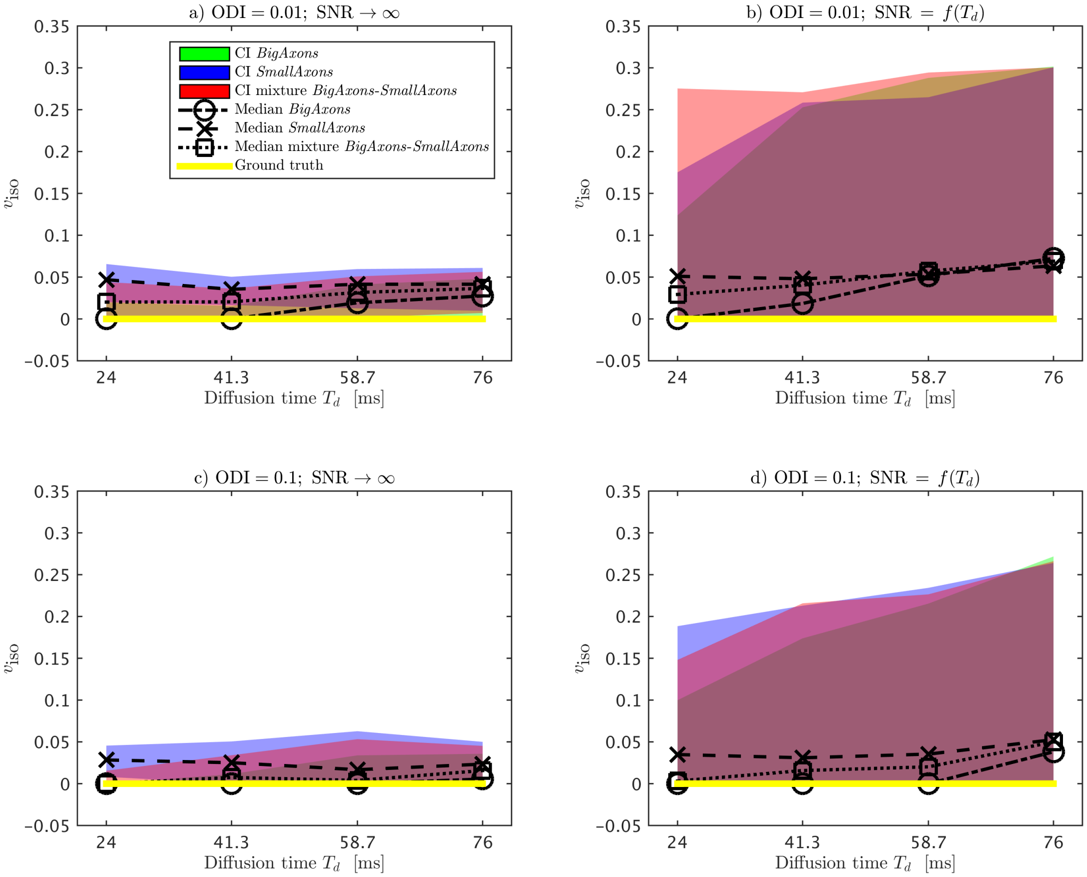

Figure 6.3: NODDI metric $v_{\text{iso}}$ obtained from fitting to synthetic signals. To the left: simulations with SNR $\rightarrow \infty$; to the right: simulations with noise. Medians and 95% confidence intervals are reported for the three simulated substrates and for two levels of orientation dispersion (top: ODI $=$ 0.01; bottom: ODI $=$ 0.1).

Several dilations ranging from 8 to 12 mm were tested, as well as different types of transformations, varying from 3D affine with 12 degrees of freedom to slice-wise with 4 to 6 degrees of freedom. The most promising approach on visual inspection relied on the estimation of a 3D affine transformation using 9 or 10 mm of dilation of the cord masks. Despite working relatively well for some slices, it provided evident fail in others. The amount of variability of the registration pipeline was therefore considered unacceptably high for it to be used.

## 6.4 Results

### 6.4.1 *In silico* study

Figures 6.3, 6.4, 6.5 and 6.6 show NODDI metrics obtained fitting the model to the synthetic data generated by substrates *BigAxons*, *SmallAxons* and a mixture of the two, as the diffusion time varies.

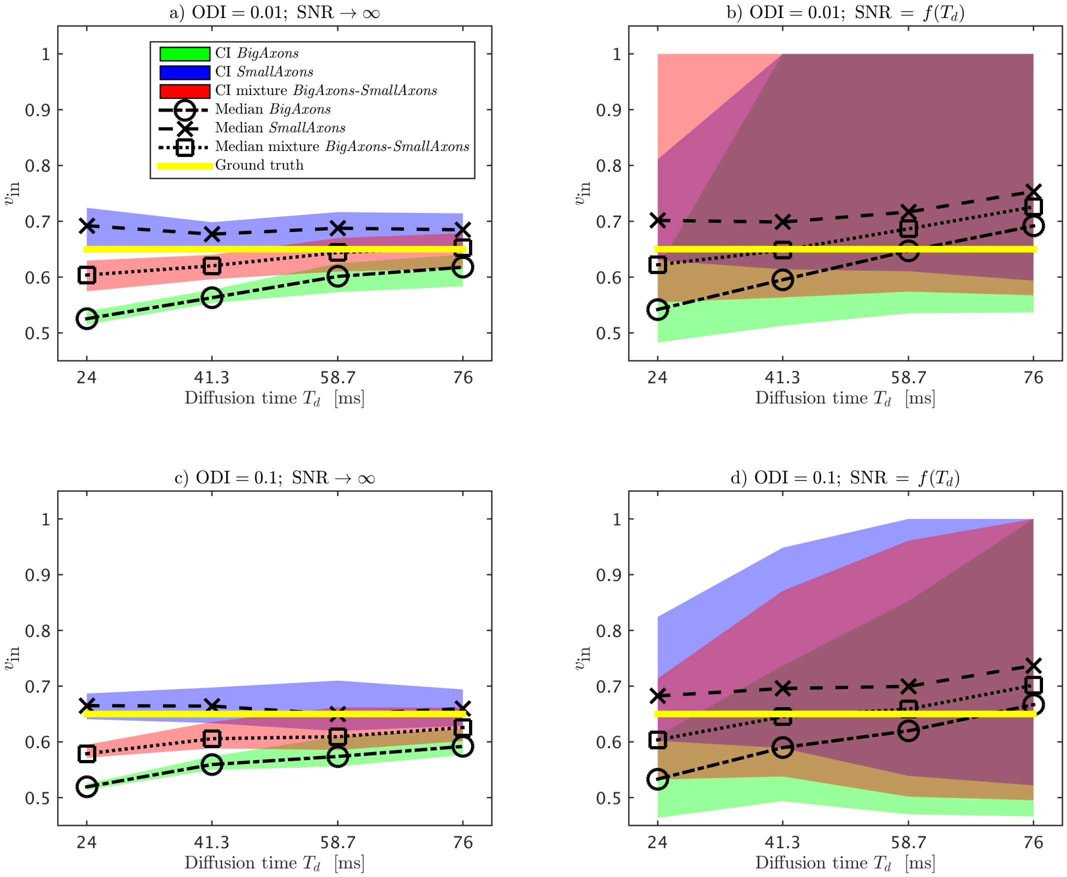

Figure 6.4: NODDI metric $v_{\text{in}}$ obtained from fitting to synthetic signals. The same representation criteria of figure 6.3 apply.

At infinite SNR, low but non-zero $v_{\text{iso}}$ values, smaller than 0.05, are obtained for all substrates with no clear diffusion time dependency.

On the other hand, metric $v_{\text{in}}$ is slightly overestimated with respect to the ground truth for substrate *SmallAxons* and the lowest orientation dispersion level, while it is estimated more accurately for the same substrate but higher orientation dispersion. For substrates *BigAxons* and the mixture *SmallAxons-BigAxons*, the fitted $v_{\text{in}}$ is in general underestimated as compared to the true underlying value. Moreover, $v_{\text{in}}$ exhibits diffusion-time dependency, since it increases as the diffusion time increases.

As far as metric $v_\mathrm{r}$ is concerned, its trend at SNR $\to \infty$ is very similar to that of $v_\mathrm{in}$, although it more accurately reflects ground truth values. For substrates characterised by the presence of big axons, i.e. substrates *BigAxons* and the mixture *SmallAxons-BigAxons*, $v_\mathrm{r}$ shows diffusion time dependency. It is underestimated for low diffusion times, with the underestimation becoming less severe as $T_d$ grows.

ODI shows no clear diffusion time dependency when the ground truth ODI equals 0.01, although the fitting systematically overestimates the true underlying ODI for all diffusion times. On the other hand, when the ground truth ODI is 0.1, the metric is underestimated at short diffusion times for all substrates, with the underestimation being reduced by increasing diffusion time $T_d$.

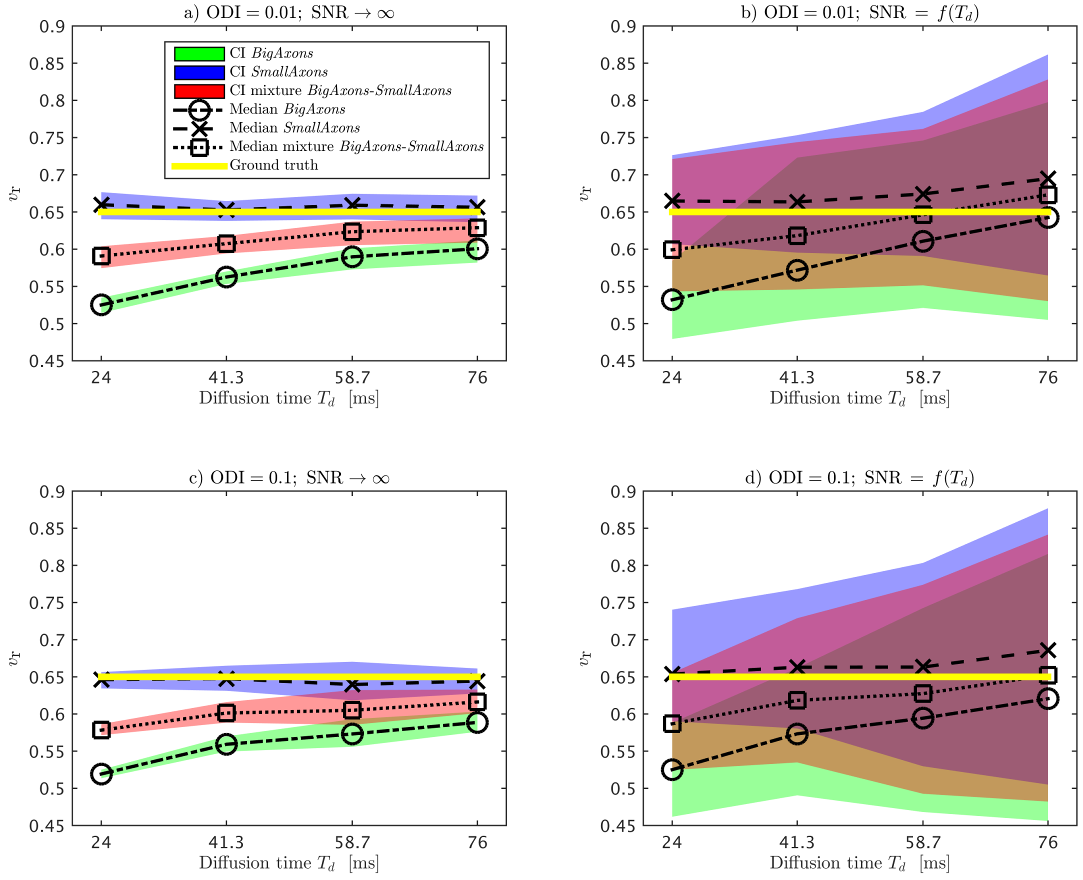

Figure 6.5: NODDI metric $v_\mathrm{r}$ obtained from fitting to synthetic signals. The same representation criteria of figure 6.3 apply.

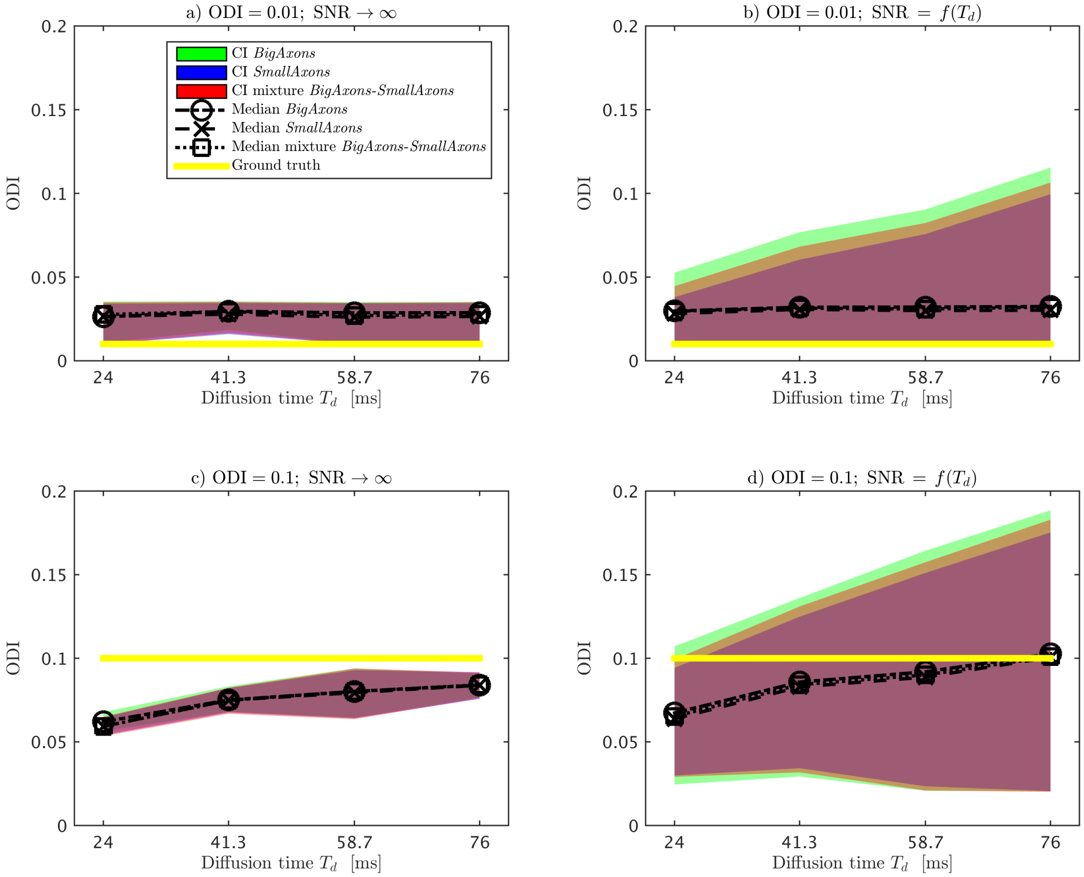

Figure 6.6: NODDI metric ODI obtained from fitting to synthetic signals. The same representation criteria of figure 6.3 apply.

Figures 6.3, 6.4, 6.5 and 6.6 also show estimates of $v_{\text{iso}}$, $v_{\text{in}}$, $v_{\text{r}}$ and ODI when noise is added to the synthetic signals according to equation 6.2.

In general, adding noise affects the precision of NODDI parameter estimation. For instance, $v_{\text{iso}}$ values up to $0.25$ are observed despite no free water compartment was employed to synthesise the signals.

Another effect of adding noise at low SNR levels is the overestimation of volume fractions $v_{\text{r}}$ and especially $v_{\text{in}}$ as compared to fitting performed at the same diffusion time but with no noise. A similar phenomenon is observed to a lower extent also for ODI, especially at the highest orientation dispersion levels.

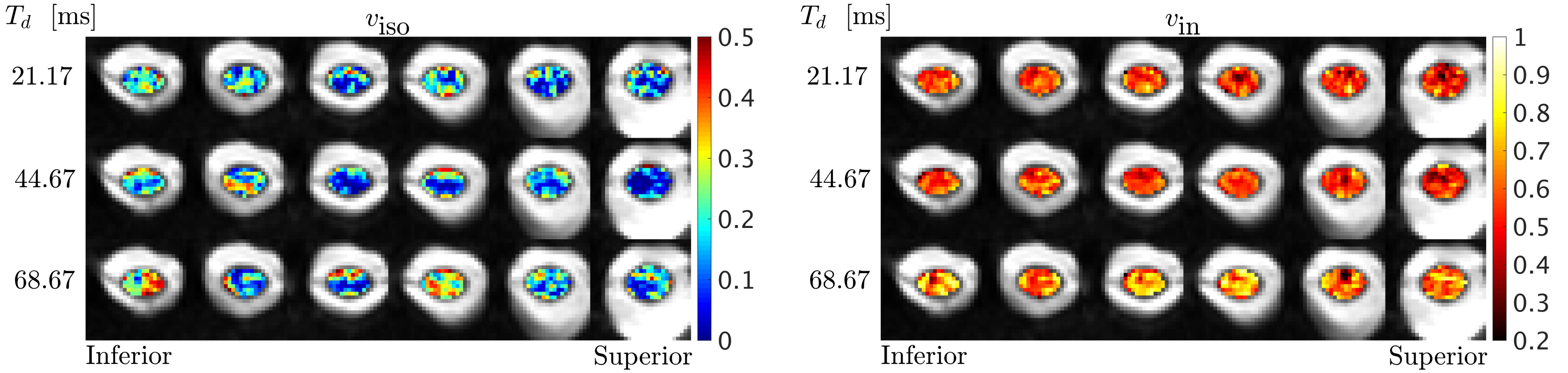
$T_d$ [ms]
$v_{\text{iso}}$
21.17
44.67
68.67
0.5
0.4
0.3
0.2
0.1
0
Inferior
Superior
$T_d$ [ms]
$v_{\text{in}}$
21.17
44.67
68.67
1
0.9
0.8
0.7
0.6
0.5
0.4
0.3
0.2
Inferior
Superior

(a) NODDI metric $v_{\text{iso}}$

(b) NODDI metric $v_{\text{in}}$

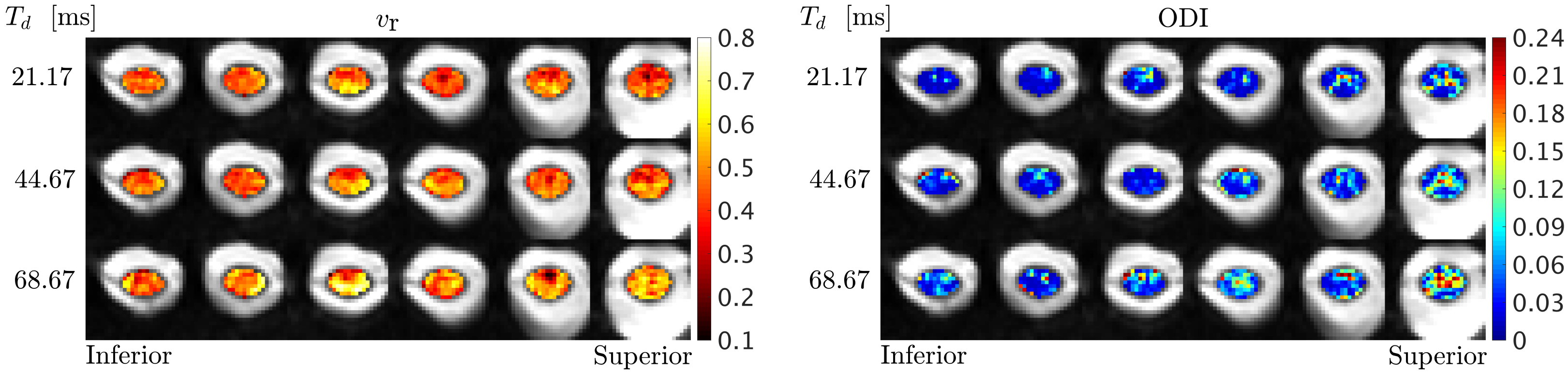
$T_d$ [ms]
$v_{\text{r}}$
21.17
44.67
68.67
0.8
0.7
0.6
0.5
0.4
0.3
0.2
0.1
Inferior
Superior
$T_d$ [ms]
ODI
21.17
44.67
68.67
0.24
0.21
0.18
0.15
0.12
0.09
0.06
0.03
0
Inferior
Superior

(c) NODDI metric $v_{\text{r}}$

(d) NODDI metric ODI

Figure 6.7: examples of NODDI metrics in the 6 most superior slices of subject 3 as the diffusion time $T_d$ varies (first scanning session). Different echo times were employed for different diffusion times, as explained in table 6.3.

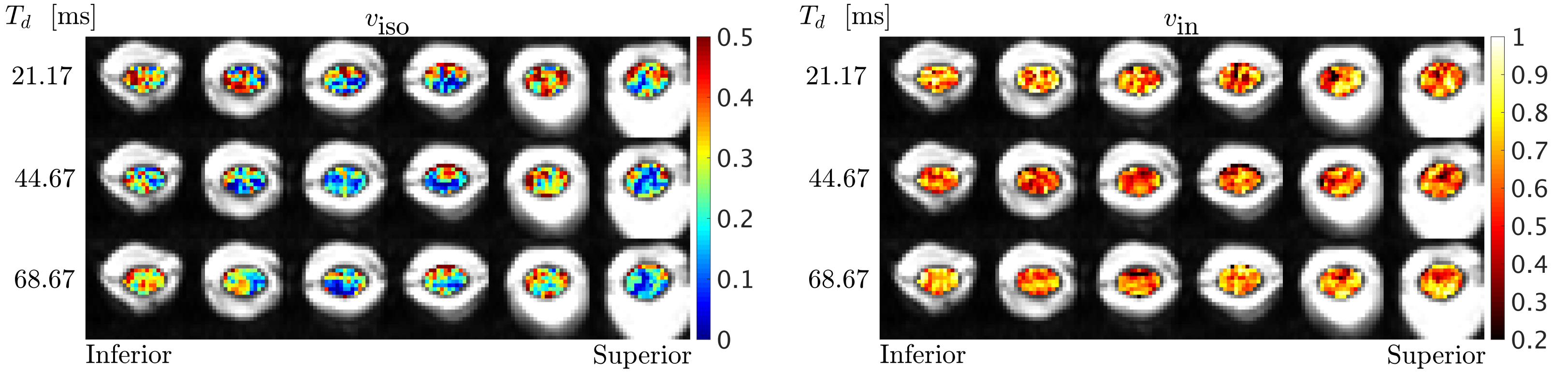
$T_d$ [ms]
$v_{\mathrm{iso}}$
21.17
44.67
68.67
Inferior
Superior
0.5
0.4
0.3
0.2
0.1
0
$T_d$ [ms]
$v_{\mathrm{in}}$
21.17
44.67
68.67
Inferior
Superior
1
0.9
0.8
0.7
0.6
0.5
0.4
0.3
0.2

(a) NODDI metric $v_{\mathrm{iso}}$

(b) NODDI metric $v_{\mathrm{in}}$

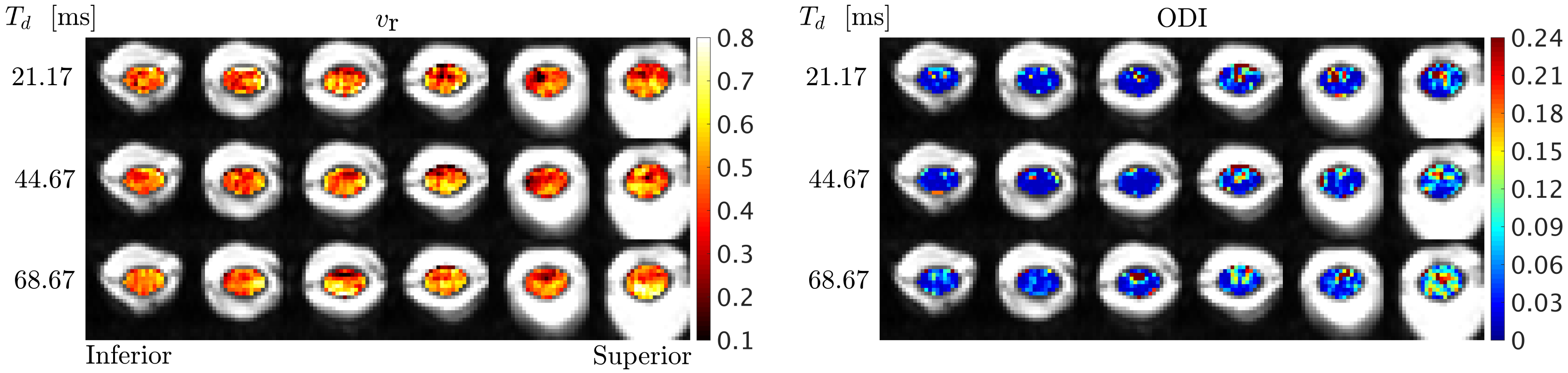
$T_d$ [ms]
$v_{\mathrm{r}}$
21.17
44.67
68.67
Inferior
Superior
0.8
0.7
0.6
0.5
0.4
0.3
0.2
0.1
$T_d$ [ms]
ODI
21.17
44.67
68.67
0.24
0.21
0.18
0.15
0.12
0.09
0.06
0.03
0

(c) NODDI metric $v_{\mathrm{r}}$

(d) NODDI metric ODI

Figure 6.8: examples of NODDI metrics in the 6 most superior slices of subject 3 as the diffusion time $T_d$ varies (second scanning session). The same echo time was employed for different diffusion times, as explained in table 6.4.

### 6.4.2 *In vivo* study

Figures 6.7 and 6.8 report NODDI metrics obtained from the second volunteer in 6 illustrative slices as the diffusion time $T_d$ varies. The trend illustrated is representative of what, to a similar extent, is observed in the other two subjects.

Metrics from the first scanning session (minimum echo time $\mathrm{T_E}$ for each diffusion time, as reported in table 6.3) are shown in figure 6.7.

Qualitative visual inspection reveals that $v_{\mathrm{iso}}$ increases as $T_d$ increases, as apparent in the first and fourth slices from the most inferior to the most superior position. Also, the metric is relatively noisy at all diffusion times. Metrics $v_{\mathrm{in}}$ and $v_{\mathrm{r}}$ increase as $T_d$ increases (see first, third, fourth and sixth slices from the most inferior to the most superior), with the former looking noisier as compared to the latter. Lastly, the figure demonstrates that ODI does not exhibit a clear trend, although in the most superior slice higher ODI is seen as $T_d$ grows from 21.17 to 68.67 ms.

Figure 6.8 shows similar information as 6.7 but with metrics obtained from the second scanning session, i.e. when $\mathrm{T_E} = 111$ ms was employed for all $T_d$ values. All metrics are less smooth then their counterparts from the first session shown in figure 6.7, especially as far as $v_{\mathrm{iso}}$ is concerned. The increase of metrics $v_{\mathrm{in}}$ and $v_{\mathrm{r}}$ is less apparent, although still noticeable in some slices, as for example in the most superior slice.

In figures 6.9 and 6.10, the distributions of NODDI metrics in WM and GM obtained from the first scanning session are illustrated for the three diffusion times. No clear trends can be observed for $v_{\mathrm{iso}}$ and ODI in GM and WM with increasing $T_d$, whereas the distributions of $v_{\mathrm{r}}$ and especially $v_{\mathrm{in}}$ appear shifted to higher values as $T_d$ increases in WM. The shift is less evident in GM, especially for subject 2. Figures 6.11 and 6.12 report similar information as figures 6.9 and 6.10, but for the second scanning session. As compared to the first scanning session, distributions are in general less smooth, especially at shorter diffusion times. Nonetheless, the shift of the distributions of $v_{\mathrm{r}}$ in WM towards higher $v_{\mathrm{r}}$ values as $T_d$ increased is still noticeable.

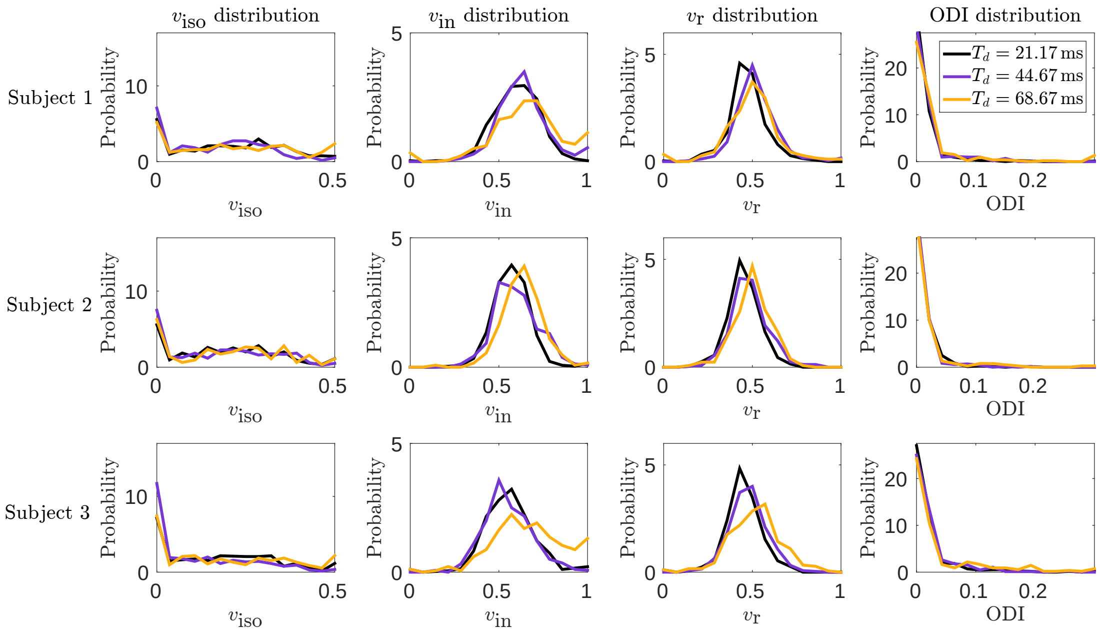

Figure 6.9: distributions of NODDI metrics in WM as the diffusion time varies in the three subject (first scanning session, with variable $\mathrm{T_E}$). From left to right, distributions of $v_{\text{iso}}$, $v_{\text{in}}$, $v_{\text{r}}$ and ODI are illustrated. From top to bottom, information regarding subjects 1 to 3 is illustrated.

## 6.5 Discussion

The objective of this study was to assess whether certain choices of the diffusion time in a PGSE experiment can affect the estimation of neurite density, as well as of the other microstructural parameters provided by NODDI. In particular, we studied in detail the effect of the presence of large axons, characteristic of the spinal cord.

For this purpose, synthetic DW signals were generated with Monte Carlo simulations to represent WM characterised by big and small axons. NODDI was employed to obtain estimates of neurite density (in the two flavours of $v_{\text{in}}$ and $v_{\text{r}}$), as well as of other cytoarchitectural parameters ($v_{\text{iso}}$ and ODI), which were compared to a known ground truth.

Furthermore, three healthy volunteers were scanned in two sessions at 3T following a NODDI-like multi-shell acquisition, acquiring images of the cervical spinal cord. In each session, three different diffusion times were probed, while achieving the same strength of the diffusion weighting. In the first session, we employed the minimum echo time $\mathrm{T_E}$ for each diffusion time, while $\mathrm{T_E}$ was constant in the second session.

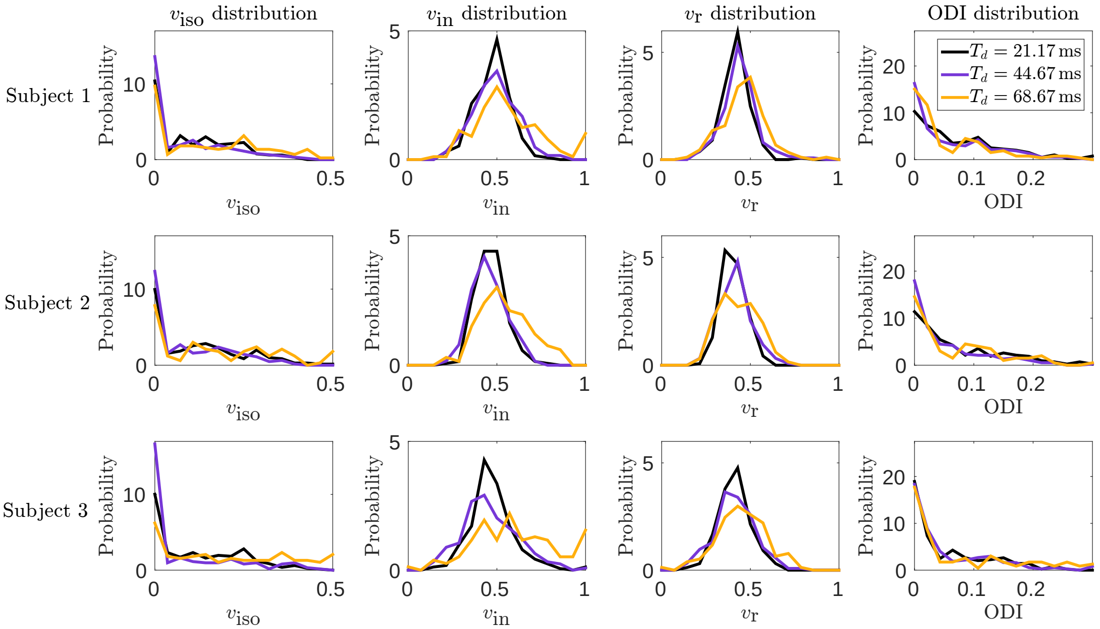

Figure 6.10: distributions of NODDI metrics in GM as the diffusion time varies in the three subject (first scanning session, with variable $\mathrm{T_E}$). Information is displayed following the same conventions of figure 6.9.

*Monte Carlo simulations:* SNR $\rightarrow \infty$

Our simulations demonstrate that short diffusion times minimising the echo time of a PGSE experiment can lead to biased neurite density estimates from NODDI in clinical settings, for microstructural geometries plausible in the spinal cord.

Neurite density is estimated accurately for a substrate with small axons, representative of brain WM areas such as the splenium of the corpus callosum, even for short diffusion times of the order of 20 ms. This is true especially if one considers metric $v_{\mathrm{r}}$ (voxel volume fraction of neurites) as opposed to $v_{\mathrm{in}}$ (neural tissue volume fraction of neurites). For substrates with bigger (but biologically plausible) axons instead, both $v_{\mathrm{r}}$ and $v_{\mathrm{in}}$ increase as the diffusion time increases. The two metrics underestimate the true underlying neurite density, and the underestimation is mitigated if the diffusion time increases, although still present at long diffusion time due to finite cylinder diameter. Therefore, theoretically short diffusion times on the order of 20 ms, although minimising DW PGSE echo time, do not seem to be sufficiently long to support the *stick* model in spinal cord WM.

In our simulations, no free water was used to generate the signals. However, since NODDI includes a free water (isotropic) compartment for the analysis of any voxel, an estimate of free water amount (isotropic volume fraction $v_{\mathrm{iso}}$) was obtained. No clear dependence of the fitted $v_{\mathrm{iso}}$ on axon diameter and diffusion time is observed. However, values of $v_{\mathrm{iso}}$ up to 0.05 can be observed even at infinite SNR. This demonstrates that the accurate quantification of free water contamination is challenging in clinical settings (with a limited number of $b$-values), and suggests that $v_{\mathrm{iso}}$ is prone to numeric instability. A non-zero $v_{\mathrm{iso}}$ seems also to affect other metrics, especially $v_{\mathrm{in}}$, which differs from the ground truth value of 0.65 even for the substrate with small axons.

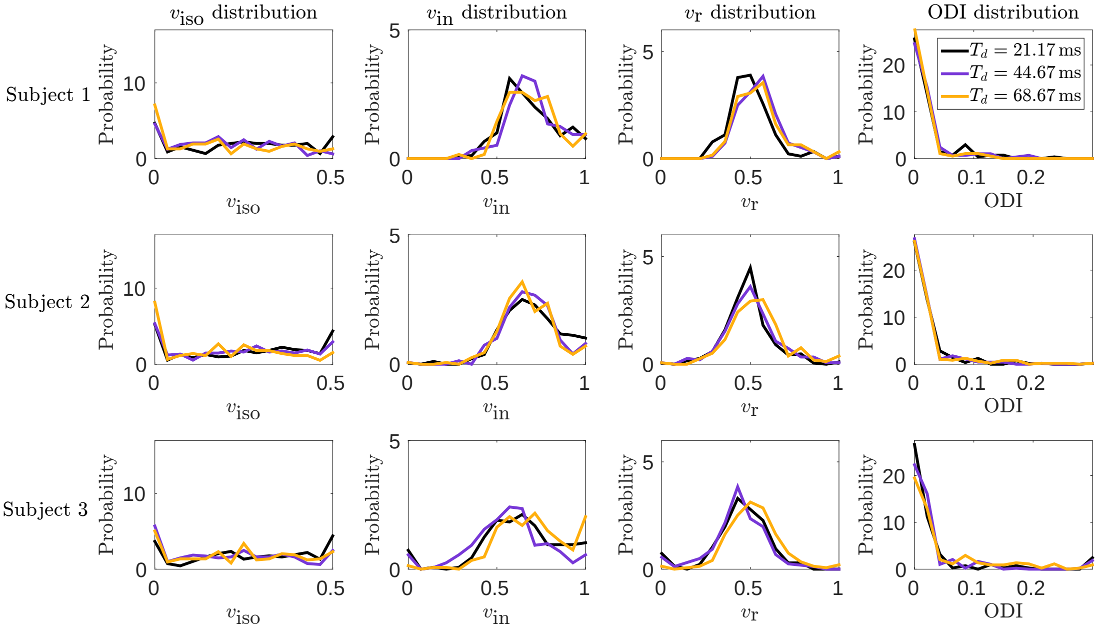

Figure 6.11: distributions of NODDI metrics in WM as the diffusion time varies in the three subject (second scanning session, with $\mathsf{T_E} = 111\,\text{ms}$ fixed for all diffusion times $T_d$). Information is displayed as in figure 6.9.

Our synthetic data simulated the presence of two levels of orientation dispersion, by means average of the signals from seven rotations of the substrates. Orientation dispersion was then quantified by NODDI ODI. For the low orientation dispersion level, no diffusion time dependency of ODI is observed, although ODI systematically overestimates the true, underlying orientation dispersion. This may be an effect of the intrinsic challenge of distinguishing subtle differences in terms of orientation coherence when neurites are almost perfectly parallel to each other. Also, the limited number of rotations employed to simulate dispersion may have contributed making the estimation of ODI challenging. At higher dispersion levels instead, for all substrates ODI increases as the diffusion time increases. We speculate that this may result from contribution of the extra-neurite space, which for the shortest and intermediate diffusion times may not have still reached the long diffusion time limit, where the tortuosity model, [215] employed by NODDI, holds.

*Monte Carlo simulations: noisy data*

Rician noise was added to the synthetic signals to levels plausible in the spinal cord *in vivo*, adjusting the SNR to account for the longer echo times (i.e. more intense $T_2$ decay) necessary to achieve longer diffusion times.

In general, the presence of noise causes variability of the parameter estimates, as demonstrated by confidence intervals becoming wider as the SNR becomes higher. $v_{\text{iso}}$ is the NODDI metric that is the most sensitive to the presence of noise. It exhibits notable numerical instability, up to the point that values up to 0.25 could be fitted even without any true presence of free water. Hence, our simulations demonstrate that it does not seem to be feasible to use $v_{\text{iso}}$ to detect subtle increases of free water in pathological processes such as oedema of neuro-inflammation in the spinal cord. Such processes could only be fully distinguished from noise-induced $v_{\text{iso}}$ fluctuations if they cause increases of free water on the order of 20 %. Therefore, $v_{\text{iso}}$ should always be interpreted with care, bearing in mind that values on the order of 0.2 can be due to excessively high noise levels.

At the lowest SNR level of 6.38 (corresponding to $T_d$ of 76 ms), $v_{\text{iso}}$ and especially $v_{\text{in}}$ are overestimated heavily as compared to values obtained at SNR $\rightarrow \infty$. This also affects $v_{\text{r}}$, which increases with increasing diffusion time even for the substrate with small axons. Such a behaviour is not observed at SNR $\rightarrow \infty$, and may be due to the higher noise-floor, known to bias diffusion MRI metrics [49]. A slight overestimation as compared to values at SNR $\rightarrow \infty$ is also observed for ODI.

In vivo *data*

Three healthy volunteers were scanned on a 3T MRI system following three two-shell diffusion encoding protocols. The protocols, identical in terms of $b$-values, differed in terms of diffusion time. Three diffusion times were probed in two MRI sessions. In the first one, the minimum echo time was employed for each diffusion time, while in the second, the same echo time was always used, to control for differences in terms of $T_2$-weighting and SNR as the echo time varies. For all subjects, sessions and diffusion times, distributions of NODDI metrics were obtained in GM and WM.

In the first scanning session, NODDI indices of neurite density ($v_{\text{in}}$ and $v_{\text{r}}$) show a trend of increase in the WM of all subjects as the diffusion time $T_d$ increases, agreeing well with results from simulations. The increase is less apparent in GM distributions, although noticeable. These observations suggest that at the shortest diffusion time we probed, the assumptions of the *stick* model were not fully met in areas with large axons. Higher accuracy may have been achieved at longer diffusion times, causing the estimates of neurite density to increase in WM, and, to a less extent, within the GM mask. In practice, it is likely that the increase in GM, which is unexpected due to the small size of dendrites as compared to axons, may be due to residual partial volume GM/WM, given the coarse resolution of our diffusion images.

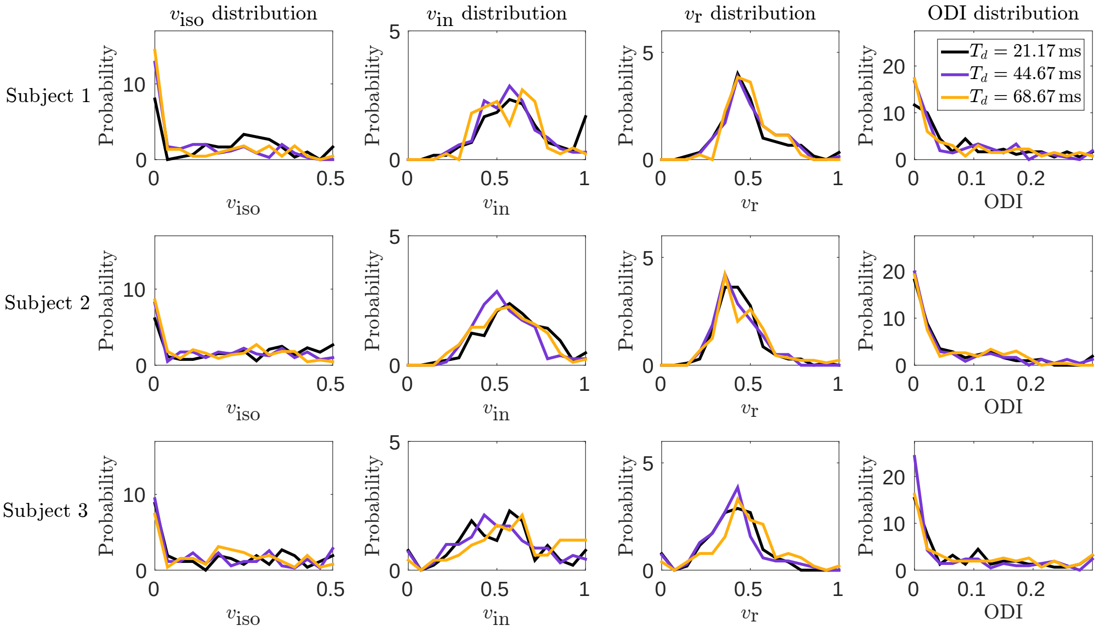

Figure 6.12: distributions of NODDI metrics in GM as the diffusion time varies in the three subject (second scanning session, with $\mathrm{T_E} = 111\,\mathrm{ms}$ fixed for all diffusion times $T_d$). Information is displayed following the conventions of figure 6.9.

Differences in terms of $T_2$-weighting and especially SNR may have contributed to the patterns of increasing $v_{\mathrm{in}}$ and $v_{\mathrm{r}}$, similarly to what is reported in the analogous situation in simulations (increase of neurite density for substrate *SmallAxons* on noisy data as $T_d$ increases, which is not seen at SNR $\to \infty$). Moreover, increasing noise levels in the first scanning session are associated to an increase of isotropic volume fraction $v_{\mathrm{iso}}$, highlighting the susceptibility of $v_{\mathrm{iso}}$ to noise. Finally, no clear trend could be noticed for ODI in our small cohort.

In the second scanning session, the same diffusion times as the first session were probed, and the same subjects were scanned. However, the echo time was constantly kept to 111 ms, to achieve the same $T_2$-weighting and the same noise level at all diffusion times. Results are in line with findings obtained from the first session, although the increase in neurite density, still noticeable, is less apparent. This points towards the fact that the increase of $v_{\mathrm{in}}$ and $v_{\mathrm{r}}$ for increasing $T_d$, evident on simple visual inspection in the first session, is partly due differences in $T_2$-weighting and noise level.

### *Limitations*

The work presented in this chapter has two main limitations.

The first one is related to the modalities followed to simulate orientation dispersion in the synthetic data. Orientation dispersion was achieved averaging the signals coming from the substrates after seven independent rotations of their orientations. Although this can effectively simulate the effect of orientation dispersion on the intra-cylinder (intra-neurite) signal, it gives rises to imperfect tortuosities of the extra-cylinder (extra-cellular) space. Nonetheless, this did not seem to impact the estimation of neurite density, since very similar trends were exhibited by metrics $v_{\text{in}}$ and $v_{\text{r}}$ for both simulated orientation dispersion levels.

The second is related to the small size of our cohort recruited for the *in vivo* part of the investigation. Although its size was sufficient to capture trends confirming results from simulations, a higher number of subjects would allow a better characterisation of the between-subject variability induced by the employment of short diffusion time.

## 6.6 Conclusion

In this work, we investigated whether certain choices of the diffusion time, in presence of large axons characteristic of the spinal cord, can affect neurite density indices from NODDI, as well as other microstructural indices.

Monte Carlo simulations of the diffusion process demonstrated that neurite density, and to a minor extent neurite orientation dispersion, can be underestimated in microstructural geometries plausible in the spinal cord if short diffusion times are employed. Longer diffusion times reduce the underestimation, which is still seen at $T_d = 76$ ms due to finite cylinder diameter.

*In vivo* data showed a trend of increasing neurite density as the diffusion time increased, also when controlling for the effects of varying $\text{T}_\text{E}$. This fact could be explained by the fact that at shortest diffusion time we probed, the assumptions of the *stick* model were not fully met in areas with large axons.

We conclude that long diffusion times can improve the accuracy of neurite density estimation from NODDI in the spinal cord, as well as of other microstructural indices characteristic of neurite morphology. Nevertheless, longer diffusion time imply longer echo times, which ultimately reduce the precision of the estimation due to lower SNR. Therefore, a trade-off between accuracy and precision has to be evaluated for each specific application.

STEAM acquisitions may help achieve better signal-to-noise levels than spin echo experiments for very long diffusion times. The feasibility of performing DW ZOOM-STEAM EPI will be evaluated, and the potential confounding effect of exchange will also be accounted for. This may be necessary should diffusion times exceed 100 ms, as suggested by recent work of other groups [133].

# *Ex vivo* diffusion MRI of the human spinal cord

## Background and motivations

In the first part of this thesis, *in vivo* data were studied. Results demonstrated that NODDI, a novel model-based DW MRI method, can be applied in the spinal cord *in vivo*, enabling the quantification of neuronal morphology in clinical scenarios.

The new metrics provided by NODDI are designed to be specific to characteristics of neuronal tissue microstructure such as density and orientation dispersion of axons and dendrites. However, NODDI relies on some assumptions that aim to capture the complexity of the microstructure underlying the DW signal in such a way that it can be handled in practice. The implications of these assumptions need to be assessed via comparison to ground truth histological indices, quantifying the actual features of the tissue that NODDI aims to measure. In this way, the specificity of NODDI metrics could be ultimately validated. This is of great importance in presence of pathology, which alters the structure of the normal, healthy neuronal tissue upon which NODDI hypotheses rely.

In this second *ex vivo* part of the PhD thesis, our objective is to confirm the specificity and the validity of NODDI metrics in the non-pathological and MS spinal cord via comparison to histology.

## Experiments

Three experimental chapters are included in this second part of the thesis. The experiments were made possible by the collaboration between UCL (Institute of Neurology, Departments of Neuroinflammation, Brain Repair and Rehabilitation and NeuroResource; Department of Computer Science and Centre for Medical Image Computing) and the University of Oxford (Nuffield Department of Clinical Neurosciences).

In chapter 7, the work carried out to design a multi-shell DW experiment at high field is presented. Moreover, the chapter also illustrates the strategy that was designed to adapt NODDI analysis from *in vivo* to *ex vivo* data, as well as the approach followed to determine the radiographic position of histological material derived from the scanned samples.

In chapter 8, digital images from histological sections of fixed human spinal cord were analysed. The objective of the analysis was to derive a histological counterpart of NODDI ODI, which quantifies the variability of neurite orientations in each voxel.

Lastly, in chapter 9, the systematic comparison between NODDI metrics and histological features derived from four spinal cord specimens (two healthy, two MS) is described. This piece of work relies on the technical achievements reported in chapters 7 and 8.

Tissue specimens were provided by the UCL NeuroResource tissue bank and by the Oxford brain bank. MRI was performed in London, at UCL, whilst histological procedures were carried out at the University of Oxford.

# Conclusions

In the second part of this thesis, technical work was carried out to implement the histological validation of NODDI metrics in the healthy and MS spinal cord. A procedure for the acquisition and the analysis of high-field DW images of *ex vivo* human spinal cord tissue was designed, as well as a strategy to find the radiographic position of histological material derived from the same tissue. Moreover, a procedure based on ST calculation was designed and optimised in order to estimate neurite orientation dispersion from histological images, i.e. a ground truth measure for NODDI ODI. These technical achievements enabled the comparison of NODDI metrics to quantitative histological features in four *ex vivo* spinal cord samples. This last piece of analysis proves that NODDI is more specific to histology than conventional DTI. NODDI ODI is specific to the underlying orientation dispersion of neuronal fibres in both healthy and MS tissue, and could be a useful biomarker of microstructural complexity. Furthermore, NODDI-derived neurite density estimates capture spatial variations of the density of axons and dendrites, but are also influenced by other factors, such as myelin density. Finally, the investigation did not allow the identification of clear associations between NODDI isotropic (free water) volume fraction and histological features, although this metric is able to demonstrate areas of focal damage.

# Chapter 7

# A pipeline for the histological validation of NODDI in the spinal cord

## 7.1 Introduction

DW MRI methods such as NODDI have the potential of probing tissue microstructure in a non-invasive fashion, thus providing novel, quantitative indices that could be highly specific biomarkers in a number of neurological conditions. Nevertheless, these innovative DW methods rely on a number of assumptions. Histological validation is therefore of the highest importance, since the validity of these assumptions and the claimed specificity of the novel indices need to be confirmed.

In previous chapters we have shown that NODDI indices may become valuable biomarkers in spinal cord applications. In this chapter, we describe our technical effort to implement a pipeline for the histological validation of NODDI indices in the non-pathological and MS spinal cord. The pipeline has been used to investigate the histological correlates of NODDI metrics, in order to confirm their specificity.

We studied fixed specimens of human spinal cord tissue (controls and MS) with the objective of implementing a reliable MRI-histology pipeline. The pipeline consists of a DW MRI protocol at 9.4T, of a procedure for NODDI analysis of *ex vivo* data and of a strategy to determine the radiographic position of histological material in the acquired MRI images.

In particular, as far as the MRI acquisition is concerned, we explored a number of protocols characterised by different image resolution, repetition time $T_R$ and number of diffusion encoding directions. Also, we studied how to adapt the model fitting as proposed for NODDI analysis of *in vivo* data for the analysis of the acquired *ex vivo* DW images.

## 7.2 Research dissemination

The main result of this chapter is the implementation of a procedure based on high-field DW MRI for the comparison of NODDI metrics to quantitative histology in *post mortem* human spinal cord tissue. The technical achievements of this chapter are the fundamentals upon which the comparison shown in chapter 9 relies. Results from chapter 9 have been disseminated in preliminary form as explained in section 9.2 of that chapter.

## 7.3 Methods

Six *post mortem* specimens of formalin-fixed non-MS and MS spinal cord from five different human subjects were employed. Our objectives were:

- to set up a rich, high-resolution DW MRI protocol at 9.4T;
- to adapt NODDI analysis as proposed for *in vivo* data for the analysis of the acquired *ex vivo* DW images;
- to design a strategy to determine the radiographic position of histological material derived from the imaged samples.

The tissue was provided by the Oxford brain bank and by the UCL NeuroResource tissue bank, following approval by a local research ethics committee and appropriate consent as per Human Tissue Authority guidelines. All experimental procedures were in compliance with the UK Parliament *Human Tissue Act*.

### 7.3.1 Samples and MRI sessions

Samples, stored in 10% formalin, were washed for 24 hours in 10 mM phosphate buffered saline (PBS) solution before undergoing MRI. PBS was replaced with freshly prepared solution every 12 hours. MRI was performed with the samples immersed in PBS, which was eventually replaced by formalin at the end of the MRI session. MRI scans were performed with the 9.4T Agilent MRI system in the basement of Queen Square House, Queen Square, Department of Brain Repair and Rehabilitation, UCL Institute of Neurology. The agreed duration of the MRI sessions between the UCL Department of Neuroinflammation and of Brain Repair and Rehabilitation was of an overnight.

The six specimens from the five subjects were scanned in five MRI sessions. A 9.4T horizontal bore scanner (Agilent Technologies, Santa Clara, CA, USA) equipped with a 60 mm inner diameter gradient coil (maximum gradient amplitude of 1 $\mathrm{T\,m^{-1}}$ and maximum slew rate of 6.7 $\mathrm{KT\,m^{-1}\,s^{-1}}$). A 33 mm diameter volume coil (Rapid Biomedical GmbH, Rimpar, Germany) was instead used for MRI signal reception.

| Subject | Sex | Specimen no. | Age at decease [years] | Cause of decease | Decease-to-fixation [hours] | MRI session(s) | Cord level | Length [cm] |
|---|---|---|---|---|---|---|---|---|
| 1, control | F | 1 | 68 | Colo-rectal metastatic tumour | 23 | 1,2,3 | Thoracic | 4.0 |
| 2, MS | F | 2 | 67 | Pneumonia, secondary to MS | 23 | 1,2,3 | Upper lumbar | 2.1 |
| | | 3 | | | | 4 | Upper lumbar | 2.4 |
| 3, control | M | 4 | 66 | Cardiac arrest | $< 48$ | 4 | Upper thoracic | 3.1 |
| 4, MS | M | 5 | 75 | Asphyxiation, secondary to MS | $< 48$ | 5 | Upper thoracic | 3.3 |
| 5, control | F | 6 | 67 | Infective exacerbation of severe end-stage COPD | $< 48$ | 5 | Upper lumbar | 2.1 |

Table 7.1: information regarding the six specimens of fixed spinal cord tissues that were used to implement a procedure for the histological validation of NODDI metrics. COPD stands for *chronic obstructive pulmonary disease*.

The first three MRI sessions were initial attempts, whilst sessions four and five led to the acquisition of useful DW MRI data that were employed for the direct comparison of NODDI metrics to histology, shown in chapter 9. During each MRI session, temperature was measured and kept stable at 35° C using a temperature probe and an MR compatible air heater connected to a small animal monitoring system (Small Animals Instruments, Inc., Stony Brook, NY, USA).

Table 7.1 provides information about the tissue specimens.

### Diffusion encoding

Table 7.2 summarises the characteristics of the DW MRI protocols. All protocols were characterised by the acquisition of six DW shells ($b = \{520, 2080, 4680, 8320, 13000, 18720\}\,\mathrm{s\,mm^{-2}}$, $\delta$, $\Delta$ and $\mathrm{T_E}$ fixed to $\delta = 12\,\mathrm{ms}$, $\Delta = 18\,\mathrm{ms}$ and $\mathrm{T_E} = 39.5\,\mathrm{ms}$ for all shells). In MRI sessions 1, 2 and 3, 56 non-collinear gradient directions were acquired for each shell. In MRI sessions 4 and 5, instead, a fewer directions were acquired, with increasing angular resolution as $b$ increased (respectively $\{6, 15, 24, 33, 42, 51\}$ directions for $b = \{520, 2080, 4680, 8320, 13000, 18720\}\,\mathrm{s\,mm^{-2}}$). In all protocols, 25 $b = 0$ images were also acquired, interleaved with DW measurements. MRI slices were not taken axially, but coronally (initially) and sagittally (final protocol). This choice was made since we did not plan to obtain histological sections axially. Axial sectioning is best suited for quantifying axonal density or axon diameter, but it does not allow the visualisation of the directions along which neuronal fibres run, preventing the calculation of any histology-derived index of neurite orientation dispersion, sought in this project.

For our diffusion acquisitions, a conventional DW PGSE sequence with single k-space line readout per $\mathrm{T_R}$ was employed. In sessions 1 and 2, the different shells were acquired one after the other, with $b$-value increasing over time. In sessions 3, 4 and 5 instead, the shells were acquired in a randomized order to get a better performance out of the gradients system by reducing the duty cycle and avoiding its overheating.

Moreover, in the first three MRI sessions, a relatively short $\mathrm{T_R}$ (1300 ms) was adopted to keep the acquisition time of each individual DW image short. In sessions 4 and 5 instead, a slightly longer $\mathrm{T_R}$ (2200 ms) was chosen. Although this implied a reduction of the total number of DW images that could be acquired in the allocated scanning slot, it improved the quality of each individual DW measurement. This comes from the fact that a longer $\mathrm{T_R}$ increases the amount of longitudinal magnetisation available for diffusion encoding, practically increasing the intrinsic SNR of each individual DW measurement.

SNR was estimated from the $b = 0$ images in each session as voxel-wise ratio between the mean and the standard deviation of the signal over the 25 repetitions of the $b = 0$ acquisitions, for qualitative comparison among diffusion protocols.

### Axial views

In all sessions, structural images were also acquired using a multi-slice spin echo sequence. The structural scan consisted of 24 axial slices, characterised by the following salient acquisition param-

| Session | $T_R$ [ms] | $T_E$ [ms] | Resolution [$\mu$m × $\mu$m × $\mu$m] | FOV [mm × mm × mm] | Slices | No. of DW images |
|---|---|---|---|---|---|---|
| 1 | 1300 | 39.5 | 200×200×800 | 24×51.2×21.6 | Coronal | 336 |
| 2 | 1300 | 39.5 | 200×200×800 | 24×51.2×21.6 | Coronal | 336 |
| 3 | 1300 | 39.5 | 150×200×500 | 19.2×51.2×10 | Coronal | 336 |
| 4 | 2200 | 39.5 | 164×200×800 | 21×51.2×16 | Sagittal | 171 |
| 5 | 2200 | 39.5 | 164×200×800 | 21×51.2×16 | Sagittal | 171 |

Table 7.2: details of the DW protocols implemented in the five MRI sessions. In each session, $\delta$ and $\Delta$ were fixed to $\delta = 12$ ms and $\Delta = 18$ ms. The diffusion encoding consisted of 6-DW shells ($b = \{520, 2080, 4680, 8320, 13000, 18720\}\,\mathrm{s\,mm^{-2}}$), with increasing angular resolution. 25 $b = 0$ images were also acquired in all MRI sessions.

eters: FOV of 25.68 × 25.68 $\mathrm{mm^2}$, slice thickness of 2 mm, matrix size of 256 × 128, $T_E = 20$ ms, $T_R = 614$ ms.

#### Effectiveness of fixative washing

Quantitative $T_2$ mapping was performed in one session (session 5) to check the effect of our 24 hours fixative wash out. $T_2$ of neural tissue is known to increase dramatically when aldehyde-fixed specimens are washed and scanned in PBS, up to the point that $T_2$, reduced by the fixation process, returns to levels comparable to values obtained from *post mortem* unfixed tissue [161]. Therefore, one would expect $T_2$ to change during a long MRI experiment involving formalin-fixed specimens immersed in PBS, if the samples were not washed from the fixative adequately. This would be caused by diffusion effects that would lead to further dilution of the fixative with the PBS, effectively reducing the concentration of the fixative within the tissue specimens.

$T_2$ maps were obtained from three multi-echo spin echo scans, performed before the start, in the middle and at the end of the diffusion experiment. The same image resolution, FOV and $T_R$ of the DW MRI data were employed. Four echoes were sampled following the 90°-excitation (sampling times $t_s = \{13, 26, 39, 52\}$ ms), and $T_2$ was fitted to the acquired data voxel-by-voxel maximising their likelihood for a Rician noise model and mono-exponential $T_2$ decay.

### 7.3.2 Adaptation of NODDI analysis for *ex vivo* DW data

We investigated how to perform NODDI analysis of our *ex vivo* data. NODDI is a model developed for *in vivo* applications, and it may require certain adjustments for *ex vivo* studies.

For instance, a fourth tissue compartment may be required to model stationary water. Previous studies have demonstrated that it is often necessary to account for non-diffusing water to analyse DW data obtained from fixed tissue [4, 146, 170]. Although the exact origin of this non-diffusing component is unclear, it has been suggested that it could correspond to water trapped within glial cells, which lose any active function after decease [4].

In this chapter, we studied whether a compartment of stationary water (the "*dot*" compartment of isotropic restriction, as proposed in [147]) is necessary to describe the DW signal measured from our samples and to improve the quality of DW MRI model fit. We also sought an optimal value of the intrinsic diffusivity of the neural tissue (parameter $d_{\|}$), which is usually not fitted in NODDI. The value employed *in vivo*, $d_{\|} = 1.70\ \mu\text{m}^2\,\text{ms}^{-1}$, may not be best suited to model our data, and here we studied the impact of changing the value of $d_{\|}$ from that value in terms of quality of fit.

The analysis was performed on the data acquired with the final diffusion encoding protocol, i.e. using data from MRI sessions 4 and 5. We studied one MRI slice of specimens 3, 4, 5 and 6 (see table 7.1), considering different tissue types: WM and GM for the control cases; non-focal WM and GM and WM focal lesion (WMFL) for the MS cases.

### Model fitting

NODDI was fitted to the whole six-shell data set with and without the *dot* compartment of isotropic restriction (respectively called NODDI-Dot and NODDI models). The NODDI model without *dot* compartment has been previously introduced in equation 4.1. When such a compartment is accounted for, the model becomes

$$s_{\text{with-dot}} \;=\; v_{\text{dot}}\, s_0 \,+\, (1 - v_{\text{dot}})\, s_{\text{without-dot}}, \tag{7.1}$$

having indicated with $s_0$ the non-DW signal, with $v_{\text{dot}}$ the volume fraction of the *dot*, with $s_{\text{without-dot}}$ the signal when no *dot* compartment is included (i.e. the expression to the right side of equation 4.1) and with $s_{\text{with-dot}}$ the signal when the *dot* is accounted for. Notably, since the *dot* describes the contribution of a stationary (non-diffusing) water pool, its signal component is not attenuated by diffusion weighting and is constant for any applied diffusion encoding gradient [147]. The introduction of the *dot* allows the explanation of residual signal well above the noise floor measured even for very intense $b$-values and for gradients parallel to WM fibres.

Both NODDI and NODDI-Dot models were fitted voxel-by-voxel with the NODDI Matlab toolbox, maximising the likelihood of the measurements given a Rician noise model. The diffusivity of the isotropic compartment $d_{\text{iso}}$ was fixed to the ADC of the PBS, since the isotropic compartment is designed to capture partial volume with surrounding liquid (ADC was estimated using the $b = 520\,\text{s}\,\text{mm}^{-2}$ shell with Camino [38], command *adcfit*). On the other hand, the intrinsic diffusivity of the neural tissue $d_{\|}$ was varied. Both NODDI and NODDI-Dot models were fitted fixing $d_{\|}$ to each of the following 12 evenly-spaced values: $\{0.10, 0.38, 0.66, 0.95, 1.23, 1.51, 1.79, 2.07, 2.35, 2.63, 2.92, 3.20\}\ \mu\text{m}^2\,\text{ms}^{-1}$.

For comparison, the DTI model was also fitted in the same voxels, with and without the *dot* compartment (models DTI and DTI-Dot). In-house Matlab code implementing the same algorithm employed to fit NODDI in the NODDI Matlab toolbox was used. In practice, the DTI-Dot model was written using a notation equivalent to the one used in equation 7.1, but plugging into the signal $s_{\text{with-dot}}$ the DTI model as expressed to the right side of equation 3.39.

All models were fitted after correcting diffusion weighting gradients to account for extra diffusion-sensitisation due to imaging/spoiling gradients fully refocused at the occurrence of the spin echo.

$b$-value and gradient direction were respectively approximated as the sequence $b$-matrix [119, 120] principal eigenvalue and eigenvector. The $b$-matrix was calculated via numeric integration of the gradient waveforms as

$$\mathbf{b} \;=\; \gamma^2 \int_0^{\mathsf{T_E}} \Big(\mathbf{F}(t) \;-\; 2\xi(t)\,\mathbf{f}\Big)\Big(\mathbf{F}(t) \;-\; 2\xi(t)\,\mathbf{f}\Big)^{\mathsf{T}} dt, \tag{7.2}$$

where $\xi(t) = 0$ for $0 \leq t < \frac{1}{2}\mathsf{T_E}$, $\xi(t) = 1$ for $\frac{1}{2}\mathsf{T_E} \leq t \leq \mathsf{T_E}$, $\mathbf{f} = \mathbf{F}(\frac{1}{2}\mathsf{T_E})$ with $\mathbf{F}(t) = \int_0^t \mathbf{G}(t')dt'$ being the primitive of the gradient vector $\mathbf{G}(t) = \Big[G_x(t) \quad G_y(t) \quad G_z(t)\Big]^{\mathsf{T}}$. $\mathbf{G}(t)$ was obtained as $\mathbf{G}(t) = \sum_i \mathbf{G}_i(t)$, including in the sum all the gradient waveforms (diffusion, imaging and spoiling) played out by the scanner such that

$$\int_0^{\frac{1}{2}\mathsf{T_E}} \mathbf{G}_i(t)\,dt \;=\; \int_{\frac{1}{2}\mathsf{T_E}}^{\mathsf{T_E}} \mathbf{G}_i(t)\,dt.$$

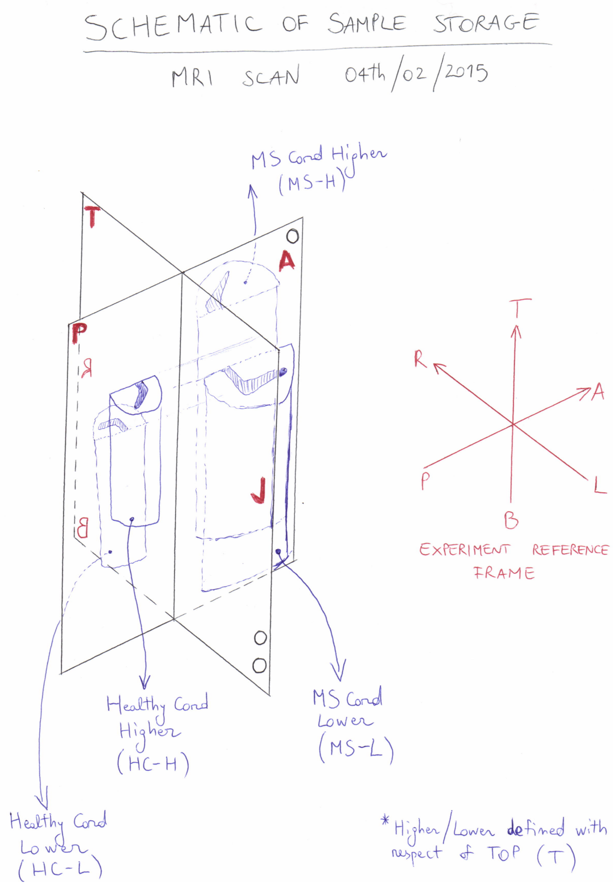
SCHEMATIC OF SAMPLE STORAGE
MRI SCAN 04th/02/2015
MS Cord Higher (MS-H)
T
A
P
R
B
J
Healthy Cord Higher (HC-H)
MS Cord Lower (MS-L)
Healthy Cord Lower (HC-L)
* Higher/Lower defined with respect of TOP (T)
T
R
A
P
L
B
EXPERIMENT REFERENCE FRAME

Figure 7.1: example of sketch drawn to plan histology after MRI session 5. The sketch shows the experiment reference frame that was designed to facilitate the identification of the radiographic position of histological material.

**Quality of fit**

In order to compare the two versions of the DTI and NODDI models with and without *dot* compartment, voxel-wise BIC [158] was calculated from the values of the maximised log-likelihood, similarly to what was shown in chapter 4, section 4.4.5. The BIC quantifies the quality of fit, while penalising model complexity in terms of number of free model parameters. Lower BIC values imply better fit.

ROI-wise median and 95% confidence intervals of the distribution of BIC values were calculated for all fitted DW MRI signal models. ROIs were drawn manually in WM and GM for the two controls and in WM, GM and WMFL for the two MS cases.

### 7.3.3 Strategy to determine the radiographic position of histological sections

Several attempts were made in order to identify the radiographic position of the histological material derived after MRI. The final strategy, described below, was followed in MRI sessions 4 and 5.

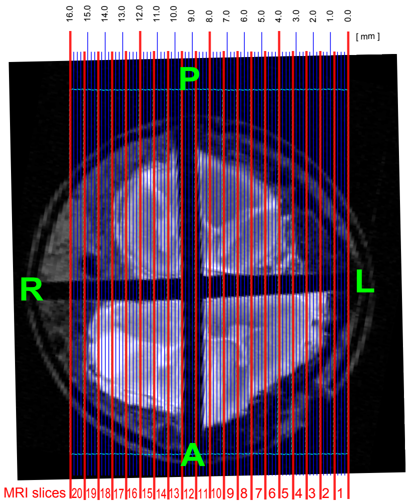

Figure 7.2: example of ruler and DW sagittal slices drawn onto the axial view of specimens 5 and 6 from MRI session 5. The image was employed to write a standard-operating-procedure document relative to that MRI session. It enabled the evaluation of the amount of histological material that had to be sliced from the surface exposed by the midsagittal cut to sample areas of interest, such as MS focal lesions. The measures shown in the ruler were inferred from the thickness of the sagittal slices.

Briefly, the strategy consists of: i) sectioning along the midsagittal plane the spinal cord specimens prior to MRI; ii) acquisition of sagittal MRI slices parallel to surface exposed by the cut; iii) slicing of histological material also in parallel from the exposed midsagittal surface, matching the radiographic fields of interest.

More in detail, the steps of the MRI and histology parts of the pipeline are listed below.

*MRI acquisition*

Our procedure allows the acquisition of MR images from two specimens per session.

1. Prior to MRI, each of the two spinal cord specimens is sectioned midline for the whole sagittal length in approximately two halves with a surgical blade;
2. the four tissue chunks are positioned in the four slots of a syringe plunger and tied with VELCRO®, while using medical bandage for padding;
3. an experiment reference frame is defined, identifying *anterior*, *posterior*, *top* and *bottom* parts of the plunger (letters A, P, T and B to be written with a non-erasable highlighter in the plunger);
4. holes made with fine point scissors in the plunger are exploited for radiographic reference (one hole made to the top, anterior part of the plunger; two holes made to the bottom, left part of the plunger).
5. the plunger is fitted into a FALCON® tube, which is finally filled with freshly prepared 10 mM PBS solution for MRI acquisition (the PBS will in fact also fill the holes in the plunger, which may then be visible).

*Histological procedures*

1. After MRI, standard histological processing steps are carried out (dehydration, paraffin-embedding);
2. specimen sizes are measured before and after paraffin-embedding, to estimate the tissue shrinkage caused by the process;
3. histological sections are sliced sagittally from the surface exposed by the midsagittal cut, consistently with the experiment reference frame introduced prior to MRI;
4. the MRI slice from which each sagittal section is taken is inferred recording the amount of material removed from the exposed surface while looking at an axial MRI view, onto which the sagittal slices have been overlaid (in doing so, the MRI slice thickness is scaled to account for tissue shrinkage, using the shrinkage factor estimated as per point 2).

Figure 7.1 shows a manual sketch illustrating the experimental reference frame that was created for MRI session number 5. The drawing was included in the standard-operating-procedure (SOP) document provided to the Oxford team, which was useful to plan histology. As a further example, the entire SOP document written after MRI session 4 is also provided in appendix A.

Figure 7.2 shows instead the axial view with sagittal slices overlaid onto it, from the same MRI session. A ruler was also added (measures inferred from sagittal slice thickness; measures shown do not account yet for tissue shrinkage).

## 7.4 Results

### 7.4.1 Samples and MRI sessions

The first three MRI sessions were preliminary acquisitions exploring the feasibility of the designed diffusion encoding protocol, as well as FOV and resolution.

In the first session, data were lost since the scanner did not save any image due to an unexpected conflict of the acquisition software. In the second session, data were acquired but had also to be discarded due to an unexpected drift of the signal throughout the acquisition, made evident by a drop of more than 50$\%$ of the signal intensity when the last and first $b = 0$ images were compared to each other. In the third session, DW images were acquired and saved. However, they were not used for the comparison NODDI-histology for two main reasons: i) the image SNR was disappointing; ii) the Oxford team did not consider reliable to match the position of MRI and histology if sections were to be obtained from a surface exposed by a cut performed after the MRI scan.

Figure 7.3 shows the SNR map estimated from the $b = 0$ images in MRI sessions 3 and 4. The SNR in session 3 is on the order of 10-15 in WM, while in session 4 is about 20-25. The SNR in session 4 is higher than in session 3, since the SNR of session 3 was considered unsatisfactory. The higher SNR level was achieved increasing the $\mathrm{T_R}$ from 1300 ms (session 3) to 2200 ms (sessions 4 and 5), while also increasing the slice thickness from 500 to 800 $\mu$m. As a consequence of this, the number of DW images had to be reduced, since the allocated scan time did not change. The number of DW directions was then reduced from 336 (session 3) to 171 (sessions 4 and 5). Moreover, it was decided to adopt increasing angular resolution of the gradients as the $b$-value increased, rather than constant. This choice is in line with the published *in vivo* NODDI protocol, where the angular resolution of the $b$-shells also increases as $b$ increases [215].

The final DW protocol consisted of 171 directions split onto 6 $b$-shells of increasing angular resolution ($b = \{$ 520, 2080, 4680, 8320, 13000, 18720 $\}$ s mm$^{-2}$, with respectively 6, 15, 24, 33, 42 and 51 diffusion sensitising gradient directions).

Figure 7.4 shows the quantitative $T_2$ map obtained from the multi-echo spin echo acquisitions performed before the start, in the middle and at the end of the DW protocol in MRI session number 5. The maps demonstrate that $T_2$ was stable throughout the diffusion MRI experiment.

### 7.4.2 Adaptation of NODDI analysis for *ex vivo* DW data

This section presents the results of the investigation aimed to adapt NODDI analysis, as developed for *in vivo* data, for the acquired *ex vivo* DW images.

Figures 7.5 and 7.6 show the quality of fit of NODDI, with and without *dot* compartment, in control and MS specimens from MRI sessions 4 and 5. For control specimen 3 (upper thoracic), the characteristic BIC $= f(d_\parallel)$ is U-shaped as a function of $d_\parallel$. The median BIC without the *dot* is always similar to the case with *dot*, but in the latter case the confidence intervals are narrower. For control specimen 6 (upper lumbar), instead, the shape of the curve BIC $= f(d_\parallel)$ resembles a U only when the *dot* is included. When a *dot*-like DW signal is not accounted for by the model in WM,

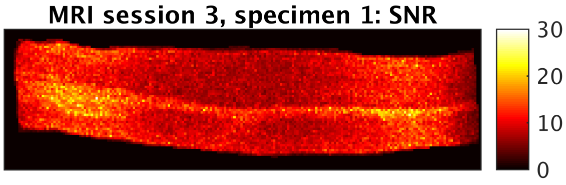
MRI session 3, specimen 1: SNR
30
20
10
0

(a) SNR in session 3.

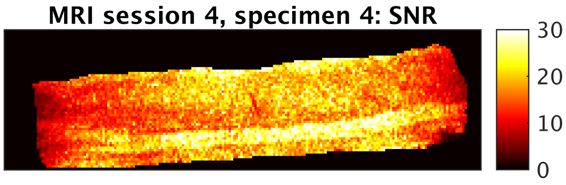
MRI session 4, specimen 4: SNR
30
20
10
0

(b) SNR in session 4.

Figure 7.3: examples of SNR map in one slice of control specimens 1 and 4, as obtained from the 25 $b = 0$ images acquired in MRI sessions 3 (specimen 1) and 4 (specimen 4).

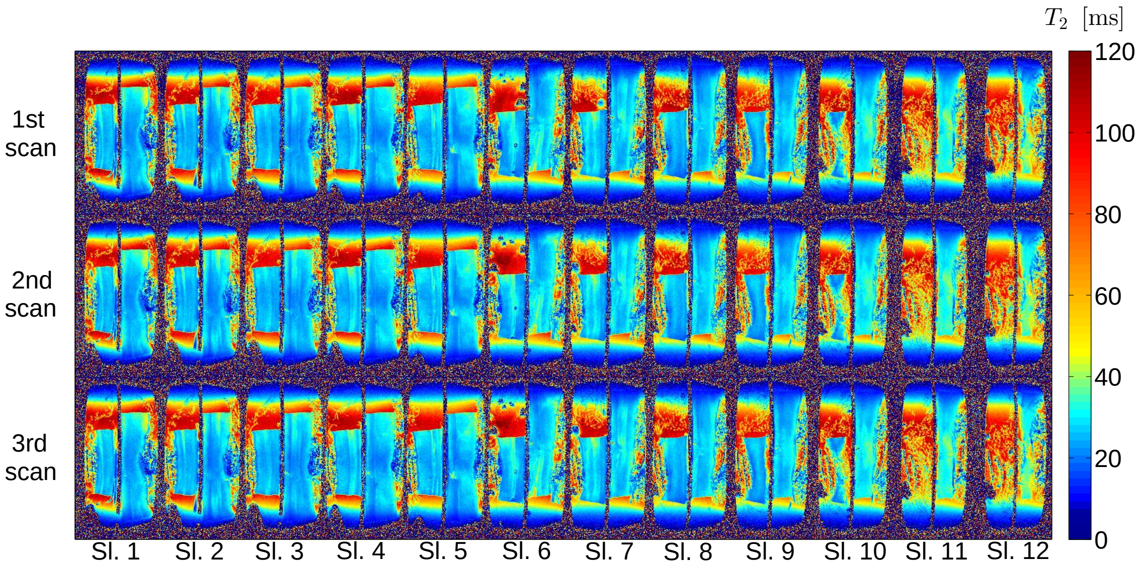
$T_2$ [ms]
120
100
80
60
40
20
0
1st scan
2nd scan
3rd scan
Sl. 1
Sl. 2
Sl. 3
Sl. 4
Sl. 5
Sl. 6
Sl. 7
Sl. 8
Sl. 9
Sl. 10
Sl. 11
Sl. 12

Figure 7.4: quantitative $T_2$ map obtained from the three multi-echo spin echo acquisitions that were performed in MRI session 5. 12 MRI slices are shown along the 12 different columns, whereas different scans are reported along different rows. Each image shows two pieces of cord: a longer one to the right (specimen number 5, upper thoracic, MS tissue) and a shorter one to the left (specimen number 6, upper lumbar, non-pathological tissue).

BIC increases as $d_{||}$ grows. Also, for specimen 6, the presence of the dot compartment narrows the range of variability of the observed BIC values.

A similar behaviour of the curve describing BIC as a function of $d_{||}$ is seen looking at the ROIs drawn on the images of the MS samples. The curve is also U-shaped, and shows a plateaux for $d_{||}$ in the range $[0.70; 2.10]$ $\mu$m$^2$ ms$^{-1}$ in all ROIs (GM, WM and WMFL) of both cases (specimen 3,

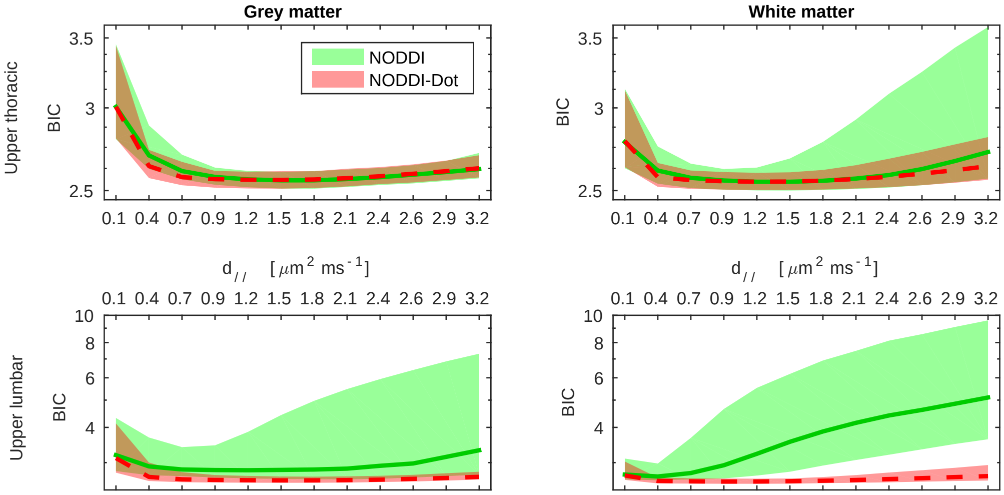

Figure 7.5: distribution of the BIC statistics as a function of $d_{\|}$ for models NODDI and NODDI-Dot in the GM and WM ROIs of control specimens 4 (to the top) and 6 (to the bottom). The median is reported as a solid line for NODDI and a dashed line for NODDI-Dot, whereas the shadowed area represents the 95% confidence interval (green for NODDI, red for NODDI-Dot).

upper lumbar; specimen 5, upper thoracic) when the *dot* compartment is accounted for. However, when that compartment is not included, BIC increases monotonically as $d_{\|}$ increases for the GM and WM ROIs in the thoracic MS specimen, and the median BIC is always higher than the median BIC obtained with the *dot*.

Lastly, we report a U-shaped BIC characteristic without *dot* for the WMFL ROI of both MS specimens and for the GM and WM ROIs of the upper lumbar case (specimen 3). In that case, the median BIC is similar to the median obtained with *dot*, but fitting without the *dot* provides wider ranges of variability for BIC.

Figures 7.7 and 7.8 convey similar information as figures 7.5 and 7.6 but for DTI. They show box plots of BIC values obtained fitting DTI with and without the *dot* compartment. In all cases, the DTI model fitted with the *dot* compartment has lower BIC than without.

### 7.4.3 Strategy to determine the radiographic position of histological sections

In figure 7.9 two MRI images from specimens 6 and 3 are shown. The figure also shows an example of histological images obtained from tissue within the same two MRI slices, according to our strategy described in section 7.3.3 of this chapter.

The same fine-scale features can be identified in both MRI and corresponding histological images by simple visual inspection. For control specimen number 6, for instance, these include a set of blood vessels, visible as dark spots within WM in both MRI and histology (indicated by red, orange and yellow arrows). For MS specimen number 3 instead, WM focal lesions and a stripe of demyelination in GM can be seen in both MRI (signal hyperintensities) and histological image (lack of stain). These are pointed out by green and violet arrows (WM focal lesions) and by a cyan arrow (stripe of demyelination in GM).

## 7.5 Discussion

In this chapter, the work carried out to implement a pipeline for the histological validation of NODDI metrics was described. We set up a rich, high-resolution DW MRI protocol at 9.4T, and adapted NODDI analysis as proposed for *in vivo* data to fit our *ex vivo* images. Moreover, we developed a strategy to identify radiographically the position of histological material.

*MRI protocol*

A high-field DW MRI protocol rich in terms of $b$-values and gradient directions was set up in order to probe the microstructure of fixed spinal cord tissue. High-field MRI enables the possibility of acquiring images with high resolution, revealing fine-scale anatomical detail. This ultimately leads to accurate and precise delineation of the microstructural properties of relatively small portions of tissue such as focal MS lesions.

The final diffusion encoding protocol consisted of 171 DW measurements spread over 6 $b$-shells with increasing angular resolution. The protocol also includes the acquisition of 25 non-DW images. The total number of images of the diffusion protocol was a trade-off between the total amount of DW data that could be acquired in the available MRI slot and the quality of each individual DW measure. This quality is controlled mainly by $\mathrm{T_R}$, to which the total scan duration is proportional.

Also, $T_2$ was monitored throughout the last MRI session to verify the effectiveness of the fixative washing. $T_2$ was stable during the whole diffusion protocol, demonstrating that 24 hours of bath in PBS were sufficient to effectively wash out the fixative, given the relatively small dimensions of the specimens (section of roughly $0.5\,\mathrm{cm}^2$, length of 2 to 4 cm).

*Model fitting of* ex vivo *data*

A procedure for NODDI analysis of *ex vivo* data was implemented. NODDI is a model developed for applications *in vivo*, and its employment for the analysis of data acquired from fixed *post mortem* tissue may require some adaptations. We investigated whether a compartment of isotropic restriction (stationary water or “*dot*” [147]) was needed to account for some effects that fixation has on the tissue, as shown in other studies [4, 146, 170]. Moreover, we assessed the impact of the choice of the intrinsic diffusivity of the neural tissue $d_{\|}$ on the quality of fit, since the values commonly employed *in vivo* may not be best suited to describe our data.

To study the role of the *dot* compartment and of the choice of $d_{\|}$, we fitted NODDI with and without *dot* for 12 values of $d_{\|}$ in $[0.10; 3.20]$ $\mu\mathrm{m}^2\,\mathrm{ms}^{-1}$, while fixing the isotropic diffusivity $d_{\mathrm{iso}}$ to the ADC of the PBS. We then derived the BIC statistics, an index of quality of fit, within different tissue types (pathological and non-pathological). A similar comparison was also performed for conventional DTI, which was fitted with and without the inclusion of the *dot* compartment.

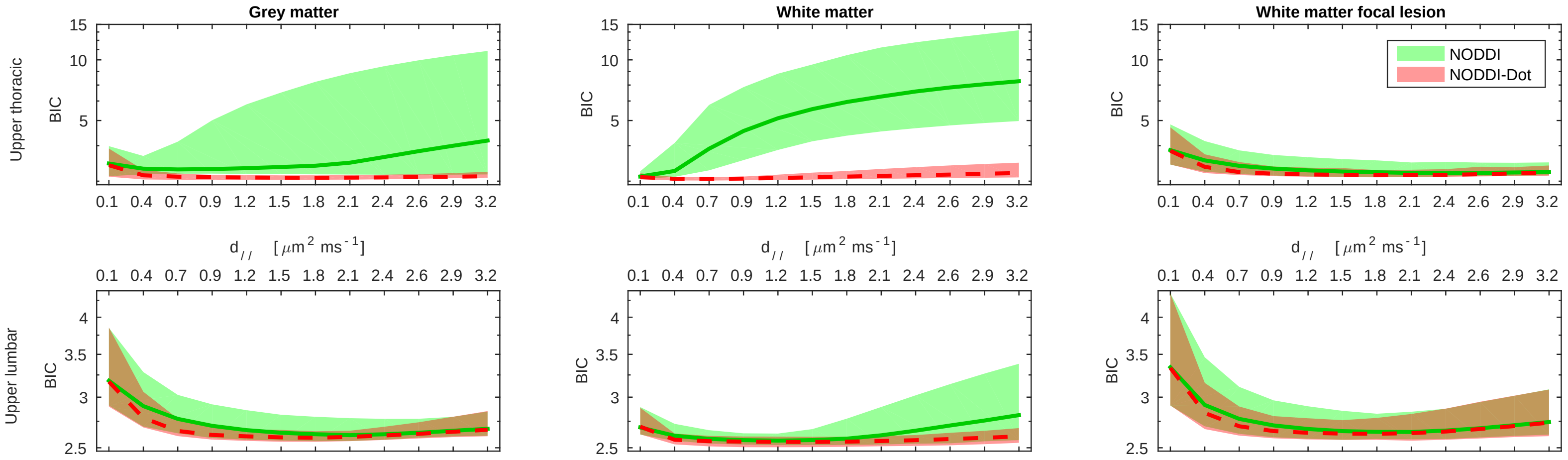

Figure 7.6: distribution of the BIC statistics as a function of parameter $d_{\|}$ for models NODDI and NODDI-Dot in the GM, non-focal WM and WM focal lesion ROIs of MS specimens 5 (upper thoracic, shown to the top) and 3 (upper lumbar, shown to the bottom). Similar conventions for the illustration as figure 7.5 are followed.

As far as NODDI is concerned, our results show that in some cases (specimen 4, control, upper thoracic; specimen 3, MS, upper lumbar), the *dot* stabilises the fit, since the confidence intervals of the BIC characteristic of the NODDI-Dot model are narrower than those of NODDI without *dot*, although the two have similar median BIC. However, in other cases (specimen 6, control, upper lumbar; specimen 5, MS, upper thoracic), the *dot* compartment plays even a more important role. In those cases, in all ROIs the quality of fit of NODDI-Dot is always better than NODDI, given the lower median BIC values. The quality of fit of NODDI without *dot* worsens as $d_{\|}$ increases, especially in WM (monotonically increasing BIC). This finding suggests the presence of a water pool characterised by extremely low apparent diffusivity, which is well described by a compartment of isotropic restriction such as the *dot*, even in the WMFL ROI, where the *dot* compartment improves the quality of fit.

Our study has also highlighted the importance of choosing an appropriate value to which the intrinsic diffusivity of the neural tissue should be constrained. For NODDI, when $d_{\text{iso}}$ is fixed to the ADC of the PBS and the *dot* compartment is included, certain choices of $d_{\|}$ provide better fit than others, as demonstrated by the characteristic curve describing BIC as a function of $d_{\|}$. The quality of fit improves as $d_{\|}$ increases from 0.10 $\mu\text{m}^2\,\text{ms}^{-1}$ to 0.70 $\mu\text{m}^2\,\text{ms}^{-1}$, reaches a plateaux for intermediate values of $d_{\|}$ in the range $[0.70; 2.10]$ $\mu\text{m}^2\,\text{ms}^{-1}$, and then worsens as $d_{\|}$ increases approaching values similar to the diffusivity of free water. This trend is consistently observed in all samples and tissue types, pathological and non-pathological.

For comparison, we assessed the impact of the inclusion of the *dot* compartment also for DTI. The higher BIC of the DTI model, with respect to the DTI-Dot one, suggests that the inclusion of the *dot* compartment is beneficial to improve the quality of fit of DTI in all tissue types.

*Strategy to determine the radiographic position of histological material*

Lastly, a strategy to determine the position in the acquired MRI images of tissue material sectioned for histological processing was developed. The strategy relies on:

- sectioning the spinal cord specimens along the midsagittal plane prior to MRI;
- acquisition of the diffusion MRI protocol sagittally, with slices taken parallel to surface exposed by the midline cut;
- acquisition of axial MRI slices for anatomical reference;
- sectioning of histological material also sagittally, from the surface exposed by the midsagittal cut.

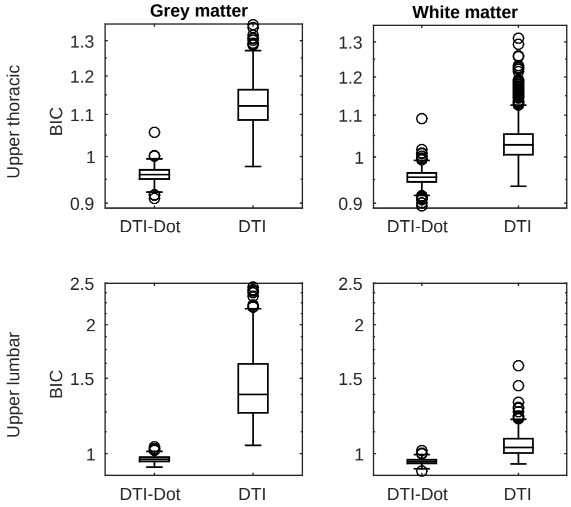

Figure 7.7: distribution of the BIC statistics shown as a box plot for models DTI and DTI-Dot in the GM and WM ROIs of control specimens 4 (upper thoracic, shown to the top) and 6 (upper lumbar, shown to the bottom).

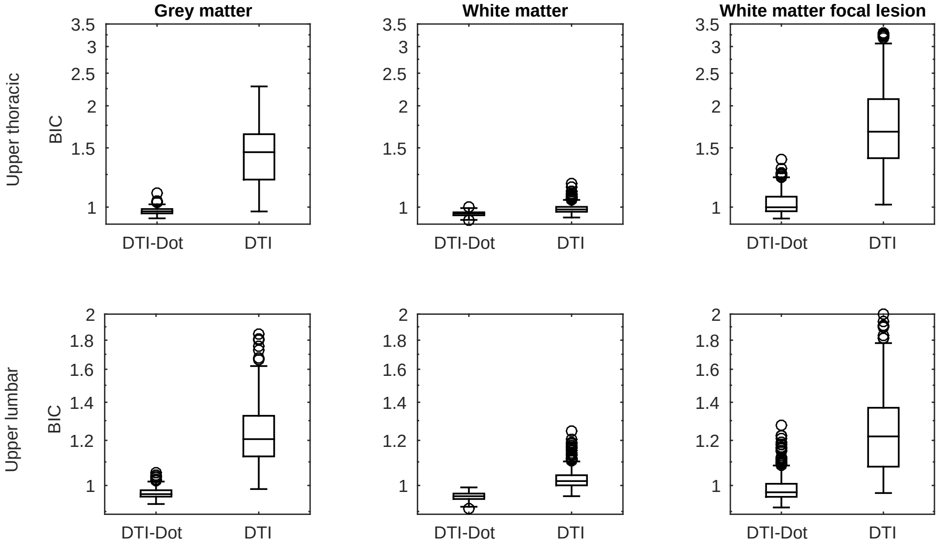

Figure 7.8: distribution of the BIC statistics shown as a box plot for models DTI and DTI-Dot in the GM, non-focal WM and WM focal lesion ROIs of MS specimens 5 (upper thoracic, shown to the top) and 3 (upper lumbar, shown to the bottom).

The sagittal acquisition of the DW protocol allows the comparison of diffusion metrics to histological features that include indices of neurite orientation dispersion. This is made possible by the fact that the histological material is also obtained sagittally, allowing the visualisation of the direction along which neuronal fibres run. Moreover, the further acquisition of axial views enables the precise identification of the radiographic position of the histological sections, which are gradually sliced from the surface exposed by the midline cut for staining.

Although full details of the histological procedures will be listed in chapter 9, visual assessment demonstrates a good correspondence MRI-histology. Examples were provided in this chapter in figure 7.9.

Therefore, the strategy to identify the radiographic position of the histological sections was considered reliable as far as it matters for the purpose of the study.

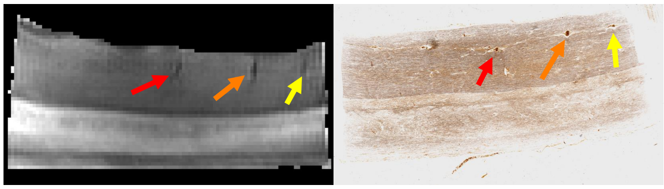

(a) specimen 6, control

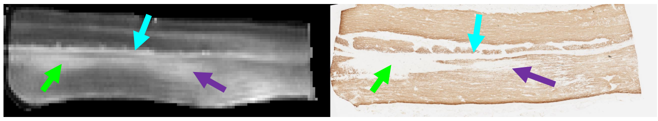

(b) specimen 3, MS

Figure 7.9: mean $b = 0$ MRI slices of specimens 6 (top, to the left) and 3 (bottom, to the left) and examples of histological images of 10 $\mu$m-thick stained sections taken within the same MRI slices (to the right). The histological image of specimen 6 is stained with Palmgren's method, while the histological image of specimen 3 is stained for myelin (proteolipid protein immunohistochemistry). Arrows indicate features identifiable in both MRI and histology.

## 7.6 Conclusion

In this chapter we have shown the technical work that we carried out to set up a pipeline enabling the histological validation of NODDI metrics in the spinal cord. A DW MRI protocol at 9.4T was implemented, and a strategy to determine the position of histological images in the MRI fields of interest was developed. Moreover, we also studied how to adapt the fitting of the NODDI model as usually performed *in vivo* to our *ex vivo* data, focussing on the benefits of introducing a compartment of isotropic restriction (the *dot*) and on the choice of the intrinsic diffusivity of the neural tissue.

We conclude that our implemented MRI-histology pipeline has the potential of providing data of good quality for the systematic comparison of NODDI metrics to quantitative histological features. Also, as far as the NODDI analysis of our *post mortem* DW images is concerned, we conclude that the fitting of both NODDI and DTI models benefits from the inclusion of the *dot* compartment. This compartment accounts for the contribution of a stationary water pool of unclear origin, which is thought to be due to water trapped within inactive glial cells or to other effects of tissue fixation

[4]. Furthermore, values of $d_{\|}$ in the range $[0.70; 2.10]$ $\mu$m$^2$ ms$^{-1}$ seem suitable to maximise the quality of the fit of NODDI to our data. Therefore, we decided to employ an intermediate value of $d_{\|} = 1.50$ $\mu$m$^2$ ms$^{-1}$ for the study that will be shown in chapter 9, where we report the histological validation of NODDI metrics obtained from MRI sessions 4 and 5.

# Chapter 8

# Estimation of neurite orientation dispersion from histological images

## 8.1 Introduction

In previous chapters, the potential of NODDI for spinal cord imaging as a feasible and more specific alternative to DTI was highlighted. NODDI provides indices of neurite morphology, namely density and orientation dispersion of neurites. Such features are potential biomarkers in neurological conditions, and may provide useful insights about tissue pathology.

Nonetheless, histological validation is essential to confirm the specificity of the indices and the validity of the model in presence of pathology. Suitable counterparts of NODDI metrics need to be identified in histological images, in order to obtain ground truth measures to which NODDI indices can be compared to. Counterparts of NODDI neurite density come naturally from histological stains and immunostains demonstrating neuronal elements. However, finding a specific counterpart of NODDI orientation dispersion index ODI is less straightforward.

In this chapter, we present the work carried out to identify a suitable histological equivalent of NODDI ODI, an index of directional coherence of axons and dendrites. In line with published examples in recent literature [21, 98, 159], we propose to compare ODI to histological measures of directional spread of neurite orientations derived from *structure tensor* (ST) [16] analysis.

ST analysis was developed in the context of computer vision as a technique to detect the local orientation of an image. The method has recently shown great potential as an automatic tool for the characterisation of neuronal fibres in histological images, as in studies of rat [22] and human brain [21] microstructure.

In the spinal cord, axial sectioning has shown great value for the quantification of spinal cord properties [40, 41, 99]. However, the method is best suited for quantifying axonal density or axon diameter, and it does not allow the visualisation of the directions along which fibres run. Conversely, stained sections taken in the sagittal plane could be used to demonstrate the directions of neuronal processes, with little amount of through-plane fibres, especially in WM. ST analysis could then be applied to estimate the local orientation of these processes, and the spread of the orientations can ultimately be taken as a histology-derived orientation dispersion, similarly to previous approaches [21].

This chapter demonstrates the feasibility of applying ST analysis to images of sagittal sections of the spinal cord to estimate of neurite orientation dispersion. In particular, we investigated in detail the impact of the choice of the spatial scale at which information is integrated to estimate orientations, employing statistical distributions defined over the unit circle. We focussed on a conventional model, the *Watson* distribution [118], and also introduced a novel concept, the *weighted-Watson* distribution. Specifically, the weighted-Watson distribution was developed to extend the conventional model and account for a further level of uncertainty when estimating local orientations.

## 8.2 Research dissemination

The results shown in this chapter are unpublished, but were used to guide the analysis that will be presented in chapter 9. A manuscript reporting the work included in this chapter is currently in preparation for submission to a peer-reviewed journal.

## 8.3 Theory

### 8.3.1 Linear symmetry detection

A single-channel, continuous image $I(x, y) \; : \; \mathbb{R}^2 \rightarrow \mathbb{R}^+$ is linearly symmetric if

$$I(x, y) = g(\eta_1 x + \eta_2 y),$$

with $g(\xi)$ being a function $g(\xi) \; : \; \mathbb{R} \rightarrow \mathbb{R}^+$ and $\eta_1$ and $\eta_2$ two real numbers. A linearly symmetric image has a Fourier transform concentrated to a line, and the direction $\mathbf{u} \in \mathbb{R}^2$ of this line identifies the orientation of the image [16]. Therefore, the image orientation can be estimated seeking concentration of energy along lines in the Fourier domain.

ST analysis allows the estimation of the direction of linear symmetry $\mathbf{u}$ in the image domain, without requiring Fourier transformation. It also allows local analysis, if only neighbourhoods of each image pixel are considered. The local ST of an image $I(x, y)$ is defined as the operator $\mathbf{J}(x, y) \; : \; \mathbb{R}^2 \rightarrow \mathbb{R}^{2\times 2}$

$$\mathbf{J}(x, y) \;=\; \begin{bmatrix} J_{1,1} & J_{1,2} \\ J_{2,1} & J_{2,2} \end{bmatrix} \overset{\text{def}}{=} \int\int_{\Omega(x,y)} \begin{bmatrix} I_x(\xi, \upsilon)^2 & I_x(\xi, \upsilon)\, I_y(\xi, \upsilon) \\ I_x(\xi, \upsilon)\, I_y(\xi, \upsilon) & I_y(\xi, \upsilon)^2 \end{bmatrix} d\xi d\upsilon \qquad (8.1)$$

with $J_{1,2} = J_{2,1}$ and with $I_x(x, y)$ and $I_y(x, y)$ being $I_x(x, y) = \frac{\partial}{\partial x} I(x, y)$ and $I_y(x, y) = \frac{\partial}{\partial y} I(x, y)$. $\Omega(x, y)$ is the neighbourhood of location $(x, y)$ and its size controls the scale of analysis. It was proven [16] that the direction of linear symmetry $\mathbf{u}(x, y)$ at location $(x, y)$ can be estimated solving

$$\mathbf{u}(x,y) \;=\; \text{arg}\min_{\mathbf{n}} \;\Big(\mathbf{n}^{\mathsf{T}}\,\mathbf{J}(x,y)\,\mathbf{n}\Big). \tag{8.2}$$

Equation 8.2 is satisfied if $\mathbf{u}(x,y)$ is chosen as the eigenvector associated to the smallest eigenvalue of $\mathbf{J}(x,y)$. In [16], it was shown that $\mathbf{u}(x,y) \;=\; [\,\cos\big(\theta(x,y)\big) \quad \sin\big(\theta(x,y)\big)\,]^{\mathsf{T}}$ can be estimated directly from $\mathbf{J}(x,y)$, since

$$\theta(x,y) \;=\; \frac{1}{2}\angle\big(J_{2,2} - J_{1,1} + j2J_{1,2}\big). \tag{8.3}$$

Above, we defined $\angle$ as the operator extracting the phase of a complex number. The angle $\theta$ describes the direction of image isointensity, whereas $\theta + \frac{\pi}{2}$ is the direction along which image intensity varies. Figure 8.1 clarifies the meaning of $\theta$.

In [16], an anisotropy index was also introduced, depending on the two eigenvalues $\lambda_1(x,y) \geq \lambda_2(x,y) \geq 0$ of $\mathbf{J}(x,y)$. The anisotropy index, here called $\alpha$, is

$$\alpha(x,y) \;=\; \frac{\lambda_1(x,y) \,-\, \lambda_2(x,y)}{\lambda_1(x,y) \,+\, \lambda_2(x,y)}. \tag{8.4}$$

$\alpha$ ranges in $[0;\,1]$ and quantifies the certainty of the estimation of $\theta$ [16]. In practice, the ST will always have a smallest eigenvalue due to noise, which will cause $\lambda_1$ and $\lambda_2$ to differ at least slightly even in areas with no local structure. Hence, an apparent local image orientation will always be found. However, the observation of $\alpha \,\rightarrow\,$ 0 points towards the absence of real local structure and to a non-certain $\theta$. On the other hand, $\alpha \,\rightarrow\,$ 1 is evidence of local linear symmetry and points to a reliable $\theta$.

In practice, the integration of information in the local neighbourhood is achieved via discrete convolution of the image with a Gaussian kernel [16]. The size of the kernel its regulated by its standard deviation $\sigma$, which therefore controls the local scale of analysis.

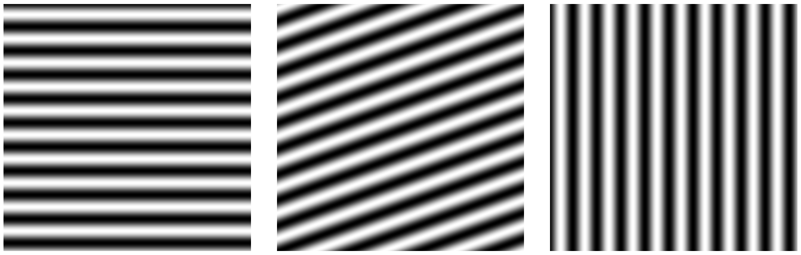
(a) $\theta = 0°$ (b) $\theta = 20°$ (c) $\theta = 90°$

Figure 8.1: meaning of angle $\theta$ clarified by grids at different orientations. $\theta + \frac{\pi}{2}$ describes the direction along which image intensity varies, whereas $\theta$ the direction of isointensity. We measure $\theta$ from the horizontal direction, oriented from left to right. If one considers the white stripes as schematic representations of stained neuronal fibres, it follows that $\theta$ can be taken as an estimate of the dominant fibre orientation.

### 8.3.2 Patch-wise statistics of ST orientation

When ST-derived orientation from histological images is compared to DW MRI indices, the analysis is usually performed at a scale comparable to the MRI voxel size. For instance, in [22] the ST orientation maps were split into patches and for each patch an histogram of the orientations was calculated and fitted to a von Mises distribution defined over the unit circle.

In this work, we propose to follow a similar approach, e.g. to divide the orientation map $\theta(x, y)$ of spinal cord histological images into patches of size comparable to the resolution of an MRI voxel. Then, directional statistics [118] can be employed to model the distribution of orientations within each patch. This allows the evaluation of indices of spread, which can be considered as estimates of neurite orientation dispersion and hence counterparts of NODDI ODI.

In particular, we focus on the Watson distribution defined over the unit circle, being bimodal in $[0; 2\pi]$ (i.e. its value is the same for orientations $+\mathbf{n}$ and $-\mathbf{n}$ [118]). This is a conventional model that describes the bimodal distribution of orientations about a mean orientation, equivalent to NODDI neurite orientation distribution, with the difference that for NODDI the distribution is defined over the unit sphere, rather than over the unit circle.

We also introduce a new bivariate probability density function, which we call *weighted-Watson distribution*. This distribution considers both ST orientation $\theta$ and anisotropy index $\alpha$ as two distinct random variables, and attempts to model them jointly, in order to account not only for the spread about a mean orientation, but also for the uncertainty of the individual orientation from each single pixel.

In conventional approaches, the only ST metric considered for analysis is the local dominant orientation $\theta$. Analysis usually provides statistics of mean and spread of $\theta$, given a sample $\Gamma = \{\theta_1, ..., \theta_N\}$ coming from several pixels of a histological image. The indices of spread, particularly, can be seen as the overall measures of uncertainty with respect to a mean orientation within the whole set $\Gamma$.

With our novel weighted-Watson distribution, a further level of uncertainty is modelled. Similarly to conventional approaches, the weighted-Watson distribution provides an index of spread about a mean orientation, given the sample $\Gamma$ of orientations from several pixels. However, due to the dependency on the anisotropy index $\alpha$, the weighted-Watson distribution also captures uncertainty at the level of the individual pixel, i.e. at the individual element $\theta_i, i = 1, ..., N$ of $\Gamma$, whose reliability is described by the value of the corresponding anisotropy index $\alpha_i$. Therefore, in our weighted-Watson model, reliable orientations contribute more than unreliable ones to the estimation of the descriptive statistics of mean and spread.

The two probability density functions are described in the next two sections, and both rely on the hypothesis that there is only one dominant orientation within a patch.

### Conventional model: the Watson distribution

Let $\theta$ be an angular random variable defined in $[0; 2\pi]$. The Watson distribution of parameters $\kappa$ and $\mu$ is defined as

$$P_\Theta(\theta; \kappa, \mu) \;=\; c\, e^{\,k \cos^2(\theta-\mu)} \tag{8.5}$$

with $\kappa \in (0; \infty)$ being the concentration of the distribution and $\mu$ describing its mean orientation. $c$ is a normalising constant that can be worked out writing $\int_0^{2\pi} P_\Theta(\theta; \kappa, \mu)\, d\theta \;=\; 1$, which provides

$$c(\kappa) \;=\; \frac{1}{2\pi\, e^{\frac{1}{2}\kappa}\, I_0\big(\frac{1}{2}\kappa\big)}$$

with $I_0(\xi) \;=\; \frac{1}{2\pi} \int_0^{2\pi} e^{\,\xi \cos(x)}\, dx$ being the modified Bessel function of the first kind and 0-th order.

The parameters $\kappa$ and $\mu$ can be estimated given a sample of $N$ observations $\Gamma \;=\; \{\theta_n \mid n = 1, ..., N\}$ via maximisation of the likelihood of the sample. Under the hypothesis of independence of the observations, it is possible to show that the maximum likelihood estimates $\hat{\kappa}$ and $\hat{\mu}$ of the parameters $\kappa$ and $\mu$ are

$$\hat{\kappa} \;=\; 2\, A^{-1}\big(1 - \mathrm{CV}\big) \tag{8.6}$$

and

$$\hat{\mu} \;=\; \frac{1}{2} \angle\!\left(\frac{1}{N} \sum_{n=1}^{N} e^{\,j\, 2\theta_n}\right), \tag{8.7}$$

where the operator $\angle$ extracts the phase of a complex number. In equation 8.6 above, we defined $A(\xi)$ as $A(\xi) \overset{\text{def}}{=} \frac{\frac{d}{d\xi} I_0(\xi)}{I_0(\xi)}$, and indicated with CV the circular variance of $\Gamma$ [118], i.e.

$$\mathrm{CV} \;=\; 1 - \left|\frac{1}{N} \sum_{n=1}^{N} e^{\,j\, 2\theta_n}\right|. \tag{8.8}$$

CV is a measure of spread of the orientation and ranges in $[0;\ 1]$, with $\mathrm{CV} = 0$ if all orientations are the same ($\theta_i = \theta_j \quad \forall\ i \neq j$) and $\mathrm{CV} = 1$ indicating maximum spread.

Lastly, the value of the log-likelihood at maximum is

$$\log L_{\max} \;=\; \frac{1}{2} N\, \hat{\kappa}\, (1 - \mathrm{CV}) \;+\; N \log\left(\frac{1}{2\pi\, I_0\big(\frac{1}{2}\hat{\kappa}\big)}\right). \tag{8.9}$$

Figure 8.2 shows the Watson distribution for different values of $\kappa$ and for a fixed $\mu$. The distribution is bimodal and has little dependence on $\theta$ for very low $\kappa$, whereas it has a peak centred on the mean orientation for higher values of $\kappa$, which gets sharper as $\kappa$ increases.

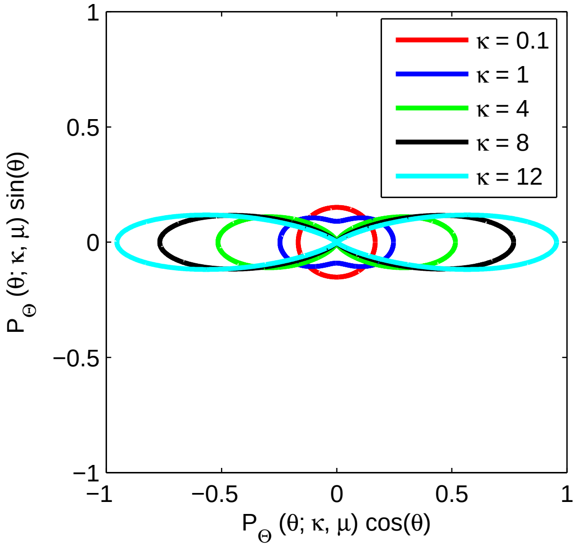

Figure 8.2: polar diagram of the Watson distribution for different values of $\kappa$ and for $\mu = \pi$.

### Our new model: the weighted-Watson distribution

If a Watson distribution is adopted to model a sample ST-derived orientations, no information about the reliability of each individual measured orientation is accounted for. Therefore, non-reliable orientations may be included when fitting the Watson distribution to the data. To limit the effect of such non-certain orientations, one can exploit the anisotropy index $\alpha$. For instance, one may want to discard orientations $\theta$ corresponding to an anisotropy index $\alpha$ below a certain threshold, although the optimal choice of this threshold is not straightforward.

We propose a different, threshold-free approach, which handles the anisotropy index $\alpha$ as another random variable. We employ $\alpha$ as a weight of $\cos^2(\theta - \mu)$ in the argument of the exponential term in equation 8.5, measuring the distance of $\theta$ from the mean $\mu$. This is equivalent to state that angles $\theta$ very different from $\mu$ contribute less to the likelihood of the model, if their corresponding $\alpha$ is low. Conversely, it hypothesises that values of $\theta$ similar to the mean orientation $\mu$ are less probable as $\alpha$ decreases. That is, the weighted-Watson framework accounts for a further level of uncertainty, at the individual pixel level.

We here introduce the bivariate weighted-Watson distribution

$$P_{A,\Theta}(\alpha, \theta; \kappa, \mu) \; = \; c\, e^{k\,\alpha \cos^2(\theta-\mu)}, \tag{8.10}$$

for $(\alpha, \theta) \in [0; 1] \times [0; 2\pi]$. $c$ is a normalisation factor such that $\int_0^1 \int_0^{2\pi} P_{A,\Theta}(\alpha, \theta; \kappa, \mu)\, d\alpha\, d\theta = 1$, found to be

$$c(\kappa) \; = \; \frac{\kappa}{2\pi \int_0^{\kappa} e^{\frac{1}{2}\xi}\, I_0\!\left(\frac{1}{2}\xi\right) d\xi} \; .$$

Integration of $P_{A,\Theta}(\alpha, \theta; \kappa, \mu)$ over either $\alpha$ or $\theta$ respectively provides the marginals of $\theta$ ($P_\Theta(\theta; \kappa, \mu) \; =$

$\int_0^1 P_{A,\Theta}(\alpha, \theta; \kappa, \mu)\, d\alpha$) and $\alpha$ ($P_A(\alpha; \kappa) = \int_0^{2\pi} P_{A,\Theta}(\alpha, \theta; \kappa, \mu)\, d\theta$). They are found to be

$$P_\Theta(\theta; \kappa, \mu) = \begin{cases} \frac{c(\kappa)}{\kappa} \; \frac{e^{\kappa \cos^2(\theta-\mu)} - 1}{\cos^2(\theta-\mu)} & \theta \neq \mu + \frac{\pi}{2} + q\pi \\ \\ c(\kappa) & \theta = \mu + \frac{\pi}{2} + q\pi \end{cases} \tag{8.11}$$

for $q = 0, \pm 1, \pm 2, ...$, and

$$P_A(\alpha; \kappa) = 2\pi\, c(k)\, e^{\frac{1}{2}\kappa\alpha}\, I_0\Big(\frac{1}{2}\kappa\alpha\Big). \tag{8.12}$$

The maximum likelihood estimates of $\kappa$ and $\mu$, for a sample of independent observations $\Gamma = \{(\alpha_n, \theta_n) \mid n = 1, ..., N\}$, are

$$\hat{\kappa} = B^{-1}\Big(\frac{\bar{\alpha} + 1 - \text{CV}}{2}\Big) \tag{8.13}$$

and

$$\hat{\mu} = \frac{1}{2} \angle \left( \frac{1}{N} \sum_{n=1}^{N} \alpha_n e^{j\, 2\theta_n} \right), \tag{8.14}$$

having indicated with $\angle$ the operator extracting the phase of a complex number.

In equation 8.13, $\bar{\alpha} = \frac{1}{N}\sum_{n=1}^{N} \alpha_n$ is the mean anisotropy index, CV is the circular variance, in this case defined as

$$\text{CV} = 1 - \left| \frac{1}{N} \sum_{n=1}^{N} \alpha_n e^{j\, 2\theta_n} \right|, \tag{8.15}$$

and $B(\xi) = -\frac{\frac{d}{d\xi} c(\xi)}{c(\xi)}$. Comparison of equations 8.14 with 8.7 and 8.15 with 8.8 proves that in the new framework, orientations associated to low anisotropy contribute less to the estimation of $\mu$ and CV.

Lastly, it can be shown that the maximised log-likelihood of the weighted-Watson model is

$$\log L_{\text{max}} = \frac{1}{2} N\, \hat{\kappa}\, (\bar{\alpha} + 1 - \text{CV}) \; + \; N \log c(\hat{\kappa}). \tag{8.16}$$

Figure 8.3 shows the bivariate weighted-Watson distribution $P_{A,\Theta}$ for different values of $\kappa$ and for $\mu = \frac{\pi}{2}$. $P_{A,\Theta}$ increases monotonically with $\alpha$ and has a bimodal peak in $\theta = \pm\mu \;\forall\, \alpha$, which is sharper as $\alpha$ increases. For low $\kappa$, $P_{A,\Theta}$ is essentially flat for all $\theta$ and $\alpha$. However, as $\kappa$ increases, the peaks become sharper and the dependence on $\alpha$ stronger. Figure 8.4 shows the marginals $P_\Theta(\theta; \kappa, \mu)$ and $P_A(\alpha; \kappa)$ for $\mu = \pi$ and different values of $\kappa$. The marginal of $\theta$ is similar to the Watson distribution, whereas $P_A(\alpha; \kappa)$ increases monotonically with $\alpha$ and is maximum for $\alpha = 1$. The peak at $\alpha = 1$ is higher for higher $\kappa$.

## 8.4 Methods

### 8.4.1 Data acquisition

We studied a set of images taken from a 10 $\mu$m thick-sagittal section of non-pathological human spinal cord. The section was derived from a formalin-fixed spinal cord segment greater than 1.5 cm in length, obtained from the Oxford brain bank following appropriate consent as per Human Tissue Authority guidelines and relevant ethics committee approval. All experimental procedures were in compliance with the UK Parliament *Human Tissue Act*.

The tissue sample was dehydrated and embedded in paraffin for sectioning with a manual microtome. The derived histological material was impregnated with an optimised [40, 41] Palmgren's silver staining method [145] for optical imaging. The method was chosen since it was previously proven to demonstrate consistently neuronal elements [41]. All histological procedures were carried in histopathology facilities at the John Radcliffe Hospital, Nuffield Department of Clinical Neurosciences, Oxford (UK).

Optical imaging was performed with an Olympus BX41 optical microscope, equipped with a Zeiss Axiocam MRc5 digital camera. The data set consisted of images of size of 2572 × 1924 pixels. Eight images were taken from GM (four at an apparent magnification of 100× and four at 200×) and 15 taken from WM (eight at an apparent magnification of 100× and seven at 200×). The pixel dimensions were 0.34 × 0.34 $\mu$m$^2$ pixel$^{-2}$ for the images acquired at 100× and 0.17 × 0.17 $\mu$m$^2$ pixel$^{-2}$ for those acquired at 200×. The FOV was comparable to the in-plane resolution of *ex vivo* diffusion MRI voxels, since it is 874 × 654 $\mu$m$^2$ for the images taken at 100× magnification and 437 × 327 $\mu$m$^2$ for those acquired at 200× magnification.

### 8.4.2 ST calculation

Routines to evaluate the ST of digital images were implemented in Matlab. The code calculates the local ST and derives the local orientation $\theta$ and its associated anisotropy index $\alpha$. For this purpose, the image partial derivatives $I_x(x, y)$ and $I_y(x, y)$ are approximated via 2D discrete convolution with derivative-of-Gaussian (DoG) kernels. Such kernels are characterised by a spread $\sigma$ that defines the local scale of analysis [21].

The Gaussian kernel $w(x, y; \sigma)$ of support $\{x = -L, ..., L\}$ and $\{y = -L, ..., L\}$ is defined as

$$w(x, y; \sigma) \; = \; c\, e^{-\frac{1}{2}\frac{x^2+y^2}{\sigma^2}} \tag{8.17}$$

with $c$ designed to obtain $\sum_{x=-L}^{L} \sum_{y=-L}^{L} w(x, y; \sigma) = 1$. The DoG kernels of support $\{x = -Q, ..., Q\}$ and $\{y = -Q, ..., Q\}$ are instead defined as

$$DoG_x(x, y; \sigma) \; = \; -\frac{x}{2\pi\sigma^2}\, e^{-\frac{1}{2}\frac{x^2+y^2}{\sigma^2}}; \qquad DoG_y(x, y; \sigma) \; = \; -\frac{y}{2\pi\sigma^2}\, e^{-\frac{1}{2}\frac{x^2+y^2}{\sigma^2}}. \tag{8.18}$$

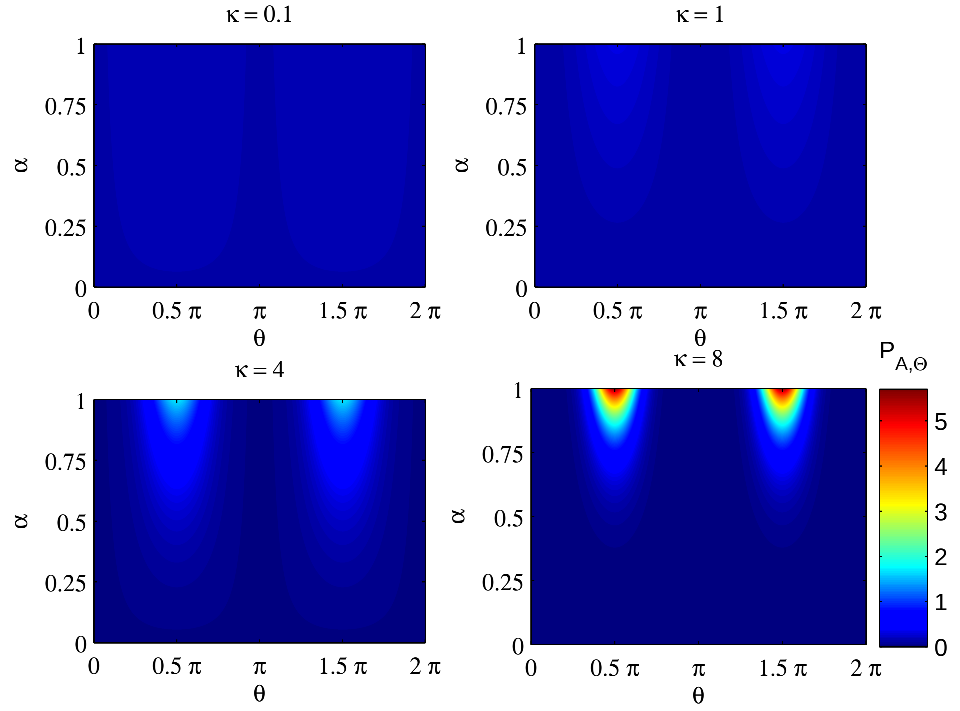

Figure 8.3: bivariate weighted-Watson distribution for different values of $\kappa$ and for $\mu = \frac{\pi}{2}$.

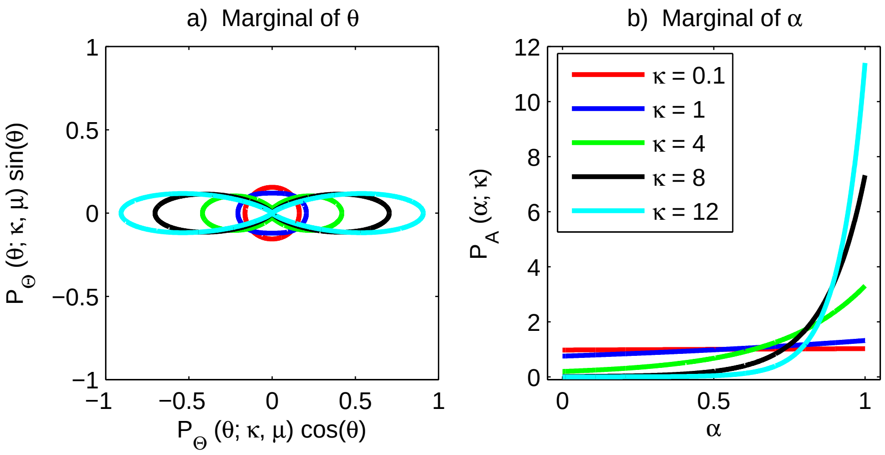

Figure 8.4: marginals of $\theta$ (a, to the left, as a polar diagram) and $\alpha$ (b, to the right) from the weighted-Watson distribution for different values of $\kappa$ and for $\mu = \pi$.

The numbers $L$ and $Q$ were chosen as in [16], so that the coefficients on the edges of the kernel window are not bigger in absolute value than 1% of the kernel peak value.

The ST $\mathbf{J}(x, y; \sigma)$ at pixel $(x, y)$ is calculated as

$$\mathbf{J}(x, y; \sigma) \;=\; w(x, y; \sigma) * \begin{bmatrix} I_x(x, y; \sigma)^2 & I_x(x, y; \sigma)\, I_y(x, y; \sigma) \\ I_x(x, y; \sigma)\, I_y(x, y; \sigma) & I_y(x, y; \sigma)^2 \end{bmatrix}$$

with $I_x(x, y)$ and $I_y(x, y)$ estimated as in [21]:

$$I_x(x, y; \sigma) \;=\; DoG_x(x, y; \sigma) * I(x, y), \tag{8.19}$$

$$I_y(x, y; \sigma) \;=\; DoG_y(x, y; \sigma) * I(x, y). \tag{8.20}$$

Above, $*$ indicates the discrete 2D convolution. All images were zero-padded before convolution with kernels $w(x, y; \sigma)$, $DoG_x(x, y; \sigma)$ and $DoG_y(x, y; \sigma)$, of an amount equal to max$(L, Q)$.

The local dominant orientation $\theta(x, y; \sigma) \in [0;\, \pi]$ is calculated according to equation 8.3, whereas the anisotropy index $\alpha(x, y; \sigma)$ is calculated as specified in equation 8.4.

The implementation was tested and validated on grids of orientation spanning the interval $[0;\, \pi]$, as those shown in figure 8.1. The implementation supports optional parallel computing, which splits the task of calculating pixel-wise $\theta(x, y; \sigma)$ and $\alpha(x, y; \sigma)$ into threads run in parallel by different processors.

### 8.4.3 ST implementation efficiency

To test the efficiency of the parallel implementation, a test was performed to estimate the computational time required to calculate the ST on a image of variable size. The image had the same number of pixels along the horizontal and vertical directions, and it was a grid similar to those depicted in figure 8.1.

We fixed $\sigma = 0.5$ pixel and run the test on a 8-core Dell Precision T1650 machine (3.5 GHz processor speed, 16 GB memory). The ST calculation was run without parallel computing (all pixels analysed one after the other) and also splitting the ST calculation into 4 parallel threads (each analysing serially a separate subset of pixels). The calculation of the ST was run 10 times per image width, and median and range of the computational time over the 10 runs were measured.

### 8.4.4 Variation of the local scale

We calculated the ST of all images in our data set varying $\sigma$ in a set of 80 evenly spaced values ranging from 0.1 to 100 pixels. For each image and each $\sigma$, the local orientation $\theta(x, y; \sigma)$ and the anisotropy index $\alpha(x, y; \sigma)$ were derived, and their distributions were approximated by normalised histograms. The maximum-likelihood estimates of the parameters of the Watson and weighted-Watson models and the corresponding maximised log-likelihoods were also calculated. In doing so, an adequate portion of each image close to the edges was removed, being influenced by the zero-padding of the filtering routines.

Standard hue-saturation-value (HSV) [21] encoding was followed to represent the ST of each image at each scale: the orientation $\theta$ was employed as hue channel; the anisotropy index $\alpha$ as saturation channel; the staining intensity as value channel.

### 8.4.5 Analysis

For each value of $\sigma$, we calculated the median and the range of the log-likelihood and of CV across images of the same tissue type (GM or WM) and acquired at the same magnification (100× or 200×). We also calculated a measure of contrast (C) and a contrast-to-noise ratio (CNR) between GM and WM for the CV statistics at each $\sigma$ as

$$\mathrm{C} = \frac{|m_{\mathrm{GM}} - m_{\mathrm{WM}}|}{\frac{1}{2}(m_{\mathrm{GM}} + m_{\mathrm{WM}})} \tag{8.21}$$

and

$$\mathrm{CNR} = \frac{|m_{\mathrm{GM}} - m_{\mathrm{WM}}|}{\sqrt{s^2_{\mathrm{GM}} + s^2_{\mathrm{WM}}}}. \tag{8.22}$$

Above, $m_{\mathrm{GM}}$ and $m_{\mathrm{WM}}$ are the mean CV whereas $s^2_{\mathrm{GM}}$ and $s^2_{\mathrm{WM}}$ are the variances of CV across GM and WM images.

## 8.5 Results

### 8.5.1 Data acquisition

Figure 8.5 shows GM and WM details from a silver stained sagittal section of human spinal cord. It demonstrates the complex architecture of dendritic trees in GM, and proves that although axons in WM follow a main direction, orientation dispersion occurs, due to phenomena such as undulation. Also, it shows that the silver staining is not entirely specific for neuronal elements, since non-neurite material is also stained in shades of brown.

### 8.5.2 ST implementation efficiency

Figure 8.6 shows the results from the test aiming to evaluate the efficiency of the parallel implementation of the ST calculation. The test reveals that if the image to be analysed is smaller than roughly 500 × 500 pixels (i.e. it contains fewer than 25 Kpixel), parallel computing is slower than non-parallel computing, due to implementation overhead. However, for images bigger than that, the parallel implementation becomes advantageous as compared to non-parallel implementation.

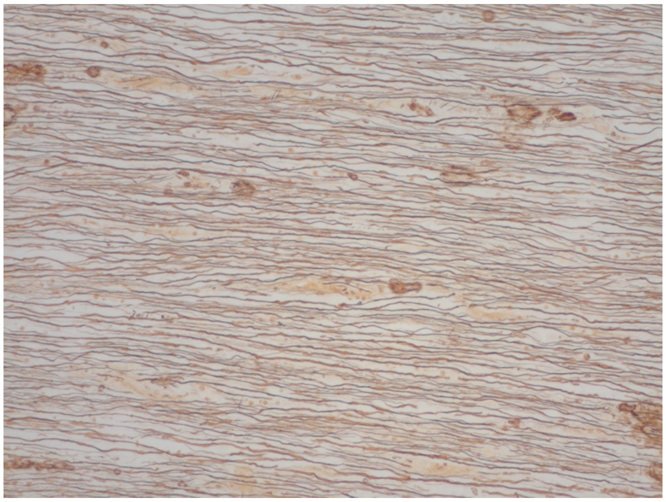

(a) image of WM

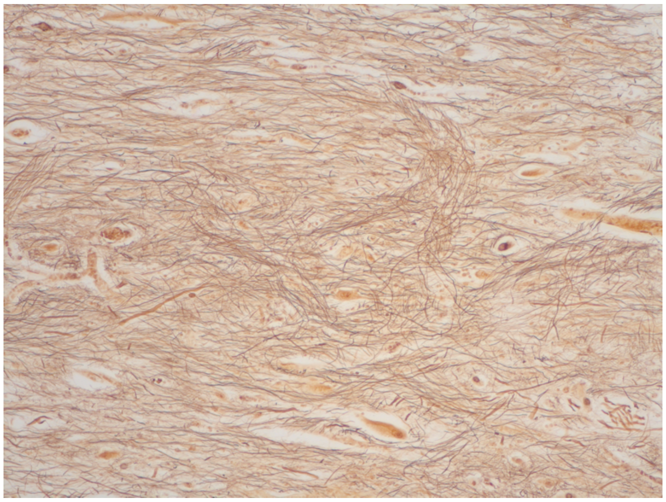

(b) image of GM

Figure 8.5: examples of images employed to demonstrate ST analysis and to study the effect of the choice of $\sigma$. Both images are taken from a sagittal section of human spinal cord (Palmgren's silver staining), at a magnification of 100×. Top image refers to WM, bottom image to GM. The FOV is $874 \times 654\,\mu\text{m}^2$.

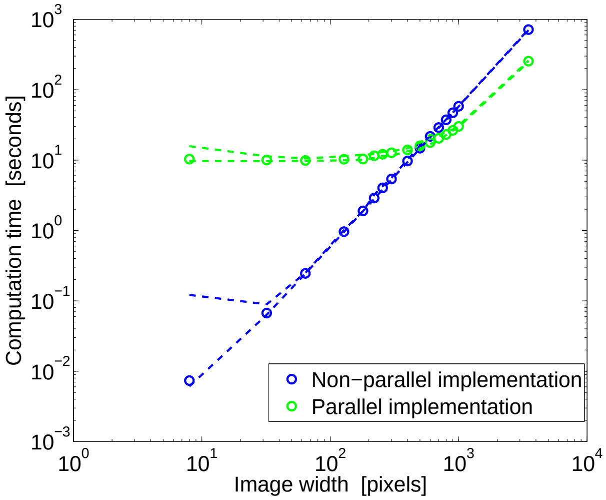

Figure 8.6: results from the test aiming to evaluate the efficiency of our parallel implementation of the ST calculation. Circles show medians, whereas dashed lines ranges of measured computation times.

### 8.5.3 ST calculation on histological images

Figure 8.7 shows the HSV representation of the ST of a WM image (100× magnification). For extremely small values of $\sigma$ (such as $\sigma = 0.1$ pixel), colours are well saturated, whilst for higher $\sigma$ the HSV encoding provides less saturated images. ST shows that axons are oriented along the left-right direction, being the images red. Nevertheless, blobs of different colours corresponding to other orientations are present, and their dimensions expand as $\sigma$ increases. Lastly, the figure shows that the size of border effects due to image zero-padding increases as $\sigma$ increases (homogeneous red and light blue areas close to the image borders).

Figure 8.8 shows similar information as figure 8.7 but for a GM image. The HSV representation is less saturated than in WM. Although a dominant hue exists (red, corresponding to left-right orientation), considerable parts of the image are coloured in blue and green and hence point towards different local orientations. For low $\sigma$, the hue of the HSV encoding varies quickly over space, whereas this variation gets smoother and smoother as $\sigma$ increases.

Figure 8.9 and 8.10 illustrate the distribution of ST-derived orientations $\theta$ for a WM and a GM image as $\sigma$ varies. The corresponding maximum-likelihood Watson and (marginal) weighted-Watson fits are also shown in green and blue. In WM, the distribution of $\theta$ has a bimodal peak at orientations close to $\theta = \pm\pi$ for all $\sigma$ values. Several peaks at different orientations can be seen for $\sigma$ as low as $\sigma = 0.1$ pixel, whereas two well distinct peaks are seen at coarser scales ($\sigma = 50.68$ pixel). The Watson and weighted-Watson fits detect these dominant peaks, and their concentration decreases when strong additional peaks are measured, as for $\sigma = 0.1$ pixel and $\sigma = 50.68$ pixel. The pattern in GM is very similar, although the concentration of the distributions is in general lower than in WM.

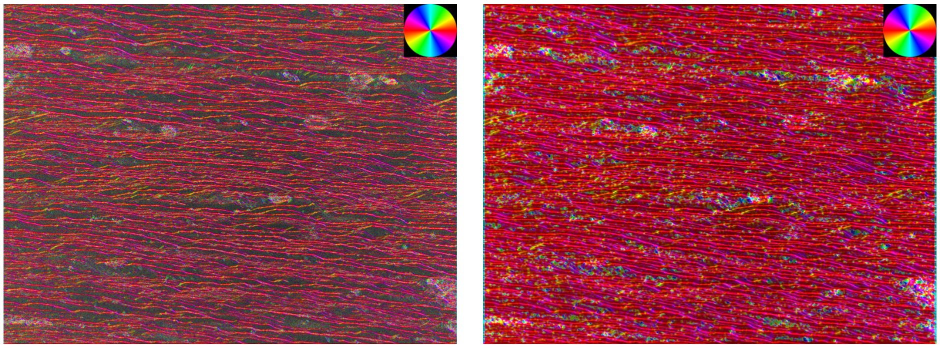

(a) $\sigma = 0.1$ pixel (b) $\sigma = 2.63$ pixel

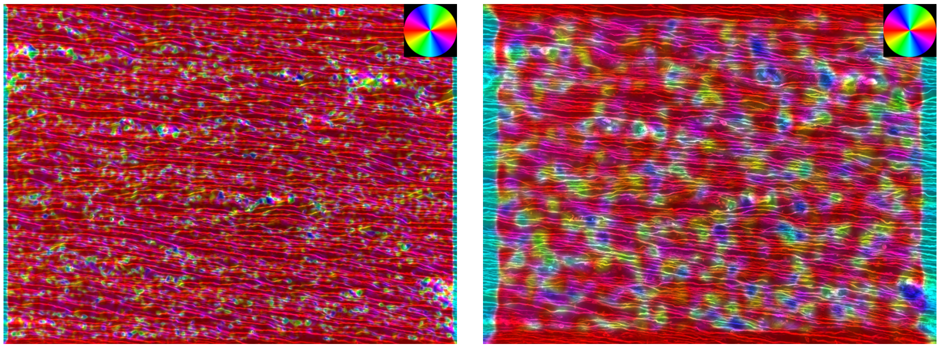

(c) $\sigma = 6.42$ pixel (d) $\sigma = 20.33$ pixel

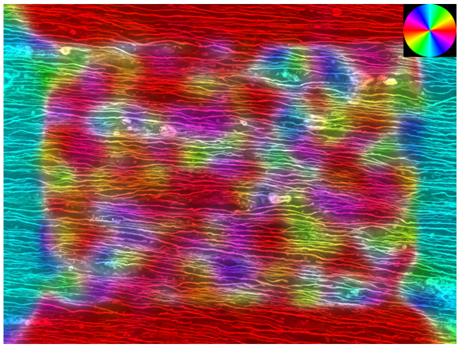

(e) $\sigma = 50.68$ pixel

Figure 8.7: HSV representation of the ST of the same WM image shown in figure 8.5. Results corresponding to various choices of $\sigma$ are presented. The colour-wheel describes how orientation is mapped onto the hue channel.

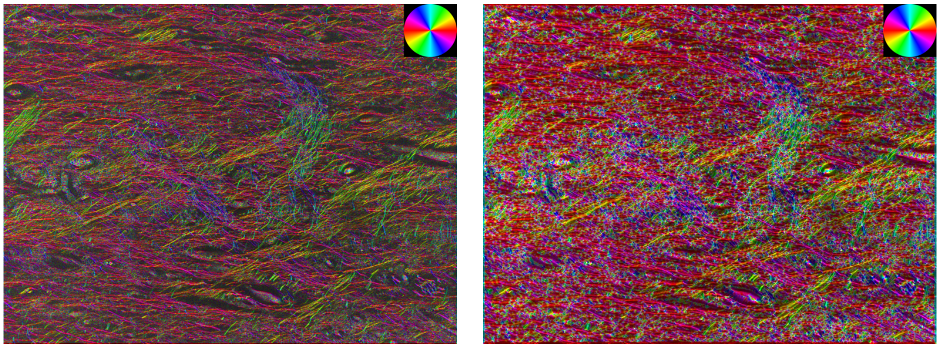

(a) $\sigma = 0.1$ pixel (b) $\sigma = 2.63$ pixel

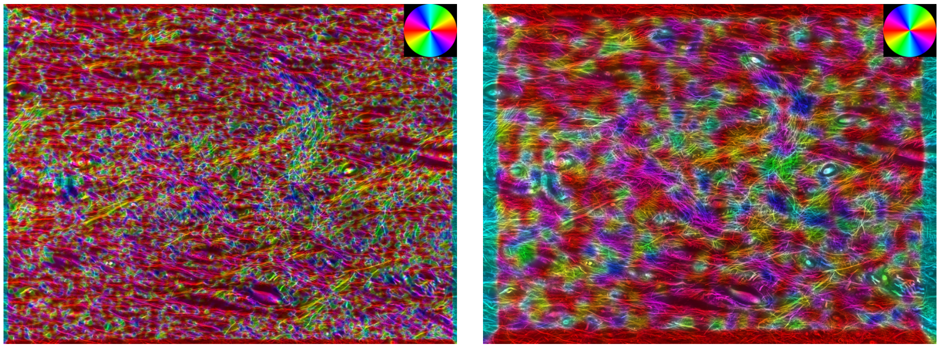

(c) $\sigma = 6.42$ pixel (d) $\sigma = 20.33$ pixel

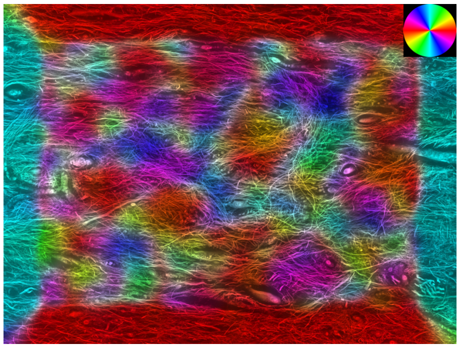

(e) $\sigma = 50.68$ pixel

Figure 8.8: HSV representation of the ST of the same GM image shown in figure 8.5. Results corresponding to various choices of $\sigma$ are presented. The colour-wheel describes how orientation is mapped onto the hue channel.

Lastly, figure 8.11 and 8.12 show the distribution of $\alpha$ in a WM and a GM image, for different $\sigma$. The experimental distribution of $\alpha$ in WM demonstrates that in general high values of $\alpha$ are more probable than low values. The distribution hits a peak at $\alpha = 1$ for $\sigma = 0.1$ pixel, $\sigma = 20.33$ pixel and $\sigma = 50.68$ pixel and for values slightly lower than 1 for $\sigma = 2.63$ pixel and $\sigma = 6.42$ pixel. The weighted-Watson fit captures the trend, showing increasing probabilities densities for increasing $\alpha$. Nevertheless, the weighted-Watson model always predicts the peak to be at $\alpha = 1$, and in general

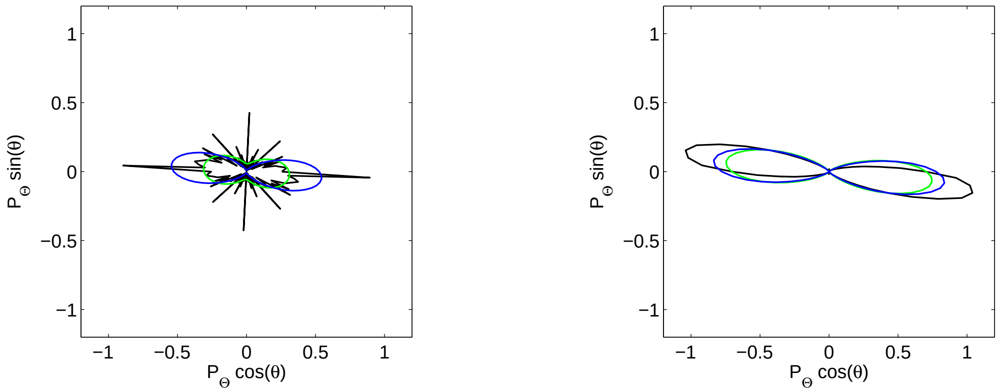

(a) $\sigma = 0.1$ pixel

(b) $\sigma = 2.63$ pixel

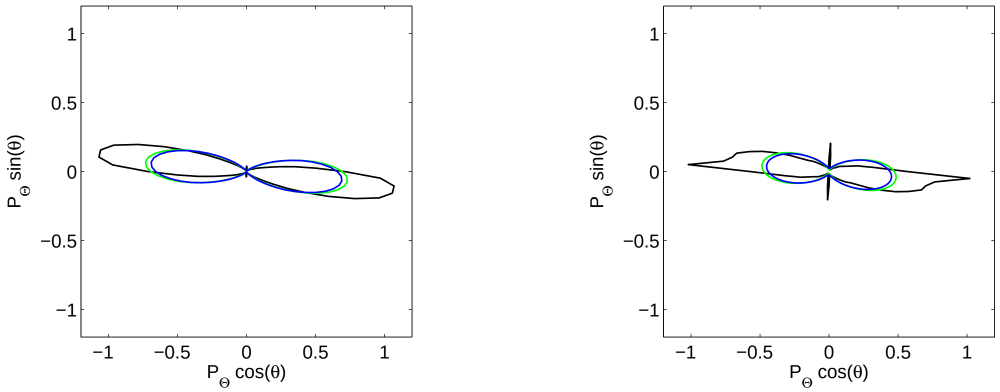

(c) $\sigma = 6.42$ pixel

(d) $\sigma = 20.33$ pixel

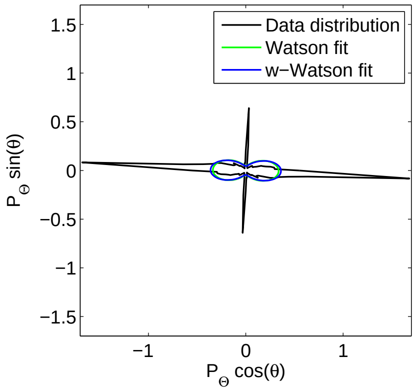

(e) $\sigma = 50.68$ pixel

Figure 8.9: distribution of ST-derived orientations $\theta$ and corresponding Watson and weighted-Watson fits for the same WM image shown in figure 8.5. Results for different choices of $\sigma$ are shown.

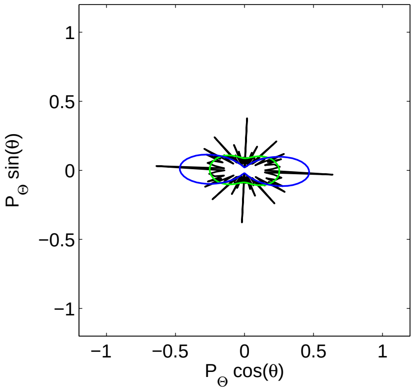

(a) $\sigma = 0.1$ pixel

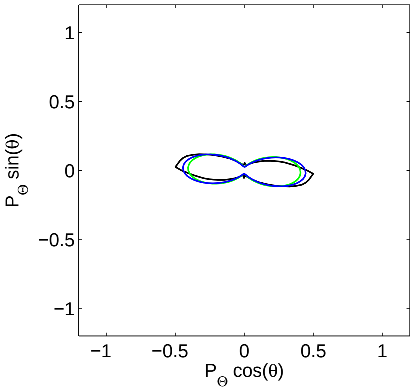

(b) $\sigma = 2.63$ pixel

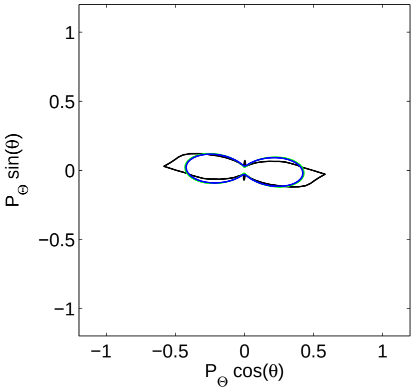

(c) $\sigma = 6.42$ pixel

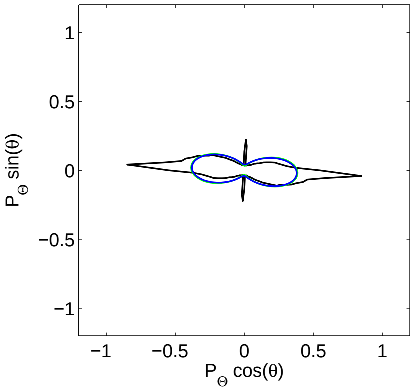

(d) $\sigma = 20.33$ pixel

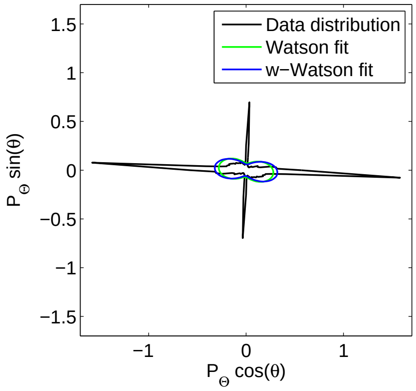

(e) $\sigma = 50.68$ pixel

Figure 8.10: distribution of ST-derived orientations $\theta$ and corresponding Watson and weighted-Watson fits for the same GM image shown in figure 8.5. Results for different choices of $\sigma$ are shown.

underestimates its amplitude. A similar behaviour is seen for GM, although the increase of the distribution for intermediate values of $\alpha$ is less sharp than in WM, and the peak value is hit at a lower $\alpha$ than in WM for $\sigma = 2.63$ pixel and $\sigma = 6.42$ pixel.

### 8.5.4 Analysis

Figure 8.13 illustrates the values of the maximised log-likelihood of the Watson and weighted-Watson models as a function of $\sigma$ for the WM (top) and the GM (bottom) images, at both magnifications of 100× and 200×. The figure shows that in WM, the log-likelihood of both models first grows and hits a local maximum, then decreases and lastly increases again. The log-likelihood of the weighted-Watson model is in all cases higher than that of Watson, and both models have higher log-likelihood in WM than in GM. The log-likelihood has a local maximum for the Watson model for $\sigma = 7.68$ pixel in WM at 100× and for $\sigma = 11.48$ pixel in WM at 200×, whereas for the weighted-Watson model the local maximum is hit at $\sigma = 2.63$ pixel in WM at 100× and at $\sigma = 5.16$ pixel in WM at 200×. The local maximum corresponds to the highest value for the weighted-Watson model. In GM, the log-likelihood of the weighted-Watson model shows a smoother dependence on $\sigma$ compared to WM, whereas that of the Watson model increases smoothly but monotonically with $\sigma$.

In figure 8.14 the behaviour of the CV as a function of $\sigma$ is illustrated. In WM, for both statistical models, the median CV decreases quickly as $\sigma$ increases from the lower limit of $\sigma = 0.1$ pixel. CV then hits a local minimum, and then increases monotonically. A similar behaviour is seen for GM, although the final increase is less steep. The minimum is hit for $\sigma = 3.89$ pixel (at 100×) and $\sigma = 6.42$ pixel (at 200×) for the weighted-Watson model in WM; at $\sigma = 6.42$ pixel (at 100×) and $\sigma = 10.22$ pixel (at 200×) for the Watson model in WM; at $\sigma = 5.16$ pixel (at 100×) and $\sigma = 14.01$ pixel (at 200×) for the weighted-Watson model in GM; at $\sigma = 10.22$ pixel (at 100×) and $\sigma = 17.8$ pixel (at 200×) for the Watson model in GM.

The contrast and the CNR between CV values in GM and WM is shown in figure 8.15. The figure demonstrates that although the Watson model provides a slightly better contrast, the CNR of the weighted-Watson model is higher than that of Watson for values of $\sigma$ close to the local maximum of the log-likelihood. Both C and CNR hit a peak at similar values for which CV is minimised. In particular, the CNR is maximum at $\sigma = 3.89$ pixel for both Watson and weighted-Watson models at 100× magnification, at $\sigma = 7.69$ pixel and at $\sigma = 6.42$ pixel for the Watson and weighted-Watson models at 200× magnification.

## 8.6 Discussion

In this chapter, we have studied the feasibility of applying ST analysis to images of sagittal sections of the spinal cord to obtain estimates of neurite orientations. We have also investigated the effect of the spatial scale of analysis on statistics of orientation dispersion evaluated from the calculated

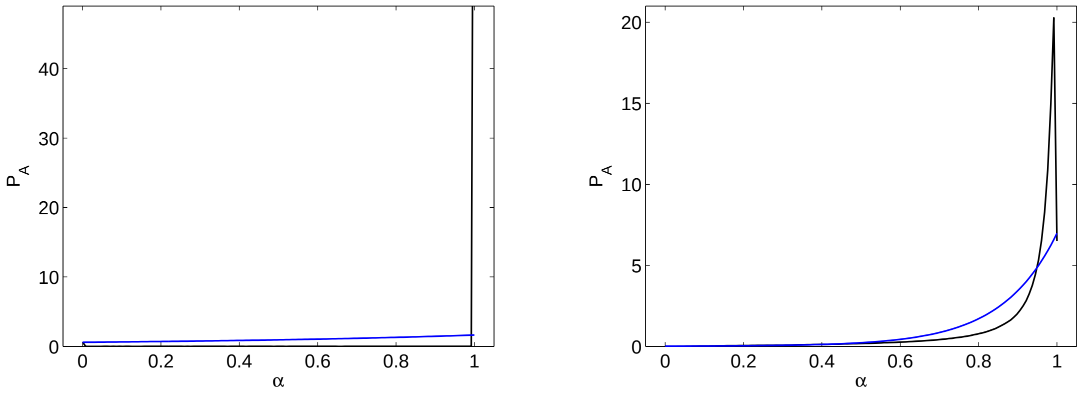

(a) $\sigma = 0.1$ pixel (b) $\sigma = 2.63$ pixel

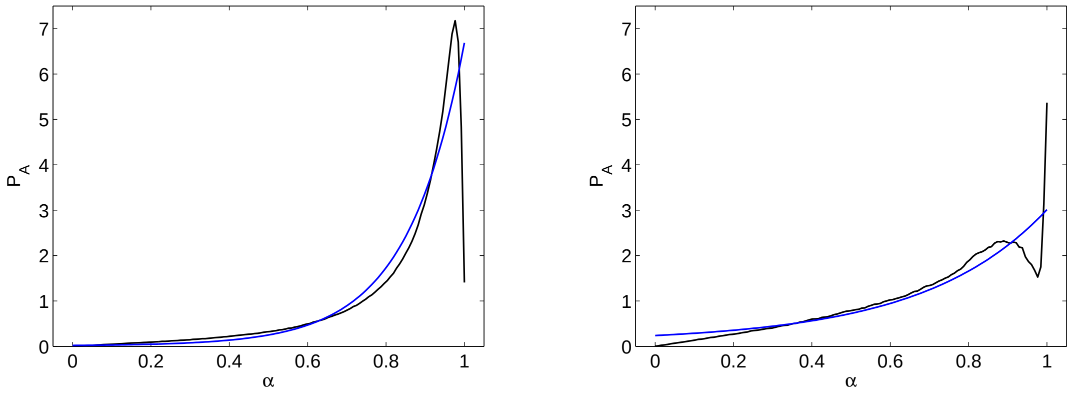

(c) $\sigma = 6.42$ pixel (d) $\sigma = 20.33$ pixel

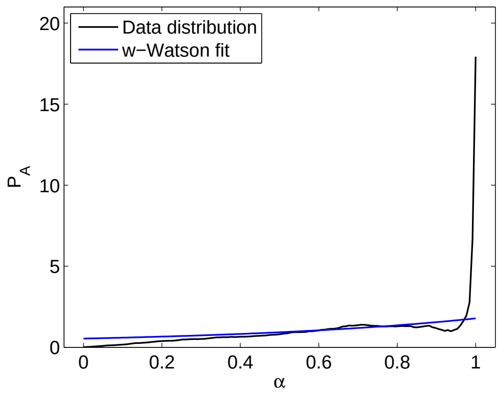

(e) $\sigma = 50.68$ pixel

Figure 8.11: distribution of ST-derived anisotropy index $\alpha$ and corresponding weighted-Watson fit for the same WM image shown in figure 8.5. Results for different choices of $\sigma$ are shown.

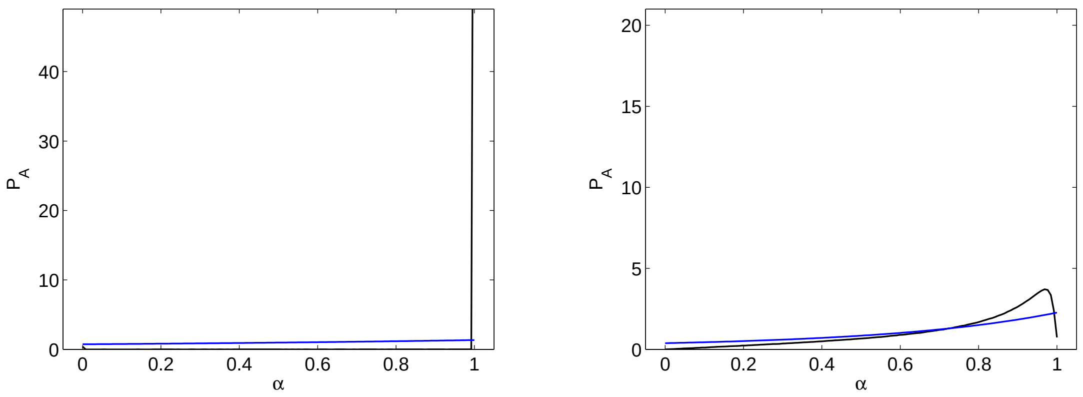

(a) $\sigma = 0.1$ pixel (b) $\sigma = 2.63$ pixel

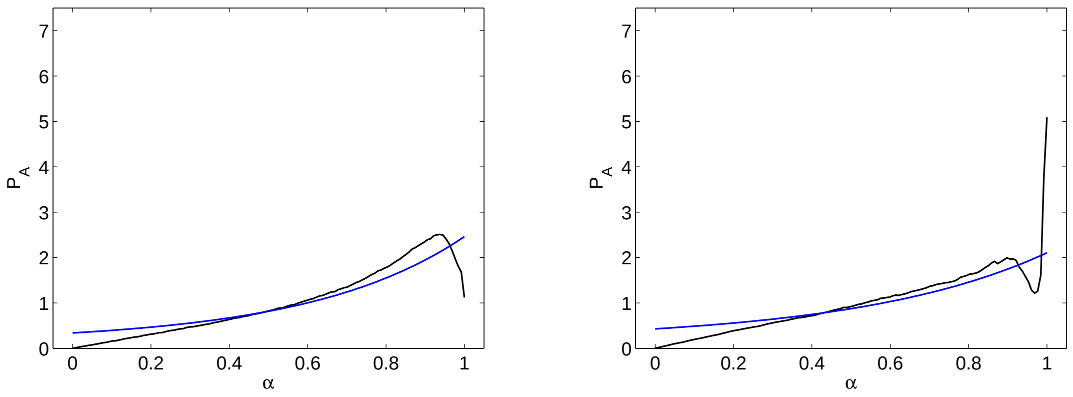

(c) $\sigma = 6.42$ pixel (d) $\sigma = 20.33$ pixel

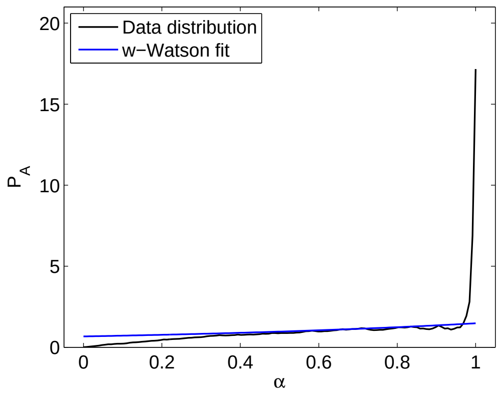

(e) $\sigma = 50.68$ pixel

Figure 8.12: distribution of ST-derived anisotropy index $\alpha$ and corresponding weighted-Watson fit for the same GM image shown in figure 8.5. Results for different choices of $\sigma$ are shown.

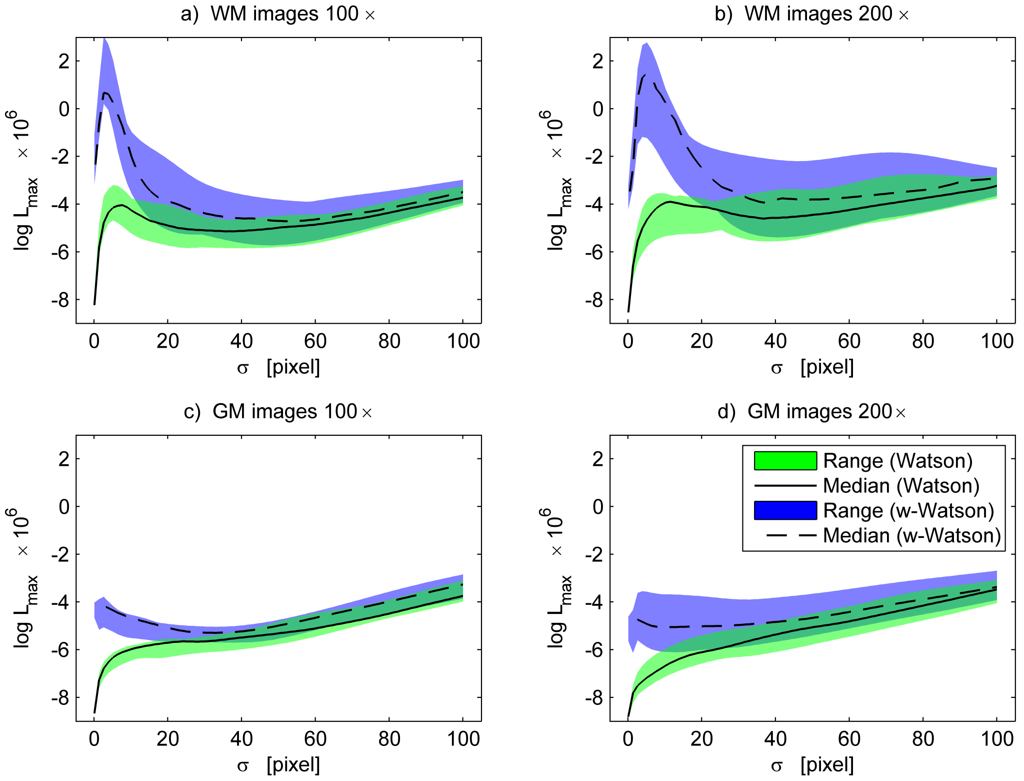

Figure 8.13: values of the maximised log-likelihood for the Watson and weighted-Watson models as a function of $\sigma$. a): WM images (100×); b): WM images (200×); c): GM images (100×); d): GM images (200×). The median of the log-likelihood is plotted as a solid (Watson) and dashed (weighted-Watson) line, whereas the range of measured log-likelihood values is shadowed in green (Watson) and blue (weighted-Watson).

ST orientations.

*Feasibility of the method*

We have proven that ST analysis applied to stained sagittal section of human spinal cord is a valid tool to obtain histological counterparts of NODDI neurite orientation dispersion index ODI. Sagittal sectioning allows the visualisation of neuronal processes, and ST analysis captures the differences in terms or neurite complexity between GM and WM, since for suitable values of the scale of analysis the spread of the estimated orientations shows a good contrast between the two tissue types.

*Variation of the local scale*

We have also investigated the effects of the choice of the scale of analysis, controlled by the parameter $\sigma$, regulating the properties of the discrete filters used to calculate the ST. For this purpose, we performed ST analysis varying $\sigma$ and employed two different directional probability densities

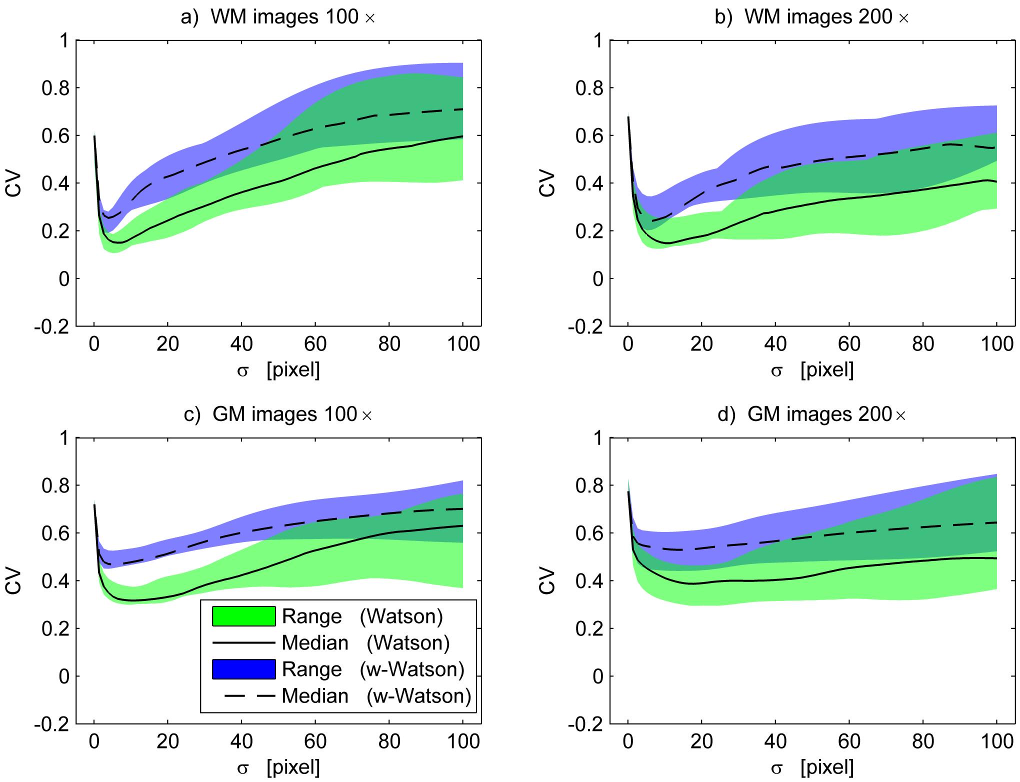

Figure 8.14: values of CV according to the Watson and weighted-Watson models as a function of $\sigma$. The same representation criteria of figure 8.13 are followed.

(one of which novel) to model the distributions of local image orientations $\theta$ and of the anisotropy index $\alpha$. In practice, the effects of the choice of $\sigma$ were characterised in terms of log-likelihood of the two models, CV and GM/WM contrast as shown by CV. Results from the set of images acquired at a magnification of 100× were in agreement with those from images acquired at 200×, with the patterns for the latter being shifted towards higher values of $\sigma$.

The main finding of this piece of investigation is that the choice of $\sigma$ does matter. $\sigma$ defines the scale at which information is integrated to characterise local structure, and tensors obtained for values of $\sigma$ very different from each other also differ notably. Extremely low $\sigma$ defines a spatial scale that may be even smaller than the characteristic length of morphological features such as the distance between distinct neuronal elements or the characteristic length of axonal undulation. Hence, their contribution towards the local value of the ST may be reduced. On the other hand, extremely high values of $\sigma$ may define a spatial scale that is too coarse, so that the differences in terms of neuronal morphology between GM and WM may be blurred and lost.

For extremely low $\sigma$, such as $\sigma = 0.1$ pixel, in both tissue types the histogram of orientations shows several spurious peaks, and the distribution of the anisotropy index $\alpha$ collapses to a delta in $\alpha = 1$, explaining the high saturation of the HSV encoding. The Watson and weighted-Watson

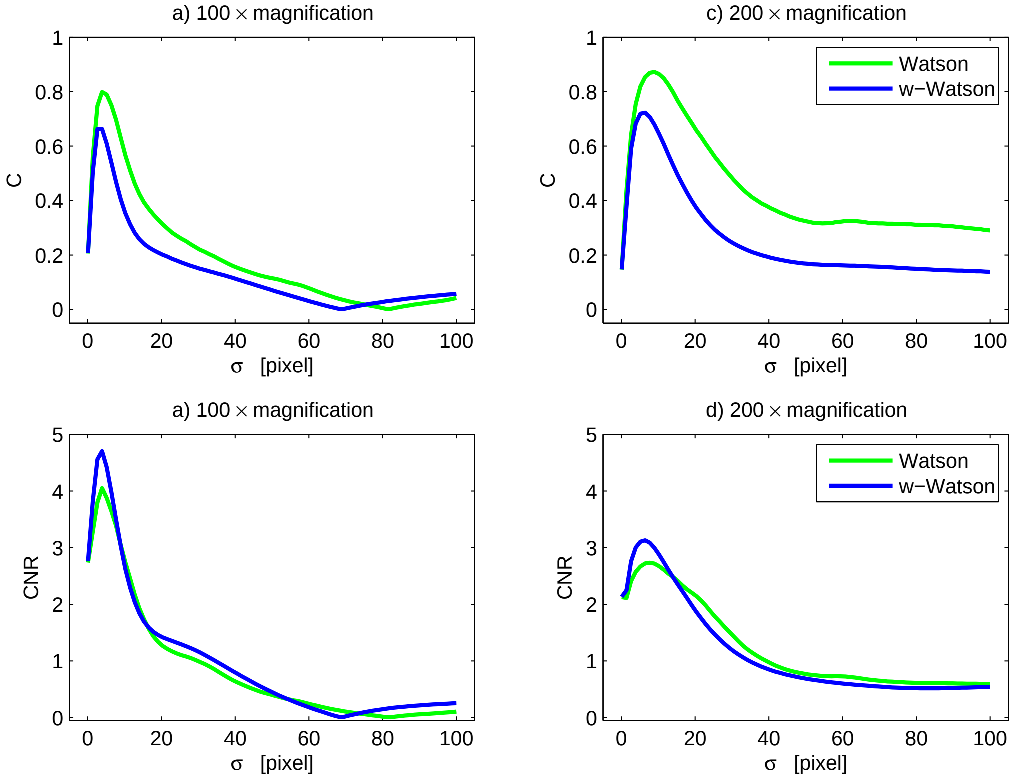

Figure 8.15: contrast and CNR between GM and WM for the CV statistics. a): contrast at 100× magnification; b): contrast at 200× magnification; c): CNR at 100× magnification; d): CNR at 200× magnification.

models do not describe the distributions appropriately. In WM, for values of $\sigma$ bigger than 0.1 pixel, both statistical models describe the data better, as revealed by the an increasing log-likelihood that also hits a maximum. At those spatial scales, the distribution of orientations is smooth and shows a bimodal peak, while the distribution of anisotropy increases for increasing $\alpha$, as indeed captured by the weighted-Watson model. Similar behaviours of the distributions are also seen in GM. In WM, for even bigger $\sigma$, the quality of fit of the models decreases and increases again, and for the Watson model is maximised at $\sigma = 100$ pixel. Generally in GM, the higher $\sigma$ is, the better the models describe the data, since the log-likelihood is essentially monotonic and hits its maximum at $\sigma = 100$ pixel. However, if $\sigma$ grows too much, i.e. bigger than roughly $\sigma = 20$ pixel, the experimental distribution of orientations shows additional peaks and the distribution of anisotropy concentrates to $\alpha = 1$ for both WM and GM. This corresponds to an extremely low contrast in terms of orientation dispersion between the two tissues, suggesting that when the spatial scale of analysis is too coarse the models overfit the data and differences in terms of neurite architecture between WM and GM are blurred and lost.

*Performance of patch-wise statistical models in WM and GM*

ST analysis appears more suitable for WM, rather than GM, since for the former a clear peak of the log-likelihood is seen and since in WM the actual values of log-likelihood are higher than in GM. This may be a consequence of the potentially higher amount of through-plane fibres in GM, which our 2D analysis cannot account for, as well as the higher amount of unspecific staining.

*Comparison between Watson and weighted-Watson models*

In this chapter we have introduced a novel model to describe the spread of ST-derived orientations of histological images of the spinal cord, the weighted-Watson distribution. We have also studied a conventional model, the Watson distribution, which is related to the NODDI neurite orientation distribution function. Our analysis reveals that the weighted-Watson model provides performance comparable, if not superior, to the standard Watson model. The log-likelihood of the weighted-Watson distribution surpasses that of Watson in WM. Unlike the Watson framework, which completely disregards the anisotropy index $\alpha$, the weighted-Watson model captures the trend of the marginal distribution of $\alpha$. It accounts for the uncertainty of orientations at the individual pixel level, without requiring any thresholding. Moreover, it also shows better CNR than the Watson distribution, although its contrast C is slightly lower.

*Limitations*

This work has two main limitations. The first, and possibly main one, is that we limited ourselves to 2D analysis, relying on the hypothesis that sagittal sectioning is adequate to capture neurite orientation dispersion equally well in both WM and GM. This is equivalent to state that there is no variation in terms of fibre orientation along the direction orthogonal to the sectioning plane, and that the amount of through-plane neurites is negligible. Although this appears as a reasonable hypothesis in WM, especially far from areas containing collateral fibres, it may not hold true for the intricate dendritic trees in GM or at the interface between WM and GM, where WM axons branch and project into GM. Nevertheless, the variation in terms of neurite orientation in our GM images was sufficient to produce an appreciable contrast between the two tissue types.

Another limitation is related to the staining method. Here, we employed Palmgren's silver staining, which has been proven to optimally demonstrate axons [41]. Nevertheless, it is non-specific, since it also impregnates cell bodies and other elements, especially in GM. Therefore, a small amount of non-neurite material can contribute to the estimation of the local orientation $\theta$ and of its dispersion. Nevertheless, undesired stained areas could always be masked out before running ST analysis.

## 8.7 Conclusion

In this chapter we studied optimal strategies of obtaining a histological-derived orientation dispersion index for the human spinal cord, for the prospective validation of NODDI ODI.

We demonstrated a ST analysis framework for sagittal histological images of the human spinal cord, which provides contrast in terms of orientation dispersion between WM and GM.

We have also introduced a new directional statistical model, the weighted-Watson distribution, and proved that it could be a valid alternative to standard directional statistics models to describe orientations as estimated from ST analysis.

Finally, we have investigated the effect of the choice of the ST scale of analysis, which was crucial for the precise characterisation of neurite orientations. Given the resolution of our histological images, values of $\sigma$ of the order of 1 $\mu$m, comparable to the characteristic length of axonal and dendritic features, seem recommendable. For our own purposes, we will use $\sigma = 0.89\,\mu$m for ST-derived estimation of neurite orientation dispersion in the next chapter.

In conclusion, ST analysis of high-resolution sagittal images is a valid tool for the histological validation of DW MRI-derived orientation dispersion metrics, such as NODDI ODI, in the spinal cord. We adopt the method for our MRI-histology comparison shown in the next chapter, and point out that careful design of the scale at which information is integrated to calculate the ST is of high importance.

# Chapter 9

# Histological correlates of NODDI metrics

## 9.1 Introduction

DW MRI methods have the potential of providing indices specific to tissue microstructure, which could become novel, useful biomarkers in a number of conditions. Such novel approaches rely on certain hypotheses that are necessary for their practical application in clinical scenarios. These hypotheses aim to capture salient features of the tissue, and are often formulated with healthy structures in mind. Comparison of the new MRI-derived metrics to ground truth histology is essential to confirm the validity of the model assumptions and to confirm the specificity of the innovative indices, while excluding the confounding effect of other factors.

We have previously shown the potential of applying NODDI to the spinal cord *in vivo* and in clinical scenarios. NODDI is designed to provide salient descriptors of neuronal morphology, notably the density and the orientation dispersion of neurites, which could be useful biomarkers in conditions such as MS.

The objective of this chapter is to validate NODDI in the non-pathological and MS spinal cord. We compared NODDI metrics obtained from fixed specimens of human spinal cord to quantitative histological measures from the same samples. We performed a similar analysis also for DTI indices, since DTI is still the most common DW MRI method in spinal cord applications. The histological features were calculated from tissue sections impregnated with Palmgren's silver method [145] to delineate neuronal processes, and from sections immunostained with primary antibodies to demonstrate myelin (proteolipid protein, PLP), inflammation (microglia, labelled with ionized calcium-binding adapter molecule 1, Iba1), astrocytes (glial fibrillary acidic protein, GFAP) and neurons/axons (phos. and non-phos. neurofilaments).

For this work, we exploited the technical achievements discussed in chapters 7 and 8, namely: i) the implementation of a rich high-resolution DW MRI protocol at high-field; ii) the adaptation of NODDI analysis from *in vivo* for *post mortem* fixed spinal cord tissue; iii) a strategy to identify the location of histological material in the MRI images, enabling the correspondence between MRI and histology; iv) the estimation of neurite orientation dispersion from sagittal histological images.

## 9.2 Research dissemination

Some of the results discussed in this chapter have been presented in preliminary, abstract form at two international scientific meetings, as listed below.

- "Histological metrics confirm microstructural characteristics of NODDI indices in multiple sclerosis spinal cord". Grussu F. et al, ISMRM annual meeting (2015), p.0909, oral presentation.
- "Quantitative histological correlates of NODDI orientation dispersion estimates in the human spinal cord". Grussu F. et al, ISMRM annual meeting (2015), p.0154, oral presentation.
- "Quantitative histological validation of NODDI MRI indices of neurite morphology in multiple sclerosis spinal cord". Grussu F. et al, 31st ECTRIMS congress (2015), p.0469, traditional poster presentation.

A manuscript is currently in preparation for submission to a peer-reviewed scientific journal.

## 9.3 Methods

We compared NODDI metrics derived from high-field DW data of formalin-fixed spinal cord tissue (two controls cases and two MS cases) to histological features obtained from the same specimens, following the pipeline presented in chapter 7. In the next sections, we summarise the steps that led to the comparison of NODDI metrics to histology.

### 9.3.1 Samples

Four samples were used for the comparison NODDI-histology. These were specimens 3, 4, 5 and 6 in chapter 7 (table 7.1, section 7.4). The non-MS specimens were obtained from subjects deceased due to non-neurological problems, while the MS specimens were obtained from progressive cases (one PPMS, one SPMS) whose decease was attributed as secondary to MS. For both controls and MS cases, one specimen was obtained from the upper thoracic spinal cord, while the other from the upper lumbar spinal cord. Details regarding the MS cases, including the disability level evaluated with the *expanded disability status scale* (EDSS) [102], are reported in table 9.1.

All samples were immersion-fixed in formalin within 48 hours from decease, and stored in 10% formalin. Tissue was obtained for employment in experimental sessions following appropriate consent and research ethics committee approval. All experimental procedures were in compliance with Human Tissue Authority guidelines and the 2004 UK Parliament *Human Tissue Act*.

### 9.3.2 High-field DW MRI

On the day preceding MRI, samples were removed from the fixative and washed in a bath of 10 mM PBS for 24 hours, with the liquid being replaced by freshly prepared solution every 12 hours. MRI was performed with the samples immersed in PBS, following the procedure described previously in section 7.3.3 of chapter 7, and summarised for completeness again below.

A 9.4T horizontal bore scanner (Agilent Technologies, Santa Clara, CA, USA) was used for imaging. The scanner is located in Queen Square House, Queen Square, Institute of Neurology (Department of Brain Repair and Rehabilitation). The MRI machine was equipped with a 60 mm inner diameter gradient coil, capable of delivering a maximum gradient strength of 1 T m$^{-1}$ with a maximum slew rate of 6.7 KT m$^{-1}$ s$^{-1}$. For signal reception, a 33 mm diameter volume coil (Rapid Biomedical GmbH, Rimpar, Germany) was used.

The MRI protocol consisted of sagittal DW images for quantitative analysis as well as axial images acquired for anatomical reference. The protocol was already discussed in chapter 7 (MRI sessions 4 and 5, also listed in table 7.2), and is summarised below.

#### Preparation of a custom-made holder for imaging

Prior to MRI, samples were sectioned in two halves by a midsagittal cut, to allow the correspondence of MRI and histology. Samples were scanned in two sessions: specimens 3 and 4 in one session, and specimens 5 and 6 in the other session, as previously reported in tables 7.1 and 7.2.

In each session, a custom-made holder was obtained placing the four chunks of tissue resulting from the cut of two samples in the four slots of a syringe plunger. The tissue was firmly tied with VELCRO® and medical bandage, and the plunger was fit inside a syringe. This was filled with freshly prepared 10 mM PBS solution, and sealed. For imaging, the holder was placed within the receiver coil, and temperature was measured and kept stable at 35° C with a temperature probe and an MRI compatible air heater, connected to an external monitoring system (Small Animals Instruments, Inc., Stony Brook, NY, USA).

#### Quantitative MRI: DW protocol

DW images were acquired sagittally, in parallel to the surface exposed by the midline cut. The diffusion encoding protocol consisted of 25 non-DW images and of 6 $b$-shells of increasing angular resolution ($b = \{520, 2080, 4680, 8320, 13000, 18720\}$ s mm$^{-2}$, with respectively 6, 15, 24, 33, 42 and 51 gradient directions; $\delta = 12$ ms and $\Delta = 18$ ms for all shells). Other parameters were: $T_E = 39.5$ ms; $T_R = 2200$ ms, resolution of 164×200×800 $\mu$m$^3$, FOV of 21×51.2×16 mm$^3$.

#### Anatomical reference: axial views

A multi-slice spin echo sequence was used to acquire axial images, which were used to plan the histological procedures. The axial scans consisted of 24 slices, with FOV of 25.68 × 25.68 mm$^2$, slice thickness of 2 mm, matrix size of 256 × 128, $T_E = 20$ ms, $T_R = 614$ ms.

| Specimen | Sex | Age at decease [years] | Cause of decease | Cord level | Length [cm] | Disease subtype | Disease duration [years] | EDSS before death |
|---|---|---|---|---|---|---|---|---|
| 3 | F | 67 | Pneumonia, secondary to MS | Upper lumbar | 2.4 | SPMS | 33 | 9.5 |
| 5 | M | 75 | Asphyxiation, secondary to MS | Upper thoracic | 3.3 | PPMS | 21 | 6.5 |

Table 9.1: information about the specimens of spinal cord tissue obtained from the MS cases.

| Name of protocol | $b$-shells $[\mathrm{s\,mm^{-2}}]$ | Gradient directions | Models used for fitting |
|---|---|---|---|
| *DataFull* | $\{520, 2080, 4680, 8320, 13000, 18720\}$ | $\{6, 15, 24, 33, 42, 51\}$ | NODDI, DTI |
| *DataGaussian* | $\{520, 2080, 4680\}$ | $\{6, 15, 24\}$ | DTI |

Table 9.2: details of the DW protocols employed to fit the NODDI and DTI models. Notice that the *dot* compartment was added to both models to improve the quality of the fitting, as common in *ex vivo* imaging.

### 9.3.3 DW MRI signal model fitting

The NODDI model was fitted to the acquired data using the NODDI Matlab toolbox. We also fitted a second model of the DW signal, DTI, since DTI is still a routine method in clinical studies of the spinal cord [203] and is known to be sensitive to diffuse MS pathology [25, 99]. In-house Matlab code implementing the same fitting algorithm as the NODDI Matlab Toolbox was used to fit the parameters of the DTI model.

#### Voxel-wise metrics

Model fitting was carried out after correcting $b$-values and gradient directions to account for additional diffusion-weighting due to imaging and spoiling gradients, as previously described in detail in section 7.3.2 of chapter 7. Both NODDI and DTI models were fitted including an additional *dot* compartment, since this improved the quality of fit, as previously discussed in chapter 7. The *dot* describes the contribution of a stationary water pool, and accounts for residual signal well above the noise floor that is measured even for very intense diffusion weighting and for gradient directions parallel to WM fibres.

For NODDI, we fixed the intrinsic diffusivity of the isotropic compartment $d_{\text{iso}}$ to the mean ADC within an ROI drawn manually in PBS voxels. Also, we fixed the intrinsic diffusivity of the neural tissue $d_{\|}$ to $d_{\|} = 1.50\ \mu\text{m}^2\,\text{ms}^{-1}$, as chapter 7 has shown that this value is a reasonable choice, providing good quality of fit.

The following voxel-wise metrics were obtained, whose meaning has been discussed in the previous chapters of this thesis. For NODDI: isotropic (free water) volume fraction ($v_{\text{iso}}$); intra-neurite tissue volume fraction ($v_{\text{in}}$); orientation dispersion index (ODI). For DTI: fractional anisotropy (FA); axial diffusivity (AD); radial diffusivity (RD); mean diffusivity (MD). Furthermore, the volume fraction of the *dot* compartment included for the fitting of both diffusion models was also obtained ($\text{DVF}_{\text{NODDI}}$ for NODDI and $\text{DVF}_{\text{DTI}}$ for DTI).

#### Data sets

The two diffusion models (NODDI and DTI, with the inclusion of the *dot* compartment) were fitted to the whole six-shell DW set of measurements (data set *DataFull*). Moreover, we fitted DTI to a reduced data set, containing only the $b = \{520, 2080, 4680\}\ \text{s}\,\text{mm}^{-2}$ shells (data set *DataGaussian*). This was done to limit the contribution of non-Gaussian diffusion, which is more evident as the $b$-value increases [33], since DTI is a model that relies on the hypothesis of Gaussianity of the diffusion process.

Table 9.2 summarises the data sets employed in this chapter.

### 9.3.4 Histological procedures

Within one month of the MRI sessions, samples were taken to the Nuffield Department of Clinical Neurosciences of the University of Oxford for histological processing.

| Metric | Symbol | Origin | Meaning |
|---|---|---|---|
| Isotropic volume fraction | $v_{\text{iso}}$ | NODDI | Amount of free water |
| Intra-neurite volume fraction | $v_{\text{in}}$ | NODDI | Amount of neural tissue occupied by neurites |
| Orientation dispersion index | ODI | NODDI | Spread of dendrite and axon orientations |
| *Dot* volume fraction | $\text{DVF}_{\text{NODDI}}$ | NODDI | Amount of stationary water |
| Fractional anisotropy | FA | DTI | Anisotropy of the diffusion profile |
| Axial diffusivity | AD | DTI | Diffusivity along the principal diffusion direction |
| Radial diffusivity | RD | DTI | Diffusivity across the principal diffusion direction |
| Mean diffusivity | MD | DTI | Mean amount of diffusion |
| *Dot* volume fraction | $\text{DVF}_{\text{DTI}}$ | DTI | Amount of stationary water |
| Circular variance | CV | Histology | Spread of dendrite and axon orientations |
| Myelin staining fraction | MSF | Histology | Density of myelin |
| Neurofilament staining fraction | NSF | Histology | Density of neuronal elements |
| Astrocyte staining fraction | ASF | Histology | Density of astrocytes |
| Microglia staining fraction | $\mu$GSF | Histology | Density of microglia |

Table 9.3: summary of the metrics derived from NODDI and DTI analysis of DW MRI data and from histology. The *dot* compartment was included in both diffusion MRI models.

### Strategy to determine the radiographic position of histological sections

Samples were dehydrated and embedded in paraffin, following standard histological procedures. Subsequently, 10 $\mu$m-thick sections were sliced manually from the formalin-fixed paraffin-embedded samples using a microtome, for subsequent staining and optical imaging. The histological material was sectioned following the strategy previously described in chapter 7, section 7.3.3. Briefly, the material was sliced sagittaly, from the surface exposed by the midline cut performed with a surgical blade prior to MRI. Consultation of the axial MRI views, onto which the sagittal slices acquired for DW imaging were overlaid, allowed the identification of the radiographic position of the histological sections. Shrinkage of the samples due to the dehydration necessary for paraffin embedding was accounted for, via measurement of the dimensions of the samples before and after the embedding process.

### Staining and optical imaging

For each spinal cord sample, four sections were obtained from two separate MRI slices (two sections per MRI slice, 200 $\mu$m apart from each other) and immunostained with primary antibodies to demonstrate myelin (proteolipid protein, PLP), inflammation (microglia labelled with Iba1), and astrocytes (glial fibrillary acidic protein, GFAP), while neurons/axons were detected by both immunohistochemistry (phosphorylated and non-phosphorylated neurofilaments) and impregnation with an optimised [40, 41] Palmgren's silver procedure [145].

Afterwards, high resolution optical images of the stained sections were acquired in digital format with an Aperio slide scanner (ScanScope AT Turbo) at a magnification of 400×, and downsampled for a final pixel resolution of $1.008 \times 1.008\,\mu\text{m}^2\,\text{pixel}^{-2}$.

## 9.3.5 Histological feature calculation

The histological images were analysed with in-house Matlab code in order to extract quantitative features to which NODDI and DTI metrics could be related. We estimated neurite orientation dispersion and the fraction of material stained by the neurofilamants, PLP, Iba1 and GFAP immunostains. Histological features were evaluated patch-by-patch, after dividing the histological images into patches of size of 164×200 $\mu\text{m}^2$, matching the within-slice MRI resolution. All histological features are defined in the range $[0;1]$.

### Neurite orientation dispersion

Neurite orientation dispersion was estimated from the sections impregnated with the Palmgren's silver method. They were preferred to the neurofilaments images since Palmgren's silver impregnation [145] more consistently demonstrates axons as compared to neurofilaments [41], at the price of a lower specificity.

The local image orientation was evaluated for all Palmgren's silver images with ST analysis. We used the same routines employed for the study described in the previous chapter, choosing $\sigma =$

0.89 $\mu$m to control the spatial scale of analysis (detailed description of the Matlab implementation available in section 8.4.2 of chapter 8).

We calculated patch-wise circular variance (CV) of ST-derived orientation according to equation 8.8 to obtain an index of neurite orientation dispersion, after manual removal of gross cell bodies and blood vessels. CV ranges in $[0;1]$, with increasing CV implying increasing orientation dispersion. CV was obtained according to a conventional Watson model, which was preferred to our weighted-Watson approach. Preliminary exploratory tests demonstrated that the values of CV obtained with the conventional Watson model (equation 8.8) and with the novel weighted-Watson model (equation 8.15) are highly correlated, and follow similar trends. For this reason, a conventional model was employed as a first exploratory step, appearing suitable for the purposes of the study.

#### Fractions of stained material

We evaluated the fractions of material labelled by the immunohistochemistry within the same patches of size 164×200 $\mu$m$^2$ employed for the calculation of the CV. As a preprocessing step, spatial linear trends of the staining intensity were removed.

For each image, a well established clustering algorithm (*k-means* with *k-means++* initialisation [6]) was run in Matlab to segment the stained material. We chose to segment three clusters, representing the space of the cover slip outside the specimen, the specimen background and the actual stained material. We considered as stained material pixels belonging to the darkest cluster.

Finally, we evaluated patch-wise fraction of stained material as the ratio between the number of pixels that were segmented in each patch and the total number of pixels in the same patch.

The following nomenclature will be employed for the indices of staining fraction, which all range in $[0;1]$: *myelin staining fraction* (MSF) for the PLP immunostaining; *neurofilament staining fraction* (NSF) for the neurofilament immunostaining; *astrocyte staining fraction* (ASF), for the GFAP immunostaining; *microglia staining fraction* ($\mu$GSF) for the Iba1 immunostaining.

Table 9.3 recapitulates the metrics the were object of analysis in this chapter.

### 9.3.6 MRI-histology registration

Histological images were registered to the corresponding MRI slices from which the histological material was obtained. The registration transformation were then applied to the quantitative histological maps, which were evaluated in native histology space.

We implemented a landmark-guided non-linear registration similar to other approaches previously reported in literature [99], basing our algorithm on Matlab routines (Image Processing Toolbox, function *fitgeotrans*). For each histological image, we proceeded as follows.

1. The histological image was downsampled to the resolution of the patch-wise maps and of the within-MRI-slice resolution (164×200 $\mu$m$^2$);
2. we visually identified and manually marked matching control points in the downsampled histological image and in the corresponding mean $b = 0$ image from MRI;

| Model no. | Equation |
|---|---|
| 1 | $m = \beta_0 + \beta_1 \text{CV} + \beta_2 \text{MSF} + \beta_3 \text{NSF} + \beta_4 \text{ASF} + \beta_5 \mu\text{GSF}$ |
| 2 | $m = \beta_0 + \beta_1 \text{CV} + \beta_2 \text{MSF} + \beta_3 \text{NSF}$ |
| 3 | $m = \beta_0 + \beta_1 \text{CV} + \beta_2 \text{NSF}$ |
| 4 | $m = \beta_0 + \beta_1 \text{MSF} + \beta_2 \text{NSF}$ |
| 5 | $m = \beta_0 + \beta_1 \text{ASF} + \beta_2 \mu\text{GSF}$ |

Table 9.4: linear regression models that were fitted to the ROI-wise mean values of NODDI and DTI metrics. In the table, $m$ stands for the generic metric obtained from NODDI ($v_{\text{iso}}$, $v_{\text{in}}$, ODI and $\text{DVF}_{\text{NODDI}}$) and DTI (FA, AD, RD, MD and $\text{DVF}_{\text{DTI}}$). The models were fitted for the controls and the MS cases separately. For NODDI, the fitting was performed considering the metrics obtained from data sets *DataFull*, whereas for DTI, metrics were derived from data sets *DataFull* and *DataGaussian*.

3. the manually marked points were employed to estimate a non-linear transformation warping the downsampled histological image to the MRI space. Among all possible transformations available in Matlab, we chose the one that maximised a *Dice coincidence index* [45], similarly to [193]. The index measures the overlap of two sets, and in this work it was calculated between: i) the outline of the sample drawn on the mean $b = 0$ image; ii) the outline of the sample drawn on the downsampled histological image (outline warped to the MRI space);
4. the estimated registration transformation was applied to warp the patch-wise map obtained from the histological image (i.e. CV if Palmgren's silver; MSF if PLP; NSF if neurofilaments; ASF if GFAP; $\mu$GSF if Iba1).

### 9.3.7 Visual inspection of quantitative maps

All MRI-derived and histology-derived quantitative metrics listed in table 9.3 were visually inspected, after warping the latter to the MRI space.

### 9.3.8 Statistical analysis

Statistical analysis was performed to investigate the association between NODDI and DTI metrics to histological features. NODDI metrics evaluated from data set *DataFull* and DTI metrics evaluated from data sets *DataFull* and *DataGaussian* were considered (see table 9.2).

Specifically, linear regression analysis was performed to assess quantitatively the association between NODDI/DTI metrics and histological parameters. The regression was run on a data set consisting of the mean values of the metrics within manually drawn ROIs. ROIs were drawn in MRI space, on the mean non-DW images, far from areas of low coil sensitivity, areas distorted by the proximity of residual air bubbles and far from interfaces, to limit the effect of misregistrations histology-MRI. In practice, the ROIs were drawn within non-focal WM and GM and within focal WM and GM lesions for the MS cases. On the other hand, for the control cases, ROIs were outlined in WM and GM.

Before running the regressions, values from the two different histological sections taken from each MRI slice were averaged.

### Choice of outcome measures and predictors

The set of ROI-wise values of MRI and histological indices was used to regress each MRI metric $m$ (outcome measure) as a linear combination of histological indices CV, MSF, NSF, ASF and $\mu$GSF (predictors). We chose MRI indices as outcome measures since in practice one would use MRI as a non-invasive probe of the underlying, unknown histological features. With an analogy borrowed from engineering, MRI indices would practically be used as "*sensors*" of the underlying histological characteristics. The scenario is similar, for instance, to that of certain chemosensors based on ISFET technology [143], used to measure concentrations of ions in solutions. Such sensors in fact provide as output a voltage or electric current, which is the true outcome of any experiment and from which the underlying ion concentration needs to be inferred. The voltage/current is practically handled as a dependent variable, and used as a probe of the ion concentration. In our view, the same holds here, since NODDI/DTI metrics are the outcome of the MRI experiment, and act as probes of the underlying microstructural properties, from which they depend.

Our analysis allows the evaluation of the sensitivity of each MRI metric $m$ with respect to the histological parameters (i.e. quantities $\frac{\partial m}{\partial \text{CV}}$, $\frac{\partial m}{\partial \text{MSF}}$, $\frac{\partial m}{\partial \text{NSF}}$, $\frac{\partial m}{\partial \text{ASF}}$ and $\frac{\partial m}{\partial \mu\text{GSF}}$), while controlling for specificity, since the effect of all histological features can be modelled jointly.

### Linear regression models

In this work, we fitted five different univariable linear regression models, independently for the control cases and the MS cases, using the R software (`http://www.r-project.org`, function *lm*). The five models are listed in table 9.4, and focus on the relation between NODDI/DTI metrics with different aspects of the neural tissue cellular environment.

The first model employs all histological features as joint predictors of MRI. In addition, we grouped histological metrics into features directly related to neurons/neurites (CV, MSF and NSF, in model number 2) and features of extra-neurite space (glial fractions ASF and $\mu$GSF, in model number 5). This allows the investigation of whether NODDI/DTI metrics are more strongly associated to one group of features, rather than the other, which follows from fitting separately models 2 and 5.

Moreover, we derived two additional models from the features mapping properties of neurons/axons (CV, MSF and NSF). Model number 3 focusses on the joint dependence of MRI metrics on the orientation dispersion and on the density of neuronal processes. These two features are believed to be key factors contributing to the diffusion signal profile in neural tissue [88, 215], and model number 3 enables the investigation of their joint contribution to the outcome MRI metrics. On the other hand, model number 4 was formulated to study specifically demyelination and axonal/neuronal loss. The model employs myelin and neurofilament density metrics (MSF and NSF) as predictors, which are expected to demonstrate respectively one of the two phenomena (demyelination for MSF; axonal/neuronal loss for NSF). The model allows the quantification of the sensitivity of each MRI metric to each of the two pathological features. These associations, if present, may have appeared weaker if inferred from model number 1, due to potential correlations among the predictors.

For each model, $\beta$-coefficients $\beta_0$, $\beta_1$, $\beta_2$, ... measure the association between outcome MRI metrics and histological predictors, providing information about the sensitivity of the outcome towards the independent variables. We adopted $p \leq 0.05$ as a threshold to detect significant associations. Moreover, the adjusted coefficient of determination (adjusted $R^2$) was taken as a measure of goodness of the model. This index quantifies the fraction of the variance of the outcome variable explained by the model, while adjusting for model complexity.

## 9.4 Results

### 9.4.1 Histological feature calculation

Figure 9.1 shows examples of the histological features that were obtained for the histological validation of NODDI. Five examples of histological images are pictured, as well as some details extracted from GM and WM. The figure highlights the nature of the features that were calculated for quantitative analysis. For instance, it demonstrates that ST analysis successfully recovers the orientation of neuronal processes, while the k-means clustering allows the identification of the material stained by the immunohistochemistry. The histology-derived index of orientation dispersion, CV, is related to the variability of the ST orientations, represented in the figure as colours on top (panels c and e). On the other hand, the fractions of stained materials (MSF for PLP images; NSF for neurofilament images; $\mu$GSF for Iba1 images; ASF for GFAP images) are proportional to the fraction of stained material segmented with k-means algorithm, represented in white onto a black background in panels h and j (myelin), m and o (neurofilaments), r and t (microglia) and w and y (astrocytes).

### 9.4.2 Quantitative maps from NODDI, DTI and histology

Figures 9.2, 9.3, 9.4 and 9.5 show quantitative maps obtained from NODDI, DTI and histology in the four samples included in this study.

*Control cases*

Maps from the upper thoracic and upper lumbar control cases are respectively shown in figures 9.2 and 9.3. Notice that MRI metrics of the thoracic specimen are affected by areas of low coil sensitivity (bottom right). No ROIs were drawn in those parts.

A number of features can be identified in the maps. For NODDI, in both samples $v_{\text{iso}}$ has a grainy texture and is in general lower than 0.2 (excluding areas of low coil sensitivity for the upper thoracic case), appearing slightly higher in GM as compared to WM. $v_{\text{in}}$ is higher in WM as compared to GM, whereas the opposite holds for ODI. A non-negligible *dot* volume fraction $\text{DVF}_{\text{NODDI}}$ is measured in both samples, with $\text{DVF}_{\text{NODDI}}$ being in general higher in WM than in GM. Also, $\text{DVF}_{\text{NODDI}}$ is higher in the upper lumbar case, as compared to the upper thoracic specimen.

As far as DTI metrics are concerned, FA is higher in WM than in GM, while RD and MD are higher in GM than in WM. On the other hand, AD appears slightly higher in GM than in WM for the upper thoracic sample, while it appears homogeneous between the two tissue types in the upper lumbar specimen.

Among the histological metrics obtained in non-pathological tissue, the orientation dispersion parameter CV is higher in GM than in WM, while the four indices of staining fraction MSF, NSF, $\mu$GSF and ASF are relatively uniform between the two neural tissue types. Figures 9.2, 9.3 also show that NSF suffers from non-uniformity of the immunohistochemical labelling, since areas on the edge of the samples are characterised by a reduced amount of staining.

*MS cases*

Quantitative indices obtained from MRI and histology relative to the two MS cases are shown in figures 9.4 (upper thoracic case) and 9.5 (upper lumbar case).

The effect of disease is evident in NODDI metrics, since focal lesions in the WM of both samples and in the GM of the upper lumbar sample are hypo/hyperintense, as compared to metrics in non-focal tissue of the same type.

NODDI $v_{\text{iso}}$ increases in focal areas of both GM and WM, while $v_{\text{in}}$, ODI and $\text{DVF}_{\text{NODDI}}$ decrease.

DTI metrics also reveal the effect of pathology in GM and WM focal lesions, since FA and $\text{DVF}_{\text{DTI}}$ decrease and all diffusivity indices increase as compared to non-focal tissue.

In both MS cases, CV decreases in focal areas as compared to non-focal tissue of similar type. Moreover, the immunohistochemical staining fractions also demonstrate focal areas of pathology, while revealing heterogeneity between the two MS cases. In the upper lumbar case, MSF, NSF, $\mu$GSF and ASF are all reduced in WM focal lesions, as well as in the GM focal lesion. In the upper thoracic case, MSF and $\mu$GSF also decrease in the WM focal lesion as compared to non-focal WM areas. However, both ASF ans NSF differ from what is observed in the upper lumbar case. ASF is higher inside the focal lesion than outside, while values of NSF are similar inside and outside.

### 9.4.3 Statistical analysis

Results of fitting the five linear regression models listed in table 9.4 are reported in full in appendix B. The same results are also described verbally below.

*Model number 1*

The first model employs all histological features as predictors of NODDI and DTI metrics.

In controls, CV is significantly associated to NODDI indices $v_{\text{in}}$, ODI and $\text{DVF}_{\text{NODDI}}$, while $v_{\text{iso}}$ is associated positively to MSF and negatively to ASF. ODI and $\text{DVF}_{\text{NODDI}}$ are associated to $\mu$GSF. The highest adjusted $R^2$ are obtained for ODI (0.885) and for $\text{DVF}_{\text{NODDI}}$ (0.811). CV is also associated to

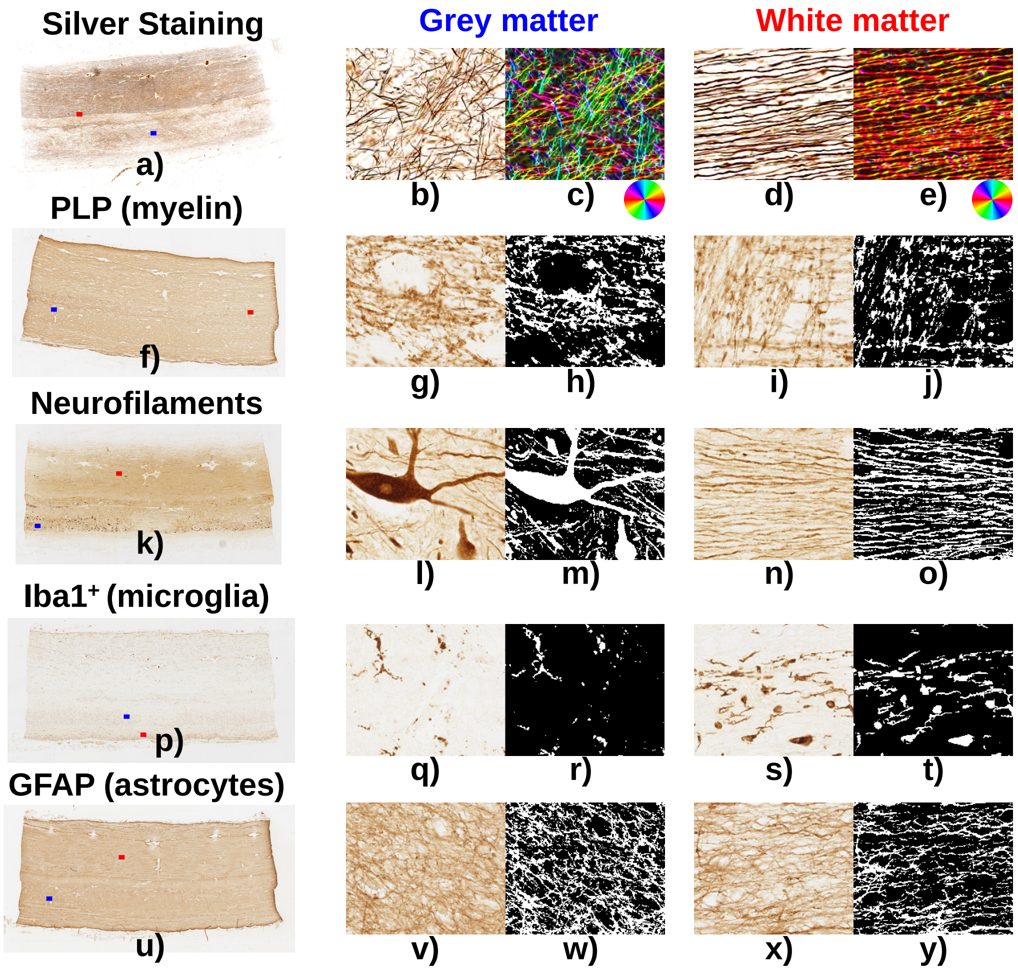

Figure 9.1: examples of the features derived from histological images of the upper lumbar control case. From top to bottom, information regarding Palmgren's silver stain, PLP immunohistochemistry (myelin), neurofilament immunohistochemistry (axons/neurons), microglia immunostaining and astrocyte labelling is pictured. A downsampled version of each type of histological image is reported to the left, as well as the position of two patches of size 164$\times$200 $\mu$m $\times$ $\mu$m in GM (blue box) and WM (red box). In the central and right columns, instead, the illustrative GM and WM patches are magnified. The results of the processing carried out on those patches is also shown. Specifically, the processing consisted of the estimation of the local orientation for Palmgren's silver images and in the segmentation of labelled material for the four immunostains.

all DTI metrics obtained from data set *DataFull*, but not to AD, for which no significant associations are detected. Furthermore, RD from data set *DataFull* shows a positive association to NSF, and DVF$_{\text{DTI}}$ is negatively associated to $\mu$GSF. DVF$_{\text{DTI}}$ has the highest adjusted $R^2$ (0.861), followed by that of FA (0.721). Fitting DTI to the Gaussian subset *DataGaussian* provides similar associations, with the values of the adjusted coefficient of determination increasing for FA and AD. However, when DTI is fitted to data set *DataGaussian*, the association between RD and NSF is not obtained.

In MS cases, significant association between all NODDI metrics but ODI to MSF is detected.

Also, a negative association between $v_{\text{iso}}$ and ASF is measured. ODI is significantly associated to CV (positive association) and, to a lesser extent, to NSF (also positive association, but weaker). Regressions performed using DTI metrics from data set *DataFull* provide results in agreement with regressions that employed metrics from data set *DataGaussian*. In both cases, DTI indices are significantly associated to MSF (positive association for FA and $\text{DVF}_{\text{DTI}}$, negative for the three diffusivities AD, RD and MD). Moreover, RD and MD are negatively associated to ASF.

*Model number 2*

The second model includes neuronal features CV, MSF and NSF as predictors of MRI metrics.

In controls, NODDI metrics $v_{\text{in}}$, ODI and $\text{DVF}_{\text{NODDI}}$ are significantly associated to CV, while $v_{\text{iso}}$ is not associated to any of the three histological predictors. DTI FA, RD, MD and $\text{DVF}_{\text{DTI}}$ from both data sets *DataFull* and *DataGaussian* are associated to CV with high significance levels (negative association for FA and $\text{DVF}_{\text{DTI}}$; positive for RD and MD). Positive association between RD and NSF is also detected when this DTI metric is obtained from data set *DataFull*, but not when is evaluated from the *DataGaussian* data set. The adjusted $R^2$ coefficients obtained for DTI metrics are comparable to values obtained for NODDI: FA obtained from data set *DataFull* exhibits the highest adjusted $R^2$ (0.833), which is slightly higher than that of NODDI ODI (0.821). $v_{\text{iso}}$ has the lowest adjusted $R^2$ among NODDI metrics (0.146), whilst AD for DTI metrics (0.010, data set *DataGaussian*).

In MS cases, no significant associations between NODDI $v_{\text{iso}}$ and histological parameters are detected. $v_{\text{in}}$ is associated positively with MSF and ODI is positively associated to CV and, to a much lesser extent, to NSF. DTI metrics from both data sets (*DataFull* and *DataGaussian*) are significantly associated to MSF. DTI FA is also associated negatively to CV, but only when evaluated from the *DataFull* data set. The highest adjusted $R^2$ is obtained for DTI metric $\text{DVF}_{\text{DTI}}$ (0.667), while the lowest for NODDI $v_{\text{iso}}$ (0.099). Finally, we report that the adjusted $R^2$ of DTI FA, AD, RD and MD (close to 0.450 for data set *DataFull* and 0.350 for data set *DataGaussian*) is lower than that of NODDI $v_{\text{in}}$ and ODI (close to 0.550).

*Model number 3*

The third model considers the only features CV and NSF as predictors of MRI metrics. The two histological features are respectively indices of orientation dispersion and of density of neuronal processes.

In controls, NODDI $v_{\text{iso}}$ is not associated to either CV or NSF. $v_{\text{in}}$ and $\text{DVF}_{\text{NODDI}}$ are negatively associated to CV; ODI is positively associated to CV, with high significance levels. DTI metrics FA, AD, RD and MD from both data sets *DataFull* and *DataGaussian* are significantly associated to CV, and RD from data set *DataFull* is positively associated to NSF. The adjusted $R^2$ is the highest for NODDI ODI among all metrics (0.819), followed by that of FA from data sets *DataFull* (0.818) and *DataGaussian* (0.740). The lowest adjusted $R^2$ values are obtained for AD (0.065 for data set *DataGaussian*; 0.091 for data set *DataFull*) and NODDI $v_{\text{iso}}$ (0.099).

In MS cases, NODDI $v_{\text{in}}$, ODI and $\text{DVF}_{\text{DTI}}$ are positively associated to NSF. Furthermore, the predictor most significantly associated to ODI is CV, while $v_{\text{iso}}$ shows no association with either CV or NSF. As far as DTI metrics are concerned, the linear regression shows that all metrics derived from the DTI model are strongly associated to NSF, with similar results being obtained from both data sets employed to fit DTI. Notably, RD shows a negative association with NSF. The highest adjusted $R^2$ is that of ODI (0.525), while the same figure is 0.255 for NODDI $v_{\text{in}}$ and close to 0.220 for DTI FA, AD, RD and MD obtained from data set *DataFull* and 0.180 when the same metrics are evaluated from *DataGaussian*. The volume fractions of the *dot* compartment $\text{DVF}_{\text{NODDI}}$ and $\text{DVF}_{\text{DTI}}$ have an adjusted $R^2$ of about 0.350.

*Model number 4*

In the fourth model, NODDI and DTI metrics are regressed as a linear combination of MSF and NSF.

No significant associations are obtained in controls, where the adjusted $R^2$ are in general lower than 0.100.

In MS cases, we observed no association between NODDI $v_{\text{iso}}$ and ODI and the two indices of staining fraction MSF and NSF. $v_{\text{in}}$ was positively associated to MSF but not to NSF, whereas $\text{DVF}_{\text{NODDI}}$ is positively associated to both histological parameters. Looking at DTI metrics in MS cases demonstrates that all DTI indices from both data sets (*DataFull* and *DataGaussian*) are significantly associated to MSF (FA and $\text{DVF}_{\text{DTI}}$ with positive sign; AD, RD and MD with negative sign). The adjusted $R^2$ is low for NODDI $v_{\text{iso}}$ and ODI (0.025 and 0.115), and is higher for diffusivities (ranging between 0.350 of RD from data set *DataGaussian* to 0.472 of AD from data set *DataGaussian*). The highest adjusted $R^2$ is obtained for the *dot* volume fractions (0.562 for $\text{DVF}_{\text{NODDI}}$ and about 0.650 for $\text{DVF}_{\text{DTI}}$ from both data sets).

*Model number 5*

The last model investigates to what extent NODDI and DTI metrics are sensitive to features of the sole extra-neurite space, namely density of microglia (metric $\mu$GSF) and astrocytes (metric ASF).

In controls, the only metrics showing significant associations to the predictors are the volume fractions of the *dot* compartments, since $\text{DVF}_{\text{NODDI}}$ and $\text{DVF}_{\text{DTI}}$ are negatively associated to $\mu$GSF, with adjusted $R^2$ close to 0.500.

Association between MRI-derived metrics and the microglia staining fraction $\mu$GSF is also detected in MS cases. All DTI metrics are significantly associated to $\mu$GSF, although the adjusted $R^2$ are low, close to 0.150 or at best 0.300 for $\text{DVF}_{\text{DTI}}$ from data set *DataFull*. In particular, $\text{DVF}_{\text{DTI}}$ is positively associated to $\mu$GSF, where instead the same association was previously reported with negative sign in control cases. Among NODDI metrics, $\text{DVF}_{\text{NODDI}}$ is positively associated to $\mu$GSF, with an adjusted $R^2$ of 0.327. Among other NODDI indices, only $v_{\text{in}}$ shows positive association to $\mu$GSF, but with a lower adjusted $R^2$ of 0.176.

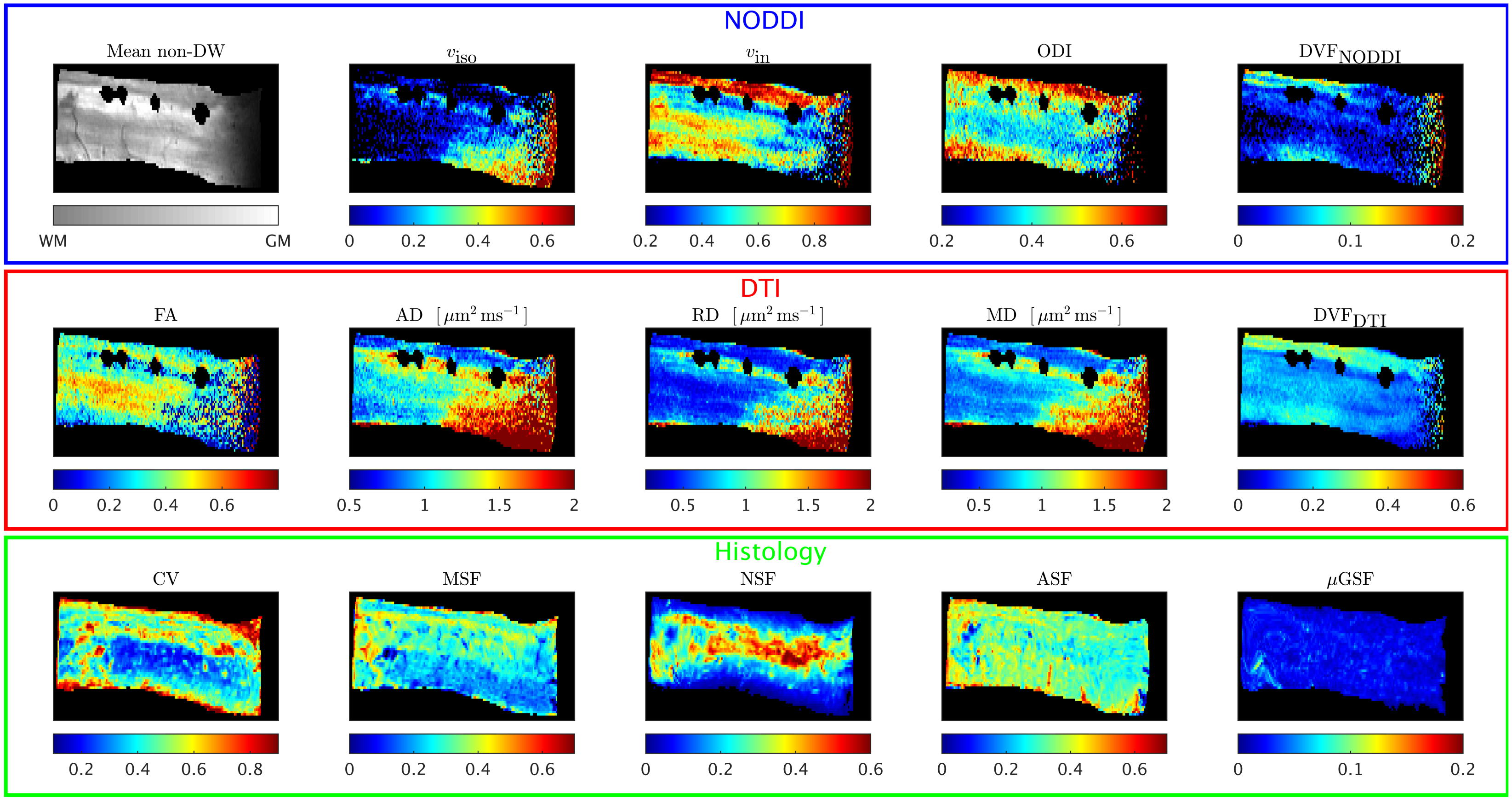
NODDI
Mean non-DW
$v_{\mathrm{iso}}$
$v_{\mathrm{in}}$
ODI
$\mathrm{DVF}_{\mathrm{NODDI}}$
WM
GM
0 0.2 0.4 0.6
0.2 0.4 0.6 0.8
0.2 0.4 0.6
0 0.1 0.2
DTI
FA
AD $[\mu\mathrm{m}^2\,\mathrm{ms}^{-1}]$
RD $[\mu\mathrm{m}^2\,\mathrm{ms}^{-1}]$
MD $[\mu\mathrm{m}^2\,\mathrm{ms}^{-1}]$
$\mathrm{DVF}_{\mathrm{DTI}}$
0 0.2 0.4 0.6
0.5 1 1.5 2
0.5 1 1.5 2
0.5 1 1.5 2
0 0.2 0.4 0.6
Histology
CV
MSF
NSF
ASF
$\mu$GSF
0.2 0.4 0.6 0.8
0 0.2 0.4 0.6
0 0.2 0.4 0.6
0 0.2 0.4 0.6
0 0.1 0.2

Figure 9.2: examples of quantitative maps derived from MRI and histology for the upper thoracic control case. The sample shown in the figure is specimen number 4 among those listed in table 7.1. NODDI metrics are shown in the first row, as well as the mean $b = 0$ image; DTI metrics in the central row; histology-derived indices in the bottom row. NODDI metrics were obtained from data set *DataFull*, whereas DTI metrics from data set *DataGaussian*. For both diffusion models, the *dot* compartment was included. Areas of image distortion due to the presence of some residual air bubbles trapped between the sample and the syringe plunger have been masked out in images obtained from MRI (first and second row). For reference, a short description of all metrics shown in the figure can be found in table 9.3.

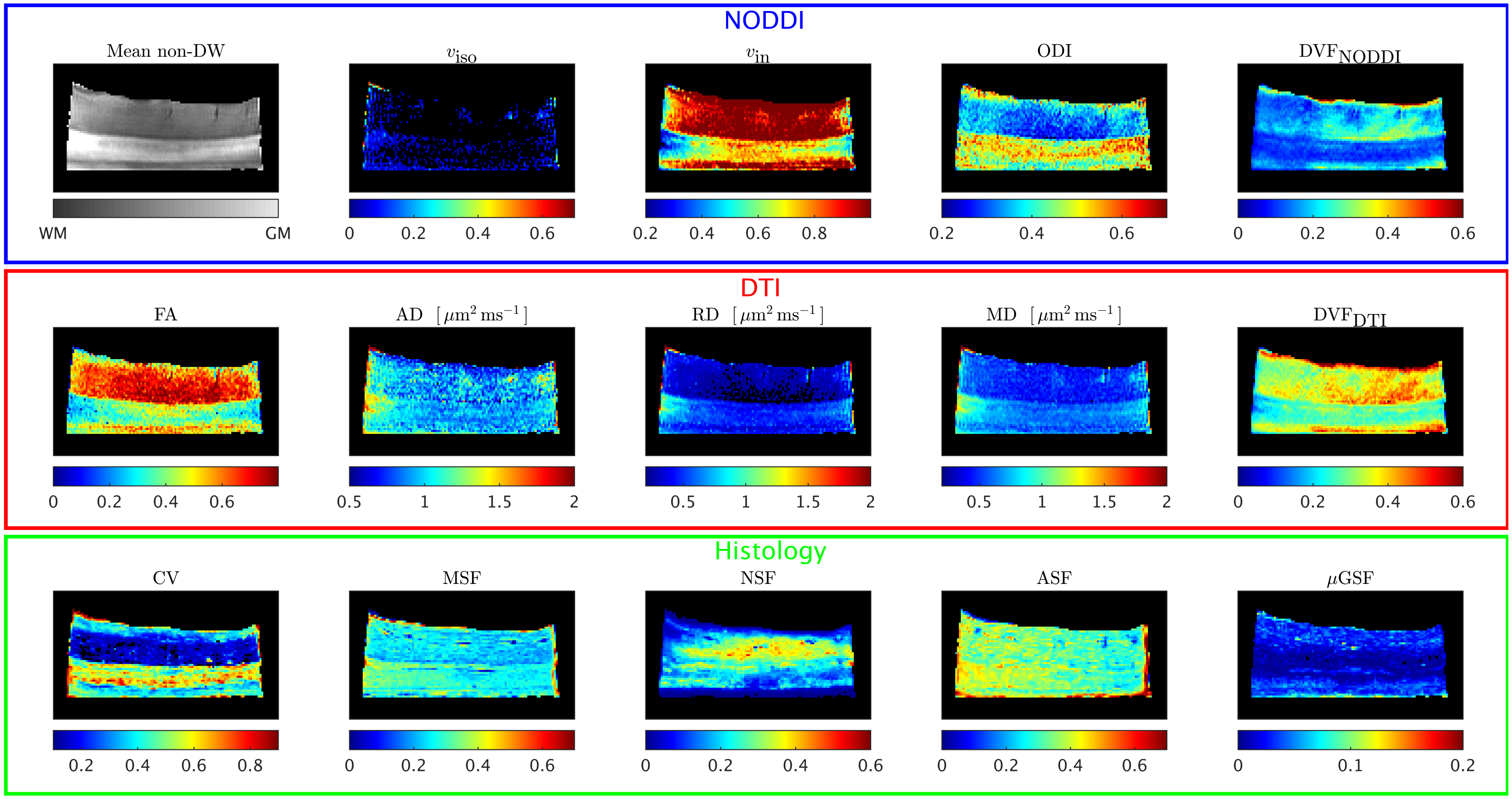
NODDI
Mean non-DW
$v_{\text{iso}}$
$v_{\text{in}}$
ODI
$\text{DVF}_{\text{NODDI}}$
WM
GM
0 0.2 0.4 0.6
0.2 0.4 0.6 0.8
0.2 0.4 0.6
0 0.2 0.4 0.6
DTI
FA
AD $[\mu\text{m}^2\,\text{ms}^{-1}]$
RD $[\mu\text{m}^2\,\text{ms}^{-1}]$
MD $[\mu\text{m}^2\,\text{ms}^{-1}]$
$\text{DVF}_{\text{DTI}}$
0 0.2 0.4 0.6
0.5 1 1.5 2
0.5 1 1.5 2
0.5 1 1.5 2
0 0.2 0.4 0.6
Histology
CV
MSF
NSF
ASF
$\mu$GSF
0.2 0.4 0.6 0.8
0 0.2 0.4 0.6
0 0.2 0.4 0.6
0 0.2 0.4 0.6
0 0.1 0.2

Figure 9.3: examples of quantitative maps derived from MRI and histology for the upper lumbar control case. The sample shown in the figure is specimen number 6 among those listed in table 7.1. The same information as figure 9.2 is shown. A short description of all metrics shown in the figure can be found in table 9.3.

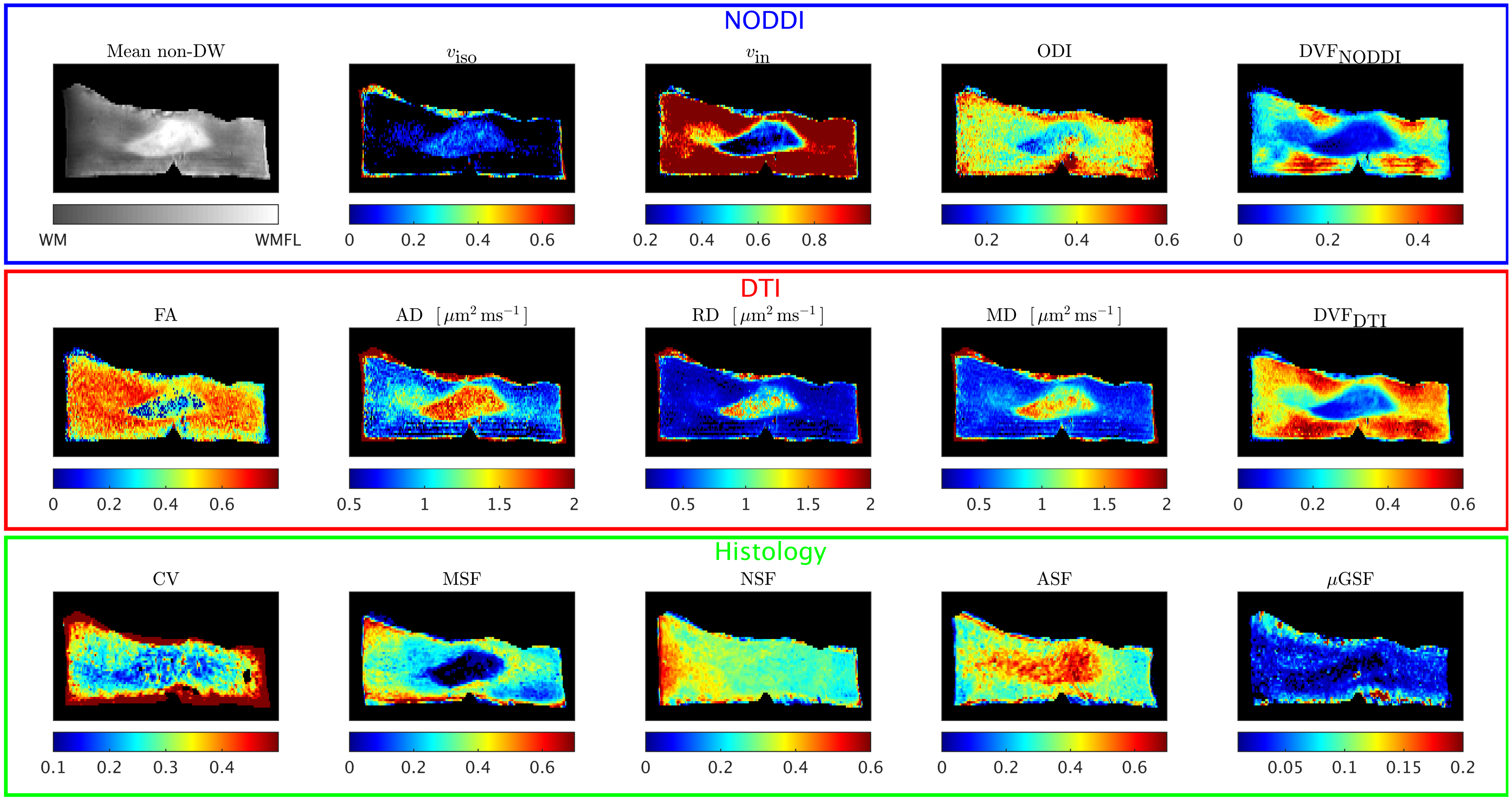
NODDI
Mean non-DW
$v_{\mathrm{iso}}$
$v_{\mathrm{in}}$
ODI
$\mathrm{DVF}_{\mathrm{NODDI}}$
WM
WMFL
0 0.2 0.4 0.6
0.2 0.4 0.6 0.8
0.2 0.4 0.6
0 0.2 0.4
DTI
FA
AD $[\mu\mathrm{m}^2\,\mathrm{ms}^{-1}]$
RD $[\mu\mathrm{m}^2\,\mathrm{ms}^{-1}]$
MD $[\mu\mathrm{m}^2\,\mathrm{ms}^{-1}]$
$\mathrm{DVF}_{\mathrm{DTI}}$
0 0.2 0.4 0.6
0.5 1 1.5 2
0.5 1 1.5 2
0.5 1 1.5 2
0 0.2 0.4 0.6
Histology
CV
MSF
NSF
ASF
$\mu$GSF
0.1 0.2 0.3 0.4
0 0.2 0.4 0.6
0 0.2 0.4 0.6
0 0.2 0.4 0.6
0.05 0.1 0.15 0.2

Figure 9.4: examples of quantitative maps derived from MRI and histology for the upper thoracic MS case. The sample shown in the figure is specimen number 5 among those listed in table 7.1. The same information as figure 9.2 is shown. A short description of all metrics shown in the figure can be found in table 9.3.

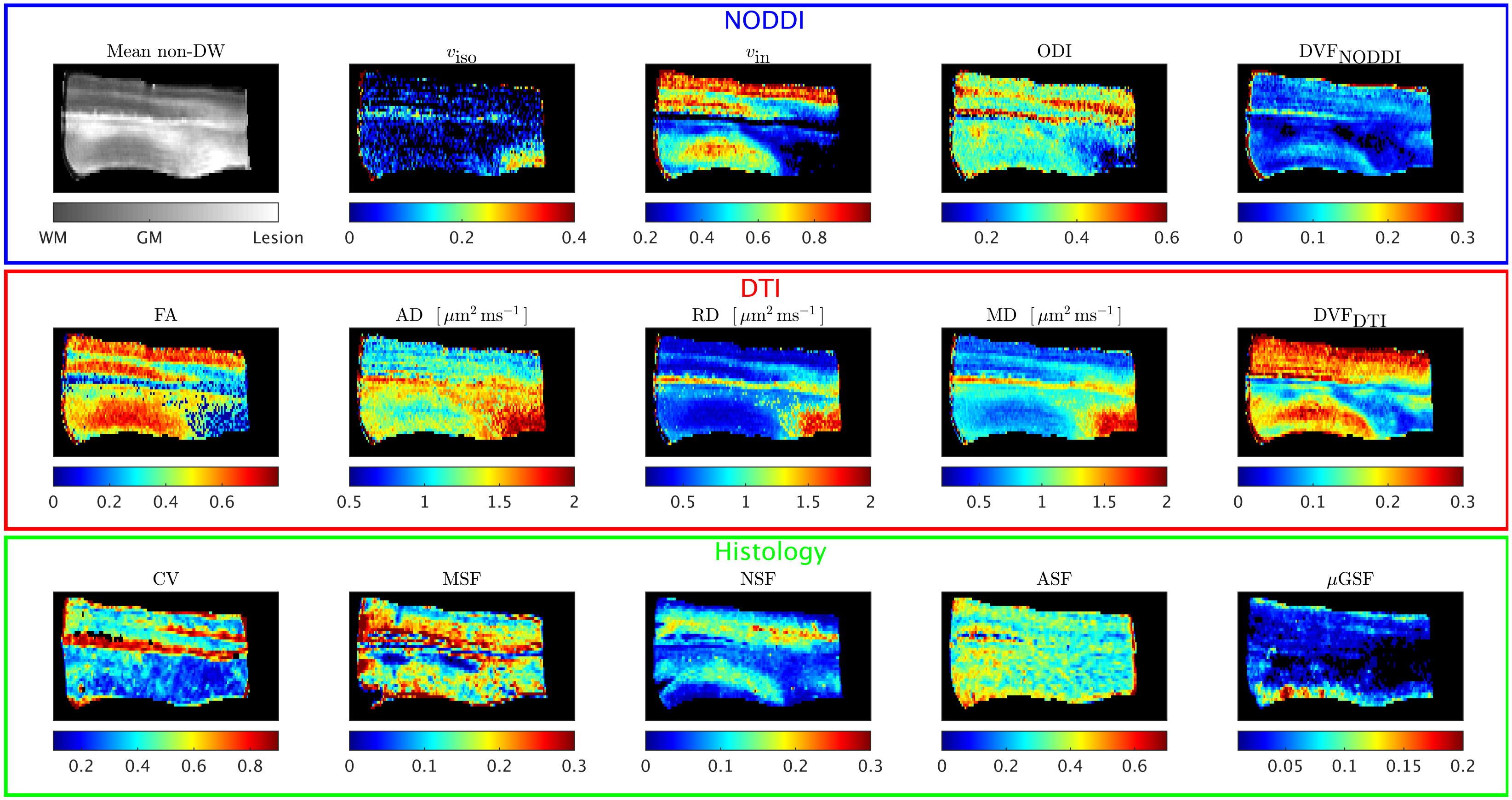
NODDI
Mean non-DW
WM
GM
Lesion
$v_{\text{iso}}$
0
0.2
0.4
$v_{\text{in}}$
0.2
0.4
0.6
0.8
ODI
0.2
0.4
0.6
$\text{DVF}_{\text{NODDI}}$
0
0.1
0.2
0.3
DTI
FA
0
0.2
0.4
0.6
AD $[\mu\text{m}^2\,\text{ms}^{-1}]$
0.5
1
1.5
2
RD $[\mu\text{m}^2\,\text{ms}^{-1}]$
0.5
1
1.5
2
MD $[\mu\text{m}^2\,\text{ms}^{-1}]$
0.5
1
1.5
2
$\text{DVF}_{\text{DTI}}$
0
0.1
0.2
0.3
Histology
CV
0.2
0.4
0.6
0.8
MSF
0
0.1
0.2
0.3
NSF
0
0.1
0.2
0.3
ASF
0
0.2
0.4
0.6
$\mu$GSF
0.05
0.1
0.15
0.2

Figure 9.5: examples of quantitative maps derived from MRI and histology for the upper lumbar MS case. The sample shown in the figure is specimen number 3 among those listed in table 7.1. The same information as figure 9.2 is shown. A short description of all metrics shown in the figure can be found in table 9.3.

## 9.5 Discussion

In this chapter we studied the histological correlates of NODDI metrics in the spinal cord. We performed MRI scans at high field on four specimens of *post mortem* human spinal cord (two non-pathological cases and two progressive cases of MS), and derived NODDI and DTI metrics. For NODDI, we obtained voxel-wise estimates of isotropic (free water) volume fraction ($v_{\text{iso}}$), intra-neurite tissue volume fraction ($v_{\text{in}}$), orientation dispersion index (ODI) and stationary water (*dot*) volume fraction ($\text{DVF}_{\text{NODDI}}$). For DTI, we instead calculated fractional anisotropy (FA), axial, radial and mean diffusivities (AD/RD/MD), as well as stationary water (*dot*) volume fraction ($\text{DVF}_{\text{DTI}}$).

Moreover, histological sections were also obtained at known radiographic position, and stained to label neurons/axons, myelin, astrocytes and microglia. Optical imaging provided high resolution images of the stained sections, which were processed with well established digital image processing methods. This provided features quantifying neurite orientation dispersion (circular variance CV) and density of myelin (MSF), neurofilaments (NSF), astrocytes (ASF) and microglia ($\mu$GSF). The histological features were finally warped to the MRI space via manual registration.

All quantitative maps were visually inspected. Furthermore, five univariable linear regression models were fitted to evaluate the sensitivity of each MRI metric to the histological features. Our regressions also controlled for specificity, since the dependence of each individual MRI metric on multiple histological features was modelled jointly.

*Trends on visual inspection: NODDI metrics*

Visual inspection proved that NODDI metrics obtained in control cases follow patterns that agree well with trends previously shown *in vivo* in chapter 4. For instance, the neurite density index $v_{\text{in}}$ is smaller in GM than in WM, while the opposite holds for the index of neurite orientation dispersion ODI.

NODDI metrics are also sensitive to MS pathology, since in the MS specimens areas of focal damage are evident in all metrics. In lesions, we observe an increase of isotropic volume fraction ($v_{\text{iso}}$), as well as a reduction of both neurite density $v_{\text{in}}$ and ODI. The reduction of $v_{\text{in}}$ is plausible since axonal loss is a known feature of MS [41], whereas the reduction of ODI in lesions, clear for instance in figure 9.4, is probably less intuitive. This latter finding suggests that neuronal fibres are more parallel in focal lesions than they are in non-focal areas. This may be indicative of a reduction of the complexity of the tissue. The reduction in complexity may affect the amount of information that can be conveyed, with consequent impairment of sensorimotor functions. Also, it is known that small fibres are more likely to be lost in the MS spinal cord, as compared to large ones [41]. Therefore, we speculate that the big axons that survive in MS lesions may be the least undulated, since we expect that the characteristic undulation length increases as the calibre of the axon increases. This may also lead to a reduction of orientation dispersion at the MRI voxel scale, as each MRI voxel would essentially contain axons characterised by less undulation.

Finally, the *dot* volume fraction $\text{DVF}_{\text{NODDI}}$ shows a contrast among tissues that reflects that of $v_{\text{in}}$, although the range of values varies notably from specimen to specimen.

*Trends on visual inspection: DTI metrics*

DTI metrics FA, RD and MD in controls are consistent with what we showed in chapter 4 *in vivo*. FA is higher in WM than in GM, RD is higher in GM than in WM and MD is rather homogeneous between the two tissue types. However, in our data AD is higher in GM than in WM, unlike what we showed *in vivo* in the previous chapters. We suspect that this could be an effect of the fixation process, which seems to have increased the restriction parallel to WM fibres, as also flagged by the relatively high values of *dot* volume fractions $\text{DVF}_{\text{NODDI}}$ and $\text{DVF}_{\text{DTI}}$ measured in WM. The presence of a highly restricted, almost stationary water pool in fixed neural tissue has been reported before [4, 146, 170], and has been attributed to water trapped in small structures such as glial cells [4].

DTI metrics detect areas of focal lesion, which are characterised by a reduction of FA and an increase of AD, RD and MD. These trends are consistent with previous literature [99]. Interestingly, despite the reduction of neurite orientation dispersion ODI in focal lesions, which we expect to be concomitant to an increase of FA (panel A of figure 4.8), we observed an overall reduction of FA. FA is influenced by both density and orientation dispersion of neuronal processes, of which NODDI ODI and $v_{\text{in}}$ provide estimates. In focal lesions, both ODI and $v_{\text{in}}$ are reduced. The former is expected to contribute to an increase of FA, whilst the second to a decrease. Overall, we observe a reduction of FA, implying that the reduction of neurite density has a stronger effect on FA than the reduction of ODI. This latter effect seems to be more subtle, and it can not be detected by looking at FA.

*Trends on visual inspection: histological metrics*

Quantitative histological maps were also obtained for the four samples, and warped to the MRI space. In controls, the staining fractions MSF (myelin), NSF (neurofilaments), ASF (astrocytes) and $\mu$GSF (microglia) are relatively homogeneous between GM and WM, whereas the orientation dispersion index CV shows a clear contrast between GM and WM. CV is higher in GM than in WM, demonstrating the higher complexity in terms or neurite orientations of the former compared to the latter. CV confirms the trend showed by NODDI ODI, which is its direct MRI counterpart.

Histological maps demonstrate MS pathology, revealing the same areas of focal lesion that are visible in MRI images. In both MS cases, for instance, CV is reduced in focal lesions. This is an important result *per se*, since to our knowledge the effect of MS pathology on neurite complexity has never been studied on histological material derived from human tissue before. Our results support the hypothesis of MS as a disease reducing the complexity of neural tissue, in line with recent findings in a cohort of MS patients at cortical level [132]. Moreover, CV confirms the trends shown by NODDI ODI, which also detects a reduction of neurite orientation dispersion in MS lesions.

The staining fractions MSF, NSF, ASF and $\mu$GSF also demonstrate focal lesions, but with certain differences between the two MS cases. In both specimens, MSF and $\mu$GSF decrease in areas of focal pathology, highlighting demyelination and suggesting the presence of little activated microglia (i.e. little inflammation). The absence of inflammation is expected, since the two MS specimens were obtained from two chronic patients who were affected by MS for more than 20 years. However, while in the upper lumbar case also NSF and ASF decrease in focal areas, in the upper thoracic case ASF and NSF do not do so. In the upper thoracic case, ASF is higher within the focal WM as compared to non-focal WM, while values of NSF are relatively similar in both. The MS lesion of this sample, well evident in figure 9.4, is therefore characterised by little amount of axonal loss, and appears as a dense astrocytic scar, a known feature of chronic MS [73]. The differences between the two MS cases are plausible and are not surprising, given the known heterogeneity of tissue injury mechanism among MS patients [105].

Interestingly, in the upper lumbar MS case, MSF and NSF decrease in focal lesions, indicating demyelination and axonal loss. On the other hand, in the upper thoracic MS case, only MSF decreases in the focal area, pointing towards demyelination but negligible axonal loss. However, the NODDI-derived index of neurite density $v_{\text{in}}$ decreases dramatically in the MS focal lesions of both cases. Therefore, the two phenomena (demyelination and axonal loss) seem to be both factors that can be associated to $v_{\text{in}}$. Although the decrease of $v_{\text{in}}$ in lesions could be a consequence of the altered permeability of the axon [104, 163], variations of myelin density may affect $v_{\text{in}}$ directly. This fact could be explained considering the multicomponent origin of spin-spin relaxation in neural tissue. Myelin water has a very short $T_2$, on the order of 10 ms *in vivo* [212]. Therefore, at the echo times usually employed in DW experiments, myelin signal decays and does not contribute to the measurements. However, in demyelinated areas, myelin is replaced by material that may have a longer $T_2$, effectively increasing the amount of MRI visible water. Therefore, this suffices *per se* to cause a reduction of the neurite density, even without occurrence of axonal loss. Ultimately, the fraction of water within neurites with respect to the total amount of visible water may decrease due to the increase of the amount of visible water, rather than due to the decrease of the amount of intra-neurite water.

*Statistical analysis: design of models*

We compared NODDI and DTI metrics obtained from the whole set of DW measurements and DTI metrics obtained from a Gaussian subset of measurements to histology. We fitted five linear regression models to quantify the strength of the association between histological features and MRI metrics. The models allow the evaluation of the sensitivity of each DW MRI metric with respect to individual histological features, while controlling for specificity.

The first model considers all histological metrics as predictors of MRI indices. The other models, instead, employ only subsets of the histological features as independent variables. They focus on specific aspects of neuronal tissue microstructure, which may not be fully characterised by model number 1, due to potential correlations among predictors (five in that model). The second model considers only neuronal features (myelin and neuronal element density; orientation dispersion), whereas features of the extra-neurite space (astrocyte and microglia density) are considered in model number 5. From model number 2, other two models are also obtained. The third model accounts for density and orientation dispersion of neuronal elements, to investigate how the two, believed to be key factors of the diffusion MRI signal profile, jointly contribute to NODDI and DTI metrics. The fourth model instead accounts for myelin and neuronal element densities, enabling the study of how demyelination and axonal/neuronal loss affect MRI indices.

*Statistical analysis: association NODDI-histology*

Overall, our statistical analysis proves that ODI is the DW MRI metric most specific to histology, among those considered in this study. Moreover, NODDI metrics are specific to neuronal elements and do not show any clear association to features of the extra-neurite space, namely density of astrocytes and microglia. This is demonstrated, for instance, by the higher adjusted $R^2$ of model 2 as compared to model 5.

The statistical analysis shows different associations between NODDI metrics and histological features in control cases and in MS cases.

In controls, the measure of orientation dispersion derived from histology, CV, is the main factor explaining the variation of all NODDI metrics. This appears as an effect of its high contrast, since the remaining metrics of staining fraction show little difference between GM and WM. Therefore, the only metric capable of explaining the between-tissue contrast of NODDI maps is CV.

On the other hand, in MS cases, the feature that drives the variability of almost all NODDI metrics is MSF, an index of myelin density. This is again quite possibly a result of the high between-region contrast of MSF. As an exception, NODDI ODI is the only MRI-derived metric that even in MS cases exhibits consistently sensitivity to CV. ODI shows no association to MSF, even when CV is not included as a predictor variable (model number 4), and has a weak, positive association to NSF. The association to NSF may be a consequence of the highest chance of observing orientation dispersion of neuronal elements when these are in a greater number (i.e. when NSF is higher). Moreover, ODI shows the highest values of the adjusted $R^2$ coefficient, demonstrating that most of the variability of ODI can be explained by the variability of histological features via linear regression. ODI faithfully replicates the patterns of histology-derived orientation dispersion, and allows the systematic detection of variations of neural tissue complexity in focal lesions, surpassing even the performance of well established DTI FA.

Our analysis demonstrates that NODDI $v_{\text{in}}$, a descriptor of axon and dendrite density, is potentially sensitive to axonal loss in MS, as demonstrated by the positive association with NSF in MS cases for model number 3. However, demyelination seems to be a phenomenon that can explain the observed trends of $v_{\text{in}}$, even more than axonal loss. This is demonstrated by the fact that NSF is not the strongest correlate of $v_{\text{in}}$ in controls, and when the sensitivities of $v_{\text{in}}$ to MSF and NSF are compared (model number 4), the former is stronger than the latter. Although the association between decrease of $v_{\text{in}}$ and demyelination could be a consequence of the increases permeability of demyelinated axons [104, 163], variations of myelin density may affect $v_{\text{in}}$ directly. The apparent reduction of neurite density in demyelinated areas could be a consequence of the increased amount of visible water, discussed above, even when neurites are not reduced in number. In demyelinated areas, myelin, which is MRI-invisible, may be replaced by MRI-visible water. Hence, $v_{\text{in}}$, which is proportional to the ratio between the intra-neurite water and the total amount of MRI-visible water, may decrease due to the increased amount of MRI visible water. Overall, $v_{\text{in}}$ appears as a surrogate index of focal damage, potentially able to convey information about both axonal loss and demyelination. $v_{\text{in}}$ on its own does not appear to suffice to distinguish between the demyelination of axonal elements and axonal loss. Nonetheless, its combination with myelin density indices from myelin water imaging [107] or quantitative magnetisation transfer [164] may help overcome this issue, as recently demonstrated in g-ratio mapping [173].

Lastly, our result do not allow the identification of strong associations between NODDI $v_{\text{iso}}$ and the histological features object of this study. NODDI $v_{\text{iso}}$ is designed to capture the amount of free water in a voxel, as in areas of partial volume with the liquid surrounding the brain parenchyma. In this chapter, we demonstrated that $v_{\text{iso}}$ is consistently hyperintense in focal WM lesions, agreeing with preliminary findings *in vivo* [156]. However, the metric did not show any clear association with histological metrics other than a negative association with the density of astrocytes (ASF), but only when all histological indices were considered as predictors. $v_{\text{iso}}$ is designed to capture the amount of free water in each MRI voxel. In our study, no histology-derived metrics quantifying this feature could be obtained, also because specimens underwent dehydration as part of the histological processing. In conclusion, the lack of association between $v_{\text{iso}}$ and our five histological features does not appear surprising.

*Statistical analysis: association DTI-histology*

As far as DTI metrics are concerned, our results were in line with previously published findings [99]. Similarly to NODDI, the main correlates of DTI metrics are CV in controls and MSF in MSF, possibly due to the high between-tissue-type contrast of CV in controls and MSF in MS cases. Moreover, DTI metrics do not show notable association to features of the extra-neurite space (density of astrocytes and microglia).

DTI metrics are sensitive to demyelination and axonal loss, but can not detect other effects of MS pathology, perhaps less evident, such as the decrease in neurite orientation dispersion. DTI FA is vaguely sensitive to CV in MS, but the sensitivity is lost in favour of a much stronger dependency on NSF when the only features included as predictors in the linear regression models are CV and NSF. This holds true even when the whole six-shell data set is used to evaluate DTI metrics, which in general provides similar results as the Gaussian data set.

Moreover, our statistical analysis provides a disappointing and weak association between AD and histological features in MS cases. In WM, AD quantifies the amount of diffusion along neuronal fibres, which, *in vivo*, is relatively free. The diffusion regime is known to be altered by fixation, since diffusion restriction has been reported even parallel to WM fibres [146, 170]. We speculate that the increased restriction parallel to WM fibres, suggested by the higher AD in GM than in WM, may be the main cause of the lack of association between histology and AD. Lack of association between AD obtained from fixed MS spinal cord and metrics quantifying axonal density have been previously reported in literature [99].

*Statistical analysis: the* dot *compartment*

In this work, we employed a compartment of isotropic restriction, the *dot*, to model stationary water and account for the high level of signal measured parallel to WM fibres even for strong diffusion weighting. This signal component has been described before, and has an unclear origin [146, 170]. We included a *dot* compartment to fit both NODDI and DTI, obtaining similar trends in terms of *dot* compartment volume fraction.

It was speculated that a *dot*-like diffusion component may arise from phenomena such as protein cross-linking and from water trapped within glial cells, which lose their active function after death [4]. In this work, we quantified the association between the *dot* volume fraction from NODDI and DTI and the local density of glial cells, measured by metrics ASF and $\mu$GSF. We detect significant associations of *dot* volume fractions with all histological metrics, but the direction of the associations (positive/negative) are not always consistent. For instance, the *dot* volume fraction is associated to $\mu$GSF positively in controls and negatively in MS cases. In view of these observations, we conclude that the *dot* volume fraction reflects an overall alteration of the diffusion properties following fixation. Moreover, our data do not allow us to conclude whether the alteration is characteristic of the intra or of the extra-neurite space, but it appears more as a global effect.

*Limitations*

A number of interesting findings have been reported and discussed in this chapter, but some limitations of our methods also need to be acknowledged.

The biggest limitation is the fact that we evaluated NODDI metrics from *ex vivo* fixed spinal cord tissue and with a non-clinical MRI protocol. It is well known that fixation alters the characteristic of biological tissues, causing phenomena such as cross-linking of proteins [161]. Therefore, NODDI metrics shown in this chapter may not be fully representative of their *in vivo* counterparts. Nevertheless, trends obtained in our controls and MS cases are in line with preliminary findings reported *in vivo* [156], suggesting by extrapolation that the conclusions of this *ex vivo* study are likely to hold also *in vivo*. Nonetheless, the comparison to histology of NODDI metrics obtained from unfixed *post mortem* tissue may help to further confirm this statement.

A number of limitation are associated to our histological procedures. Most importantly, histological indices and MRI metrics were obtained from slivers of tissue whose thickness was considerably different compared to each other. Our MRI protocol consisted of 800 $\mu$m-thick slices, whereas the histological staining was performed on 10 $\mu$m-thick sections. As a consequence of this, portions of tissue that did contribute to the MRI signal were not included in the evaluation of histological features, leading to a potential underestimation of the association between MRI and histology. To limit this effect, we derived two different histological sections per MRI slice, sampling the tissue at two different locations, 200 $\mu$m apart.

The inherent 2D nature of our histological images may have affected the estimation of neurite orientation dispersion via calculation of the index CV from ST analysis. The contribution of through-plane neurites was ignored by our 2D method, leading to a potential underestimation of orientation dispersion in areas such as GM. However, this did not seem to affect the possibility of discriminating between-tissue differences in terms of orientation dispersion, since CV exhibited clear betwee-tissue contrast in both controls and MS cases. Recent published work has shown that 3D ST analysis of confocal microscopy data can provide invaluable information for the validation of DW MRI [98]. Nevertheless, these 3D approaches are limited to small portions of tissue due to their requirements in terms of computational power. Therefore, for our purposes, 2D analysis sufficed for the characterisation of the wide range of tissue types that were included in the study, even at the price of reduced accuracy.

Another limitation of our work is related to unspecific staining affecting the Palmgren's silver images. In Palmgren's silver impregnation, blood vessels, neuronal and non-neuronal cell bodies as well as neuropil are labelled. Although most of these structures were manually removed, some of them may have remained and contributed to the estimation of neurite orientation dispersion. Tests demonstrated that the inclusion of such unwanted material did not bias the calculation of CV. CV maps qualitatively similar to those shown in this chapter were obtained when the spread of ST orientations was calculated only considering pixels within neurites, which were detected with a crude thresholding of the image intensity.

The labelling of neuronal cell bodies also influenced the NSF map, which describes the patch-wise density of phosphorylated and non-phosphorylated neurofilaments. In our images, neurofilament immunohistochemistry labelled not only axons and dendrites, but also the cell bodies of neurons. Therefore, although NSF is the closest counterpart of NODDI $v_{\text{in}}$, it is rather an index of *neuronal density* rather than *neurite density*. Therefore, we speculate that a more specific histology-derived marker of neurite density may exhibit higher association with $v_{\text{in}}$ than what NSF does.

Another limitation of our histological procedures is to do with staining non-uniformity. Within-image and between-image non-uniformities were clearly appreciable in a number of our histological images. A considerable amount of code was implemented to correct these issues via removal of linear trends of image intensities and via segmentation of the stained material. In spite of this effort, minor residual non-uniformities still affect metrics such as NSF, potentially leading to an underestimation of the real association between MRI metrics and histological indices.

## 9.6 Conclusion

In this chapter we compared NODDI metrics to histology, with the aim of validating their specificity in non-pathological and MS spinal cord. NODDI metrics were obtained from fixed spinal cord tissue and related to five different measures provided by histology. A similar analysis was also performed for DTI, since DTI is still a common method in clinical studies of spinal cord conditions.

NODDI accurately captures the dispersion of axon and dendrite orientations, and improves the specificity of routine methods such as DTI. NODDI ODI faithfully replicates its histology-derived counterpart CV, and is the only metric among those considered capable of detecting in a consistent manner alterations of orientation dispersion associated with MS pathology. NODDI also offers sensitivity to the density of axons and dendrites, although it provides indices of neurite density that are also influenced by demyelination. This could be a direct consequence of the increased amount of visibile water that follows demyelination, although the altered permeability of demyelinated neurites may also play a role.

In conclusion, NODDI offers a unique opportunity to study changes of neural tissue microstructure. With NODDI it becomes feasible to detect subtle effects of neurodegenerative diseases on neuronal tissue complexity, which can not be measured with standard DW MRI methods. However, NODDI on its own can not distinguish between demyelination and axonal loss. Therefore, we also conclude that NODDI would benefit from complementary MRI contrasts that are also commonly applied in MS, such as myelin water imaging or quantitative magnetisation transfer.

# Chapter 10

# Conclusions

This PhD thesis shows the work carried out to advance the state-of-the-art of spinal cord MRI in MS, a demyelinating, inflammatory and neurodegenerative disease of the central nervous system.

## 10.1 Key findings

We studied in detail the potential of NODDI, a novel DW MRI technique that tries to overcome the limitations of conventional methods, which are sensitive to macroscopic aspects of diseases and do not detect early microscopic tissue damage. NODDI belongs to an emerging family of microstructural imaging methods, and provides metrics that could be new useful biomarkers in MS. Our key findings are that:

1. NODDI, originally proposed for *in vivo* brain imaging, can also be performed in the spinal cord in clinically feasible scans;
2. NODDI can detect reliably variations of axon and dendrite orientation dispersion due to pathology, unlike conventional DTI;
3. NODDI metrics offer new opportunities to study how neurodegenerative diseases such as MS alter neural tissue complexity.

## 10.2 Summary

Conventional MRI is commonly employed in the MS spinal cord for the detection of focal lesion number and volume as well as for measuring atrophy. These are certainly useful outcome measures, but alone provide a partial explanation for the progression of the disability and do not characterise diffuse abnormality. Conversely, a number of emerging MRI methods are currently under investigation in MS. These new techniques measure quantitatively biophysical properties of tissues, and unlike conventional methods have the potential of better characterising widespread tissue damage.

They could provide new insights about MS pathology *in vivo*, as well as more accurate diagnosis, prognosis and treatment monitoring in clinical trials.

Among the new quantitative methods, DW MRI exploits the random motion of water molecules as a non-invasive probe of neural tissue microstructure. NODDI is a model-based DW MRI technique that provides estimates of the density and of the orientation dispersion of neuronal processes. These biophysically relevant metrics may be useful biomarkers also in the spinal cord, where they could prove useful to disentangle different pathophysiological features of MS.

NODDI was developed to improve the specificity of DW MRI in clinically feasible acquisitions, and in this PhD thesis we explore its potential for the spinal cord, with a focus on MS. For this purpose, *in vivo* and *post mortem* MRI data were acquired and analysed. Specifically, our research objectives were:

1. to demonstrate that NODDI is feasible in the human spinal cord *in vivo* and in clinical times (i.e. in approximately 20 minutes);
2. to relate NODDI indices to metrics obtained from DTI, another DW MRI method that is routinely employed in MRI-based research of the spinal cord;
3. to investigate whether NODDI analysis could be performed on standard (single-shell) DW data;
4. to assess how certain microstructural features typical of the spinal cord influence NODDI metrics;
5. to validate the specificity of NODDI indices in the non-pathological and MS spinal cord via comparison to quantitative histology.

## 10.3 General conclusions

In view of the data in our possession, we conclude that NODDI provides new opportunities to study neurodegenerative diseases such as MS in the spinal cord. NODDI offers the invaluable advantage of measuring accurately neurite orientation dispersion, thus enabling the detection of subtle effects that MS pathology has on tissue complexity. NODDI also offers sensitivity to axon and dendrite density, but on its own can not fully resolve demyelination from axonal loss.

Clinical studies where DW MRI data of the spinal cord are acquired would benefit from NODDI analysis, as compared to DTI. New and more specific research questions could be investigated, at the price of the acquisition of more DW images and of the recruitment of more subjects, due to the lower reproducibility scores of NODDI metrics, as opposed to those of DTI.

We also conclude that NODDI, and more generally DW MRI on its own, is not sufficient to obtain a complete picture describing the effects that complex diseases such as MS have on the spinal cord. NODDI could be a key element of a more general multi-modal MRI approach, where other techniques such as myelin water imaging or quantitative magnetisation transfer would provide complementary information.

## 10.4 Specific conclusions from *in vivo* studies

In the first part of this thesis, *in vivo* DW MRI images were acquired on healthy volunteers and analysed with NODDI and DTI. Moreover, *in silico* and *in vivo* data were studied to characterise how axon diameter distributions typical of the spinal cord influence the patterns of NODDI metrics. Our work led to a publication in a peer-reviewed scientific journal and to the presentation of intermediate results to several international meetings. Another manuscript is currently in preparation for submission to a peer-reviewed journal.

Following careful analysis and interpretation of our *in vivo* data, we conclude what follows.

1. NODDI is feasible in the human spinal cord and in clinical settings (i.e. in about 20 minutes).
2. NODDI describes the acquired data better than more naïve techniques such as DTI.
3. However, NODDI is slightly less reproducible than DTI, and therefore would benefit from recent advances in MRI technology that increase the number of images acquired per unit of time.
4. NODDI can separate the two main sources of diffusion anisotropy in neural tissue, i.e. the density and the orientation dispersion of neuronal processes.
5. NODDI estimates of orientation dispersion show high contrast between GM and WM, and in the latter type of tissue may also be able to demonstrate crossing fibres.
6. NODDI isotropic volume fraction is highly sensitive to noise. Therefore, its employment for the measurement of subtle increases of free water in pathology is difficult, at least for current SNR levels of *in vivo* DW MRI of the spinal cord.
7. NODDI analysis of standard (single $b$-value) DW data is challenging: high $b$-values are in general required, and the analysis is not well suited for WM.
8. The employment of short diffusion times can reduce the accuracy of NODDI metrics in geometries plausible in the spinal cord, characterised by the presence of large axons.
9. Long diffusion times can improve the accuracy of NODDI neurite density estimation, but reduce the precision due to the longer echo times required, which cause more intense $T_2$ decay. Hence, a trade-off accuracy-precision needs to be evaluated for each specific application.

Dissemination of results is essential to scientific knowledge, and the conclusions of our *in vivo* work listed above were presented at international meetings and in a scientific journal.

Conclusions from 1 to 6 were included in a peer-reviewed journal publication:

- “Neurite orientation dispersion and density imaging of the healthy cervical spinal cord *in vivo*”, Grussu F. et al, NeuroImage (2015), vol. 111, p.590-601 (reference [67]).

Previously, preliminary findings were also presented at scientific meetings as:

- “*In vivo* estimation of neuronal orientation dispersion and density of the human spinal cord”. Grussu F. et al, International Society for Magnetic Resonance in Medicine (ISMRM) workshop “Multiple sclerosis as a whole-brain disease” (2013), oral presentation.
- “Neurite orientation dispersion and density imaging of the cervical cord *in vivo*”. Grussu F. et al, ISMRM annual meeting (2014), p.1720, traditional poster.

Conclusion number 7 is the main message of these two works:

- “Single-shell diffusion MRI NODDI with *in vivo* cervical cord data”. Grussu F. et al, ISMRM annual meeting (2014), p.1716, traditional poster.
- “Characterisation of single-shell NODDI fitting in spinal cord grey and white matter”. Grussu F. et al, British Chapter of ISMRM annual meeting (2014), traditional poster.

Conclusions number 8 and 9 were recently included in an abstract, submitted for consideration to the 2016 ISMRM annual meeting:

- “Axon diameter distribution influences diffusion-derived axonal density estimation in the human spinal cord: *in silico* and *in vivo* evidence”. Grussu F. et al, ISMRM annual meeting (2016), p.2009, traditional poster.

## 10.5 Specific conclusions from *ex vivo* studies

The second part of the thesis presented our work *ex vivo*. We compared NODDI metrics to quantitative histological features to confirm their specificity in non-pathological and MS spinal cord tissue. A considerable amount of preliminary technical work was required to enable the comparison. We implemented a high-field DW MRI protocol and developed a strategy to obtain histological material from the spinal cord specimens at known radiographic position. Moreover, we implemented and optimised a ST analysis framework for the estimation of neurite orientation dispersion from histological images. We studied sections impregnated with Palmgren’s silver method, and developed a novel probability density function, the *weighted-Watson distribution*, that may provide useful descriptive statistics of orientation dispersion.

In view of the data that we collected *ex vivo*, we conclude what follows.

1. Our MRI-histology pipeline allows the acquisition of data of good quality, suitable for the systematic comparison of MRI-derived metrics with quantitative histological features.
2. ST analysis of sagittal histological images of the human spinal cord is a valuable method for the estimation of neurite orientation dispersion.
3. However, careful design of the spatial scale at which information is integrated to calculate the ST is necessary.
4. Our weighted-Watson distribution could be a valid alternative to standard directional statistics models.

5. NODDI orientation dispersion index is confirmed by histology. NODDI accurately captures the dispersion of axon and dendrite orientations, improving the specificity of naïve DW MRI methods.
6. NODDI enables the detection of subtle variations of tissue complexity in terms of neurite orientation dispersion in MS pathology, which can not be captured with simpler methods such as DTI.
7. NODDI is sensitive to axon and dendrite density, but can not distinguish between demyelination and axonal loss.
8. NODDI isotropic volume fraction is a potential biomarker in diseases such as MS, since it demonstrates focal tissue damage. However, its employment *in vivo* is limited by its high sensitivity to noise.

Our *ex vivo* work led to a total of three abstracts that were accepted at two different international conferences. Moreover, two manuscripts are currently in preparation for submission to peer-reviewed journals. The abstract submissions accepted at scientific meetings focussed on the findings listed above in conclusions 5 to 8. They were:

- "Histological metrics confirm microstructural characteristics of NODDI indices in multiple sclerosis spinal cord". Grussu F. et al, ISMRM annual meeting (2015), p.0909, oral presentation.
- "Quantitative histological correlates of NODDI orientation dispersion estimates in the human spinal cord". Grussu F. et al, ISMRM annual meeting (2015), p.0154, oral presentation.
- "Quantitative histological validation of NODDI MRI indices of neurite morphology in multiple sclerosis spinal cord". Grussu F. et al, 31st congress of the European Committee for the Research and Treatment in Multiple Sclerosis (ECTRIMS 2015), p.0469, traditional poster presentation.

## 10.6 Future directions

Each research study naturally leads to new questions and prompts further investigation, and in this section we discuss a number of future directions that emerge from this thesis.

Our work has demonstrated that more specific information about spinal cord pathology can be obtained from quantitative MRI, exploiting models of the underlying biology. We employed NODDI to model how tissue microstructure influences diffusion MRI signals. Our work proved that NODDI offers new opportunities to study MS pathology in the spinal cord.

However, as any model, NODDI is not perfect. It relies on some assumptions that seem to work well for healthy tissue, but may not always hold true in pathology. A limitation of NODDI is that the intrinsic diffusivities of the tissue compartments are usually fixed to some *a priori* values and are not estimated from the data. Although this alleviates the ill-posedness that characterises the inversion of the NODDI model, it could potentially bias the fitting of the other parameters when wrong priors are adopted [80, 81]. Another limitation comes from the fact that NODDI employs a simple model for the extra-neurite space, which does not account for phenomena such as diffusion time dependency of the extra-neurite signal [26].

In future, improvements to the technique may come from the optimisation of parameters of the diffusion encoding protocol that go beyond the simple $b$-value. For instance, diffusion times such that the assumptions of the extra-neurite signal model are better verified could be probed. Furthermore, other cutting-edge diffusion MRI models that relax the hypotheses of the NODDI technique could be tested, and their performance could be compared to NODDI. For instance, these may include the recently published *spherical mean technique* [95], or approaches that avoid non-linear fitting and infer microstructural parameters from the cumulant expansion of the DW MRI signal [59, 137].

Our investigation has also shown that advanced techniques such as NODDI are sensitive to noise and imperfections of the input data, which impair their reproducibility. Therefore, future work is required to improve the quality of the DW data themselves. This may include: i) improved noise characterisation [190]; ii) denoising and reduction of the noise floor [49]; iii) better motion correction; iv) increase of the number of images acquired per unit of time with multiband imaging [55]; v) single-fibre direction optimisation of the diffusion encoding [157].

One of the findings of our research was that the accuracy of neurite density estimation in the spinal cord can benefit from long diffusion times. However, longer diffusion times require longer echo times, which would reduce the precision of the estimation due to the more intense $T_2$ decay (i.e. lower SNR). A comparison between the accuracy and the precision of neurite density estimation as derived from STEAM and from spin echo is therefore of interest. STEAM can provide at best half of the signal level of a spin echo experiment, but allows the employment of long diffusion times without penalisation in terms of $T_2$ decay.

Furthermore, we also demonstrated that NODDI analysis of single-shell DW data of the spinal cord is challenging. This hampers the possibility of analysing retrospectively with NODDI routine single $b$-value acquisitions, which seem to support only simple models. However, recent innovative methods could be used to enable NODDI analysis even on such data. The methods transfer the information contained in high quality data sets to enhance data from standard acquisitions or to alleviate the ill-posedness of certain analyses. In our context, multi-shell DW acquisitions of the spinal cord could be practically used to train algorithms capable of predicting NODDI metrics from single $b$-value data sets. As an example, maximum *a posteriori* fitting with population-based priors could be used [178]. Equivalently, *image quality transfer*, a supervised algorithm based on random forest linear regression [5], could also be tested.

Other future work could lead to the integration of NODDI, or of other DW MRI methods, in a multi-modal MRI framework. For instance, techniques such as myelin water imaging or quantitative magnetisation transfer in conjunction with NODDI could lead to the differentiation of axonal loss, demyelination and perhaps remyelination in MS. New experiments in this direction should be designed and performed. They could include not only *in vivo* and *ex vivo* imaging, but also support from computer simulations.

We conclude remarking that all that is developed should always have patients in mind, who represent the real demand behind our effort to improve quantitative imaging in clinically feasible scan times.

# Appendices

# Appendix A

# Example of SOP document used to plan histological procedures

In this appendix we report the SOP document that was written to plan the histological procedures after MRI session number 4. The document provides an example of the practical and effective communication between UCL and the University of Oxford, which enabled the analyses described in chapters 7, 8 and 9.

# Standard operating procedure: MRI scan 10th/ 09/2014

## Sample preparation

- 24h before MRI scan, sample was taken out of formalin.
- Sample was put in ~500ml PBS solution 10 mM for 24h.
- PBS solution was replaced every 12h.
- Samples were cut for the whole sagittal length in approximately two halves with surgical blade.
- The four tissue chunks were positioned in the four slots of a syringe plunger and tied with Velcro. Medical bandage was used for padding. Holes made in the syringe plunger.
- The plunger was fitted into a Falcon tube, which was then filled with freshly prepared PBS solution 10 mM.

**Cut of healthy sample**

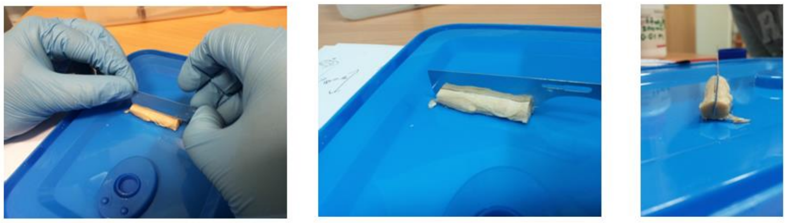

**Cut of MS sample**

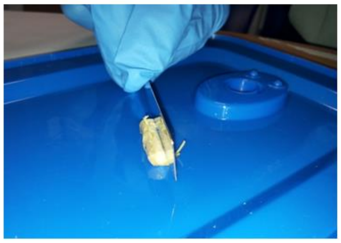

Figure 1: mid-sagittal sectioning of the specimens.

## Experiment reference frame

The following reference frame has been defined.

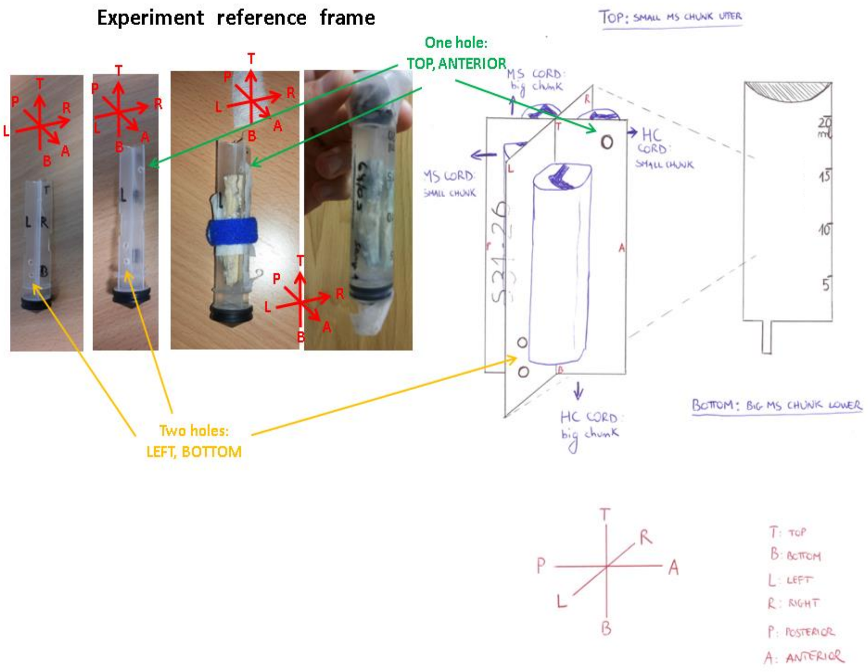
Experiment reference frame
T
P
R
L
B
A
One hole:
TOP, ANTERIOR
Two holes:
LEFT, BOTTOM
TOP: SMALL MS CHUNK UPPER
MS CORD: big chunk
HC CORD: SMALL CHUNK
MS CORD: SMALL CHUNK
HC CORD: big chunk
S31-26
BOTTOM: BIG MS CHUNK LOWER
20 ml
15
10
5
T: TOP
B: BOTTOM
L: LEFT
R: RIGHT
P: POSTERIOR
A: ANTERIOR

Figure 2: experiment reference frame.

## MRI setup

- 9.4T Agilent Scanner with 1000mT/m gradient
- 33mm diameter coil (Rapid Quadrature)
- Centre of both 2 samples is approximately aligned with centre of coil & centre of magnet
- Temperature was monitored and kept stable at 35C using a MR compatible sample heater.

## MRI positioning protocol

- T2-weighted axial images for MRI and histology planning
- Axial: FOV 25.6 x 25.68 mm$^2$ / 24 slices (2 mm thick); 256 x 128 matrix.

## NODDI protocol

- Sagittal slices covering both samples.
- NODDI model fitted to the data in order to obtain voxel-wise estimates of **isotropic volume fraction, intra-neurite volume fraction** and **neurite orientation dispersion index**.

## Localisation of sagittal slices onto axial view

The figure below clarifies the localisation of the diffusion-weighted sagittal slices in the experiment reference frame and in an axial view.

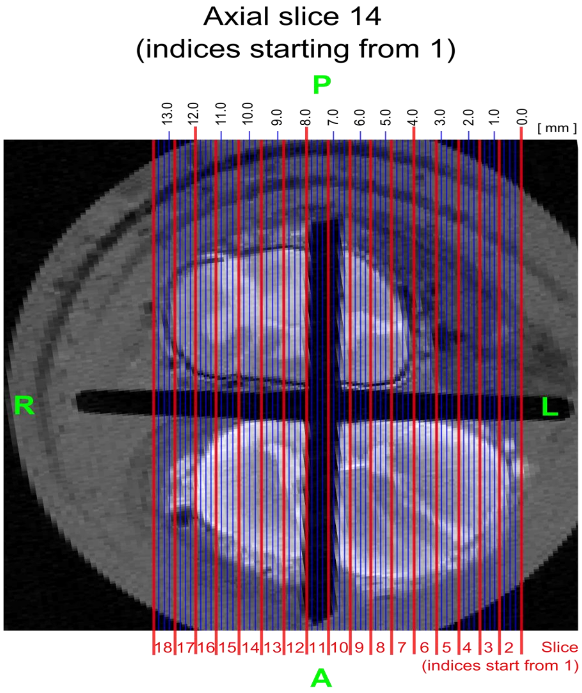
Axial slice 14
(indices starting from 1)
P
13.0
12.0
11.0
10.0
9.0
8.0
7.0
6.0
5.0
4.0
3.0
2.0
1.0
0.0
[ mm ]
R
L
18
17
16
15
14
13
12
11
10
9
8
7
6
5
4
3
2
Slice
(indices start from 1)
A

Figure 3: sagittal slices overlaid onto axial slice 14.

## Proposed cuts: healthy cord

The figure below shows the proposed cuts for the healthy cord sample.

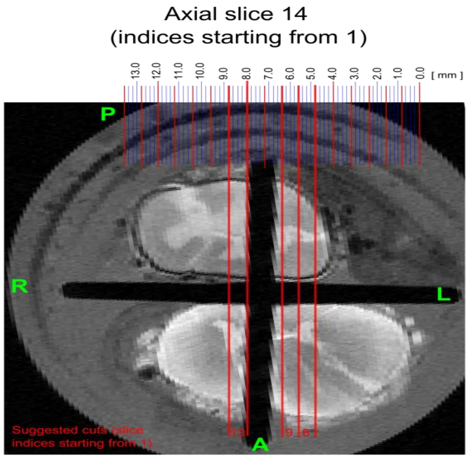
Axial slice 14
(indices starting from 1)
13.0
12.0
11.0
10.0
9.0
8.0
7.0
6.0
5.0
4.0
3.0
2.0
1.0
0.0
[ mm ]
P
R
L
A
12
9
8
Suggested cuts (slice indices starting from 1)

Figure 4: suggested cuts for the healthy cord.

## Proposed cuts: MS cord

The figure below shows the proposed cuts for the MS cord sample.

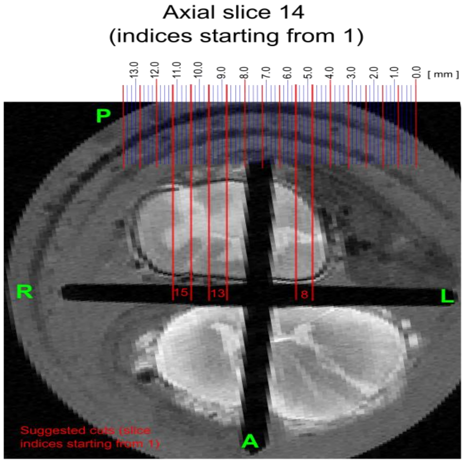
Axial slice 14
(indices starting from 1)
13.0
12.0
11.0
10.0
9.0
8.0
7.0
6.0
5.0
4.0
3.0
2.0
1.0
0.0
[ mm ]
P
R
L
A
15
13
8
Suggested cuts (slice indices starting from 1)

Figure 5: suggested cuts for the MS cord.

## Sagittal MRI slices

The images below show the mean non-diffusion-weighted images from the sagittal acquisition.

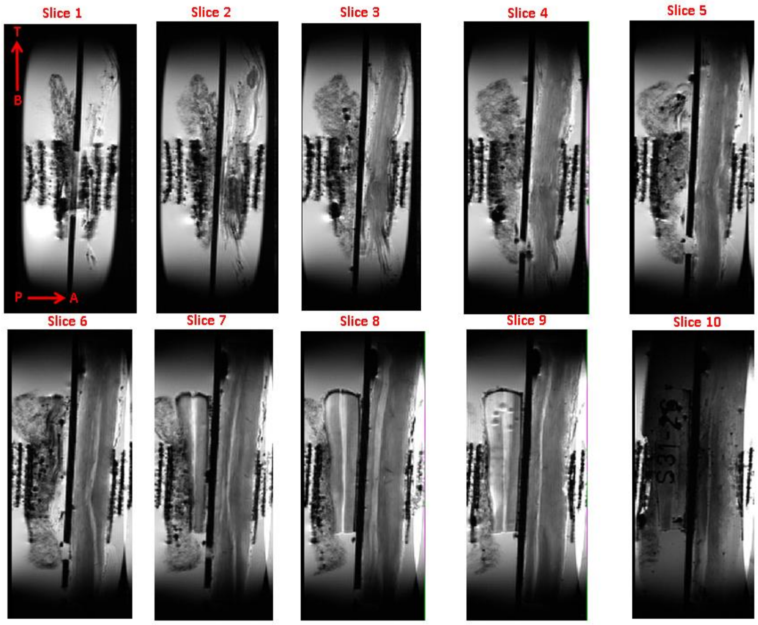
Slice 1
Slice 2
Slice 3
Slice 4
Slice 5
T
B
P
A
Slice 6
Slice 7
Slice 8
Slice 9
Slice 10

Figure 6: mean non-DW images (sagittal slices 1 to 10).

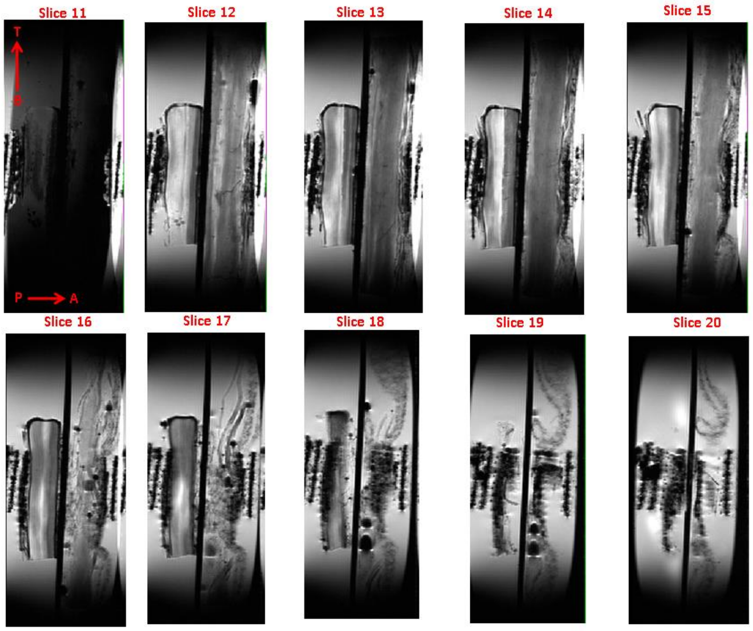
Slice 11
Slice 12
Slice 13
Slice 14
Slice 15
T
P
A
Slice 16
Slice 17
Slice 18
Slice 19
Slice 20

Figure 7: mean non-DW images (sagittal slices 11 to 20).

## Sample restoration

- After scan, Velcro and medical bandage were removed, and the plunger with the four tissue chunks was inserted into an empty syringe.
- The syringe was filled with formalin buffered with PBS.
- Storage back in fridge until further processing.

# Appendix B

# Fitting of linear regression models: relationship MRI-histology

In this appendix we report in full the results of fitting the five linear regression models listed in table 9.4. We use a light shade of grey to flag associations between histological features and MRI-derived metrics characterised by a $p$-value $p \leq 0.05$.

The results reported in this appendix are introduced and discussed in sections 9.4.3 and 9.5 of chapter 9. A description of the metrics used as predictors (histology-derived) and as outcome measures (MRI-derived) in the linear regression models can be found in table 9.3.

**Control cases, model no. 1**

$m = \beta_0 + \beta_1\,\mathrm{CV} + \beta_2\,\mathrm{MSF} + \beta_3\,\mathrm{NSF} + \beta_4\,\mathrm{ASF} + \beta_5\,\mu\mathrm{GSF}$

| | $\beta_0$ | | $\beta_1$ | | $\beta_2$ | | $\beta_3$ | | $\beta_4$ | | $\beta_5$ | | |
|---|---|---|---|---|---|---|---|---|---|---|---|---|---|
| Metric $m$ | Coeff. | $p$ | Coeff. | $p$ | Coeff. | $p$ | Coeff. | $p$ | Coeff. | $p$ | Coeff. | $p$ | Adjusted $R^2$ |
| **NODDI: fitting to data set *DataFull*** | | | | | | | | | | | | | |
| $v_{\text{iso}}$ | 0.103 | 0.427 | 0.081 | 0.142 | 0.369 | 0.049 | 0.197 | 0.083 | $-0.825$ | 0.042 | 1.115 | 0.074 | 0.391 |
| $v_{\text{in}}$ | 0.779 | 0.049 | $-0.848$ | $< 10^{-4}$ | 0.225 | 0.655 | $-0.357$ | 0.259 | 1.124 | 0.309 | $-2.372$ | 0.177 | 0.607 |
| ODI | 0.225 | 0.031 | 0.431 | $< 10^{-7}$ | 0.146 | 0.272 | $-0.133$ | 0.112 | 0.211 | 0.457 | $-1.400$ | 0.006 | 0.885 |
| $\mathrm{DVF}_{\mathrm{NODDI}}$ | 0.428 | 0.001 | $-0.196$ | $< 10^{-3}$ | $-0.287$ | 0.062 | 0.023 | 0.795 | $-0.238$ | 0.450 | $-3.614$ | $< 10^{-5}$ | 0.811 |
| **DTI: fitting to data set *DataFull*** | | | | | | | | | | | | | |
| FA | 0.913 | 0.013 | $-0.963$ | $< 10^{-5}$ | $-0.156$ | 0.727 | $-0.494$ | 0.090 | 0.418 | 0.666 | $-1.866$ | 0.230 | 0.721 |
| AD | 1.292 | 0.017 | 0.232 | 0.260 | 0.170 | 0.796 | 0.329 | 0.423 | $-2.106$ | 0.154 | 2.367 | 0.298 | 0.003 |
| RD | 0.288 | 0.546 | 1.014 | $< 10^{-3}$ | 0.383 | 0.554 | 0.860 | 0.045 | $-1.928$ | 0.181 | 3.083 | 0.172 | 0.597 |
| MD | 0.623 | 0.192 | 0.753 | 0.001 | 0.312 | 0.621 | 0.683 | 0.095 | $-1.988$ | 0.159 | 2.844 | 0.195 | 0.456 |
| $\mathrm{DVF}_{\mathrm{DTI}}$ | 0.488 | $< 10^{-3}$ | $-0.267$ | $< 10^{-5}$ | $-0.236$ | 0.080 | $-0.069$ | 0.390 | 0.019 | 0.944 | $-3.500$ | $< 10^{-6}$ | 0.861 |
| **DTI: fitting to data set *DataGaussian*** | | | | | | | | | | | | | |
| FA | 0.786 | 0.003 | $-0.840$ | $< 10^{-6}$ | $-0.500$ | 0.111 | $-0.164$ | 0.381 | 0.576 | 0.381 | $-0.294$ | 0.773 | 0.820 |
| AD | 1.465 | 0.001 | 0.280 | 0.190 | 0.126 | 0.853 | 0.631 | 0.146 | $-2.402$ | 0.117 | 3.377 | 0.157 | 0.160 |
| RD | 0.377 | 0.459 | 1.045 | $< 10^{-3}$ | 0.727 | 0.298 | 0.729 | 0.101 | $-2.136$ | 0.165 | 2.487 | 0.294 | 0.573 |
| MD | 0.740 | 0.152 | 0.790 | 0.002 | 0.527 | 0.441 | 0.696 | 0.111 | $-2.225$ | 0.144 | 2.784 | 0.236 | 0.445 |
| $\mathrm{DVF}_{\mathrm{DTI}}$ | 0.512 | $< 10^{-3}$ | $-2.806$ | $< 10^{-5}$ | 0.168 | 0.219 | $-0.089$ | 0.290 | 0.064 | 0.825 | $-3.496$ | $< 10^{-5}$ | 0.851 |

Table B.1: results obtained from fitting the linear regression model number 1 in the control cases. The values of the $\beta$ coefficients are provided, as well as the corresponding $p$-values (a light shade of grey flags $p \leq 0.05$). The adjusted coefficient of determination (adjusted $R^2$) is also included. All coefficients $\beta_0, ..., \beta_5$ have units of $[\mu\mathrm{m}^2\ \mathrm{ms}^{-1}]$ for DTI metrics AD, RD and MD. For all other NODDI and DTI metrics, the coefficients are dimensionless.

**MS cases, model no. 1**

$$m = \beta_0 + \beta_1\,\text{CV} + \beta_2\,\text{MSF} + \beta_3\,\text{NSF} + \beta_4\,\text{ASF} + \beta_5\,\mu\text{GSF}$$

| | $\beta_0$ | | $\beta_1$ | | $\beta_2$ | | $\beta_3$ | | $\beta_4$ | | $\beta_5$ | | |
|---|---|---|---|---|---|---|---|---|---|---|---|---|---|
| Metric $m$ | Coeff. | $p$ | Coeff. | $p$ | Coeff. | $p$ | Coeff. | $p$ | Coeff. | $p$ | Coeff. | $p$ | Adjusted $R^2$ |
| **NODDI: fitting to data set *DataFull*** | | | | | | | | | | | | | |
| $v_{\text{iso}}$ | 0.299 | 0.003 | $-0.111$ | 0.179 | $-0.383$ | 0.021 | 0.192 | 0.245 | $-0.461$ | 0.019 | $-0.419$ | 0.295 | 0.144 |
| $v_{\text{in}}$ | $-0.133$ | 0.646 | $-0.150$ | 0.571 | 2.249 | $< 10^{-3}$ | 0.014 | 0.979 | 0.865 | 0.159 | 1.595 | 0.223 | 0.581 |
| ODI | 0.146 | 0.111 | 0.315 | $< 10^{-3}$ | 0.120 | 0.446 | 0.387 | 0.025 | $-0.055$ | 0.765 | $-0.320$ | 0.421 | 0.497 |
| $\text{DVF}_{\text{NODDI}}$ | $-0.032$ | 0.710 | $-0.020$ | 0.801 | 0.452 | 0.006 | 0.132 | 0.404 | 0.045 | 0.798 | 0.617 | 0.115 | 0.563 |
| **DTI: fitting to data set *DataFull*** | | | | | | | | | | | | | |
| FA | $-0.041$ | 0.854 | $-0.218$ | 0.288 | 1.488 | $< 10^{-3}$ | $-0.233$ | 0.570 | 0.794 | 0.097 | 1.369 | 0.178 | 0.482 |
| AD | 2.149 | $< 10^{-5}$ | $-0.298$ | 0.377 | $-2.266$ | 0.002 | 0.003 | 0.997 | $-1.318$ | 0.096 | $-2.326$ | 0.166 | 0.461 |
| RD | 2.014 | $< 10^{-3}$ | $-0.099$ | 0.810 | $-3.093$ | $< 10^{-3}$ | 0.208 | 0.801 | $-1.984$ | 0.044 | $-3.230$ | 0.118 | 0.510 |
| MD | 2.059 | $< 10^{-4}$ | $-0.165$ | 0.661 | $-2.817$ | $< 10^{-3}$ | 0.140 | 0.854 | $-1.762$ | 0.049 | $-2.929$ | 0.122 | 0.510 |
| $\text{DVF}_{\text{DTI}}$ | $-0.043$ | 0.641 | $-0.017$ | 0.839 | 0.715 | $< 10^{-3}$ | 0.122 | 0.470 | 0.176 | 0.359 | 0.698 | 0.097 | 0.673 |
| **DTI: fitting to data set *DataGaussian*** | | | | | | | | | | | | | |
| FA | $-0.004$ | 0.984 | $-0.162$ | 0.401 | 1.228 | 0.003 | $-0.298$ | 0.442 | 0.858 | 0.060 | 1.647 | 0.089 | 0.435 |
| AD | 2.225 | $< 10^{-6}$ | $-0.239$ | 0.421 | $-2.244$ | $< 10^{-3}$ | 0.152 | 0.799 | $-1.175$ | 0.091 | $-2.011$ | 0.172 | 0.486 |
| RD | 1.994 | $< 10^{-3}$ | $-0.079$ | 0.854 | $-2.756$ | 0.003 | 0.341 | 0.693 | $-2.079$ | 0.043 | $-3.298$ | 0.126 | 0.422 |
| MD | 2.071 | $< 10^{-4}$ | $-0.132$ | 0.724 | $-2.586$ | 0.001 | 0.278 | 0.713 | $-1.779$ | 0.047 | $-2.869$ | 0.127 | 0.450 |
| $\text{DVF}_{\text{DTI}}$ | $-0.045$ | 0.665 | $-0.019$ | 0.840 | 0.832 | $< 10^{-3}$ | 0.151 | 0.435 | 0.214 | 0.331 | 0.775 | 0.107 | 0.680 |

Table B.2: results obtained from fitting the linear regression model number 1 in the MS cases. The values of the $\beta$ coefficients are provided, as well as the corresponding $p$-values (a light shade of grey flags $p \leq 0.05$). The adjusted coefficient of determination (adjusted $R^2$) is also included. All coefficients $\beta_0, ..., \beta_5$ have units of $[\mu\text{m}^2\ \text{ms}^{-1}]$ for DTI metrics AD, RD and MD. For all other NODDI and DTI metrics, the coefficients are dimensionless.

**Control cases, model no. 2**

$$m \;=\; \beta_0 \;+\; \beta_1\,\text{CV} \;+\; \beta_2\,\text{MSF} \;+\; \beta_3\,\text{NSF}$$

|  | $\beta_0$ |  | $\beta_1$ |  | $\beta_2$ |  | $\beta_3$ |  |  |
|---|---|---|---|---|---|---|---|---|---|
| Metric $m$ | Coeff. | $p$ | Coeff. | $p$ | Coeff. | $p$ | Coeff. | $p$ | Adjusted $R^2$ |
| **NODDI: fitting to data set *DataFull*** |  |  |  |  |  |  |  |  |  |
| $v_{\text{iso}}$ | $-0.114$ | 0.079 | 0.073 | 0.252 | 0.272 | 0.182 | 0.211 | 0.109 | 0.146 |
| $v_{\text{in}}$ | 1.047 | $< 10^{-5}$ | $-0.837$ | $< 10^{-4}$ | 0.354 | 0.480 | $-0.374$ | 0.249 | 0.581 |
| ODI | 0.243 | $< 10^{-3}$ | 0.434 | $< 10^{-6}$ | 0.166 | 0.293 | $-0.133$ | 0.193 | 0.821 |
| $\text{DVF}_{\text{NODDI}}$ | 0.235 | 0.020 | $-0.195$ | 0.050 | $-0.328$ | 0.273 | 0.040 | 0.831 | 0.149 |
| **DTI: fitting to data set *DataFull*** |  |  |  |  |  |  |  |  |  |
| FA | 0.980 | $< 10^{-5}$ | $-0.959$ | $< 10^{-5}$ | $-0.112$ | 0.793 | $-0.497$ | 0.082 | 0.725 |
| AD | 0.722 | 0.003 | 0.212 | 0.316 | $-0.079$ | 0.904 | 0.367 | 0.388 | 0.092 |
| RD | $-0.204$ | 0.328 | 0.995 | $< 10^{-3}$ | 0.158 | 0.809 | 0.891 | 0.046 | 0.549 |
| MD | 0.105 | 0.602 | 0.734 | 0.002 | 0.079 | 0.902 | 0.717 | 0.094 | 0.391 |
| $\text{DVF}_{\text{DTI}}$ | 0.378 | $< 10^{-3}$ | $-0.264$ | 0.008 | $-0.246$ | 0.382 | $-0.058$ | 0.744 | 0.283 |
| **DTI: fitting to data set *DataGaussian*** |  |  |  |  |  |  |  |  |  |
| FA | 0.953 | $< 10^{-8}$ | $-0.835$ | $< 10^{-7}$ | $-0.430$ | 0.136 | $-0.176$ | 0.330 | 0.833 |
| AD | 0.838 | 0.001 | 0.257 | 0.260 | $-0.157$ | 0.825 | 0.673 | 0.149 | 0.010 |
| RD | $-0.198$ | 0.362 | 1.025 | $< 10^{-3}$ | 0.474 | 0.491 | 0.767 | 0.094 | 0.541 |
| MD | 0.147 | 0.495 | 0.769 | 0.002 | 0.264 | 0.701 | 0.735 | 0.107 | 0.383 |
| $\text{DVF}_{\text{DTI}}$ | 0.416 | $< 10^{-3}$ | $-0.277$ | 0.006 | $-0.173$ | 0.540 | $-0.079$ | 0.660 | 0.290 |

Table B.3: results obtained from fitting the linear regression model number 2 in the control cases. Information is displayed using similar conventions as table B.1. All coefficients $\beta_0, ..., \beta_3$ have units of $[\mu\text{m}^2\ \text{ms}^{-1}]$ for DTI metrics AD, RD and MD, while they are dimensionless for all other metrics.

**MS cases, model no. 2**

$$m \;=\; \beta_0 \;+\; \beta_1\,\mathrm{CV} \;+\; \beta_2\,\mathrm{MSF} \;+\; \beta_3\,\mathrm{NSF}$$

| | $\beta_0$ | | $\beta_1$ | | $\beta_2$ | | $\beta_3$ | | |
|---|---|---|---|---|---|---|---|---|---|
| Metric $m$ | Coeff. | $p$ | Coeff. | $p$ | Coeff. | $p$ | Coeff. | $p$ | Adjusted $R^2$ |
| **NODDI: fitting to data set *DataFull*** | | | | | | | | | |
| $v_{\text{iso}}$ | 0.104 | 0.029 | −0.017 | 0.825 | −0.197 | 0.189 | −0.014 | 0.913 | 0.099 |
| $v_{\text{in}}$ | 0.224 | 0.109 | −0.324 | 0.178 | 1.940 | $< 10^{-3}$ | 0.580 | 0.134 | 0.570 |
| ODI | 0.126 | 0.004 | 0.326 | $< 10^{-4}$ | 0.129 | 0.333 | 0.303 | 0.012 | 0.525 |
| $\text{DVF}_{\text{NODDI}}$ | −0.019 | 0.634 | −0.028 | 0.692 | 0.462 | 0.002 | 0.280 | 0.020 | 0.547 |
| **DTI: fitting to data set *DataFull*** | | | | | | | | | |
| FA | 0.289 | 0.012 | −0.378 | 0.050 | 1.199 | 0.002 | 0.265 | 0.384 | 0.448 |
| AD | 1.602 | $< 10^{-8}$ | −0.033 | 0.914 | −1.790 | 0.005 | −0.837 | 0.104 | 0.423 |
| RD | 1.187 | $< 10^{-4}$ | 0.302 | 0.439 | −2.362 | 0.003 | −0.995 | 0.124 | 0.443 |
| MD | 1.326 | $< 10^{-6}$ | 0.190 | 0.591 | −2.171 | 0.003 | −0.942 | 0.111 | 0.445 |
| $\text{DVF}_{\text{DTI}}$ | 0.026 | 0.557 | −0.052 | 0.494 | 0.670 | $< 10^{-4}$ | 0.321 | 0.014 | 0.658 |
| **DTI: fitting to data set *DataGaussian*** | | | | | | | | | |
| FA | 0.350 | 0.002 | −0.334 | 0.072 | 0.924 | 0.011 | 0.278 | 0.347 | 0.362 |
| AD | 1.736 | $< 10^{-10}$ | −0.002 | 0.994 | −1.816 | 0.001 | −0.583 | 0.193 | 0.450 |
| RD | 1.128 | $< 10^{-4}$ | 0.341 | 0.401 | −1.986 | 0.015 | −0.900 | 0.179 | 0.343 |
| MD | 1.331 | $< 10^{-6}$ | 0.227 | 0.521 | −1.930 | 0.007 | −0.795 | 0.174 | 0.379 |
| $\text{DVF}_{\text{DTI}}$ | 0.039 | 0.441 | −0.061 | 0.476 | 0.774 | $< 10^{-4}$ | 0.375 | 0.012 | 0.667 |

Table B.4: results obtained from fitting the linear regression model number 2 in the MS cases. Information is displayed using similar conventions as table B.1. All coefficients $\beta_0, ..., \beta_3$ have units of $[\mu\text{m}^2\ \text{ms}^{-1}]$ for DTI metrics AD, RD and MD, while they are dimensionless for all other metrics.

**Control cases, model no. 3**

$$m \;=\; \beta_0 \;+\; \beta_1\,\text{CV} \;+\; \beta_2\,\text{NSF}$$

| | $\beta_0$ | | $\beta_1$ | | $\beta_2$ | | |
|---|---|---|---|---|---|---|---|
| Metric $m$ | Coeff. | $p$ | Coeff. | $p$ | Coeff. | $p$ | Adjusted $R^2$ |
| **NODDI: fitting to data set *DataFull*** | | | | | | | |
| $v_{\text{iso}}$ | $-0.055$ | 0.236 | 0.079 | 0.231 | 0.225 | 0.096 | 0.099 |
| $v_{\text{in}}$ | 1.125 | $< 10^{-8}$ | $-0.830$ | $< 10^{-4}$ | $-0.356$ | 0.262 | 0.593 |
| ODI | 0.280 | $< 10^{-6}$ | 0.437 | $< 10^{-7}$ | $-0.125$ | 0.220 | 0.819 |
| $\text{DVF}_{\text{NODDI}}$ | 0.163 | 0.023 | $-0.201$ | 0.044 | 0.024 | 0.900 | 0.135 |
| **DTI: fitting to data set *DataFull*** | | | | | | | |
| FA | 0.955 | $< 10^{-8}$ | $-0.960$ | $< 10^{-6}$ | $-0.502$ | 0.070 | 0.740 |
| AD | 0.705 | $< 10^{-3}$ | 0.211 | 0.304 | 0.363 | 0.377 | 0.091 |
| RD | $-0.169$ | 0.242 | 0.998 | $< 10^{-3}$ | 0.899 | 0.038 | 0.574 |
| MD | 0.122 | 0.381 | 0.736 | 0.001 | 0.721 | 0.081 | 0.427 |
| $\text{DVF}_{\text{DTI}}$ | 0.324 | $< 10^{-4}$ | $-0.269$ | 0.006 | $-0.070$ | 0.690 | 0.291 |
| **DTI: fitting to data set *DataGaussian*** | | | | | | | |
| FA | 0.859 | $< 10^{-9}$ | $-0.843$ | $< 10^{-7}$ | $-0.197$ | 0.293 | 0.818 |
| AD | 0.803 | $< 10^{-4}$ | 0.254 | 0.251 | 0.665 | 0.141 | 0.065 |
| RD | $-0.093$ | 0.535 | 1.034 | $< 10^{-3}$ | 0.790 | 0.079 | 0.554 |
| MD | 0.206 | 0.178 | 0.774 | 0.002 | 0.748 | 0.092 | 0.414 |
| $\text{DVF}_{\text{DTI}}$ | 0.378 | $< 10^{-5}$ | $-0.280$ | 0.004 | $-0.087$ | 0.618 | 0.315 |

Table B.5: results obtained from fitting the linear regression model number 3 in the control cases. Information is displayed using similar conventions as table B.1. Coefficients $\beta_0$, $\beta_1$ and $\beta_2$ have units of $[\mu\text{m}^2\ \text{ms}^{-1}]$ for DTI metrics AD, RD and MD, while they are dimensionless for all other metrics.

**MS cases, model no. 3**

$$m \;=\; \beta_0 \;+\; \beta_1\,\text{CV} \;+\; \beta_2\,\text{NSF}$$

| | $\beta_0$ | | $\beta_1$ | | $\beta_2$ | | |
|---|---|---|---|---|---|---|---|
| Metric $m$ | Coeff. | $p$ | Coeff. | $p$ | Coeff. | $p$ | Adjusted $R^2$ |
| | | | **NODDI: fitting to data set *DataFull*** | | | | |
| $v_{\text{iso}}$ | 0.102 | 0.034 | $-0.034$ | 0.662 | $-0.095$ | 0.405 | 0.031 |
| $v_{\text{in}}$ | 0.244 | 0.182 | $-0.157$ | 0.609 | 1.379 | 0.004 | 0.255 |
| ODI | 0.127 | 0.004 | 0.337 | $< 10^{-4}$ | 0.356 | 0.001 | 0.525 |
| $\text{DVF}_{\text{NODDI}}$ | $-0.015$ | 0.762 | 0.012 | 0.886 | 0.470 | $< 10^{-3}$ | 0.340 |
| | | | **DTI: fitting to data set *DataFull*** | | | | |
| FA | 0.301 | 0.026 | $-0.275$ | 0.217 | 0.759 | 0.024 | 0.207 |
| AD | 1.584 | $< 10^{-7}$ | $-0.187$ | 0.595 | $-1.573$ | 0.005 | 0.223 |
| RD | 1.164 | $< 10^{-3}$ | 0.098 | 0.827 | $-1.967$ | 0.005 | 0.229 |
| MD | 1.304 | $< 10^{-4}$ | 0.003 | 0.994 | $-1.836$ | 0.005 | 0.231 |
| $\text{DVF}_{\text{DTI}}$ | 0.032 | 0.589 | 0.006 | 0.954 | 0.596 | $< 10^{-3}$ | 0.364 |
| | | | **DTI: fitting to data set *DataGaussian*** | | | | |
| FA | 0.359 | 0.004 | $-0.255$ | 0.208 | 0.658 | 0.030 | 0.195 |
| AD | 1.719 | $< 10^{-8}$ | $-0.158$ | 0.625 | $-1.331$ | 0.008 | 0.187 |
| RD | 1.108 | $< 10^{-3}$ | 0.170 | 0.701 | $-1.718$ | 0.012 | 0.188 |
| MD | 1.311 | $< 10^{-5}$ | 0.061 | 0.878 | $-1.589$ | 0.010 | 0.191 |
| $\text{DVF}_{\text{DTI}}$ | 0.046 | 0.501 | 0.005 | 0.964 | 0.694 | $< 10^{-3}$ | 0.371 |

Table B.6: results obtained from fitting the linear regression model number 3 in the MS cases. Information is displayed using similar conventions as table B.1. Coefficients $\beta_0$, $\beta_1$ and $\beta_2$ have units of $[\mu\text{m}^2\ \text{ms}^{-1}]$ for DTI metrics AD, RD and MD, while they are dimensionless for all other metrics.

**Control cases, model no. 4**

$m = \beta_0 + \beta_1\,\text{MSF} + \beta_2\,\text{NSF}$

| | $\beta_0$ | | $\beta_1$ | | $\beta_2$ | | |
|---|---|---|---|---|---|---|---|
| Metric $m$ | Coeff. | $p$ | Coeff. | $p$ | Coeff. | $p$ | Adjusted $R^2$ |
| **NODDI: fitting to data set *DataFull*** | | | | | | | |
| $v_{\text{iso}}$ | $-0.085$ | 0.150 | 0.286 | 0.165 | 0.188 | 0.149 | 0.125 |
| $v_{\text{in}}$ | 0.711 | 0.006 | 0.194 | 0.810 | $-0.111$ | 0.828 | 0.006 |
| ODI | 0.417 | 0.001 | 0.249 | 0.502 | $-0.270$ | 0.257 | 0.090 |
| $\text{DVF}_{\text{NODDI}}$ | 0.157 | 0.102 | $-0.366$ | 0.265 | 0.101 | 0.620 | 0.080 |
| **DTI: fitting to data set *DataFull*** | | | | | | | |
| FA | 0.596 | 0.024 | $-0.295$ | 0.729 | $-0.195$ | 0.716 | 0.016 |
| AD | 0.807 | $< 10^{-3}$ | $-0.039$ | 0.953 | 0.300 | 0.473 | 0.031 |
| RD | 0.195 | 0.499 | 0.348 | 0.728 | 0.578 | 0.365 | 0.058 |
| MD | 0.399 | 0.111 | 0.219 | 0.794 | 0.486 | 0.366 | 0.054 |
| $\text{DVF}_{\text{DTI}}$ | 0.272 | 0.011 | $-0.296$ | 0.386 | 0.025 | 0.907 | 0.044 |
| **DTI: fitting to data set *DataGaussian*** | | | | | | | |
| FA | 0.619 | 0.006 | $-0.560$ | 0.405 | 0.087 | 0.845 | 0.041 |
| AD | 0.941 | $< 10^{-3}$ | $-0.107$ | 0.880 | 0.592 | 0.199 | 0.095 |
| RD | 0.213 | 0.477 | 0.670 | 0.520 | 0.444 | 0.500 | 0.054 |
| MD | 0.455 | 0.088 | 0.411 | 0.646 | 0.493 | 0.387 | 0.059 |
| $\text{DVF}_{\text{DTI}}$ | 0.304 | 0.006 | $-0.226$ | 0.516 | 0.008 | 0.970 | 0.250 |

Table B.7: results obtained from fitting the linear regression model number 4 in the control cases. Information is displayed using similar conventions as table B.1. Coefficients $\beta_0$, $\beta_1$ and $\beta_2$ have units of $[\mu\text{m}^2\ \text{ms}^{-1}]$ for DTI metrics AD, RD and MD, while they are dimensionless for all other metrics.

**MS cases, model no. 4**

$m \;=\; \beta_0 \;+\; \beta_1\,\text{MSF} \;+\; \beta_2\,\text{NSF}$

| | $\beta_0$ | | $\beta_1$ | | $\beta_2$ | | |
|---|---|---|---|---|---|---|---|
| Metric $m$ | Coeff. | $p$ | Coeff. | $p$ | Coeff. | $p$ | Adjusted $R^2$ |
| **NODDI: fitting to data set *DataFull*** | | | | | | | |
| $v_{\text{iso}}$ | 0.096 | 0.002 | $-0.202$ | 0.163 | $-0.007$ | 0.956 | 0.025 |
| $v_{\text{in}}$ | 0.083 | 0.366 | 1.840 | $< 10^{-3}$ | 0.715 | 0.068 | 0.554 |
| ODI | 0.269 | $< 10^{-7}$ | 0.230 | 0.202 | 0.167 | 0.269 | 0.115 |
| $\text{DVF}_{\text{NODDI}}$ | $-0.032$ | 0.231 | 0.453 | 0.002 | 0.292 | 0.012 | 0.562 |
| **DTI: fitting to data set *DataFull*** | | | | | | | |
| FA | 0.122 | 0.110 | 1.082 | 0.007 | 0.422 | 0.182 | 0.376 |
| AD | 1.587 | $< 10^{-12}$ | $-1.800$ | 0.003 | $-0.823$ | 0.091 | 0.446 |
| RD | 1.320 | $< 10^{-8}$ | $-2.269$ | 0.004 | $-1.120$ | 0.074 | 0.451 |
| MD | 1.409 | $< 10^{-10}$ | $-2.112$ | 0.003 | $-1.021$ | 0.072 | 0.463 |
| $\text{DVF}_{\text{DTI}}$ | 0.003 | 0.917 | 0.654 | $< 10^{-4}$ | 0.342 | 0.007 | 0.665 |
| **DTI: fitting to data set *DataGaussian*** | | | | | | | |
| FA | 0.203 | 0.008 | 0.821 | 0.027 | 0.416 | 0.169 | 0.297 |
| AD | 1.736 | $< 10^{-14}$ | $-1.817$ | 0.001 | $-0.582$ | 0.170 | 0.472 |
| RD | 1.278 | $< 10^{-8}$ | $-1.881$ | 0.018 | $-1.042$ | 0.109 | 0.350 |
| MD | 1.430 | $< 10^{-10}$ | $-1.859$ | 0.008 | $-0.889$ | 0.113 | 0.393 |
| $\text{DVF}_{\text{DTI}}$ | 0.012 | 0.720 | 0.755 | $< 10^{-4}$ | 0.401 | 0.006 | 0.673 |

Table B.8: results obtained from fitting the linear regression model number 4 in the MS cases. Information is displayed using similar conventions as table B.1. Coefficients $\beta_0$, $\beta_1$ and $\beta_2$ have units of $[\mu\text{m}^2\ \text{ms}^{-1}]$ for DTI metrics AD, RD and MD, while they are dimensionless for all other metrics.

**Control cases, model no. 5**

$m \ = \ \beta_0 \ + \ \beta_1\,\text{ASF} \ + \ \beta_2\,\mu\text{GSF}$

| | $\beta_0$ | | $\beta_1$ | | $\beta_2$ | | |
|---|---|---|---|---|---|---|---|
| Metric $m$ | Coeff. | $p$ | Coeff. | $p$ | Coeff. | $p$ | Adjusted $R^2$ |
| | | | **NODDI: fitting to data set *DataFull*** | | | | |
| $v_{\text{iso}}$ | 0.201 | 0.183 | $-0.614$ | 0.170 | 1.092 | 0.136 | 0.109 |
| $v_{\text{in}}$ | 0.519 | 0.373 | 0.850 | 0.619 | $-2.252$ | 0.422 | 0.050 |
| ODI | 0.266 | 0.331 | 0.566 | 0.481 | $-1.438$ | 0.277 | 0.092 |
| $\text{DVF}_{\text{NODDI}}$ | 0.386 | 0.022 | $-0.516$ | 0.268 | $-3.594$ | $< 10^{-3}$ | 0.555 |
| | | | **DTI: fitting to data set *DataFull*** | | | | |
| FA | 0.568 | 0.365 | $-0.107$ | 0.953 | $-1.723$ | 0.566 | 0.020 |
| AD | 1.451 | 0.004 | $-1.950$ | 0.151 | 2.317 | 0.290 | 0.065 |
| RD | 0.775 | 0.295 | $-1.326$ | 0.541 | 2.907 | 0.413 | 0.058 |
| MD | 1.001 | 0.111 | $-1.534$ | 0.395 | 2.710 | 0.358 | 0.086 |
| $\text{DVF}_{\text{DTI}}$ | 0.405 | 0.034 | $-0.251$ | 0.635 | $-3.465$ | $< 10^{-3}$ | 0.445 |
| | | | **DTI: fitting to data set *DataGaussian*** | | | | |
| FA | 0.555 | 0.296 | $-0.146$ | 0.925 | $-0.189$ | 0.940 | 0.001 |
| AD | 1.732 | 0.002 | $-2.311$ | 0.121 | 3.299 | 0.171 | 0.118 |
| RD | 0.844 | 0.275 | $-1.293$ | 0.567 | 2.318 | 0.530 | 0.041 |
| MD | 1.140 | 0.090 | $-1.632$ | 0.397 | 2.645 | 0.400 | 0.078 |
| $\text{DVF}_{\text{DTI}}$ | 0.423 | 0.032 | $-0.171$ | 0.753 | $-3.458$ | $< 10^{-3}$ | 0.424 |

Table B.9: results obtained from fitting the linear regression model number 5 in the control cases. Information is displayed using similar conventions as table B.1. Coefficients $\beta_0$, $\beta_1$ and $\beta_2$ have units of $[\mu\text{m}^2\ \text{ms}^{-1}]$ for DTI metrics AD, RD and MD, while they are dimensionless for all other metrics.

**MS cases, model no. 5**

$m = \beta_0 + \beta_1\,\text{ASF} + \beta_2\,\mu\text{GSF}$

| | $\beta_0$ | | $\beta_1$ | | $\beta_2$ | | |
|---|---|---|---|---|---|---|---|
| Metric $m$ | Coeff. | $p$ | Coeff. | $p$ | Coeff. | $p$ | Adjusted $R^2$ |
| **NODDI: fitting to data set *DataFull*** | | | | | | | |
| $v_{\text{iso}}$ | 0.134 | 0.023 | −0.156 | 0.280 | −0.262 | 0.385 | 0.064 |
| $v_{\text{in}}$ | 0.247 | 0.300 | 0.262 | 0.664 | 3.471 | 0.010 | 0.176 |
| ODI | 0.414 | $< 10^{-5}$ | −0.250 | 0.179 | 0.267 | 0.487 | 0.029 |
| $\text{DVF}_{\text{NODDI}}$ | 0.054 | 0.386 | −0.038 | 0.811 | 1.232 | $< 10^{-3}$ | 0.327 |
| **DTI: fitting to data set *DataFull*** | | | | | | | |
| FA | 0.118 | 0.480 | 0.417 | 0.329 | 2.239 | 0.017 | 0.152 |
| AD | 1.426 | $< 10^{-4}$ | −0.276 | 0.684 | −3.837 | 0.012 | 0.168 |
| RD | 1.264 | $< 10^{-3}$ | −0.780 | 0.367 | −5.140 | 0.008 | 0.195 |
| MD | 1.318 | $< 10^{-3}$ | −0.612 | 0.439 | −4.706 | 0.008 | 0.192 |
| $\text{DVF}_{\text{DTI}}$ | 0.102 | 0.197 | $> -10^{-3}$ | 0.998 | 1.495 | 0.001 | 0.300 |
| **DTI: fitting to data set *DataGaussian*** | | | | | | | |
| FA | 0.140 | 0.341 | 0.490 | 0.195 | 2.150 | 0.010 | 0.195 |
| AD | 1.553 | $< 10^{-6}$ | −0.142 | 0.819 | −3.267 | 0.018 | 0.143 |
| RD | 1.335 | $< 10^{-3}$ | −0.957 | 0.254 | −4.711 | 0.011 | 0.182 |
| MD | 1.408 | $< 10^{-6}$ | −0.685 | 0.362 | −4.230 | 0.011 | 0.174 |
| $\text{DVF}_{\text{DTI}}$ | 0.124 | 0.177 | 0.010 | 0.964 | 1.719 | 0.002 | 0.296 |

Table B.10: results obtained from fitting the linear regression model number 5 in the MS cases. Information is displayed using similar conventions as table B.1. Coefficients $\beta_0$, $\beta_1$ and $\beta_2$ have units of $[\mu\text{m}^2\ \text{ms}^{-1}]$ for DTI metrics AD, RD and MD, while they are dimensionless for all other metrics.

# Bibliography

[1] F Aboitiz, AB Scheibel, RS Fisher, and E Zaidel. Fiber composition of the human corpus callosum. *Brain research*, 598(1):143–153, 1992.

[2] I Aganj, C Lenglet, G Sapiro, E Yacoub, K Ugurbil, and N Harel. Reconstruction of the orientation distribution function in single-and multiple-shell q-ball imaging within constant solid angle. *Magnetic Resonance in Medicine*, 64(2):554–566, 2010.

[3] F Agosta, B Benedetti, MA Rocca, P Valsasina, M Rovaris, G Comi, and M Filippi. Quantification of cervical cord pathology in primary progressive MS using diffusion tensor MRI. *Neurology*, 64(4):631–635, 2005.

[4] DC Alexander, PL Hubbard, MG Hall, EA Moore, M Ptito, GJM Parker, and TB Dyrby. Orientationally invariant indices of axon diameter and density from diffusion MRI. *NeuroImage*, 52(4):1374–1389, 2010.

[5] DC Alexander, D Zikic, J Zhang, H Zhang, and A Criminisi. Image quality transfer via random forest regression: applications in diffusion MRI. In *proceedings of Medical Image Computing and Computer-Assisted Intervention* (MICCAI) *meeting*, pages 225–232, 2014.

[6] D Arthur and S Vassilvitskii. k-means++: the advantages of careful seeding. In *proceedings of the eighteenth annual ACM-SIAM symposium on discrete algorithms, Society for Industrial and Applied Mathematics*, pages 1027–1035, 2007.

[7] Y Assaf, T Blumenfeld-Katzir, Y Yovel, and PJ Basser. AxCaliber: a method for measuring axon diameter distribution from diffusion MRI. *Magnetic Resonance in Medicine*, 59(6):1347–1354, 2008.

[8] Y Assaf, RZ Freidlin, GK Rohde, and PJ Basser. New modeling and experimental framework to characterize hindered and restricted water diffusion in brain white matter. *Magnetic Resonance in Medicine*, 52(5):965–978, 2004.

[9] M Axer, K Amunts, D Grässel, C Palm, J Dammers, H Axer, U Pietrzyk, and K Zilles. A novel approach to the human connectome: ultra-high resolution mapping of fiber tracts in the brain. *NeuroImage*, 54(2):1091–1101, 2011.

[10] CA Baron and C Beaulieu. Oscillating gradient spin-echo (OGSE) diffusion tensor imaging of the human brain. *Magnetic Resonance in Medicine*, 72(3):726–736, 2014.

[11] JW Bartlett and C Frost. Reliability, repeatability and reproducibility: analysis of measurement errors in continuous variables. *Ultrasound in Obstetrics and Gynecology*, 31(4):466–475, 2008.

[12] PJ Basser, J Mattiello, and D LeBihan. MR diffusion tensor spectroscopy and imaging. *Biophysical Journal*, 66(1):259–267, 1994.

[13] PJ Basser and C Pierpaoli. Microstructural and physiological features of tissues elucidated by quantitative-diffusion-tensor MRI. *Journal of Magnetic Resonance*, 213(2):560–570, 2011.

[14] C Beaulieu. The basis of anisotropic water diffusion in the nervous system – a technical review. *NMR in Biomedicine*, 15(7-8):435–455, 2002.

[15] TEJ Behrens, MW Woolrich, M Jenkinson, H Johansen-Berg, RG Nunes, S Clare, PM Matthews, JM Brady, and SM Smith. Characterization and propagation of uncertainty in diffusion-weighted MR imaging. *Magnetic Resonance in Medicine*, 50(5):1077–1088, 2003.

[16] J Bigün and GH Granlund. Optimal orientation detection of linear symmetry. In *proceedings of the* IEEE *first international conference on computer vision*, pages 433–438, 1987.

[17] T Billiet, B Mädler, F D'Arco, R Peeters, S Deprez, E Plasschaert, A Leemans, H Zhang, BV den Bergh, M Vandenbulcke, E Legius, S Sunaert, and L Emsell. Characterizing the microstructural basis of "unidentified bright objects" in neurofibromatosis type 1: a combined in vivo multicomponent T2 relaxation and multi-shell diffusion MRI analysis. *NeuroImage: Clinical*, 4:649–658, 2014.

[18] F Bloch. Nuclear induction. *Physical review*, 70(7-8):460, 1946.

[19] N Bloembergen, EM Purcell, and RV Pound. Relaxation effects in nuclear magnetic resonance absorption. *Physical Review*, 73(7):679, 1948.

[20] JCJ Bot, ELA Blezer, W Kamphorst, GJ Lycklama a Nijeholt, HJ Ader, JA Castelijns, E Bergers, R Ravid, C Polman, and F Barkhof. The spinal cord in multiple sclerosis: relationship of high-spatial-resolution quantitative MR imaging findings to histopathologic results. *Radiology*, 233(2):531–540, 2004.

[21] MD Budde and J Annese. Quantification of anisotropy and fiber orientation in human brain histological sections. *Frontiers in Integrative Neuroscience*, 7, 2013.

[22] MD Budde and JA Frank. Examining brain microstructure using structure tensor analysis of histological sections. *NeuroImage*, 63(1):1–10, 2012.

[23] MD Budde, L Janes, E Gold, LC Turtzo, and JA Frank. The contribution of gliosis to diffusion tensor anisotropy and tractography following traumatic brain injury: validation in the rat using Fourier analysis of stained tissue sections. *Brain*, 134(8):2248–2260, 2011.

[24] MD Budde, JH Kim, HF Liang, JH Russell, AH Cross, and SK Song. Axonal injury detected by in vivo diffusion tensor imaging correlates with neurological disability in a mouse model of multiple sclerosis. *NMR in Biomedicine*, 21(6):589–597, 2008.

[25] MD Budde, M Xie, AH Cross, and SK Song. Axial diffusivity is the primary correlate of axonal injury in the EAE spinal cord: a quantitative pixelwise analysis. *The Journal of Neuroscience*, 29(9):2805–2813, 2009.

[26] LM Burcaw, E Fieremans, and DS Novikov. Mesoscopic structure of neuronal tracts from time-dependent diffusion. *NeuroImage*, 114:18–37, 2015.

[27] F Calamante, JD Tournier, GD Jackson, and A Connelly. Track-density imaging (TDI): super-resolution white matter imaging using whole-brain track-density mapping. *NeuroImage*, 53(4):1233–1243, 2010.

[28] PT Callaghan, A Coy, D MacGowan, KJ Packer, and FO Zelaya. Diffraction-like effects in NMR diffusion studies of fluids in porous solids. *Nature*, 351:467–469, 1991.

[29] HY Carr and EM Purcell. Effects of diffusion on free precession in nuclear magnetic resonance experiments. *Physical Review*, 94(3):630, 1954.

[30] AS Choe, I Stepniewska, DC Colvin, Z Ding, and AW Anderson. Validation of diffusion tensor MRI in the central nervous system using light microscopy: quantitative comparison of fiber properties. *NMR in Biomedicine*, 25(7):900–908, 2012.

[31] O Ciccarelli, F Barkhof, B Bodini, N De Stefano, X Golay, K Nicolay, D Pelletier, PJW Pouwels, SA Smith, CAM Wheeler-Kingshott, B Stankoff, T Yousry, and DH Miller. Pathogenesis of multiple sclerosis: insights from molecular and metabolic imaging. *The Lancet Neurology*, 13(8):807–822, 2014.

[32] O Ciccarelli, CA Wheeler-Kingshott, MA McLean, M Cercignani, K Wimpey, DH Miller, and AJ Thompson. Spinal cord spectroscopy and diffusion-based tractography to assess acute disability in multiple sclerosis. *Brain*, 130(8):2220–2231, 2007.

[33] CA Clark and D Le Bihan. Water diffusion compartmentation and anisotropy at high b values in the human brain. *Magnetic Resonance in Medicine*, 44(6):852–859, 2000.

[34] J Cohen-Adad, MM El Mendili, S Lehéricy, PF Pradat, S Blancho, S Rossignol, and H Benali. Demyelination and degeneration in the injured human spinal cord detected with diffusion and magnetization transfer MRI. *NeuroImage*, 55(3):1024–1033, 2011.

[35] J Cohen-Adad, MME Mendili, R Morizot-Koutlidis, S Lehéricy, V Meininger, S Blancho, S Rossignol, H Benali, and PF Pradat. Involvement of spinal sensory pathway in ALS and specificity of cord atrophy to lower motor neuron degeneration. *Amyotrophic Lateral Sclerosis and Frontotemporal Degeneration*, 14(1):30–38, 2013.

[36] J Cohen-Adad and CAM Wheeler-Kingshott. *Quantitative MRI of the spinal cord*. Academic Press, 2014.

[37] A Compston and A Coles. Multiple sclerosis. *The Lancet*, 372:1502–1517, 2008.

[38] PA Cook, Y Bai, S Nedjati-Gilani, KK Seunarine, MG Hall, GJ Parker, and DC Alexander. Camino: open-source diffusion-MRI reconstruction and processing. In *proceedings of the 14th meeting of the International Society for Magnetic Resonance in Medicine* (ISMRM), page 2759, 2006.

[39] J Correale. The role of microglial activation in disease progression. *Multiple Sclerosis Journal*, 20(10):1288–1295, 2014.

[40] GC DeLuca, R Alterman, JL Martin, A Mittal, S Blundell, S Bird, H Beale, L San Hong, and MM Esiri. Casting light on multiple sclerosis heterogeneity: the role of HLA-DRB1 on spinal cord pathology. *Brain*, 134(4):1025–1034, 2013.

[41] GC DeLuca, GC Ebers, and MM Esiri. Axonal loss in multiple sclerosis: a pathological survey of the corticospinal and sensory tracts. *Brain*, 127(5):1009–1018, 2004.

[42] SCL Deoni, BK Rutt, T Arun, C Pierpaoli, and DK Jones. Gleaning multicomponent T1 and T2 information from steady-state imaging data. *Magnetic Resonance in Medicine*, 60(6):1372–1387, 2008.

[43] M Descoteaux, R Deriche, D Le Bihan, JF Mangin, and C Poupon. Multiple q-shell diffusion propagator imaging. *Medical Image Analysis*, 15(4):603–621, 2011.

[44] A Deshmane, V Gulani, MA Griswold, and N Seiberlich. Parallel MR imaging. *Journal of Magnetic Resonance Imaging*, 36(1):55–72, 2012.

[45] LR Dice. Measures of the amount of ecologic association between species. *Ecology*, 26(3):297–302, 1945.

[46] DC Douglass and DW McCall. Diffusion in paraffin hydrocarbons. *The Journal of Physical Chemistry*, 62(9):1102–1107, 1958.

[47] R Dutta and BD Trapp. Relapsing and progressive forms of multiple sclerosis: insights from pathology. *Current opinion in Neurology*, 27(3):271–278, 2014.

[48] T Duval, JA McNab, K Setsompop, T Witzel, T Schneider, SY Huang, B Keil, EC Klawiter, LL Wald, and J Cohen-Adad. In vivo mapping of human spinal cord microstructure at 300mT/m. *NeuroImage*, 118:494–507, 2015.

[49] C Eichner, SF Cauley, J Cohen-Adad, HE Möller, R Turner, K Setsompop, and LL Wald. Real diffusion-weighted MRI enabling true signal averaging and increased diffusion contrast. *NeuroImage*, 122:373–384, 2015.

[50] A Einstein. On the movement of small particles suspended in stationary liquids required by the molecular-kinetic theory of heat. *Annalen der Physik (in German)*, 322(8):549–560, 1905.

[51] BM Ellingson, N Salamon, AJ Hardy, and LT Holly. Prediction of neurological impairment in cervical spondylotic myelopathy using a combination of diffusion MRI and proton MR spectroscopy. *PloS one*, 10(10):e0139451, 2015.

[52] D Facon, A Ozanne, P Fillard, JF Lepeintre, C Tournoux-Facon, and D Ducreux. MR diffusion tensor imaging and fiber tracking in spinal cord compression. *American Journal of Neuroradiology*, 26(6):1587–1594, 2005.

[53] MF Falangola, DN Guilfoyle, A Tabesh, ES Hui, X Nie, JH Jensen, SV Gerum, C Hu, J LaFrancois, HR Collins, and JA Helpern. Histological correlation of diffusional kurtosis and white matter modeling metrics in cuprizone-induced corpus callosum demyelination. *NMR in Biomedicine*, 27(8):948–957, 2014.

[54] JAD Farrell, SA Smith, EM Gordon-Lipkin, DS Reich, PA Calabresi, and P van Zijl. High b-value q-space diffusion-weighted MRI of the human cervical spinal cord in vivo: feasibility and application to multiple sclerosis. *Magnetic Resonance in Medicine*, 59(5):1079–1089, 2008.

[55] DA Feinberg and K Setsompop. Ultra-fast MRI of the human brain with simultaneous multi-slice imaging. *Journal of magnetic resonance*, 229:90–100, 2013.

[56] HKP Feirabend, H Choufoer, S Ploeger, J Holsheimer, and JD Van Gool. Morphometry of human superficial dorsal and dorsolateral column fibres: significance to spinal cord stimulation. *Brain*, 125(5):1137–1149, 2002.

[57] FRE Fenrich, C Beaulieu, and PS Allen. Relaxation times and microstructures. *NMR in Biomedicine*, 14(2):133–139, 2001.

[58] U Ferizi, T Schneider, M Tariq, CAM Wheeler-Kingshott, H Zhang, and DC Alexander. The importance of being dispersed: a ranking of diffusion MRI models for fibre dispersion using in vivo human brain data. In *proceedings of Medical Image Computing and Computer-Assisted Intervention* (MICCAI) *meeting*, pages 74–81, 2013.

[59] E Fieremans, JH Jensen, and JA Helpern. White matter characterization with diffusional kurtosis imaging. *NeuroImage*, 58(1):177–188, 2011.

[60] NI Fisher, T Lewis, and BJJ Embleton. *Statistical analysis of spherical data*. Cambridge university press, 1987.

[61] J Frahm, KD Merboldt, W Hänicke, and A Haase. Stimulated echo imaging. *Journal of Magnetic Resonance (1969)*, 64(1):81–93, 1985.

[62] AF Frøhlich, SN Jespersen, L Østergaard, and VG Kiselev. The effect of impermeable boundaries of arbitrary geometry on the apparent diffusion coefficient. *Journal of Magnetic Resonance*, 194(1):128–135, 2008.

[63] A Gass, MA Rocca, F Agosta, O Ciccarelli, D Chard, P Valsasina, JCW Brooks, A Bischof, P Eisele, L Kappos, F Barkhof, M Filippi, and for the MAGNIMS Study Group. MRI monitoring of pathological changes in the spinal cord in patients with multiple sclerosis. *The Lancet Neurology*, 14(4):443–454, 2015.

[64] DN Greve and B Fischl. Accurate and robust brain image alignment using boundary-based registration. *NeuroImage*, 48(1):63–72, 2009.

[65] T Gringel, W Schulz-Schaeffer, E Elolf, A Frölich, P Dechent, and G Helms. Optimized high-resolution mapping of magnetization transfer (MT) at 3 Tesla for direct visualization of substructures of the human thalamus in clinically feasible measurement time. *Journal of Magnetic Resonance Imaging*, 29(6):1285–1292, 2009.

[66] MA Griswold, PM Jakob, RM Heidemann, M Nittka, V Jellus, J Wang, B Kiefer, and A Haase. Generalized autocalibrating partially parallel acquisitions (GRAPPA). *Magnetic resonance in medicine*, 47(6):1202–1210, 2002.

[67] F Grussu, T Schneider, H Zhang, DC Alexander, and CAM Wheeler-Kingshott. Neurite orientation dispersion and density imaging of the healthy cervical spinal cord in vivo. *NeuroImage*, 111:590–601, 2015.

[68] H Gudbjartsson and S Patz. The Rician distribution of noisy MRI data. *Magnetic Resonance in Medicine*, 34(6):910–914, 1995.

[69] EM Haacke, RW Brown, MR Thompson, and R Venkatesan. *Magnetic resonance imaging: physical principles and sequence design*. John Wiley & Sons, 1999.

[70] G Häggqvist. Analyse der faserverteilung in einem rückenmarkquerschnitt (th 3). *Z Mikrosk Anat Forsch*, 39:1–34, 1936.

[71] EL Hahn. Spin echoes. *Physical Review*, 80(4):580, 1950.

[72] L Haider. Inflammation, iron, energy failure, and oxidative stress in the pathogenesis of multiple sclerosis. *Oxidative Medicine and Cellular Longevity*, 2015, 2015.

[73] JE Holley, D Gveric, J Newcombe, ML Cuzner, and NJ Gutowski. Astrocyte characterization in the multiple sclerosis glial scar. *Neuropathology and Applied Neurobiology*, 29(5):434–444, 2003.

[74] MA Horsfield, S Sala, M Neema, M Absinta, A Bakshi, MP Sormani, MA Rocca, R Bakshi, and M Filippi. Rapid semi-automatic segmentation of the spinal cord from magnetic resonance images: application in multiple sclerosis. *NeuroImage*, 50(2):446–455, 2010.

[75] PL Hubbard, FL Zhou, SJ Eichhorn, and GJM Parker. Biomimetic phantom for the validation of diffusion magnetic resonance imaging. *Magnetic Resonance in Medicine*, 73(1):299–305, 2015.

[76] C Ingo, RL Magin, L Colon-Perez, W Triplett, and TH Mareci. On random walks and entropy in diffusion-weighted magnetic resonance imaging studies of neural tissue. *Magnetic Resonance in Medicine*, 71(2):617–627, 2014.

[77] KM Jansons and DC Alexander. Persistent angular structure: new insights from diffusion magnetic resonance imaging data. *Inverse problems*, 19(5):1031, 2003.

[78] VA Janve, Z Zu, SY Yao, K Li, FL Zhang, KJ Wilson, X Ou, MD Does, S Subramaniam, and DF Gochberg. The radial diffusivity and magnetization transfer pool size ratio are sensitive markers for demyelination in a rat model of type III multiple sclerosis (MS) lesions. *NeuroImage*, 74:298–305, 2013.

[79] S Jbabdi and H Johansen-Berg. Tractography: where do we go from here? *Brain Connectivity*, 1(3):169–183, 2011.

[80] IO Jelescu, J Veraart, V Adisetiyo, SS Milla, DS Novikov, and E Fieremans. One diffusion acquisition and different white matter models: how does microstructure change in human early development based on WMTI and NODDI? *NeuroImage*, 107:242–256, 2015.

[81] IO Jelescu, J Veraart, E Fieremans, and DS Novikov. Degeneracy in model parameter estimation for multi-compartmental diffusion in neuronal tissue. *NMR in Biomedicine*, 29(1):33–47, 2016.

[82] M Jenkinson, P Bannister, M Brady, and S Smith. Improved optimization for the robust and accurate linear registration and motion correction of brain images. *NeuroImage*, 17(2):825–841, 2002.

[83] M Jenkinson and S Smith. A global optimisation method for robust affine registration of brain images. *Medical Image Analysis*, 5(2):143–156, 2001.

[84] JH Jensen, JA Helpern, A Ramani, H Lu, and K Kaczynski. Diffusional kurtosis imaging: the quantification of non-gaussian water diffusion by means of magnetic resonance imaging. *Magnetic Resonance in Medicine*, 53(6):1432–1440, 2005.

[85] SN Jespersen, CR Bjarkam, JR Nyengaard, MM Chakravarty, B Hansen, T Vosegaard, L Østergaard, D Yablonskiy, NC Nielsen, and P Vestergaard-Poulsen. Neurite density from magnetic resonance diffusion measurements at ultrahigh field: comparison with light microscopy and electron microscopy. *NeuroImage*, 49(1):205–216, 2010.

[86] SN Jespersen and N Buhl. The displacement correlation tensor: microstructure, ensemble anisotropy and curving fibers. *Journal of Magnetic Resonance*, 208(1):34–43, 2011.

[87] SN Jespersen, CD Kroenke, L Østergaard, JJH Ackerman, and DA Yablonskiy. Modeling dendrite density from magnetic resonance diffusion measurements. *NeuroImage*, 34(4):1473–1486, 2007.

[88] SN Jespersen, LA Leigland, A Cornea, and CD Kroenke. Determination of axonal and dendritic orientation distributions within the developing cerebral cortex by diffusion tensor imaging. *IEEE Transactions on Medical Imaging*, 31(1):16–32, 2012.

[89] SN Jespersen, H Lundell, CK Sønderby, and TB Dyrby. Orientationally invariant metrics of apparent compartment eccentricity from double pulsed field gradient diffusion experiments. *NMR in Biomedicine*, 26(12):1647–1662, 2013.

[90] H Johansen-Berg and TEJ Behrens. Diffusion MRI: from quantitative measurement to in-vivo neuroanatomy. *Academic Press*, 2009.

[91] JB Johnson. Thermal agitation of electricity in conductors. *Physical review*, 32(1):97, 1928.

[92] DK Jones. Diffusion MRI: theory, methods and applications. *Oxford University Press*, 2010.

[93] DK Jones and PJ Basser. "Squashing peanuts and smashing pumpkins": how noise distorts diffusion-weighted MR data. *Magnetic Resonance in Medicine*, 52(5):979–993, 2004.

[94] A Jubran. Pulse oximetry. *Critical Care*, 19(1):1–7, 2015.

[95] E Kaden, F Kruggel, and DC Alexander. Quantitative mapping of the per-axon diffusion coefficients in brain white matter. *Magnetic Resonance in Medicine*, 75(4):1752–1763, 2016.

[96] H Kearney, DH Miller, and O Ciccarelli. Spinal cord MRI in multiple sclerosis – diagnostic, prognostic and clinical value. *Nature Reviews Neurology*, 11:327–338, 2015.

[97] H Kearney, T Schneider, MC Yiannakas, DR Altmann, CAM Wheeler-Kingshott, O Ciccarelli, and DH Miller. Spinal cord grey matter abnormalities are associated with secondary progression and physical disability in multiple sclerosis. *Journal of Neurology, Neurosurgery and Psychiatry*, 86(6):608–614, 2015.

[98] AR Khan, A Cornea, LA Leigland, SG Kohama, SN Jespersen, and CD Kroenke. 3D structure tensor analysis of light microscopy data for validating diffusion MRI. *NeuroImage*, 111:192–203, 2015.

[99] EC Klawiter, RE Schmidt, K Trinkaus, HF Liang, MD Budde, RT Naismith, SK Song, AH Cross, and TL Benzinger. Radial diffusivity predicts demyelination in *ex vivo* multiple sclerosis spinal cords. *NeuroImage*, 55(4):1454–1460, 2011.

[100] ME Komlosh, E Özarslan, MJ Lizak, F Horkay, V Schram, N Shemesh, Y Cohen, and PJ Basser. Pore diameter mapping using double pulsed-field gradient MRI and its validation using a novel glass capillary array phantom. *Journal of Magnetic Resonance*, 208(1):128–135, 2011.

[101] N Kunz, H Zhang, L Vasung, KR O'Brien, Y Assaf, F Lazeyras, DC Alexander, and PS Hüppi. Assessing white matter microstructure of the newborn with multi-shell diffusion MRI and biophysical compartment models. *NeuroImage*, 96:288–299, 2014.

[102] JF Kurtzke. Rating neurologic impairment in multiple sclerosis – an expanded disability status scale (EDSS). *Neurology*, 33(11):1444–1452, 1983.

[103] S Lasič, F Szczepankiewicz, S Eriksson, M Nilsson, and D Topgaard. Microanisotropy imaging: quantification of microscopic diffusion anisotropy and orientational order parameter by diffusion MRI with magic-angle spinning of the q-vector. *Frontiers in Physics*, 2:11, 2014.

[104] H Lassmann. Axonal injury in multiple sclerosis. *Journal of Neurology, Neurosurgery & Psychiatry*, 74(6):695–697, 2003.

[105] H Lassmann, W Brück, and CF Lucchinetti. The immunopathology of multiple sclerosis: an overview. *Brain Pathology*, 17(2):210–218, 2007.

[106] C Laule, P Kozlowski, E Leung, DKB Li, AL MacKay, and GRW Moore. Myelin water imaging of multiple sclerosis at 7 T: correlations with histopathology. *NeuroImage*, 40(4):1575–1580, 2008.

[107] C Laule, IM Vavasour, Y Zhao, AL Traboulsee, J Oger, JD Vavasour, AL Mackay, and DKB Li. Two-year study of cervical cord volume and myelin water in primary progressive multiple sclerosis. *Multiple Sclerosis*, 16(6):670–677, 2010.

[108] D Le Bihan. Looking into the functional architecture of the brain with diffusion MRI. *Nature Reviews Neuroscience*, 4(6):469–480, 2003.

[109] D Le Bihan, E Breton, D Lallemand, ML Aubin, J Vignaud, and M Laval-Jeantet. Separation of diffusion and perfusion in intravoxel incoherent motion MR imaging. *Radiology*, 168(2):497–505, 1988.

[110] TB Leergaard, NS White, A De Crespigny, I Bolstad, H D'Arceuil, JG Bjaalie, and AM Dale. Quantitative histological validation of diffusion MRI fiber orientation distributions in the rat brain. *PloS one*, 5(1):e8595, 2010.

[111] T Liimatainen, DJ Sorce, R O'Connell, M Garwood, and S Michaeli. MRI contrast from relaxation along a fictitious field (RAFF). *Magnetic Resonance in Medicine*, 64(4):983–994, 2010.

[112] C Lukas, MH Sombekke, B Bellenberg, HK Hahn, V Popescu, K Bendfeldt, EW Radue, A Gass, SJ Borgwardt, L Kappos, Y Naegelin, DL Knol, CH Polman, JJG Geurts, F Barkhof, and H Vrenken. Relevance of spinal cord abnormalities to clinical disability in multiple sclerosis: MR imaging findings in a large cohort of patients. *Radiology*, 269(2):542–52, 2013.

[113] H Lundell, JB Nielsen, M Ptito, and TB Dyrby. Distribution of collateral fibers in the monkey cervical spinal cord detected with diffusion-weighted magnetic resonance imaging. *Neuroimage*, 56(3):923–929, 2011.

[114] AL Mackay, K Whittall, J Adler, D Li, D Paty, and D Graeb. In vivo visualization of myelin water in brain by magnetic resonance. *Magnetic Resonance in Medicine*, 31(6):673–677, 1994.

[115] DH Mahad, BD Trapp, and H Lassmann. Pathological mechanisms in progressive multiple sclerosis. *The Lancet Neurology*, 14(2):183–193, 2015.

[116] S Maki, M Koda, M Ota, Y Oikawa, K Kamiya, T Inada, T Furuya, K Takahashi, Y Masuda, K Matsumoto, M Kojima, T Obata, and M Yamazaki. Reduced field-of-view diffusion tensor imaging of the spinal cord shows motor dysfunction of the lower extremities in patients with cervical compression myelopathy. *Spine (early view)*, 2015.

[117] M Makino, K Mimatsu, H Saito, N Konishi, and Y Hashizume. Morphometric study of myelinated fibers in human cervical spinal cord white matter. *Spine*, 21(9):1010–1016, 1996.

[118] KV Mardia and PE Jupp. Directional statistics, volume 494. John Wiley & Sons, 2009.

[119] J Mattiello, PJ Basser, and D Le Bihan. The b matrix in diffusion tensor echo-planar imaging. *Magnetic Resonance in Medicine*, 37(2):292–300, 1997.

[120] J Mattiello, PJ Basser, and D LeBihan. Analytical expressions for the b matrix in NMR diffusion imaging and spectroscopy. *Journal of magnetic resonance, Series A*, 108(2):131–141, 1994.

[121] JW McDonald and C Sadowsky. Spinal-cord injury. *The Lancet*, 359(9304):417–425, 2002.

[122] DJ McHugh, F Zhou, PL Cristinacce Hubbard, JH Naish, and GJM Parker. Ground truth for diffusion MRI in cancer: a model-based investigation of a novel tissue-mimetic material. In *proceedings of Medical Image Computing and Computer-Assisted Intervention* (MICCAI) *meeting*, pages 179–190, 2015.

[123] KD Merboldt, W Hanicke, and J Frahm. Self-diffusion NMR imaging using stimulated echoes. *Journal of Magnetic Resonance*, 64(3):479–486, 1985.

[124] L Minati and WP Weglarz. Physical foundations, models, and methods of diffusion magnetic resonance imaging of the brain: a review. *Concepts in Magnetic Resonance Part A*, 30(5):278–307, 2007.

[125] PP Mitra and BI Halperin. Effects of finite gradient-pulse widths in pulsed-field-gradient diffusion measurements. *Journal of Magnetic Resonance, Series A*, 113(1):94–101, 1995.

[126] PP Mitra, PN Sen, LM Schwartz, and P Le Doussal. Diffusion propagator as a probe of the structure of porous media. *Physical Review Letters*, 68(24):3555, 1992.

[127] M Modat, MJ Cardoso, P Daga, D Cash, NC Fox, and S Ourselin. Inverse-consistent symmetric free form deformation. In *Biomedical Image Registration*, pages 79–88. Springer, 2012.

[128] M Modat, GR Ridgway, ZA Taylor, M Lehmann, J Barnes, DJ Hawkes, NC Fox, and S Ourselin. Fast free-form deformation using graphics processing units. *Computer methods and programs in biomedicine*, 98(3):278–284, 2010.

[129] S Mohammadi, P Freund, T Feiweier, A Curt, and N Weiskopf. The impact of post-processing on spinal cord diffusion tensor imaging. *NeuroImage*, 70:377–385, 2013.

[130] BF Moroney, T Stait-Gardner, B Ghadirian, NN Yadav, and WS Price. Numerical analysis of NMR diffusion measurements in the short gradient pulse limit. *Journal of Magnetic Resonance*, 234:165–175, 2013.

[131] JP Mottershead, K Schmierer, M Clemence, JS Thornton, F Scaravilli, GJ Barker, PS Tofts, J Newcombe, ML Cuzner, RJ Ordidge, WI McDonald, and DH Miller. High field MRI correlates of myelin content and axonal density in multiple sclerosis. *Journal of Neurology*, 250(11):1293–1301, 2003.

[132] N Muhlert, V Sethi, T Schneider, P Daga, L Cipolotti, HA Haroon, GJM Parker, S Ourselin, CAM Wheeler-Kingshott, DH Miller, MA Ron, and DC Chard. Diffusion MRI-based cortical complexity alterations associated with executive function in multiple sclerosis. *Journal of Magnetic Resonance Imaging*, 38(1):54–63, 2013.

[133] M Nilsson, J Lätt, E Nordh, R Wirestam, F Ståhlberg, and S Brockstedt. On the effects of a varied diffusion time in vivo: is the diffusion in white matter restricted? *Magnetic resonance imaging*, 27(2):176–187, 2009.

[134] M Nilsson, J Lätt, D van Westen, S Brockstedt, S Lasič, F Ståhlberg, and D Topgaard. Noninvasive mapping of water diffusional exchange in the human brain using filter-exchange imaging. *Magnetic Resonance in Medicine*, 69(6):1572–1580, 2013.

[135] M Nilsson, D van Westen, F Ståhlberg, PC Sundgren, and J Lätt. The role of tissue microstructure and water exchange in biophysical modelling of diffusion in white matter. *Magnetic Resonance Materials in Physics, Biology and Medicine*, 26(4):345–370, 2013.

[136] L Ning, F Laun, Y Gur, EVR DiBella, S Deslauriers-Gauthier, T Megherbi, A Ghosh, M Zucchelli, G Menegaz, R Fick, S St-Jean, M Paquette, R Aranda, M Descoteaux, R Deriche, L O'Donnell, and Y Rathi. Sparse reconstruction challenge for diffusion MRI: validation on a physical phantom to determine which acquisition scheme and analysis method to use? *Medical Image Analysis*, 26(1):316–331, 2015.

[137] DS Novikov, IO Jelescu, and E Fieremans. From diffusion signal moments to neurite diffusivities, volume fraction and orientation distribution: an exact solution. In *proceedings of the 23rd meeting of the International Society for Magnetic Resonance in Medicine* (ISMRM), page 0469, 2015.

[138] DS Novikov, JH Jensen, JA Helpern, and E Fieremans. Revealing mesoscopic structural universality with diffusion. *Proceedings of the National Academy of Sciences*, 111(14):5088–5093, 2014.

[139] H Nyquist. Thermal agitation of electric charge in conductors. *Physical review*, 32(1):110, 1928.

[140] J Oh, S Saidha, M Chen, SA Smith, J Prince, C Jones, M Diener-West, PCM van Zijl, DS Reich, and PA Calabresi. Spinal cord quantitative MRI discriminates between disability levels in multiple sclerosis. *Neurology*, 80(6):540–547, 2013.

[141] GG Ortiz, FP Pacheco-Moisés, MA Macías-Islas, LJ Flores-Alvarado, MA Mireles-Ramírez, ED González-Renovato, VE Hernández-Navarro, AL Sánchez-López, and MA Alatorre-Jiménez. Role of the blood–brain barrier in multiple sclerosis. *Archives of medical research*, 45(8):687–697, 2014.

[142] E Özarslan and PJ Basser. MR diffusion – "diffraction" phenomenon in multi-pulse-field-gradient experiments. *Journal of Magnetic Resonance*, 188(2):285–294, 2007.

[143] B Palan, FV Santos, JM Karam, B Courtois, and M Husak. New ISFET sensor interface circuit for biomedical applications. *Sensors and Actuators B: Chemical*, 57(1):63–68, 1999.

[144] D Paling, BS Solanky, F Riemer, DJ Tozer, CAM Wheeler-Kingshott, R Kapoor, X Golay, and DH Miller. Sodium accumulation is associated with disability and a progressive course in multiple sclerosis. *Brain*, 136(7):2305–2317, 2013.

[145] A Palmgren. Specific silver staining of nerve fibres - 1. Technique for vertebrates. *Acta Zoologica*, 41(3):239–265, 1960.

[146] E Panagiotaki, H Fonteijn, B Siow, MG Hall, A Price, MF Lythgoe, and DC Alexander. Two-compartment models of the diffusion MR signal in brain white matter. In *proceedings of Medical Image Computing and Computer-Assisted Intervention* (MICCAI) *meeting*, pages 329–336, 2009.

[147] E Panagiotaki, T Schneider, B Siow, MG Hall, MF Lythgoe, and DC Alexander. Compartment models of the diffusion MR signal in brain white matter: a taxonomy and comparison. *NeuroImage*, 59(3):2241–2254, 2012.

[148] E Panagiotaki, S Walker-Samuel, B Siow, SP Johnson, V Rajkumar, RB Pedley, MF Lythgoe, and DC Alexander. Noninvasive quantification of solid tumor microstructure using VERDICT MRI. *Cancer Research*, 74(7):1902–1912, 2014.

[149] M Petracca, L Fleysher, N Oesingmann, and M Inglese. Sodium MRI of multiple sclerosis. *NMR in Biomedicine (ahead of print)*, 2015.

[150] KP Pruessmann, M Weiger, MB Scheidegger, and P Boesiger. SENSE: sensitivity encoding for fast MRI. *Magnetic resonance in medicine*, 42(5):952–962, 1999.

[151] NA Rangwala, DB Hackney, W Dai, and DC Alsop. Diffusion restriction in the human spinal cord characterized in vivo with high b-value STEAM diffusion imaging. *NeuroImage*, 82:416–425, 2013.

[152] PJ Ross, LM Broche, and DJ Lurie. Rapid field-cycling MRI using fast spin-echo. *Magnetic Resonance in Medicine*, 73(3):1120–1124, 2015.

[153] S Sasaki, Y Tsutsumi, K Yamane, H Sakuma, and S Maruyama. Sporadic amyotrophic lateral sclerosis with extensive neurological involvement. *Acta Neuropathologica*, 84(2):211–215, 1992.

[154] M Schachter, MD Does, AW Anderson, and JC Gore. Measurements of restricted diffusion using an oscillating gradient spin-echo sequence. *Journal of Magnetic Resonance*, 147(2):232–237, 2000.

[155] K Schmierer, CAM Wheeler-Kingshott, PA Boulby, F Scaravilli, DR Altmann, GJ Barker, PS Tofts, and DH Miller. Diffusion tensor imaging of *post mortem* multiple sclerosis brain. *NeuroImage*, 35(2):467–477, 2007.

[156] T Schneider, W Brownlee, H Zhang, O Ciccarelli, DH Miller, and CAM Wheeler-Kingshott. Application of multi-shell NODDI in multiple sclerosis. In *proceedings of the 22nd meeting of the International Society for Magnetic Resonance in Medicine* (ISMRM), page 0019, 2014.

[157] T Schneider, CAM Wheeler-Kingshott, and DC Alexander. In-vivo estimates of axonal characteristics using optimized diffusion MRI protocols for single fibre orientation. In *proceedings of Medical Image Computing and Computer-Assisted Intervention* (MICCAI) *meeting*, pages 623–630, 2010.

[158] G Schwarz. Estimating the dimension of a model. *The Annals of Statistics*, 6(2):461–464, 1978.

[159] A Seehaus, A Roebroeck, M Bastiani, L Fonseca, H Bratzke, N Lori, A Vilanova, R Goebel, and R Galuske. Histological validation of high-resolution DTI in human post mortem tissue. *Frontiers in Neuroanatomy*, 9, 2015.

[160] N Shemesh, D Barazany, O Sadan, L Bar, Y Zur, Y Barhum, N Sochen, D Offen, Y Assaf, and Y Cohen. Mapping apparent eccentricity and residual ensemble anisotropy in the gray matter using angular double-pulsed-field-gradient MRI. *Magnetic Resonance in Medicine*, 68(3):794–806, 2012.

[161] TM Shepherd, PE Thelwall, GJ Stanisz, and SJ Blackband. Aldehyde fixative solutions alter the water relaxation and diffusion properties of nervous tissue. *Magnetic Resonance in Medicine*, 62(1):26–34, 2009.

[162] LA Shepp and BF Logan. The Fourier reconstruction of a head section. *IEEE Transactions on nuclear science*, 21(3):21–43, 1974.

[163] M Shintaku, A Hirano, and JF Llena. Increased diameter of demyelinated axons in chronic multiple sclerosis of the spinal cord. *Neuropathology and applied neurobiology*, 14(6):505–510, 1988.

[164] AK Smith, RD Dortch, LM Dethrage, and SA Smith. Rapid, high-resolution quantitative magnetization transfer MRI of the human spinal cord. *NeuroImage*, 95:106–116, 2014.

[165] SA Smith, RAE Edden, JAD Farrell, PB Barker, and P Van Zijl. Measurement of T1 and T2 in the cervical spinal cord at 3 Tesla. *Magnetic Resonance in Medicine*, 60(1):213–219, 2008.

[166] SA Smith, CK Jones, A Gifford, V Belegu, BA Chodkowski, JAD Farrell, BA Landman, DS Reich, PA Calabresi, JW McDonald, and PC van Zijl. Reproducibility of tract-specific magnetization transfer and diffusion tensor imaging in the cervical spinal cord at 3 Tesla. *NMR in Biomedicine*, 23(2):207–217, 2010.

[167] SK Song, J Yoshino, TQ Le, SJ Lin, SW Sun, AH Cross, and RC Armstrong. Demyelination increases radial diffusivity in corpus callosum of mouse brain. *NeuroImage*, 26(1):132–140, 2005.

[168] SN Sotiropoulos, TEJ Behrens, and S Jbabdi. Ball and rackets: inferring fiber fanning from diffusion-weighted MRI. *NeuroImage*, 60(2):1412–1425, 2012.

[169] SN Sotiropoulos, S Moeller, S Jbabdi, J Xu, JL Andersson, EJ Auerbach, E Yacoub, D Feinberg, K Setsompop, LL Wald, TEJ Behrens, K Ugurbil, and C Lenglet. Effects of image reconstruction on fiber orientation mapping from multichannel diffusion MRI: reducing the noise floor using SENSE. *Magnetic Resonance in Medicine*, 70(6):1682–1689, 2013.

[170] GJ Stanisz, GA Wright, RM Henkelman, and A Szafer. An analytical model of restricted diffusion in bovine optic nerve. *Magnetic Resonance in Medicine*, 37(1):103–111, 1997.

[171] MK Stehling, R Turner, and P Mansfield. Echo-planar imaging: magnetic resonance imaging in a fraction of a second. *Science*, 254(5028):43–50, 1991.

[172] EO Stejskal and JE Tanner. Spin diffusion measurements: spin echoes in the presence of a time-dependent field gradient. *The Journal of Chemical Physics*, 42(1):288–292, 1965.

[173] N Stikov, JSW Campbell, T Stroh, M Lavelée, S Frey, J Novek, S Nuara, MK Ho, BJ Bedell, RF Dougherty, IR Leppert, M Boudreau, S Narayanan, T Duval, J Cohen-Adad, PA Picard, A Gasecka, D Coté, and GB Pike. In vivo histology of the myelin g-ratio with magnetic resonance imaging. *NeuroImage*, 118:397–405, 2015.

[174] PW Stroman, C Wheeler-Kingshott, M Bacon, JM Schwab, R Bosma, J Brooks, D Cadotte, T Carlstedt, O Ciccarelli, J Cohen-Adad, A Curt, N Evangelou, MG Fehlings, M Filippi, BJ Kelley, S Kollias, A Mackay, CA Porro, S Smith, SM Strittmatter, P Summers, and I Tracey. The current state-of-the-art of spinal cord imaging: methods. *NeuroImage*, 84:1070–1081, 2014.

[175] P Summers, A Bauleo, S Favilla, F Cretti, F Lui, and C Porro. Gross structure of magnetic field inhomogeneity in the human cervical spinal cord. In *proceedings of the 22nd meeting of the International Society for Magnetic Resonance in Medicine* (ISMRM), page 1721, 2014.

[176] P Summers, P Staempfli, T Jaermann, S Kwiecinski, and S Kollias. A preliminary study of the effects of trigger timing on diffusion tensor imaging of the human spinal cord. *American Journal of Neuroradiology*, 27(9):1952–1961, 2006.

[177] F Szczepankiewicz, S Lasič, D van Westen, PC Sundgren, E Englund, CF Westin, F Ståhlberg, J Lätt, D Topgaard, and M Nilsson. Quantification of microscopic diffusion anisotropy disentangles effects of orientation dispersion from microstructure: applications in healthy volunteers and in brain tumors. *NeuroImage*, 104:241–252, 2015.

[178] M Taquet, B Scherrer, N Boumal, JM Peters, B Macq, and SK Warfield. Improved fidelity of brain microstructure mapping from single-shell diffusion MRI. *Medical Image Analysis*, 26(1):268–286, 2015.

[179] CH Tator and MG Fehlings. Review of the secondary injury theory of acute spinal cord trauma with emphasis on vascular mechanisms. *Journal of Neurosurgery*, 75(1):15–26, 1991.

[180] P Tofts. *Quantitative MRI of the brain: measuring changes caused by disease*. John Wiley & Sons, 2005.

[181] HC Torrey. Bloch equations with diffusion terms. *Physical Review*, 104(3):563, 1956.

[182] J Tournier, F Calamante, DG Gadian, and A Connelly. Direct estimation of the fiber orientation density function from diffusion-weighted MRI data using spherical deconvolution. *NeuroImage*, 23(3):1176–1185, 2004.

[183] J Tournier, Chun-Hung Yeh, Fernando Calamante, Kuan-Hung Cho, Alan Connelly, and CP Lin. Resolving crossing fibres using constrained spherical deconvolution: validation using diffusion-weighted imaging phantom data. *NeuroImage*, 42(2):617–625, 2008.

[184] A Tristán-Vega, CF Westin, and S Aja-Fernández. Estimation of fiber orientation probability density functions in high angular resolution diffusion imaging. *NeuroImage*, 47(2):638–650, 2009.

[185] C Tso, GM Currie, D Gilmore, and H Kiat. Electrocardiography: a technologist's guide to interpretation. *Journal of Nuclear Medicine Technology*, 43(4):247–252, 2015.

[186] DS Tuch. Q-ball imaging. *Magnetic Resonance in Medicine*, 52(6):1358–1372, 2004.

[187] DS Tuch, TG Reese, MR Wiegell, N Makris, JW Belliveau, and VJ Wedeen. High angular resolution diffusion imaging reveals intravoxel white matter fiber heterogeneity. *Magnetic Resonance in Medicine*, 48(4):577–582, 2002.

[188] C Tur, S Ramagopalan, DR Altmann, B Bodini, M Cercignani, Z Khaleeli, DH Miller, AJ Thompson, and O Ciccarelli. HLA-DRB1*15 influences the development of brain tissue damage in early PPMS. *Neurology*, 83(19):1712–1718, 2014.

[189] A Vedantam, MB Jirjis, BD Schmit, MC Wang, JL Ulmer, and SN Kurpad. Characterization and limitations of diffusion tensor imaging metrics in the cervical spinal cord in neurologically intact subjects. *Journal of Magnetic Resonance Imaging*, 38(4):861–867, 2013.

[190] J Veraart, E Fieremans, and DS Novikov. Diffusion MRI noise mapping using random matrix theory. *Magnetic Resonance in Medicine (early view)*, 2015.

[191] T Verma and J Cohen-Adad. Effect of respiration on the B0 field in the human spinal cord at 3T. *Magnetic Resonance in Medicine*, 72(6):1629–1636, 2014.

[192] H Wang, J Zhu, and T Akkin. Serial optical coherence scanner for large-scale brain imaging at microscopic resolution. *NeuroImage*, 84:1007–1017, 2014.

[193] H Wang, J Zhu, M Reuter, LN Vinke, A Yendiki, DA Boas, B Fischl, and T Akkin. Cross-validation of serial optical coherence scanning and diffusion tensor imaging: a study on neural fiber maps in human medulla oblongata. *NeuroImage*, 100:395–404, 2014.

[194] X Wang, MF Cusick, Y Wang, P Sun, JE Libbey, K Trinkaus, RS Fujinami, and SK Song. Diffusion basis spectrum imaging detects and distinguishes coexisting subclinical inflammation, demyelination and axonal injury in experimental autoimmune encephalomyelitis mice. *NMR in Biomedicine*, 27(7):843–852, 2014.

[195] Y Wang, P Sun, Q Wang, K Trinkaus, RE Schmidt, RT Naismith, AH Cross, and SK Song. Differentiation and quantification of inflammation, demyelination and axon injury or loss in multiple sclerosis. *Brain*, 138(5):1223–1238, 2015.

[196] Y Wang, Q Wang, JP Haldar, FC Yeh, M Xie, P Sun, TW Tu, K Trinkaus, RS Klein, AH Cross, and SK Song. Quantification of increased cellularity during inflammatory demyelination. *Brain*, 134(12):3590–3601, 2011.

[197] JP Wansapura, SK Holland, RS Dunn, and WS Ball. NMR relaxation times in the human brain at 3.0 Tesla. *Journal of magnetic resonance imaging*, 9(4):531–538, 1999.

[198] VJ Wedeen, P Hagmann, WYI Tseng, TG Reese, and RM Weisskoff. Mapping complex tissue architecture with diffusion spectrum magnetic resonance imaging. *Magnetic Resonance in Medicine*, 54(6):1377–1386, 2005.

[199] M Weigel. Extended phase graphs: dephasing, RF pulses, and echoes – pure and simple. *Journal of Magnetic Resonance Imaging*, 41(2):266–295, 2015.

[200] Q Wen, DAC Kelley, S Banerjee, JM Lupo, SM Chang, D Xu, CP Hess, and SJ Nelson. Clinically feasible NODDI characterization of glioma using multiband EPI at 7 T. *NeuroImage: Clinical*, 9:291–299, 2015.

[201] WA Wesselink, J Holsheimer, B Nuttin, HBK Boom, GW King, JM Gybels, and P de Sutter. Estimation of fiber diameters in the spinal dorsal columns from clinical data. *IEEE Transactions on Biomedical Engineering*, 45(11):1355–1362, 1998.

[202] CF Westin, F Szczepankiewicz, O Pasternak, E Özarslan, D Topgaard, H Knutsson, and M Nilsson. Measurement tensors in diffusion MRI: generalizing the concept of diffusion encoding. In *proceedings of Medical Image Computing and Computer-Assisted Intervention* (MICCAI) *meeting*, pages 209–216, 2014.

[203] CA Wheeler-Kingshott, PW Stroman, JM Schwab, M Bacon, R Bosma, J Brooks, DW Cadotte, T Carlstedt, O Ciccarelli, J Cohen-Adad, A Curt, N Evangelou, MG Fehlings, M Filippi, BJ Kelley, S Kollias, A Mackay, C Porro, S Smith, SM Strittmatter, P Summers, and I Tracey. The current state-of-the-art of spinal cord imaging: applications. *NeuroImage*, 84:1082–1093, 2014.

[204] CAM Wheeler-Kingshott and M Cercignani. About “axial” and “radial” diffusivities. *Magnetic Resonance in Medicine*, 61(5):1255–1260, 2009.

[205] CAM Wheeler-Kingshott, SJ Hickman, GJM Parker, O Ciccarelli, MR Symms, DH Miller, and GJ Barker. Investigating cervical spinal cord structure using *axial* diffusion tensor imaging. *NeuroImage*, 16(1):93–102, 2002.

[206] CAM Wheeler-Kingshott, GJM Parker, MR Symms, SJ Hickman, PS Tofts, DH Miller, and GJ Barker. ADC mapping of the human optic nerve: increased resolution, coverage, and reliability with CSF-suppressed ZOOM-EPI. *Magnetic Resonance in Medicine*, 47(1):24–31, 2002.

[207] NS White, TB Leergaard, H D’Arceuil, JG Bjaalie, and AM Dale. Probing tissue microstructure with restriction spectrum imaging: histological and theoretical validation. *Human Brain Mapping*, 34(2):327–346, 2013.

[208] BJ Wilm, J Svensson, A Henning, KP Pruessmann, P Boesiger, and SS Kollias. Reduced field-of-view MRI using outer volume suppression for spinal cord diffusion imaging. *Magnetic Resonance in Medicine*, 57(3):625–630, 2007.

[209] GP Winston, C Micallef, MR Symms, DC Alexander, JS Duncan, and H Zhang. Advanced diffusion imaging sequences could aid assessing patients with focal cortical dysplasia and epilepsy. *Epilepsy Research*, 108(2):336–339, 2014.

[210] C Wisnieff, S Ramanan, J Olesik, S Gauthier, Y Wang, and D Pitt. Quantitative susceptibility mapping (QSM) of white matter multiple sclerosis lesions: interpreting positive susceptibility and the presence of iron. *Magnetic Resonance in Medicine*, 74(2):564–570, 2005.

[211] D Wu, D Reisinger, J Xu, SA Fatemi, P van Zijl, S Mori, and J Zhang. Localized diffusion magnetic resonance micro-imaging of the live mouse brain. *NeuroImage*, 91:12–20, 2014.

[212] Y Wu, AL Alexander, JO Fleming, ID Duncan, and AS Field. Myelin water fraction in human cervical spinal cord in vivo. *Journal of computer assisted tomography*, 30(2):304–306, 2006.

[213] J Xu, JS Shimony, EC Klawiter, AZ Snyder, K Trinkaus, RT Naismith, TLS Benzinger, AH Cross, and SK Song. Improved in vivo diffusion tensor imaging of human cervical spinal cord. *NeuroImage*, 67:64–76, 2013.

[214] DA Yablonskiy, GL Bretthorst, and JJH Ackerman. Statistical model for diffusion attenuated MR signal. *Magnetic Resonance in Medicine*, 50(4):664–669, 2003.

[215] H Zhang, T Schneider, CA Wheeler-Kingshott, and DC Alexander. NODDI: practical in vivo neurite orientation dispersion and density imaging of the human brain. *NeuroImage*, 61(4):1000–1016, 2012.